

THREE STUDIES IN HIGH-FIELD MR ENGINEERING: SAR REDUCTION
THROUGH SEQUENTIAL RF PULSES, A SYSTEM FOR B1+ STEERING, AND A
LOW-COMPLEXITY MULTI-NUCLEI ARRAY COIL

A Dissertation

by

CHENHAO SUN

Submitted to the Graduate and Professional School of
Texas A&M University
in partial fulfillment of the requirements for the degree of

DOCTOR OF PHILOSOPHY

Chair of Committee,	Steven M. Wright
Committee Members,	Jim Xiuquan Ji
	Mary P. McDougall
	Scott L. Miller
Head of Department,	Miroslav M. Begovic

May 2022

Major Subject: Electrical Engineering

Copyright 2022 Chenhao Sun

ABSTRACT

Recent years have seen great development in ultra-high-field (UHF) magnetic resonance imaging (MRI). In particular, the advantage of increased sensitivity available at UHF and the scan time acceleration enabled by parallel imaging can together offer unprecedented imaging detail. However, technical challenges, such as B_1^+ inhomogeneity and specific absorption rate (SAR) also come with the UHF scanner. A head coil array at 9.4T using a novel transmit approach of serial transmit parallel receive (ST_xPR_x) is modeled and analyzed in this doctoral work. By transmitting each coil element in an array sequentially rather than simultaneously, a 25.7% peak SAR reduction can be found. For MRI applications with significant SAR concerns, such as lower-gamma nuclei imaging, this work provides a potential alternative approach. To mitigate the image inhomogeneity issue at 7T, an add-on B_1^+ steering system is reported in this doctoral work. By using a house-designed phase shifter array and associated circuitry, 8 transmit channels with independent phase control can be created to drive an 8-channel transmit coil array, yet with only two transmitters installed on the scanner. By using the conjugate-phase steering method, an approximately $2.6 \times 4.2 \text{ cm}^2$ very homogenous B_1^+ region and approximately $5.9 \times 8.9 \text{ cm}^2$ fairly homogenous B_1^+ region can be generated at any targeting point in phantom. This work suggests a different hardware approach to gain the new degree of freedom of controllable transmit B_1^+ pattern in parallel imaging.

Along with the development of higher B_0 strength, multi-nuclei MRI have become increasingly popular since both the anatomical detail from proton and the physiological process from X-nuclei can be acquired simultaneously. As the essential tool in multi-nuclei MRI, the multi-tuned RF array coil suffers from the excessive complexity of the multi-tuned retrofit of the current decoupling mechanism. A novel strategy aimed at simplifying multi-nuclei array coil's decoupling procedure is investigated in this doctoral work. High impedance preamplifier and transformer are experimented to achieve coil decoupling in a broadband way. The preliminary test result validates the feasibility of achieving decoupling for a broader frequency range, yet the decoupling bandwidth and coil sensitivity in this approach are currently limited by the characteristic of the transformer.

ACKNOWLEDGMENTS

I would like to thank my parents for their constant support, encouragement, and the sacrifices they made. Without the opportunity they provided for me, I could never achieve this work.

I would like to thank my advisor, Dr. Wright, for guiding me through the high and low points in my research with his great patience and scientific expertise. I am grateful for these wonderful research opportunities that he provided for me to learn, experiment, and collaborate.

I would like to thank my colleagues, who once helped, shared knowledge, and worked with me, Dr. John Bosshard, Dr. Neal Hollingsworth, Dr. Jiaming Cui, Dr. Stephen Ogier, Dr. Dheyaa Alkandari, Dr. Matthew Wilcox, Dr. Wen-Yang Chiang, Kevin Patel, Minyu Gu, Courtney Bauer, Jue Hou, Madavan Raja Viswanath, and Joseph Busher.

CONTRIBUTORS AND FUNDING SOURCES

Contributors

This work was supervised by a dissertation committee consisting of Professor Steven Wright [advisor] and Professor Jim Ji, Professor Scott Miller of the Department of Electrical and Computer Engineering, and Professor Mary McDougall of the Department of Biomedical Engineering.

The data analysis for Chapter III was conducted under the help of Dr. Keith Thulborn of the Department of Radiology, Physiology, and Biophysics at the University of Illinois at Chicago.

The MRI experiments for Chapter IV were conducted under the help of Dr. Ivan Dimitrov and Dr. Sergey Cheshkov of Advanced Imaging Research Center at Texas Southwestern Medical Center. The hardware for Chapter IV was conducted in collaboration with Kevin Patel and Dr. Neal Hollingsworth of the Department of Electrical and Computer Engineering. The dipole array for Chapter IV was conducted by Dr. Matthew Wilcox of the Department of Biomedical Engineering.

The MRI experiments for Chapter V were conducted under the help of Dr. John Bosshard of the Department of Engineering Technology & Industrial Distribution. The phantom and ^{23}Na volume coil for Chapter V was conducted by Joseph Busher of the Department of Biomedical Engineering.

All other work conducted for the dissertation was completed by the student independently.

Funding Sources

This work was also made possible in part by Cancer Prevention and Research Institute of Texas under Grant Number RP160847, as well as the National Institutes of Health under Grant Number 5R21EB028516-02.

Its contents are solely the responsibility of the authors and do not necessarily represent the official views of the CPRIT and NIH.

NOMENCLATURE

BBB	Beaglebone Black
CNR	Contrast to Noise Ratio
DUT	Device Under Test
EMF	Electromotive Force
FDTD	Finite-Difference Time-Domain
I/O	Input/Output
LNA	Low Noise Amplifier
MCU	Microcontroller
MN	Matching Network
MRI	Magnetic Resonance Imaging
NF	Noise Figure
OPA	Operational Amplifier
PCB	Printed Circuit Board
RF	Radiofrequency
ROI	Region of Interest
SAR	Specific Absorption Rate
SNR	Signal to Noise Ratio
STxPRx	Serial Transmit Parallel Receive
UHF	Ultra-High-Field
VNA	Vector Network Analyzer

TABLE OF CONTENTS

	Page
ABSTRACT	ii
ACKNOWLEDGMENTS.....	iv
CONTRIBUTORS AND FUNDING SOURCES.....	v
NOMENCLATURE.....	vii
TABLE OF CONTENTS	viii
LIST OF FIGURES.....	x
LIST OF TABLES	xvi
CHAPTER I INTRODUCTION	1
1.1 Ultra-High Field MRI and B_1^+ shimming	1
1.2 Multi-Nuclei MRI	5
1.3 Dissertation Organization.....	9
CHAPTER II BACKGROUND.....	11
2.1 SAR in MRI	11
2.3 B_1^+ /RF shimming.....	12
2.5 Multi-Nuclei MRI Coil	13
CHAPTER III SAR MODELLING FOR SERIAL TRANSMIT PARALLEL RECEIVE COIL ARRAY.....	17
3.1 Overview.	17
3.2 Model Building in Remcom and B_1^+ /E Field Simulation.....	19
3.3 First Scaling for Equal Net Input Power	21
3.4 Second Scaling for Equal 90° Tip Angle at Brain Center.....	26
3.5 Final Results for SAR	28
CHAPTER IV AN ADD-ON SYSTEM TO ENABLE DYNAMIC B_1^+ STEERING FOR TRANSMIT ARRAYS AT 7T.....	32
4.1 System Overview	32

4.2 Wilkinson Power Divider.....	35
4.3 Phase Shifter Module	36
4.4 Control and Measure Module.....	40
4.5 Simulation Study.....	46
4.6 Bench Validation.....	51
4.7 Imaging on 7T Scanner	54
4.8 B_1^+ Results Analysis and Discussion	57
4.9 Summary	59
CHAPTER V INVESTIGATION OF DECOUPLING MULTI-NUCLEI SURFACE COIL ARRAY USING HIGH IMPEDANCE PREAMPLIFIER.....	61
5.1 Overview of Proposed Decoupling Strategy	61
5.2 High Impedance Preamplifier: Operational Amplifier.....	66
5.3 Matching Network with Ferrite Core Transformer	79
5.4 Matching Network with Air-Core transformer	88
5.5 Imaging Validation.....	102
5.6 Discussion and Future Potential.....	116
5.7 Summary	121
CHAPTER VI CONCLUSIONS	123
REFERENCES	126
APPENDIX A SUPPLEMENTARY MATERIAL FOR HEAD COIL ARRAY ANALYSIS	138
APPENDIX B SUPPLEMENTARY MATERIAL FOR B_1^+ STEERING SYSTEM..	152
B.1 Drawing of PIN Diode Driver Board.	152
B.2 Drawing of Phase Shifter Board.....	159
APPENDIX C SUPPLEMENTARY MATERIAL FOR HIGH IMPEDANCE DECOUPLING PREAMPLIFIER	168
C.1 Main Function.....	168
C.2 Sub-Functions.....	180

LIST OF FIGURES

	Page
Figure 1. Double resonating a coil using LCC trap circuits. LCC trap circuit can provide a smaller capacitance at higher frequency and a bigger capacitance at lower frequency, and therefore can resonate a single coil at two frequencies.....	14
Figure 2. Dual-tuned surface coil using PIN diode switch. Forward biasing the PIN diode allows additional capacitance to be added on the coil for lower frequency tuning, and reverse biasing the PIN diode disables the extra capacitance for higher frequency tuning.....	15
Figure 3. Double-nuclei surface coil using nesting structure.....	16
Figure 4. Overview of the SAR calculation workflow.....	18
Figure 5. Picture of the general geometry of head coil array built-in Remcom.....	20
Figure 6. Cross-section view of the head model and coil array that was used in SAR modeling.....	20
Figure 7. Simulated B_1^+ map (μT) of each coil after the 1 st scaling for equal net input power (1W).....	23
Figure 8 Simulated tip angle map (degree) of each coil after the 1 st scaling for equal net input power (1W).....	24
Figure 9. Simulated B_1^+ maps (Top) and tip angle maps (Bottom) for series mode (Left) and parallel mode (Right), after the 1 st scaling for equal net input power (4W).....	25
Figure 10. Simulated B_1^+ maps (Top) and tip angle maps(Bottom) for series mode (Left) and parallel mode (Right), after the 2 nd scaling for equal tip angle at brain center (90°).	27
Figure 11. Simulated SAR map (W/kg) of each coil after the 1 st and 2 nd scaling.....	29
Figure 12. Simulated SAR map (W/kg) of series mode (Left) and parallel mode (Right) after the 1 st and 2 nd scaling.....	30
Figure 13 An overview of the add-on B_1^+ steering system. Transmit pulses from scanner's power amplifiers were first split into 8 channels, next routed through phase shifter array to be properly phase-shifted, then routed through	

8 channel TR switch and finally get transmitted out from coil array. Figure courtesy ⁴³	33
Figure 14 Overview of hardware of B_1^+ steering system. (A) A non-magnetic server rack can be placed inside the magnetic room. From top to bottom: 8 channel TR switch, 8 channel phase shifter array, 2 channel four-way power divider, and control & measure module. (B) Schematic of TR switch. (C) Another compact server rack placed inside the instrument room, From the top to bottom: TPI & testing amplifier for performing self-check onsite, and BBB Bridge & power supply for driving the whole system. Figure courtesy ⁴³	34
Figure 15. Picture of four-way Wilkinson power divider. This four-way power divider was built from three cascaded regular two-way power dividers. On each divider, two coaxial cables (length of $\lambda/4$ at 298MHz) and one high-power 100 Ω resistor are used. An aluminum heatsink is used under each 100 Ω resistor (on the opposite side of PCB).	35
Figure 16 Overview of phase shifter's schematic and layout. (A) General circuit for phase shifters. (B) 50 Ω termination bits can either block the transmit pulse or allow the pulse to pass through. (C) The transmission line bit can either add a 22.5° or 180° phase delay to the transmit pulse or allow it to pass through. (D) Lumped element bit can either add a 45° or 90° phase delay to the transmit pulse or allow it to pass through. (E) The picture of phase shifter PCB. Figure courtesy ⁴³	39
Figure 17. Picture of a phase shifter module cased inside the enclosure.	40
Figure 18. Overview of control and measurement module. Figure courtesy ⁴³	41
Figure 19. Picture of the control and measure module with annotations of different parts.....	43
Figure 20. Picture of power supply and Beagle Bone Black module with annotations of different parts.	44
Figure 21. Picture of TPI and testing power amplifier module with annotations of different parts.....	45
Figure 22. Overview of the simulation model in Remcom XFDTD. An almond shape uniform phantom (Major axis length of 35.5cm, Minor axis length of 26cm, Conductivity of 0.31 S/m, Permittivity of 45) was built for mimicking abdomen, and 8 dipoles were placed around the phantom as coil array. 8 simulated B+ magnitude maps from individual dipole are shown around the model.	47

Figure 23. Simulated parallel-firing B_1^+ magnitude map with conventional birdcage excitation mode at 298MHz, where Tx pulse' phase of each coil element are $0^\circ, 45^\circ \dots 315^\circ$ degrees. Inhomogeneity of central brightening and undesired nulls can be observed due to the standing wave effect.	48
Figure 24. Simulated Parallel-Firing B_1^+ Magnitude Maps with different target points (Red Maker) of B_1^+ Steering.....	50
Figure 25. Overview of the bench measurement setup. A cross probe installed on a 2-dimensional positioner system is inserted into the phantom and can be moved around to map out the B_1^{\pm} field. Bench-measured B_1^+ magnitude maps from each coil are shown around the setup.	52
Figure 26. Bench-measured parallel-firing B_1^+ magnitude maps with different target points (Red Maker) of B_1^+ Steering.	53
Figure 27. Overview of the system's setup when tested with 7T scanner. The phantom/dipole array was placed on the patient table, and the phase-shifter system was placed near the patient table to interface with the dipole array and scanner's I/O. 8 images of individual coil transmit/receive are shown on the peripheral.	55
Figure 28. B_1^+ steering results acquired on 7T scanner that targeted at 3 different points. The yellow markers indicate where the targeted points locate.	56
Figure 29. Comparison of B_1^+ steering results acquired from simulation (A-C), bench measurement (D-F), and 7T scanner (G-I). The red maker indicates the target point for B_1^+ steering. Figure courtesy ⁴³	58
Figure 30. Conjugate Matching Configuration gives maximum RF power delivery between coil and preamplifier. In this configuration the coil's reactance is canceled thus maximum RF current can be induced on the coil and cause coupling.	62
Figure 31. Roemer's Configuration, using LC and Low impedance preamplifier to create high Z on the coil for additional decoupling, but with a penalty of impedance mismatch as well as narrow operatable frequency	63
Figure 32. Proposed configuration using high impedance preamplifier to decouple coil and use a broadband transformer as the matching network between coil and preamplifier	65
Figure 33. Calculated OPA NF with different Rf or Rg value for investigating optimal performance.	67

Figure 34. Calculated Ideal NF of OPA, versus pure real source resistance (Left), or complex source impedance (Right). The real source resistance in the left figure is plot as a red line on the smith chart as well.....	68
Figure 35. Schematic and picture of the validation OPA board.....	69
Figure 36. Bench measured OPA gain and NF for different values of Rf and Rg for validating the calculation.....	70
Figure 37. Overview and picture of the bench SNR and decoupling measurement setup.....	72
Figure 38. Bench-measured SNR at 1H (200MHz) versus different source impedance (Top). Calculated OPA NF when considering input parasitic capacitance. The agreement can be found between bench measurement and calculation. ...	74
Figure 39. Measured decoupling of a test 4cm coil matched to different impedance and connected with OPA, at 1H Larmor frequency of 200.123MHz.....	75
Figure 40. Bench-measured SNR at 23Na (53MHz) versus different source impedance (Top). Calculated OPA NF when considering input parasitic capacitance. The agreement can be found between bench measurement and calculation.....	77
Figure 41. Measured decoupling of a test 4cm coil matched to different impedance and connected with OPA, at 23Na Larmor frequency of 52.93MHz.....	78
Figure 42. Bench testing performance of two commercial ferrite core transformers	81
Figure 43. Pictures of (a) reference coil with conventional matching network and (b) DUT coil with a single triple-tuned series matching network and transformer WB36-1L.....	83
Figure 44. Bench decoupling measurement both for reference and DUT.....	85
Figure 45. Bench SNR and coil Q measurement both for reference and DUT.....	87
Figure 46. Bench testing performance of the house-built air core transformers.....	90
Figure 47. Schematic and picture of (AB) the reference coil and (C) the testing coil using LCC network and air-core transformer.....	92
Figure 48. Bench decoupling measurement of reference coil and testing double-tuned coil using an air-core transformer and high impedance preamplifier.....	94
Figure 49. Bench SNR and matched impedance of both reference coil and testing coil.	95

Figure 50. Schematic and picture of the testing coil using varactor for tuning and transformer for matching.	99
Figure 51. Bench measurement decoupling, matched impedance, and SNR performance of testing coil using varactor diode and transformer.	100
Figure 52. Measured loss of varactor diode at different frequencies.	101
Figure 53. Pictures of scanner testing setup. (A) Transmit-only 1H birdcage coil. (B) Transmit-only ^{23}Na birdcage coil. (B) Testing phantom for 2x3 loop coil array. (D) Receive-only loop coils/preamplifiers setup of reference coils (left) and testing coils (right).	103
Figure 54. 1H imaging results acquired using two reference 50Ω loop coils with standard 50Ω preamplifier.	105
Figure 55. 1H imaging results acquired using two reference 50Ω loop coils with isolation preamplifier.	106
Figure 56. 1H imaging results acquired using two testing loop coils with LCC and transformer as matching network, and high impedance OPA as the preamplifier. The coupling between the two coils is reduced, however a minor residual pattern can still be observed.	107
Figure 57. 1H SNR comparison between the reference coil in figure 47 (A) with isolation preamplifier or with 50Ω preamplifier, and the testing coil with LCC, transformer in figure 47 (C), and high impedance OPA.	108
Figure 58. ^{23}Na imaging results acquired using two reference 50Ω loop coils with standard 50Ω preamplifier.	109
Figure 59. 1H imaging results acquired using two reference 50Ω loop coils with isolation preamplifier.	110
Figure 60. ^{23}Na imaging results acquired using two testing loop coils with LCC and transformer as matching network, and high impedance OPA as the preamplifier. The coupling between the two coils is reduced.	111
Figure 61. ^{23}Na SNR comparison between the reference coil in figure 48 (B) with isolation preamplifier or with 50Ω preamplifier, and the testing coil with LCC, transformer in figure 47 (C), and high impedance OPA.	112
Figure 62. Bench validation of parallel varactor network as the possible multi-nuclei tuning element.	120

Figure 63. Overview of the PIN diode driver board. Each PCB contains 3 identical driver circuit that controls each bit of the phase shifter individually.	152
Figure 64. One of the three PIN diode driver circuits. The rest two are the same.	153
Figure 65. PCB layout and fabrication aid, front layer.	154
Figure 66. PCB layout and fabrication aid, bottom layer.....	154
Figure 67. Pictures of the assembled Pin diode driver board.....	155
Figure 68. Pictures of the Pin diode driver board inside the RF shield case, with indications of connection.....	156
Figure 69. Overview of the phase shifter circuit, which consists of 5 different bits in series.	159
Figure 70. Schematic of 50Ω termination bit.....	160
Figure 71. Schematic of 180°-bit.	160
Figure 72. Schematic of 22.5° bit.....	161
Figure 73. Schematic of 45°-bit.	161
Figure 74. Schematic of 90°-bit.	162
Figure 75. Top view of layout and picture of an assembled board containing 22.5°-bit, 45°-bit, and 90°-bit.	163
Figure 76. Top view of layout and picture of an assembled board containing 50Ω termination bit and 180°-bit.....	164
Figure 77. Bottom view of layout and picture of an assembled board.....	165

LIST OF TABLES

	Page
Table 1. Summary of information in SAR scaling.....	21
Table 2. The measured sizes of very and fairly homogenous regions were generated when B_1^+ Steering to different target points, for both simulation, bench measurement, and 7T scanner.....	59
Table 3. Summary of the measured SNR and decoupling for both ^{23}Na and ^1H at 4.7T. The linear SNR of the testing coil is calculated based on the raw SNR and then normalized to the reference case acquired with WanTcom isolation preamplifier.....	116
Table 4. Bill of materials for PIN diode driver circuit.	157
Table 5. Bill of materials for phase shifter circuit.....	166

CHAPTER I

INTRODUCTION

Magnetic resonance imaging (MRI) has become one of the most important diagnostic tools in medicine because of its superior soft-tissue contrast and no ionizing radiation. After the first imaging result was presented by Lauterbur¹ in 1973, hardware and technologies of magnetic resonance imaging have been extensively developed by researchers and engineers. The magnet, the core of an MRI scanner, has evolved from resistive 0.3 Tesla² in the early days to superconducting 7 tesla³ and even higher⁴. The modern gradient coil/amplifier can achieve astonishing gradient strength of 300mT/m⁵, while 1-2mT/m can only be generated in the 1980s⁶. As for RF coils, multi-channel transmit and receive coil array⁷⁻⁹ has been commonly used nowadays. These early-stage small solenoidal RF coils¹⁰ have been forgotten in modern clinical MRI. Among all the important technology development, parallel imaging¹¹ can be considered as one of the most important milestones due to numerous advantages. Another hot topic today is multi-nuclei MRI¹².

1.1 Ultra-High Field MRI and B_1^+ shimming

Ultra-high-field ($\geq 7\text{T}$) MRI has become increasingly popular in the last decade, because of its significant advantages in terms of signal-to-noise ratio and contrast-to-noise ratio. However, the UHF scanner also comes with technical issues that need to be

addressed, such as B_1^+ inhomogeneity¹³⁻¹⁸ and increased specific absorption rate (SAR)¹⁹.

The increased SAR at ultra-high-field is an intrinsic problem and has become a major limiting factor for the ultra-high-field scanner²⁰. The relation of SAR²¹ is shown below.

$$SAR \propto \frac{\sigma * B_0^2 * \alpha^2 * D}{\rho}$$

Where σ is the conductivity of the tissue, B_0 is the strength of the static magnetic field, α is the flip angle induced by the transmit pulse, D is the duty cycle of the transmit pulse, and ρ is the density of the tissue. As we can see that the SAR is proportional to the square of the B_0 field, which means for the same patient and the same tip angle, the SAR level at 7T is approximately 5.44 times higher than at 3T. On top of this, the higher Larmor frequency on the UHF scanner led to shorter RF penetration depth, thus requiring higher RF power and thus SAR to achieve the same tip angle at the body center¹⁹. Therefore, the increased SAR level led to a much tighter safety threshold when operating at UHF.

To mitigate the SAR issue at ultra-high field, a novel MRI transmit approach of serial transmit parallel receive (ST_xPR_x) was proposed²². The conventional parallel transmit approach excites each element at the same time, therefore the electric field generated by each element can potentially be aligned and cause SAR hot spot. Instead, the ST_xPR_x approach excites each transmit element sequentially so that the SAR dissipated from each element can only be accumulated linearly. Chapter III of this

dissertation describes the modeling and analysis of the improvement of local maximum SAR when using the ST_xPR_x approach.

B_1^+ inhomogeneity is mainly caused by the decreased wavelength of RF pulse with higher Larmor frequency. For example, at 7 tesla (1H Larmor frequency of 300MHz) the radio wavelength is around 12cm inside human tissue²³. This wavelength has become comparable to the size of the brain or extremity and is even shorter relative to the human abdomen. Therefore, some standing wave effect can almost always be observed in 7T imaging when conventional birdcage excitation mode is used²⁴. When a relatively small object (e.g., human brain) is studied, the short-wavelength effect often appears as a well-documented artifact of “central brightening”^{14,15,24,25}, where the object center usually yields higher SNR than the peripheral. When a relatively large object (e.g., human abdomen) is studied, the inhomogeneity often shows as unexpected flip angle hotspots and nulls^{23,26} disturbing the overall imaging quality. Additionally, the inhomogeneity of the B_1^+ pattern is subject-dependent²⁷, which further complicates the exploration of the UHF scanner in clinical body imaging.

Many methods have been proposed to mitigate these issues, such as adiabatic pulse sequence²⁸, dark mode transmit array²⁹, butler matrix with TIAMO^{30,31}, traveling wave excitation³², and dedicated transmit coil design^{33,34}. Among these approaches, RF shimming or B_1^+ shimming can be considered as the most flexible method³⁵. The general concept of parallel transmit is, instead of using a single channel volume coil for transmit (conventionally a birdcage coil) where the B_1^+ field cannot vary and honestly does not perform well at UHF, multiple transmit elements fed with independent RF pulse are used

to synthesize an improved field pattern, similar with the concept of the phased array in a radar system. Since the total B_1^+ field is the superposition of individual transmit element's B_1^+ field, a more homogenous B_1^+ pattern^{25,26,36-41} or lower SAR level^{19,26} can be achieved by carefully manipulating each element's RF pulse's amplitude and phase. Like the advantages brought by the parallel receive coil array, the use of parallel transmit introduces a new degree of freedom (controllable B_1^+ field pattern and E field pattern) and allows researchers to mitigate some of the transmit issues associated with UHF MRI.

The form of RF shimming is flexible in that the weights of 3 main goals (despite others existing), highest B_1^+ homogeneity, maximum B_1^+ magnitude, and minimum SAR level over a certain ROI can be adjusted according to the strategy of shimming. Despite the diversity of the shimming method, they are all relied on the ability to control the RF waveform on each transmit coil, which until very recently most UHF scanners did not have. Even now, most scanner systems are sold with at most eight channels of independent RF control, which may still not be sufficient for many shimming applications³⁹. Various studies have proposed different approaches to perform B_1^+ shimming. The most convenient way is adding RF cables with different length^{25,42} or using mechanical phase shifter³⁷, thus the phase for each transmit coil can be shimmed. These methods demonstrated the feasibility of B_1^+ shimming, however, they are cumbersome and impractical in clinical use. B_1^+ shimming can be performed most effectively by using an independent transmitter (power amplifier) for each transmit coil since both amplitude and phase (or even distinctive waveform) on each coil can be

adjusted according to the need. However, it comes with a very high associate cost, complexity as well as concerns of local SAR hotspot. So far, the parallel transmitter array has not been easily available to the majority of the researchers.

An add-on B_1^+ steering system was reported to enable multi-channel dynamic B_1^+ steering (phase-only) on a 7T scanner with only 2 transmitters⁴³. The Wilkinson power dividers are first used to split 2 channel power amplifiers evenly into 8 RF channels. High power digitally-controlled phase shifter units are then applied on each RF channel to manipulate the transmit phase. Therefore, with only 2 power amplifiers (most scanners has), 8 phase-independent RF channel can be generated for driving an 8 channel transmit coil array. Chapter IV of this dissertation describes the design, manufacturing, and testing of this system.

1.2 Multi-Nuclei MRI

Conventionally, proton (^1H) is the most used nucleus in MRI diagnostic routine. All other non- ^1H imageable nuclei, known as X-nuclei, are less practiced in clinical MRI due to different reasons. The major issue with X-nuclei is their MR signal is significantly harder to be detected when compared to proton. The MR SNR of a nucleus is shown as an equation below⁴⁴.

$$SNR \propto c * I(I + 1) * \gamma^x$$

Where c is the typical in-vivo concentration, I is the magnetic spin moment, γ is the gyromagnetic ratio of the nucleus, and x is a constant between 2-2.75 depending on different situations. Compared to proton (^1H holds the highest γ 42.58MHz/T and

highest c 79mol/L), almost all X-nuclei have significantly lower γ and c. For instance, ^{13}C has γ of 10.71MHz/T and c of 0.005 mol/L, ^{31}P has γ of 17.25MHz/T and c of 0.003mol/L, ^{23}Na have γ of 11.27MHz/T and c of 0.041mol/L⁴⁴. As a consequence, the lower γ and c of X-nuclei lead to their in-vivo SNR more than two orders of magnitude lower than ^1H ⁴⁴, which makes it difficult to deal with in the beginning. As an extreme example, SNR ^{13}C is five orders of magnitude lower than ^1H . X-nuclei MRI also requires dedicated hardware, such as coils, receivers, and broadband power amplifiers that can be operated at their Larmor frequencies.

Despite the challenges, X-nuclei MRI can reveal various unique information that conventional proton images can't, such as cellular metabolic process⁴⁵⁻⁴⁷, knowledge of different organs⁴⁸⁻⁵², and diseases⁵³⁻⁵⁶. Since the first ^{23}Na results were reported by Hilal et al. in 1983⁵⁷, countless efforts have been made to improve the imaging and spectroscopy quality of X-nuclei MRI. With the help of higher B_0 strength, improved array coil structures, enhanced gradient field and other novel technologies such as hyperpolarization⁵⁸, the practicability of X-nuclei MRI has been increased and it has become a hot topic among researchers.

As the device being closest to the patient, the array coil plays an important role in getting good images, especially when dealing with the low detectability of X-nuclei. A conventional single-tune X-nuclei array coil can be optimized for a dedicated frequency, therefore be able to provide uncompromised sensitivity⁴⁷. Recently, the use of multi-nuclei array coil has become increasingly popular among researchers, although some SNR sacrifice at one or both frequencies usually cannot be avoided due to the increased

level of complexity and component losses⁴⁷. The advantage is that the multi-nuclei array coil can acquire ^1H 's anatomical information and X-nuclei's physiological information simultaneously over the same imaging ROI. It can save multi-nuclei MR's scan time by combining different nucleus' scans into one, or improve the spatial resolution of images by using the same scan time, as well as improve patient comfort since changing coil setup for different nuclei is not required⁴⁵.

So far, most prototype multi-nuclei array coils were built by nesting/co-registering two or more layers of array coil operated at a single Larmor frequency⁵⁹⁻⁶⁶. Another method is using PIN diodes to switch the resonating circuit on the coil thus the operating frequency of the coil can be changed^{67,68}. There are other novel methods to achieve multiple frequencies as well, such as metamaterial-inspired coil⁶⁹ and coplanar interlayer gapped microstrip⁷⁰. However, these technologies currently are still just proofs of concept and are hard to be arrayed for practical use.

These proposed array coil designs provided the necessary tools to support preliminary multi-nuclei studies, but their limitations are obvious too. The major issue that all these methods can't avoid is the excessive complexity mainly due to the decoupling mechanism and the resulting performance loss. Decoupling surface coils at the same frequency is mostly achieved by geometric overlapping⁷¹, isolation preamplifier⁷¹ as well as inductive/capacitive compensation^{72,73}. Besides overlapping, which can't provide sufficient decoupling on its own if the array has more than 3 coils, the other two decoupling methods are both limited to a single frequency since lumped elements network (capacitors and inductor) are necessary for these approaches. Thus, for

both nested type and PIN diode switch type multi-nuclei array coil, dedicated decoupling circuitry with isolation preamplifiers at each Larmor frequency is required to hold sufficient decoupling between coils. Decoupling surface coils at different frequencies is also essential and mostly done by adding parallel-resonant trap circuits (LC trap) on the coil. The trap circuit creates high impedance at one frequency to block the coupling current (often at the other nucleus' Larmor frequency), but only add some minor reactance at its own nucleus' Larmor frequency and therefore does not disturb the coil's performance significantly. Since a lossy passive network needs to be placed on the coil, ohmic loss and thermal noise introduced by the capacitor and especially the inductor inevitably decreased the Q-factor and the sensitivity of the coil. Additionally, this approach becomes cumbersome when more than two nuclei need to be operated since even more ohm losses are further added on the coil if multiple LC traps were needed. Decoupling structures are necessary for multi-nuclei array coil, yet also are a major limiting factor. The excessive complexity introduced by multiple decoupling circuitry together restricts the scale of multi-nuclei array coil's total channel count and the number of the imageable nucleus, as well as the sensitivity of array coil at both Larmor frequencies are inevitably compromised.

To potentially moderate the complexity of the current approaches, a novel decoupling strategy for multi-nuclei array coil is investigated. Instead of using lumped element matching network and isolation preamplifier to block the induced RF current, a preamplifier with high input impedance itself can be directly used to decouple array coil.

Chapter V of this dissertation discusses the design, test, and results of the proposed approach.

1.3 Dissertation Organization

This dissertation is divided into five chapters. Chapter I summarizes some current status and challenges in certain MRI research topics, such as the implementation of B_1^+ shimming and multi-nuclei array coil design. And general motivations of these works and the organization of this dissertation are described in this chapter entitled introduction. Chapter II discusses some background and commonly used methods in parallel MRI both on transmit and receive, such as SAR, B_1^+ shimming, and multi-nuclei coil. Chapter III describes the modeling work for an 8 channel hexagonal head coil array and the SAR simulation for a serial transmit parallel receive pulse sequence (STxPRx). Electromagnetic simulation results are first acquired and shown based on the head and coil models built in Remcom. And post-processing of the B_1^+ field and SAR level according to the STxPRx pulse sequence is then discussed. Chapter IV describes the design and implementation of the 7T B_1^+ steering system. An overview of the system is first explained, followed by the engineering details of each subsystem. Electromagnetic simulation, bench measurement validation, and testing results on the 7T scanner are then discussed. Chapter V describes the investigation of a novel decoupling approach for multi-nuclei array coils. The configuration of this approach is first explained and compared to the conventional method. The design, optimization, and preliminary testing

results are then described and discussed. Chapter VI finally concludes this dissertation and reviews the potential of possible future work.

CHAPTER II

BACKGROUND

2.1 SAR in MRI

The operation of MRI relies on the transmission and reception of a time-varying B1 field through RF coils. According to Faraday's law of induction, a time-varying magnetic field is always accompanied by a spatially varying E field, which induces an electromotive force (EMF) inside a lossy object (patient body) and thus produces heating of the body. If the temperature of some in-vivo regions rises beyond the safety threshold due to the heating of the transmit pulse, RF burns are caused.

The specific absorption rate (SAR) is used to characterize this heating effect, define as below²¹:

$$SAR = \frac{\text{total RF energy dissipated in sample (Joules)}}{\text{exposure time (second)} * \text{sample weight (Kg)}} \text{ (Watts/Kg)}$$

The more energy dissipated in the patient during the scan, the higher the SAR level will be. Authorities like The International Electrotechnical Commission (IEC) and USA's Food and Drug Administration (FDA) set the standards for SAR limitations. For example, in IEC's standard, the whole-body SAR, head SAR, and maximum rise of core temperature are limited to 4 W/kg, 3.2 W/kg, and 1°C for the safe operation. While the whole-body SAR or head SAR can be estimated by the total amount of transmit power and the subject's weight, the maximum local SAR is harder to be accurately determined⁷⁴. Numerical calculations using human models, such as finite difference time domain (FDTD), are often used to predict the SAR pattern inside a body^{75,76}.

2.3 B_1^+ /RF shimming

Different from the conventional transmit architecture (often be a single channel transmitter and a volume coil), B_1^+ shimming requires multiple transmit coil elements that fed with their own tailored RF pulses. Since the total B_1^+ /E field is the superposition of each channel's B_1^+ /E field, an improved total B_1^+ field/E field can be obtained by carefully “shimming” each channel's B_1^+ field or E field, as shown in the equation below³⁵:

$$B_{1,total}^+(r, t) = \sum_{i=1}^{Nt} B_{1,i}^+(r, t) = \sum_{i=1}^{Nt} p_i(t) * S_{B1+,i}(r)$$
$$E_{total}(r, t) = \sum_{i=1}^{Nt} E_i(r, t) = \sum_{i=1}^{Nt} p_i(t) * S_{E,i}(r)$$

Where Nt is the number of transmit coils, p_i is the transmit pulse on the i th coil, and $S_{B1+,i}$ and $S_{E,i}$ are the B_1^+ field “sensitivity” profile and E field profile of i th coil.

The sensitivity profiles solely depend on the coil structure and phantom/object, which can be obtained either in simulation for theoretical study or through B_1^+ mapping sequence on the scanner for actual scanner experiment. The key of B_1^+ shimming is manipulating each transmit element's specific RF pulses (p_i) to achieve a better total B_1^+ field or total E field. The most straightforward way of performing B_1^+ shimming is keeping the pulse on each element in the same shape but scaled with a special complex weighting factor (w_e), which means the amplitude and phase of the RF pulse on each element are controlled according to shimming strategy. In practice, a convenient way of achieving this is adding transmission lines with different lengths (for delaying phase)

and attenuators with different attenuation levels (for changing amplitude), although being cumbersome and lossy. More sophisticated B_1^+ shimming methods, such as modulating pulses during the scans⁷⁷, can be accomplished if hardware allows. There are different ways to determine what pulse p_i should be used on each channel depending on the goals of shimming³⁵. The most straightforward way is optimizing a cost function containing different constraints, such as B_1^+ homogeneity (usually characterized as the standard deviation of B_1^+ field intensity over a certain ROI), average flip angle (calculated based on the mean of B_1^+ field intensity), and SAR level (calculated based on the E field and phantom property). By iterating the amplitude and phase of RF pulse p_i on each transmit element, the cost function can be minimized and lead to an optimal shim solution p_i .

2.5 Multi-Nuclei MRI Coil

To acquire information of multiple nuclei simultaneously, a multi-tuned or multi-nuclei coil is needed. Different types of multi-tune mechanisms are commonly used, such as dual-tune LCC trap circuit⁷⁸, pin diode switching circuit⁶⁷, nesting multiple coils⁷⁹, and so on.

A common way to double tune a single coil, like a surface coil or a low-pass birdcage coil, is using an LCC trap circuit, as shown in Figure 1.

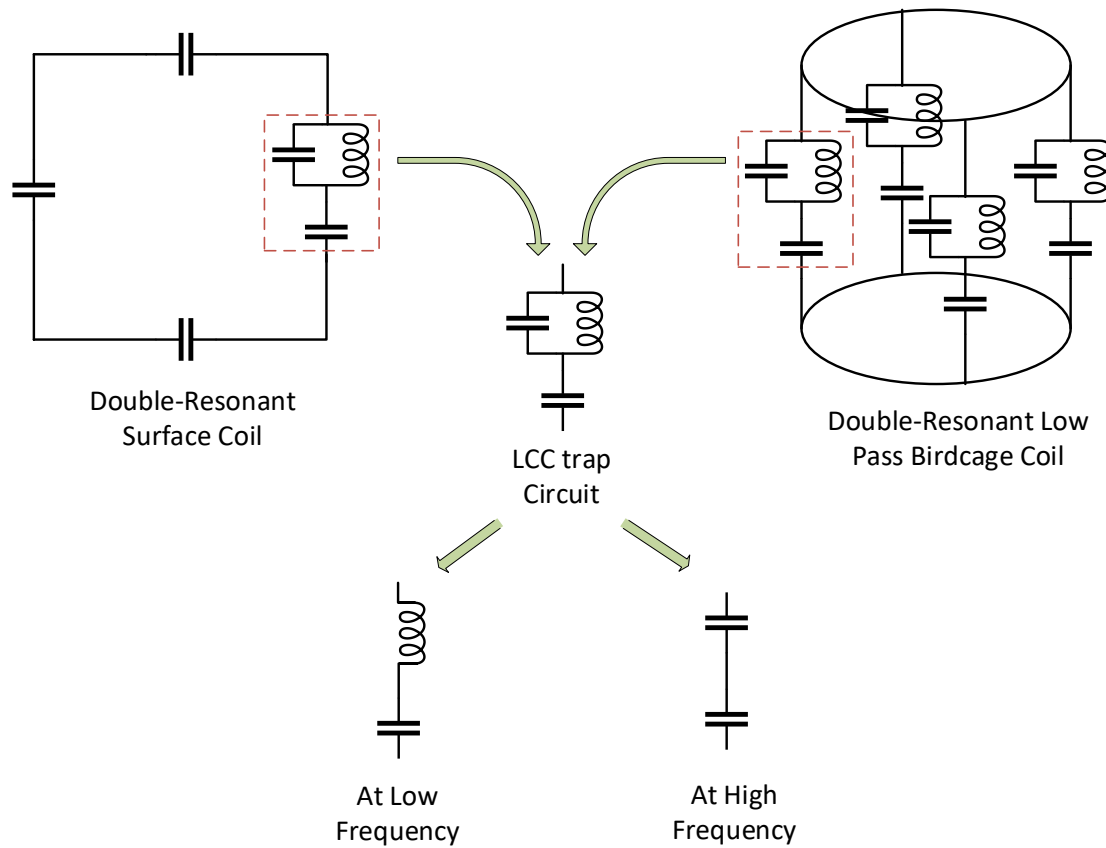


Figure 1. Double resonating a coil using LCC trap circuits. LCC trap circuit can provide a smaller capacitance at higher frequency and a bigger capacitance at lower frequency, and therefore can resonate a single coil at two frequencies.

LC trap circuits can provide different impedance at different frequencies. At lower frequency, the LC trap can be equivalent to a capacitor, and at higher frequency, the LC trap can be equivalent to an inductor. Together the LCC trap (LC + C) can provide a smaller capacitance at a higher frequency and a bigger capacitance at a lower frequency, therefore is capable of resonating a single coil at two different frequencies. Another way to achieve multiple operating frequencies is using PIN diodes to switch resonate circuitry, as shown in Figure 2.

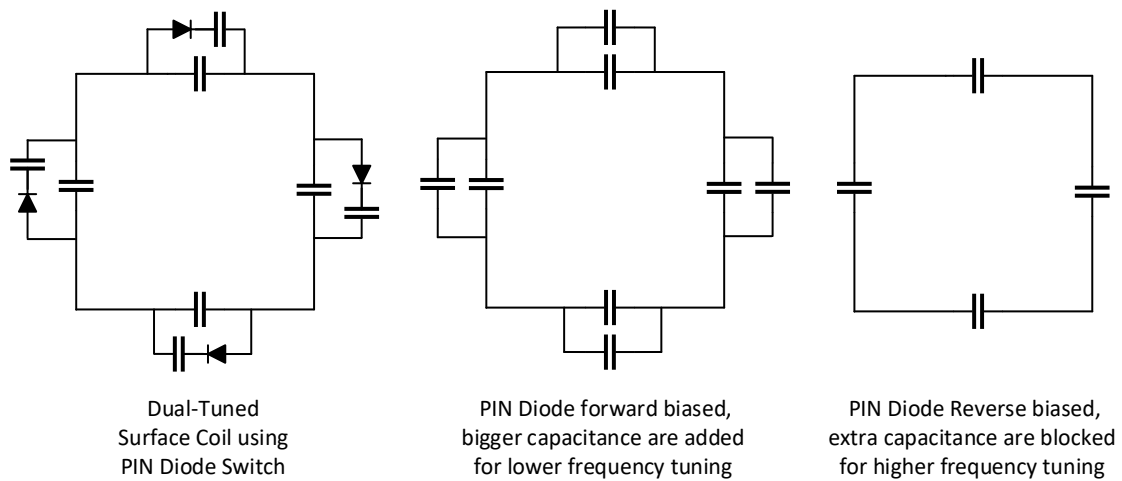


Figure 2. Dual-tuned surface coil using PIN diode switch. Forward biasing the PIN diode allows additional capacitance to be added on the coil for lower frequency tuning, and reverse biasing the PIN diode disables the extra capacitance for higher frequency tuning.

The functionality of the PIN diode is an RF switch controlled by DC. By forward biasing (short-circuit) or reverse biasing (open-circuit) the PIN diode, we can alter or switch tuning network and therefore adjust the resonating frequency for a single coil. Co-registering or nesting multiple coils operating at different frequencies is also a widely-used method to achieve multi-nuclei capability, shown in Figure 3.

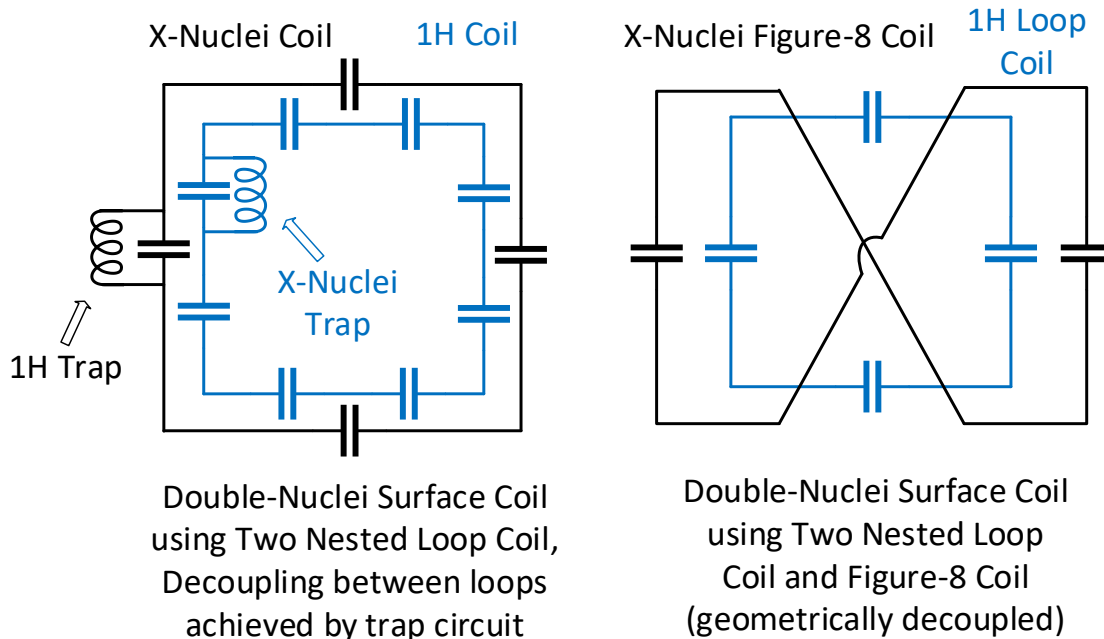


Figure 3. Double-nuclei surface coil using nesting structure.

Nesting two loop coils resonating at different frequencies can accomplish multi-nuclei operation simultaneously in the most straightforward way. However, the coupling between two loop coils can cause issues such as matching/tuning shifting, SNR loss, and so on. Therefore, LC trap circuits are usually added on loop to block the RF current induced by the other coil. A self-decoupled nesting double-nuclei surface coil can be achieved by nesting coils with orthogonal B_1^+ fields, such as loop coil and figure-8 coil.

CHAPTER III

SAR MODELLING FOR SERIAL TRANSMIT PARALLEL RECEIVE COIL ARRAY

3.1 Overview.

The serial transmit approach excite each coil in series so that the B_1^+ field generated by each coil in combination can still provide the same tip-angle in the field of view, but the electric fields generated by each coil cannot add up at the same time and potentially form an undesired SAR hotspot together. Therefore, the local maximum SAR level can be reduced by using this approach. Since the SAR level of this time-interleaved excitation approach is hard to simulate directly in the commercial software that we were using (Remcom XFDTD 7.4), thus some post-processing was done to calculate SAR based on results from the software modeling and actual pulse sequence parameters.

An overview of the SAR calculation workflow is shown in Figure 4, including four main steps: (1) simulate raw B_1^+ field/SAR maps in Remcom XFDTD, (2) first scaling for equal net input power, (3) Second scaling for equal tip angle, (4) generate the final SAR results for comparing. Raw B_1^+ /SAR maps were first generated in Remcom XFDTD as matrices and exported into MATLAB for post-processing. The conventional parallel transmit mode was simulated while all coils excite simultaneously, and the series-transmit mode was simulated as each coil exciting separately and then summed later in MATLAB. Two major scalings were performed on the B_1^+ /SAR maps to ensure fair comparison on both net input power and tip angle between the two modes.

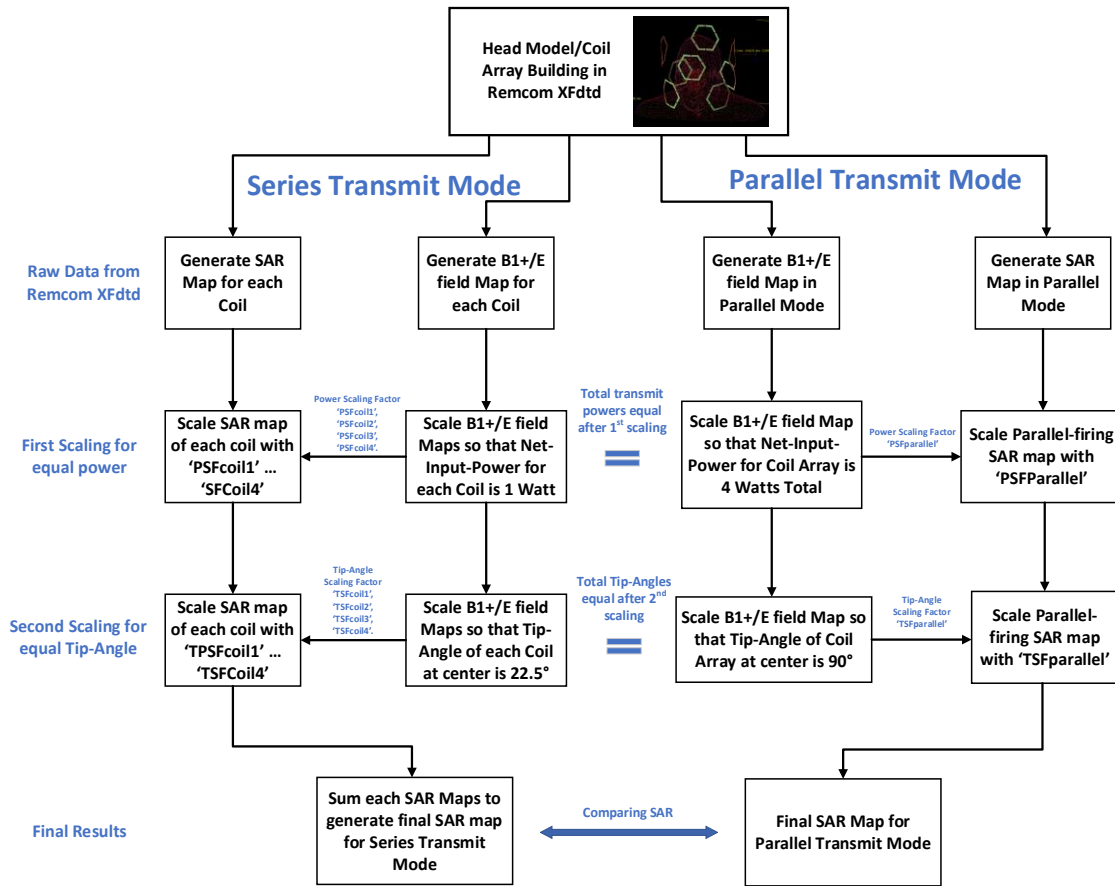


Figure 4. Overview of the SAR calculation workflow.

3.2 Model Building in Remcom and B1+/E Field Simulation.

A human head model (AF “MAN” 1mm) and 8 channel hexagonal loop coil array were modeled in Remcom XFDTD, shown in Figure 5. The human head model used in this simulation was included in the Remcom library and shows the anatomical details with 1mm uniform grid size. Two rings of hexagonal coils array were modeled around the head with a vertical distance of 12 cm from coil center to coil center. Each ring contains 4 uniformly distributed curved hexagonal coils with an outer diameter of 11cm and copper width of 0.63cm. Each coil was modeled with 6 gaps and each gap has one 3.6pF capacitor connected across. Each coil was fed with a high-impedance current source (1000Ω and 1A) to mitigate the potential coupling between each coil. By using a current source with the source impedance much higher than the coil, the current flowing into the coil can be forced to be whatever the source output, therefore eliminating the coupling-induced current on each coil. Another way to explain this is high impedance source directly adds a big real impedance in series with the coil, therefore immediately damping the current induced by coupling. Although a huge mismatch between source and coil exists, the available power can be boosted so that the net input power, in this case, equals the net input power of the actual properly 50Ω -matched case.

Figure 5 shows the general geometry of the head model and 8 channel coil array's position. However, to better validate the concept only 4 channels (One ring) were used in the simulation for demonstration. And the 4 coils were placed around the brain at 45° , 135° , 225° , and 315° , as shown in Figure 6.

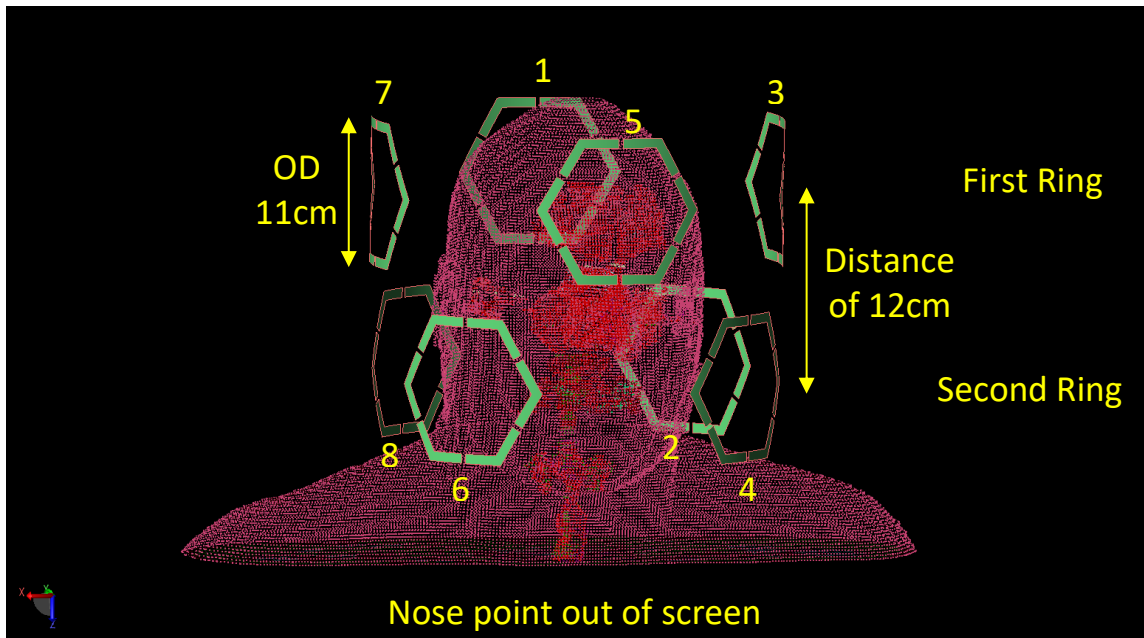


Figure 5. Picture of the general geometry of head coil array built-in Remcom.

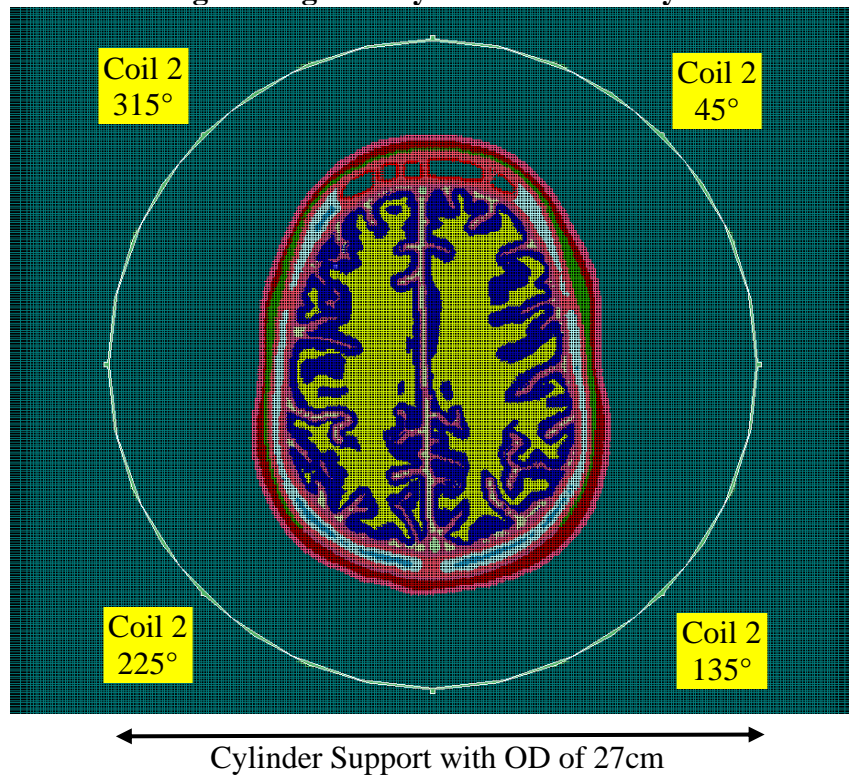


Figure 6. Cross-section view of the head model and coil array that was used in SAR modeling.

3.3 First Scaling for Equal Net Input Power

In total, 5 B_1^+ field maps were simulated and then imported into MATLAB for post-processing: 4 B_1^+ maps generated by each coil and 1 four-channel parallel-firing B_1^+ maps. Since the impedance of each coil has some minor difference in simulation, the raw unscaled net input power is different between each coil as well as between series and parallel mode. Table 1 shows the coil details of simulated coils:

Table 1. Summary of information in SAR scaling.

		Series Mode				Parallel Mode			
		Coil1	Coil2	Coil3	Coil4	Coil1	Coil2	Coil3	Coil4
Raw data unscaled	Impedance (Ω)	6.82+ j10.93	6.78+ j10.97	7.40+ j11.42	7.38+ j11.35	8.69+ j11.20	7.22+ j10.04	9.42+ j11.93	7.79+ j10.40
	Current (A)	0.993	0.993	0.992	0.992	0.991	0.992	0.990	0.992
	Net Input Power (W)	3.364	3.344	3.649	3.636	4.268	3.55	4.622	3.835
First scaling	Power Scaling Factor (PSF)	0.297	0.299	0.274	0.275	0.2456			
	Net Input Power (W)	1.000	0.999	0.999	0.999	3.9971			
Second Scaling	Tip Angle Scaling Factor (TSF)	6.6011				7.2021			
	Net Input Power (W)	174.285				207.333			
SAR after both scaling	Peak 10g SAR (W/kg)	0.3200				0.4310			
	Averaged 10g SAR (W/kg)	0.1768				0.1902			

With the use of high impedance current sources, the input current on each coil was roughly the same around 0.992A. However, since the simulated coils in parallel-firing mode have roughly $1\sim 2\Omega$ higher real impedance, the raw net input power is roughly 1W high for each coil. To fairly compare the series mode and parallel mode, their net input powers were scaled to the same 4W total in the first scaling. In parallel mode, a common power scaling factor PSF_{parallel} of 0.2456 was applied on all 4 coils, making the total net input power for the coil array to be 3.9971W (ideally 4W). In series mode, separate power scaling factors for each coil, PSF_{coil1} , PSF_{coil2} , PSF_{coil3} , and PSF_{coil4} , were applied on each coil to make the net input power of 1.0001W, 0.9999W, 0.9998W, and 0.9999 W (ideal 1W). With the total net input powers to be the same, the power scaling factors were applied on the B_1^+ maps and SAR map. The power-scaled B_1^+ maps of each coil for series mode were shown in Figure 7.

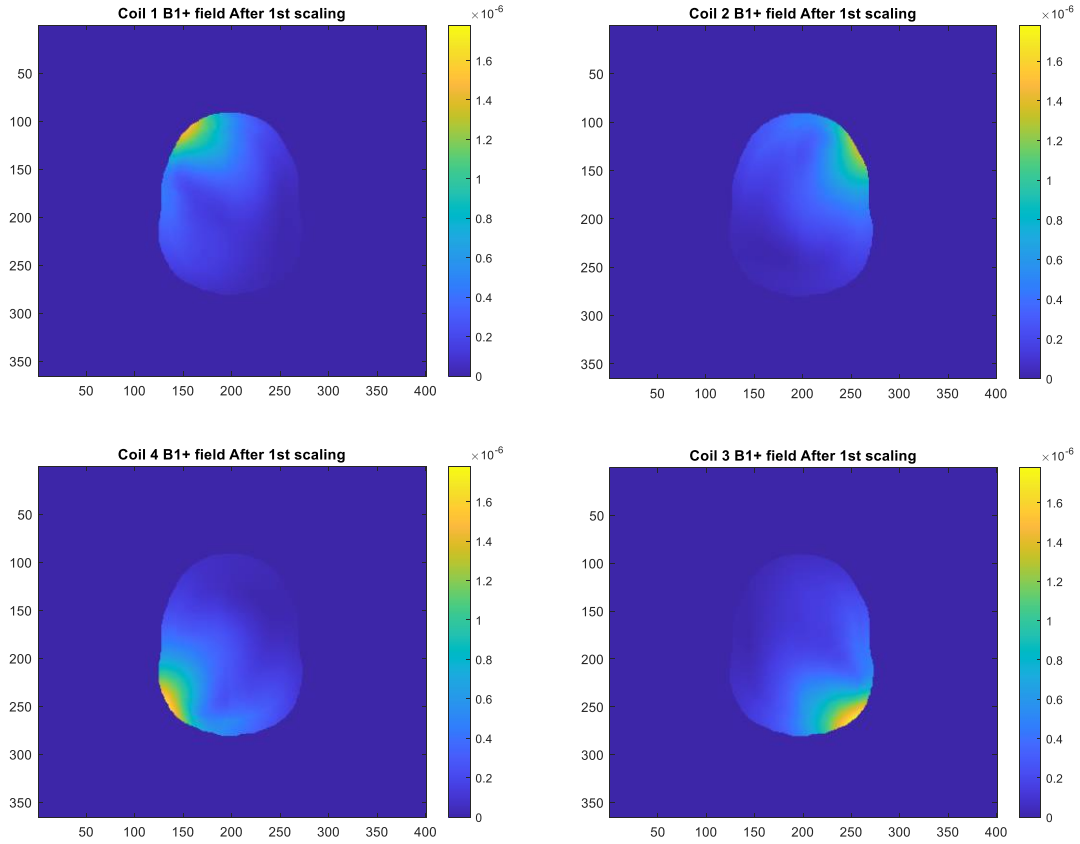


Figure 7. Simulated B_1^+ map (μT) of each coil after the 1st scaling for equal net input power (1W).

The tip-angle maps of each coil in the series mode were generated based on the B_1^+ maps, shown in Figure 8. The following equation was used to convert the B_1^+ to tip angle:

$$Tip\ Angle^\circ = 2\pi * \gamma * \tau * (B_1^+) * (180^\circ/\pi)$$

Where the gyromagnetic ratio γ for ^1H is 42.57 (MHz/T), the transmit pulse width τ for this sequence is 1ms, the (B_1^+) field is from the previous simulation, and $(180^\circ/\pi)$ is the unit conversion from radius to degree.

Since only 1W net input power is used for each coil the tip angle is low and did not represent the practical case.

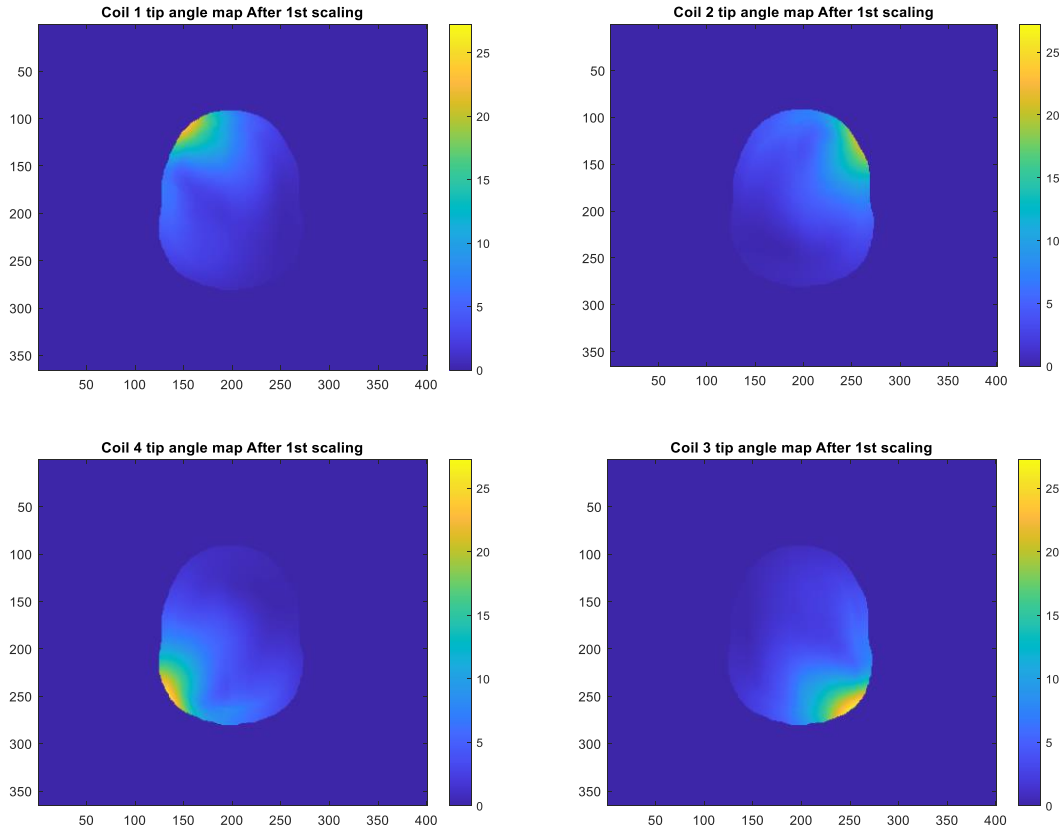


Figure 8 Simulated tip angle map (degree) of each coil after the 1st scaling for equal net input power (1W).

The parallel firing B_1^+ maps and series firing B_1^+ maps after power scaling are shown in Figure 9. Parallel transmit B_1^+ was generated by scaling the raw B_1^+ maps of all 4 coils transmit at the same time. Serial transmit B_1^+ map was summed upon separately scaled B_1^+ map of each coil. Tip angle maps for both modes generated using the same conversion were also shown. Again, with only 4W net input power for two modes, the tip angles are low and do not represent the actual case.

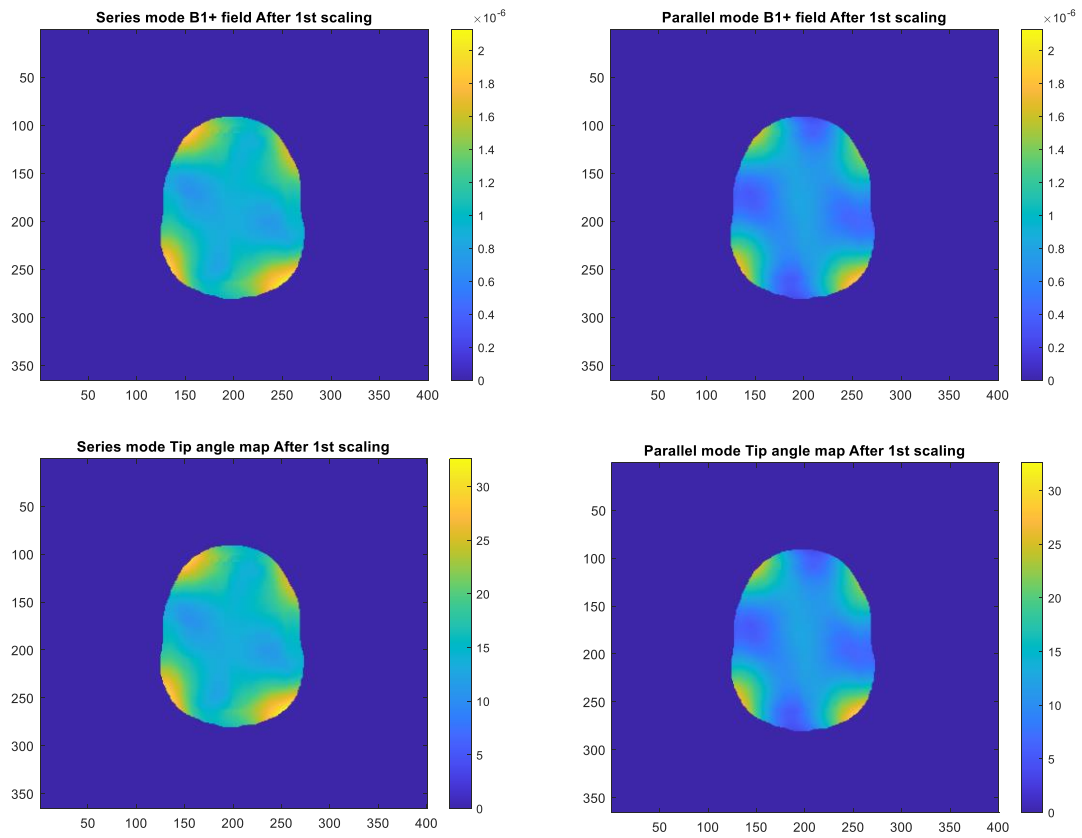


Figure 9. Simulated B_1^+ maps (Top) and tip angle maps (Bottom) for series mode (Left) and parallel mode (Right), after the 1st scaling for equal net input power (4W).

3.4 Second Scaling for Equal 90° Tip Angle at Brain Center

Since the tip angle is too low, a second scaling was applied on both series mode and parallel mode to boost up B_1^+ maps and tip angle maps, as shown in Figure 10. Separate tip angle scaling factors were applied on each mode to reach the same 90° tip angle at the brain center. For parallel mode, a tip angle scaling factor $\text{TSF}_{\text{parallel}}$ of 7.2021 was used so that center of the brain can reach 90° within 1ms transmit pulse width in theory. For the series mode, a tip angle scaling factor $\text{TSF}_{\text{series}}$ was used so that center of the brain can reach 90°. Therefore, after this second round tip angle scaling the total net input powers have been scaled to 207.33W for parallel mode, and 174.28W for parallel mode.

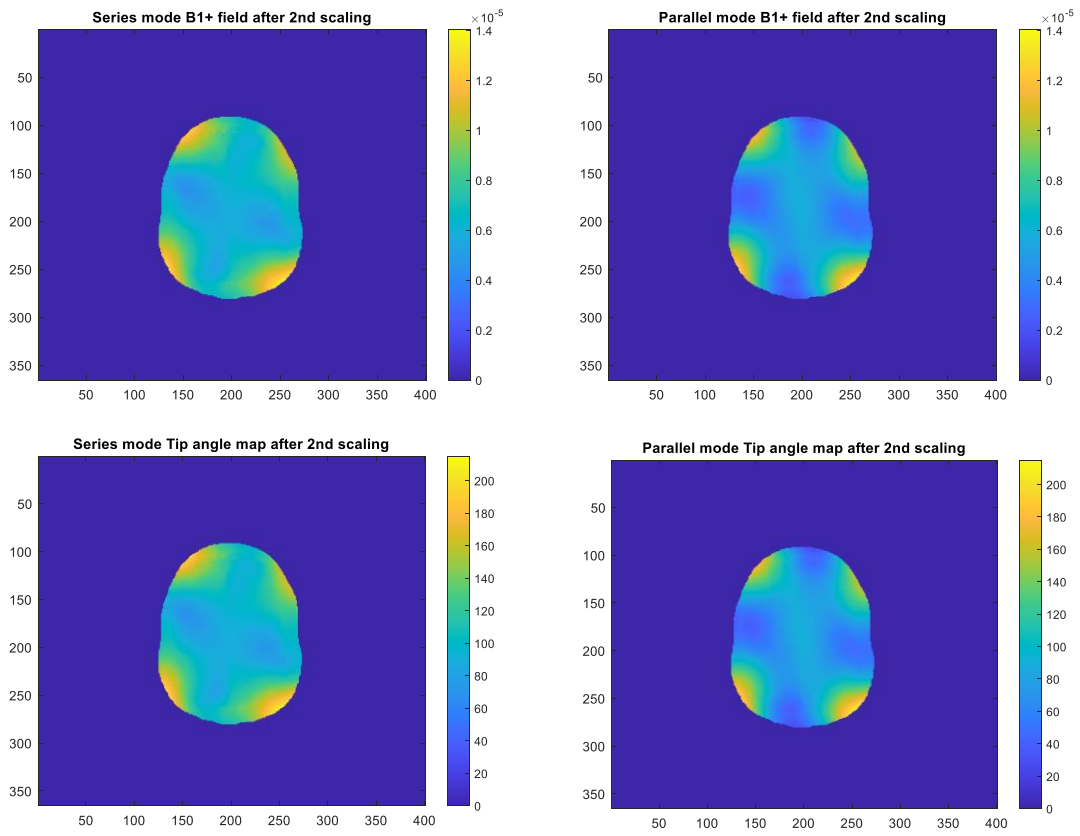


Figure 10. Simulated B_1^+ maps (Top) and tip angle maps (Bottom) for series mode (Left) and parallel mode (Right), after the 2nd scaling for equal tip angle at brain center (90°).

3.5 Final Results for SAR

The raw SAR maps generated by Remcom were scaled with both two scaling factors (power scaling factor, and tip angle scaling factor) as described in previous sections. The equation used for scaling is shown as follow:

$$SAR(scaled) = SAR(raw) * PSF * TSF^2$$

The power scaling factor (PSF) can be directly applied to the raw SAR because they are linearly related. SAR is in terms of Watt/kg, and PSF in this calculation is in terms of Watt/Watt. Therefore, the unit remains the same after the scaling of PSF ($\frac{Watt}{kg} * \frac{Watt}{Watt} = \frac{Watt}{kg}$). The tip angle scaling factor, however, has to be applied with the square on SAR since they have different units, shown as below:

$$TSF \left(\frac{Degree}{Degree} \right) \propto B1Ratio \left(\frac{Tesla}{Tesla} \right) \propto CurrentRatio \left(\frac{A}{A} \right) \propto \sqrt{PowerRatio} \left(\sqrt{\frac{Watt}{Watt}} \right)$$

The tip angle scaling factor is in terms of degree/degree, which is linearly converted from the μ Tesla/ μ Tesla of scaled/unscaled B_1^+ field. B_1^+ field is then linearly related to the current on the coil, therefore related to the net in the put power of coil with square root. Thus, to scale SAR (Watt/kg), TSP has to be applied with square (\propto Watt/Watt). The parallel transmit SAR map was scaled with two scaling factors directly. The serial transmit SAR map was generated by summing the scaled SAR maps from each coil, shown in Figure 11.

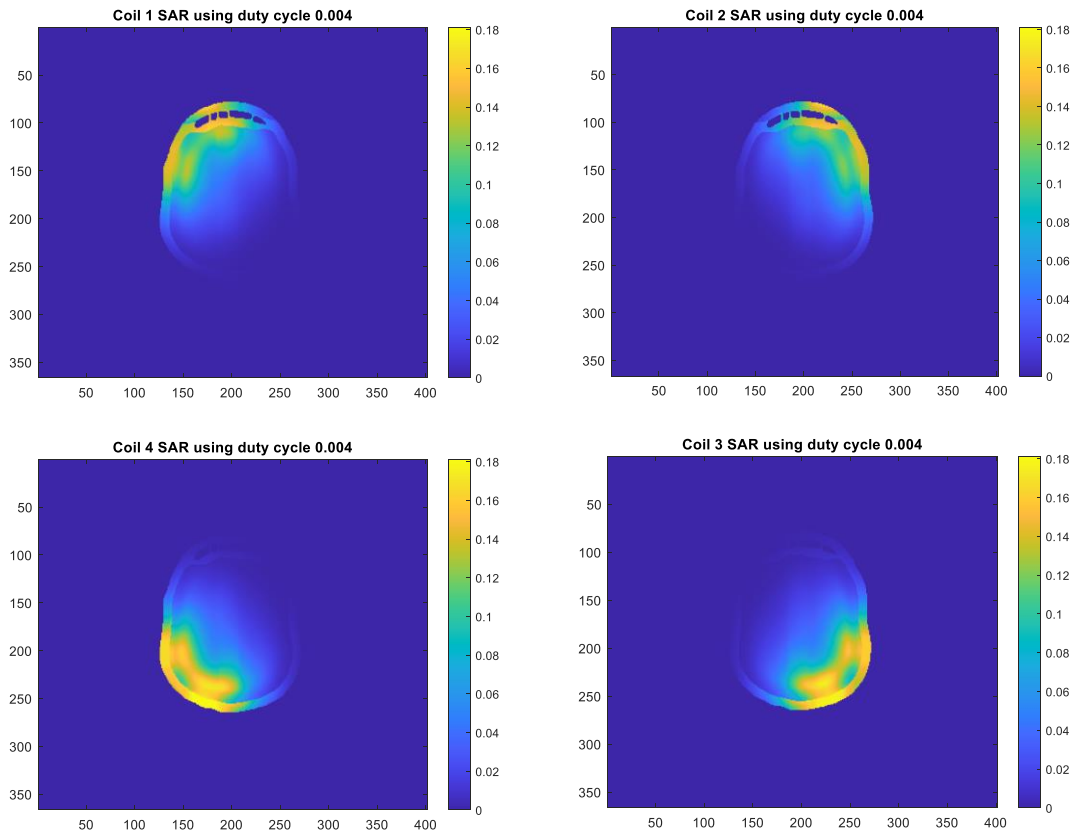


Figure 11. Simulated SAR map (W/kg) of each coil after the 1st and 2nd scaling.

The final results of the fully scaled serial transmit SAR map and fully scaled parallel transmit SAR map are shown in Figure 12. As we can see that two SAR “hotspots” with a relatively higher maximum 10g SAR value (0.4310 Watt/kg) can be observed in the parallel transmit SAR maps. In comparison, the serial transmit mode has a relatively lower maximum 10g SAR value (0.3200 Watt/kg). The same can be observed on the averaged 10g SAR level that serial transmit mode generates 0.1768 (Watt/kg) on average and parallel transmit mode generates 0.1902 (Watt/kg) on average.

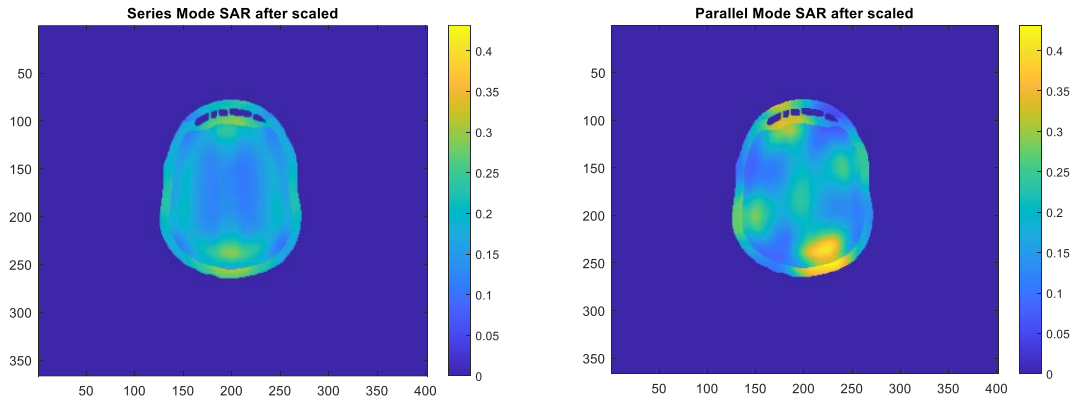


Figure 12. Simulated SAR map (W/kg) of series mode (Left) and parallel mode (Right) after the 1st and 2nd scaling.

Two reasons are believed to contribute to the lower SAR of serial transmit mode. The first reason is that for the series mode the B_1^+ field and E field from of each coil are generated in a time-interleaved way, therefore the SAR (produced from E field) from each coil can only be accumulated linearly in the brain. However, for the parallel mode B_1^+ field and E field are generated simultaneously from each coil. And the E field from different coils can be canceled or summed at different positions depending on the E field's phase at the point. If the E fields from different coils align accidentally at a point and lead to increasement in the total E field's magnitude, the SAR level at the point can be boosted with the square of the E field's increasement, as shown in the equation.

$$SAR \propto \frac{\sigma * E^2}{\rho}$$

Where σ is the conductivity of the sample, ρ is the density of the sample and E is the RMS electric field at the sample.

The second reason of having lower calculated SAR is that serial transmit mode requires relatively lower net input power to reach 90° tip angle. Compared to parallel transmit mode's 207.3W net input power, the serial transmit mode requires only 174.3W, which is about 84.08% of the parallel transmit mode. After the first scaling when the net input powers of both series mode and transmit mode have been scaled to the same level of 4 Watts, serial transmit mode generate 13.63° tip angle at the brain center and parallel transmit mode generate 12.5° at the brain center after 1ms of transmit pulse. Therefore, the relatively lower transmit efficiency of parallel mode leads to a higher power requirement when the same 90° tip angle needs to be reached. Similar to the first reason that E fields from different coils are not able to align and form a SAR hotspot in serial transmit mode, the B_1^+ field from each coil are not able to cancel each other and therefore lose the total B_1^+ intensity at certain positions. Another way to explain this is in serial transmit mode, the tip angles generated by each coil can only be accumulated linearly and positively, while some B_1^+ cancellations inevitably exist in parallel transmit mode.

In general, the computational results presented in this chapter confirm the experimental conclusions of decreased local max SAR when each coil transmits sequentially, and the calculated SAR maps were published along with the experiment results²². This work provides a novel approach for MRI applications with significant SAR concerns, such as lower-gamma nuclei imaging or patients with implanted medical devices²².

CHAPTER IV
AN ADD-ON SYSTEM TO ENABLE DYNAMIC B_1^+ STEERING FOR TRANSMIT
ARRAYS AT 7T

4.1 System Overview

This add-on B_1^+ steering system is designed to provide 8-channel dynamic phase control capability for the 7T scanner with only 2 installed transmitters channels⁴³.

Without requiring 8 channel parallel transmitter, it allows the 7T scanner to perform 8 channel dynamic B_1^+ steering or shimming in a low-cost, low-complexity way. Similar to the concept of beamforming in the antenna theory, the key to achieving B_1^+ steering is the ability to accurately control transmit pulse's phase on each coil element.

An overview of this B_1^+ steering system⁴³ was shown in Figure 13. The core of this B_1^+ steering system is the 8 channel high-power digitally-controlled phase shifter array. Each channel can provide 360° phase control with 22.5° resolution for each transmit pulse. Since the phase delay added by the module is remotely operated by the control module and without the need for manual switching cables, the dynamic B_1^+ steering can therefore be performed in real-time. The transmit pulse from the 7T scanner's 2 channel power amplifiers were first equally split into 8 channel through two house-built four-way Wilkinson power dividers. Each channel was then routed through a phase shifter module with its phase properly controlled. Finally, phase-delayed transmit pulses go through a house-built 8 channel TR switch and get transmitted out from each coil element. An additional set of small pick-up probes are placed near the transmit coil

array to sample the transmit pulse, together with the measurement module the real phase on each coil can be measured as feedback for the final phase solution.

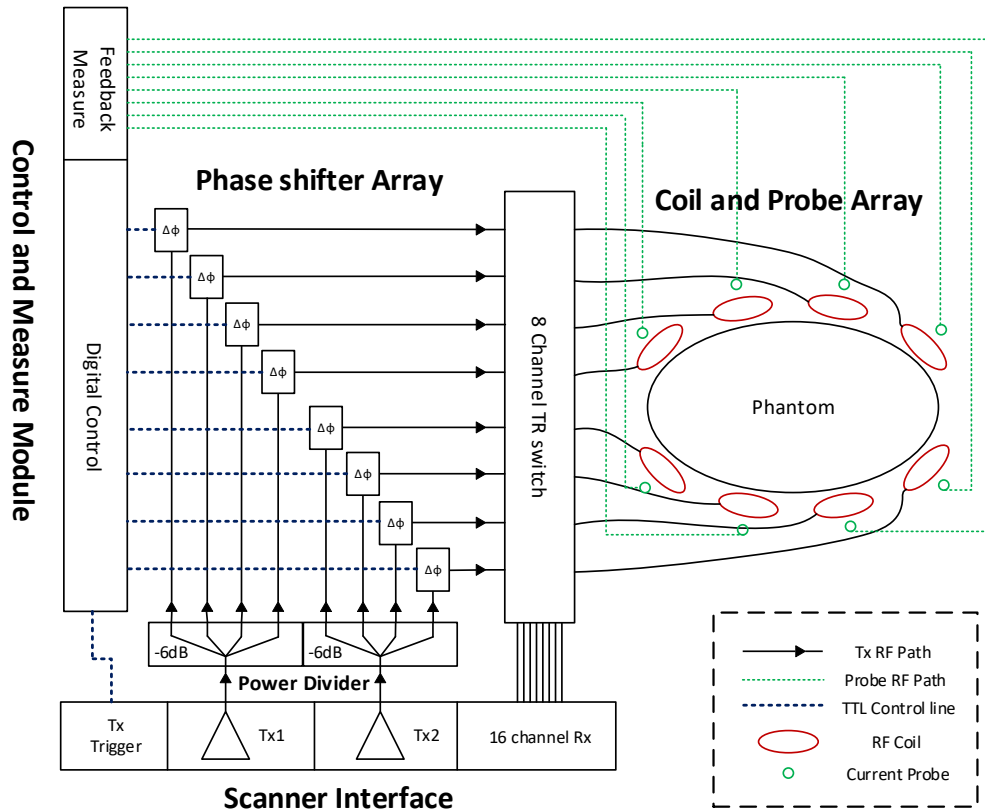


Figure 13 An overview of the add-on B_1^+ steering system. Transmit pulses from scanner’s power amplifiers were first split into 8 channels, next routed through phase shifter array to be properly phase-shifted, then routed through 8 channel TR switch and finally get transmitted out from coil array. Figure courtesy⁴³.

The picture of this system⁴³ is shown in Figure 14. The hardware of this system is mainly cased in two separate parts. The non-magnetic server rack in Figure 14 A contains the core modules in this system: 8 channel TR switch, 8 channel phase shifter array, 2 channel power divider, and the control & measure module. The whole rack/modules are only slightly magnetic, and therefore can be used inside the magnet room (with some medical-grade sandbags blocking the wheel). The compact server rack

shown in Figure 14 C contains the supporting modules for the system: TPI & Testing amplifier for performing self-check onsite, beagle bone black for bridging the command between computer and MCU in the control module, and the power supply module for driving the whole system. The proper connection between each subpart is attached in the appendix.

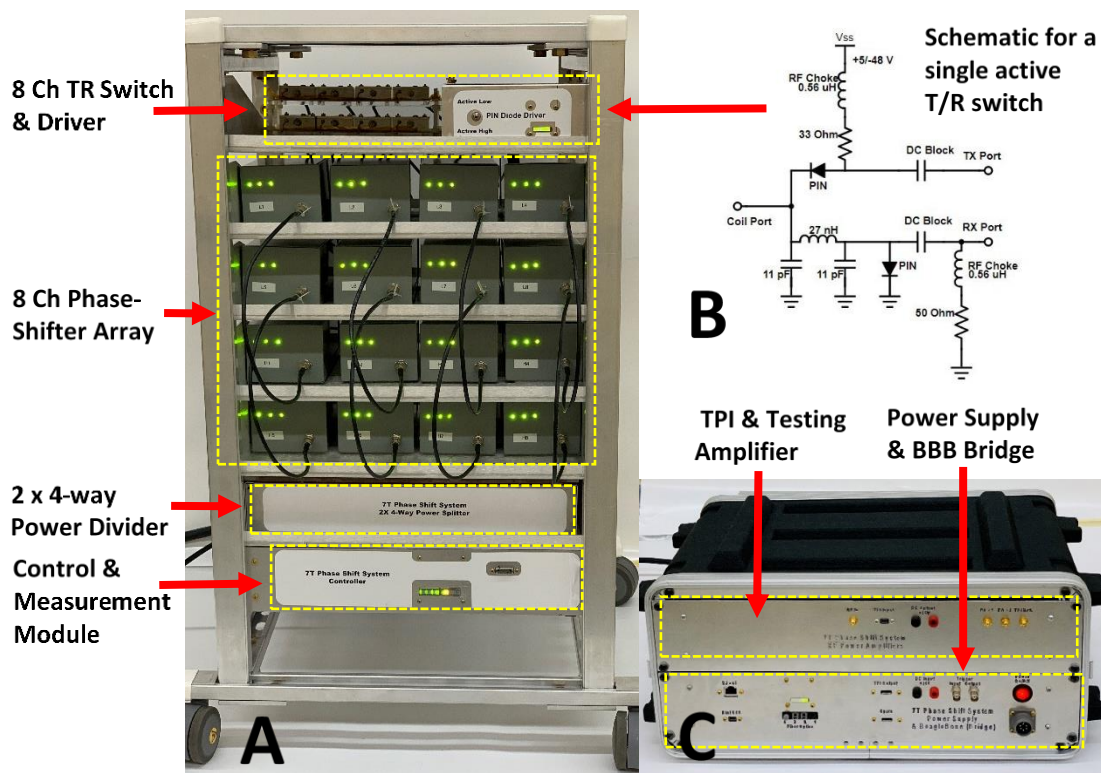


Figure 14 Overview of hardware of B_1^+ steering system. (A) A non-magnetic server rack can be placed inside the magnetic room. From top to bottom: 8 channel TR switch, 8 channel phase shifter array, 2 channel four-way power divider, and control & measure module. (B) Schematic of TR switch. (C) Another compact server rack placed inside the instrument room, From the top to bottom: TPI & testing amplifier for performing self-check onsite, and BBB Bridge & power supply for driving the whole system. Figure courtesy⁴³.

4.2 Wilkinson Power Divider

To split the scanner's two-channel transmitter into 8 RF channels, two four-way Wilkinson power dividers⁸⁰ were constructed in house, shown in Figure 15. Each four-way divider was cascaded from three regular two-way power dividers. Each two-way power divider was built using two 75Ω $\lambda/4$ transmission lines and a high power 100Ω resistor (AVX Corp, Myrtle Beach, SC) so that both ports maintaining 50Ω impedance. Aluminum heatsinks were attached to the bottom of all high-power resistors through pre-cut slots on the 4oz PCB and thermal compound, to properly dissipate the heat generated during the high power transmission. All two four-way dividers were cased inside an aluminum closure with a vented lid. The maximum insertion loss measured on each RF path is 0.35dB, and the minimum isolation between each output port is 25dB.

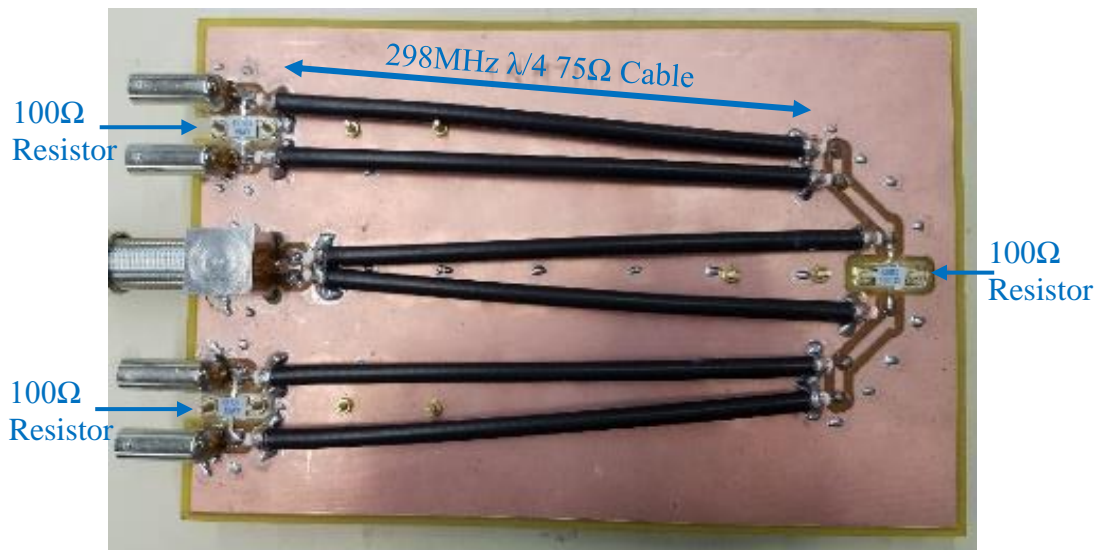


Figure 15. Picture of four-way Wilkinson power divider. This four-way power divider was built from three cascaded regular two-way power dividers. On each divider, two coaxial cables (length of $\lambda/4$ at 298MHz) and one high-power 100Ω

resistor are used. An aluminum heatsink is used under each 100 Ω resistor (on the opposite side of PCB).

4.3 Phase Shifter Module

An overview of phase shifter⁴³ is shown in Figure 16. In short, each phase shifter module consists of 5 binary bits in series: 50 Ω termination, 22.5°, 45°, 90° and 180°.

The first 50 Ω termination bit in the front provides the ability to terminate the transmit power into a high-power 50 Ω resistor when this bit is set to ON state. When the 50 Ω bit is set to OFF state, it allows transmit power to pass through with some minor insertion loss added. The rest 4 phase-shifting bits follow the same switching mechanism, they can either provide the proper relative phase delay when switching to ON or let the transmit pulse pass through without adding relative phase delay when switching to OFF. Therefore, 4 separate binary bits together provide $2^4 = 16$ different phase-shift combination of 22.5°, 45°, 67.5°, 90°, 112.5°, 135°, 157.5°, 180°, 202.5°, 225°, 247.5°, 270°, 292.5°, 315°, 337.5°, therefore cover the full 360° range with a resolution of 22.5°. Since each of these bits functions independently, finer resolution can be achieved by adding phase-shifting bits with smaller designed phase delays, of course with the penalty of more insertion loss.

Simply speaking, all these binary bits use multiple pin diodes(MA4P7001F-1072T) to switch the transmit pulse to different RF paths. Since the diodes are designed to be in series on the RF path, the models with the less power-handling rate but less parasitic capacitance can be used to minimize insertion loss. Figure 16 A shows the general circuit used on all bits, where two DC controls and one DC ground are provided

to the core circuit all with proper RF chocking. In theory, one good RF chock (big inductor), or a piece of $\lambda/4$ transmission line with RF-short and DC-open capacitor in front will provide enough RF blocking for the DC lines. However, in reality with these inevitable parasitic components existing on the PCB, the theoretical solution is not enough. Especially in this PCB design (details in appendix), the DC lines and DC ground are first routed from the bottom PCB and then brought into the RF circuit through a bottom-to-top via, where significant parasitic shunt capacitance is introduced here. To provide enough RF blocking impedance, the final solution was found through fine-tuning on the bench where $\lambda/5$ transmission lines are first used (since some parasitic electrical length is already introduced by line' trace and the non-ideal RF-short capacitor), and with an additional 480nH RF inductor (to further push the impedance RF signal sees to near open-circuit).

Figure 16 BCD show the RF circuit of different bits, but with a similar switching mechanism. For 50 Ω bit, forward biasing D1 and reverse biasing D2 allow the transmit pulse to pass through, and vice versa reverse biasing D1 and forward biasing D2 allows the transmit pulse to be dissipated on the 50 Ω resistor. For the phase-shifting bit, two different types of phase shifters are used. The lumped element bit introduce the phase delay by a high-pass-tee filer circuit (C1, C2, and L in Figure 16 D), forward biasing D1, and reverse biasing D2 allow transmit pulse to pass, while reverse biasing D1 and forward biasing D2 force the transmit pulse pass through the tee circuit therefore phase delay was added. Lumped element design is more compact (used on 45 $^\circ$ and 90 $^\circ$ bit) however requires impractical component value when the desired phase-shift is

exceedingly small or large. Therefore, a second type of transmission line bit is used for 22.5° and 180° , where proper phase delay is introduced by a piece of transmission line with a certain length. Similar to the other bits, forward biasing D1 and reverse biasing D2 and D3 allow transmit pulse to pass, and reverse biasing D1 and forward biasing D2 allow proper phase delay caused by transmission line(TL) to be added to the pulse. Forward or reverse biasing of each diode are controlled by the pin diode drivers⁸¹, which are then operated by the control system. The driver provides either +150mA or -48V to the pin diode through RF blocking circuit. Details of the pin diode driver are attached in the appendix. In general, 5 bits are placed on two separate PCBs as motherboards with a daughterboard of pin diode driver is plugged on each, shown in Figure 16 E. And each set is cased in an aluminum enclosure for RF shielding with 3 LEDs equipped to indicate the ON/OFF states of each bit, shown in Figure 17. To avoid the high-power transmit pulse coupling into the pin diode driver's DC circuit through the electromagnetic emission, customized RF cages are applied on each motherboard to tightly shield the RF circuitry. A small power/TTL distribution board is used on top to easier split the lines coming from the control system. To further avoid RF signal getting into the DC circuit, all the DC lines are twist-paired with their ground line, although the case ground already exists for DC. In general, two modules are used for each channel, and in total 16 modules for 8 channels are placed on 4 shelves of the server rack shown in Figure 14 A.

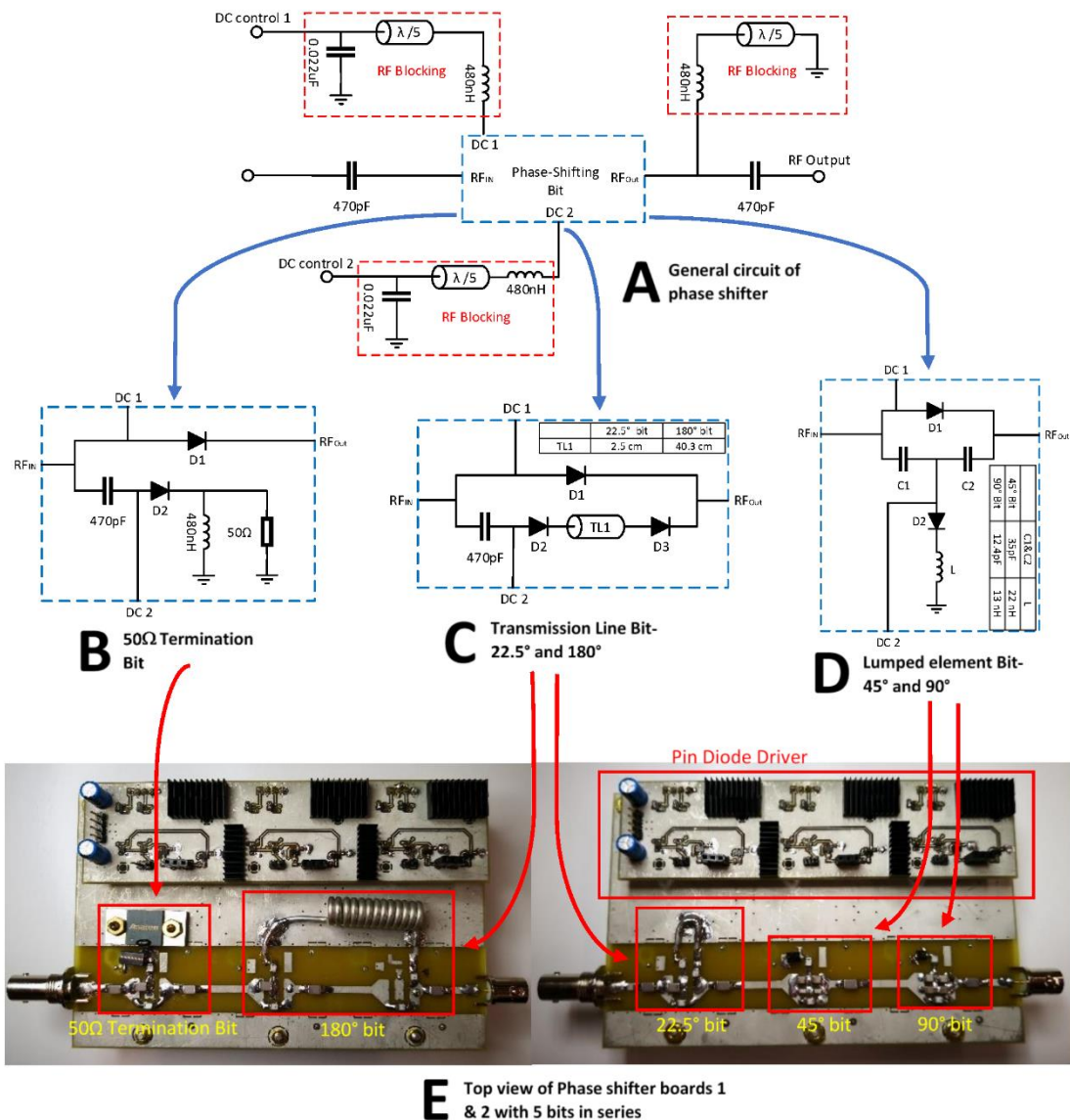


Figure 16 Overview of phase shifter's schematic and layout. (A) General circuit for phase shifters. (B) 50 Ω termination bits can either block the transmit pulse or allow the pulse to pass through. (C) The transmission line bit can either add a 22.5° or 180° phase delay to the transmit pulse or allow it to pass through. (D) Lumped element bit can either add a 45° or 90° phase delay to the transmit pulse or allow it to pass through. (E) The picture of phase shifter PCB. Figure courtesy⁴³.

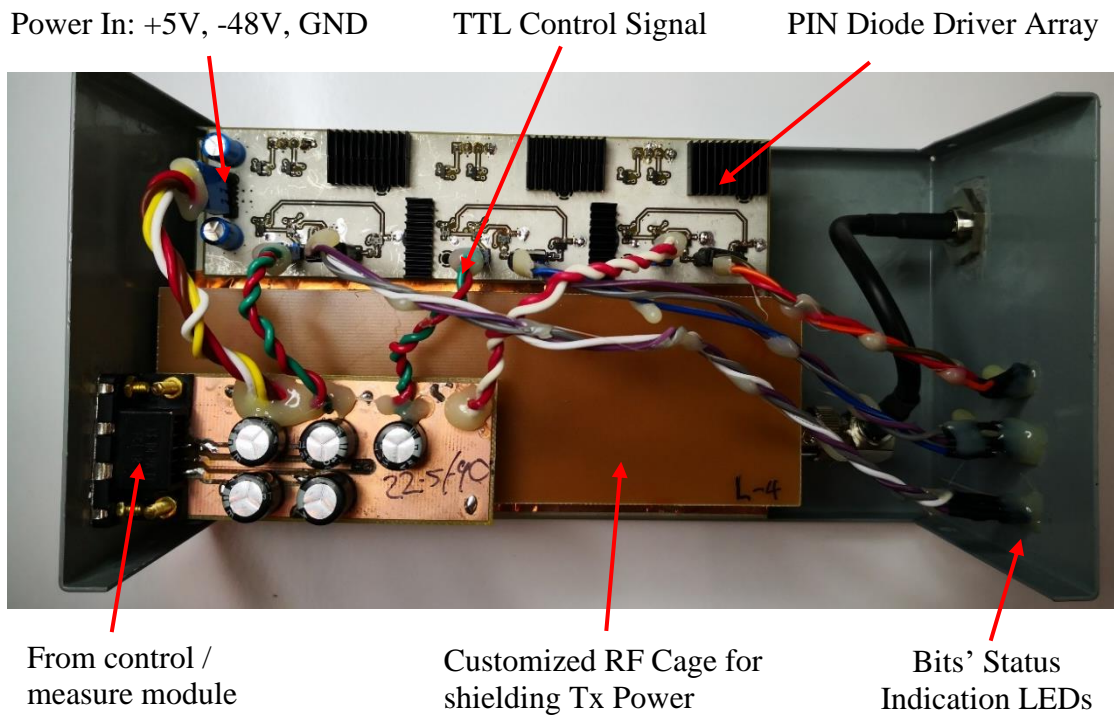


Figure 17. Picture of a phase shifter module cased inside the enclosure.

4.4 Control and Measure Module

To control the phase shifter remotely, the control system⁴³ was developed, shown in Figure 18. A computer first sends out commands to a beagle bone black, which then relay the command through long fiber optics to the microcontroller AVR-H128 that controlled the phase shifter array. The computer and beagle bone black are placed in the console room so that it can be operated easily by the scientist. Microcontroller AVR-H128 is placed inside the control/measure module sitting on the bottom shelf of the server rack shown in Figure 14 A to directly control the phase shifter array. The fiber-optic connection between the BBB and MCU is used to avoid SNR contamination from digital clock noise of regular USB or ethernet cable.

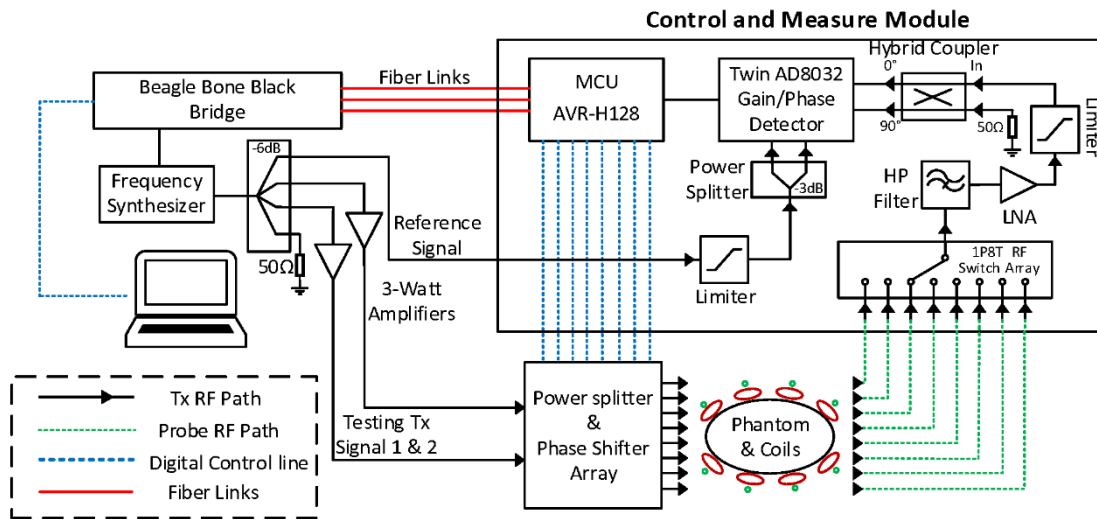


Figure 18. Overview of control and measurement module. Figure courtesy⁴³.

To measure the phase of the transmit pulse on the coil element ultimately, a measure system⁴³ was developed. A set of sensing pickup probes are placed near the coil array to sample a small portion of the transmit pulse and send it back to the system to be measured. These sampled signals are first selected by a 1P8T RF switch array so that only one channel's signal needs to be measured at one time. And then all other channels' signals are measured one by one in series. Although this selective approach needs a relatively longer measurement time (~60ms for all) since all 8 channels are measured in series. But it significantly reduces the amount of receive channel we need inside the system, therefore saving a lot of space and hardware cost. The selected signal is then routed through a series of signal conditioning devices: high-pass filter, LNA, power limiter and arrive at the AD8032 gain/phase detector to be measured, pictures shown in Figure 19. The AD8032 can detect two signals' relative power level difference and relative phase difference, and output gain/phase difference as two voltages, which can

then be measured and processed by the microcontroller. Since a single AD8032 board can only detect relative phase difference in the 180° range, two AD8032 and a 90° hybrid coupler⁸² are used together to measure the full range of 360° . In this system, the selected feedback signal is compared against a static known reference signal generated from the TPI and testing amplifier module (shown in Figure 14 C), so that its power level and phase can be accurately measured. To test this system on the bench, a testing transmit system was also built to mimic the scanner's transmitter. A frequency synthesizer TPI controlled by the beagle bone black generates a 298MHz sinewave as the frequency source, which is then split into 4 channels using a four-way power divider, shown in Figure 21. One of the four outputs is used as the static known reference signal for the twin AD8032 to detect feedback signals. Two of the outputs are amplified by two 3-Watt power amplifiers and then routed to the main power dividers and phase shifter array as the testing "transmit pulse".

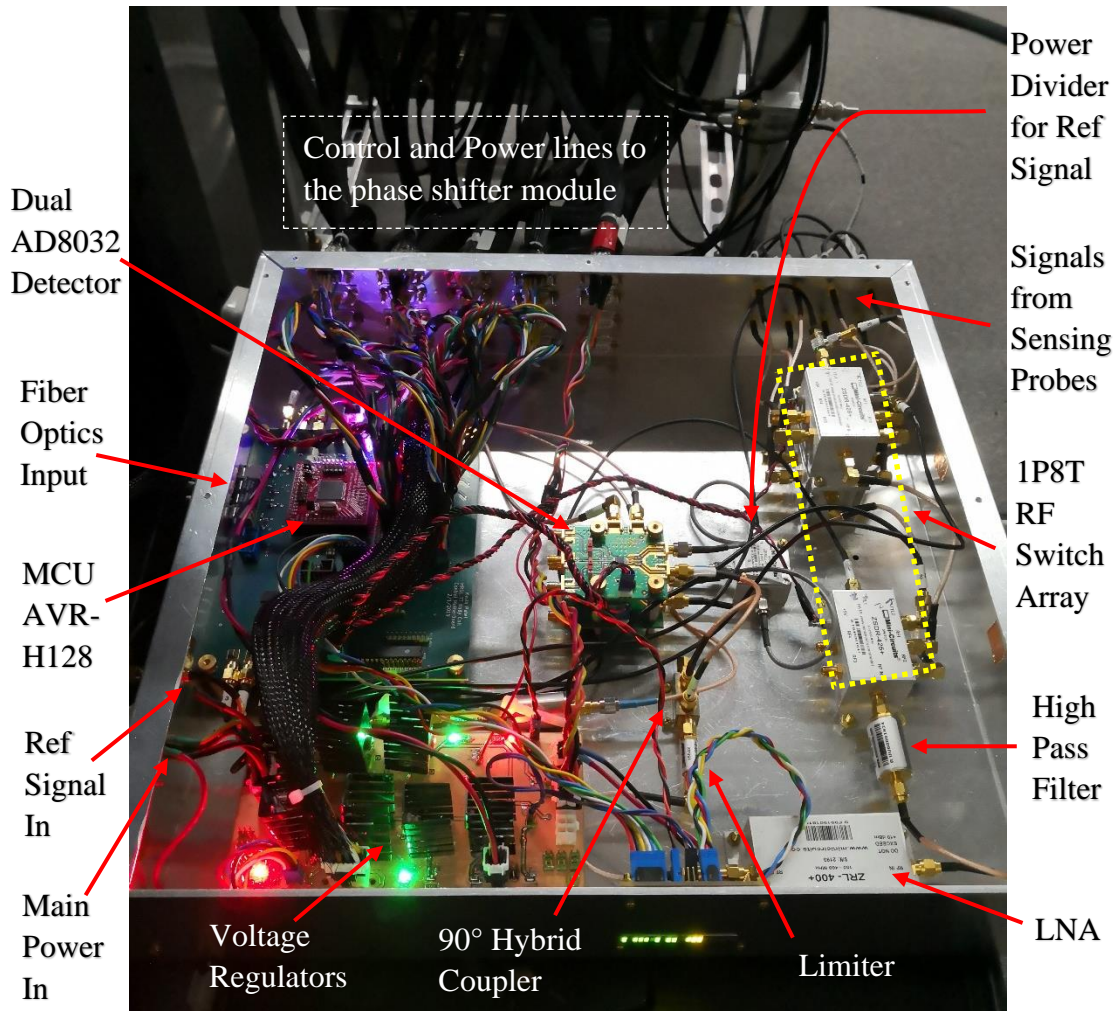


Figure 19. Picture of the control and measure module with annotations of different parts.

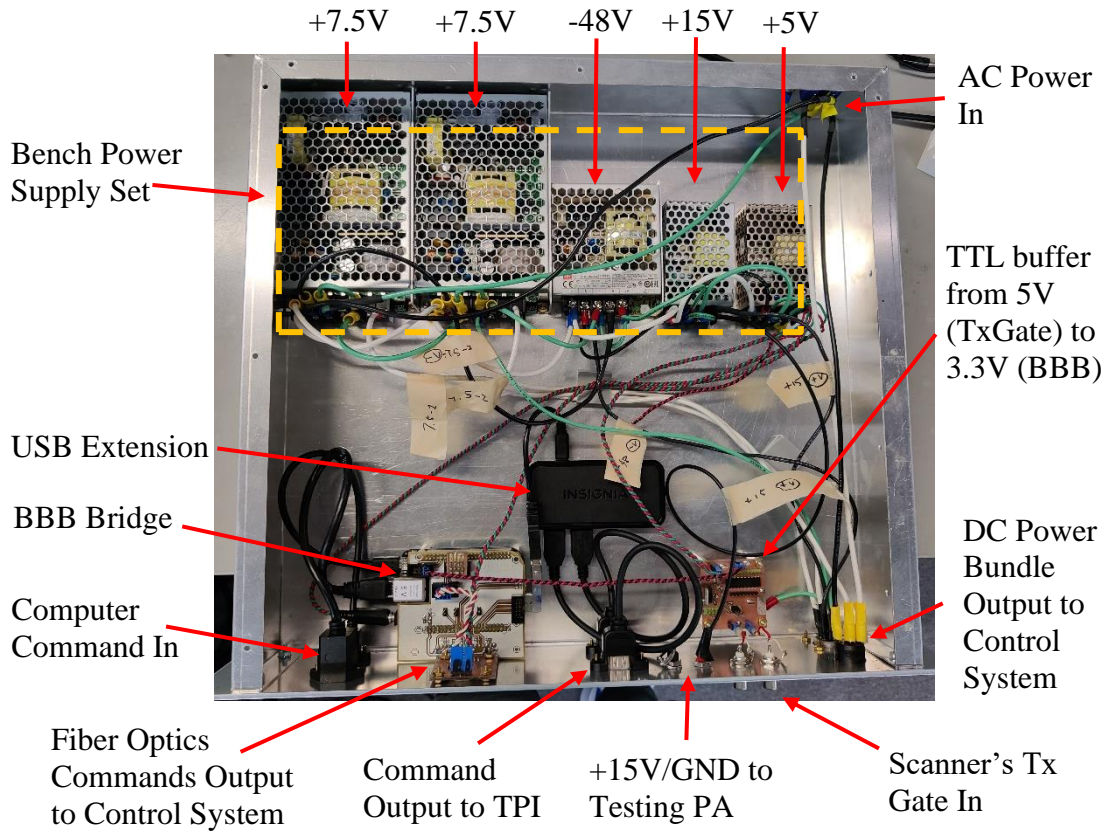


Figure 20. Picture of power supply and Beagle Bone Black module with annotations of different parts.

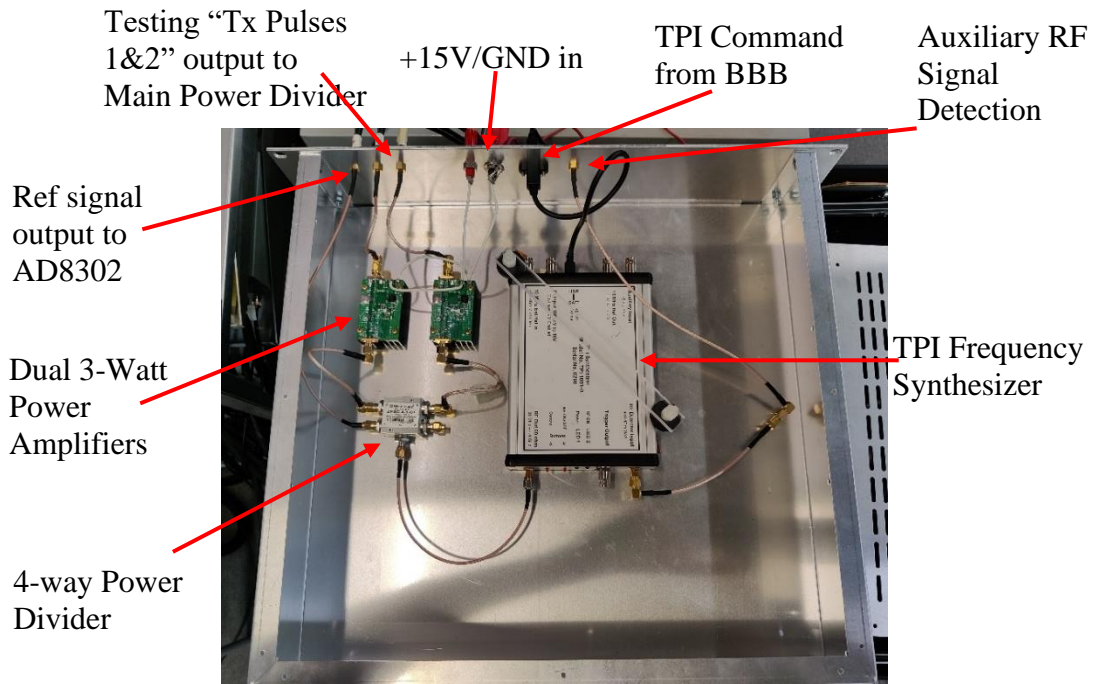


Figure 21. Picture of TPI and testing power amplifier module with annotations of different parts.

4.5 Simulation Study

To validate the concept of B_1^+ Steering, a series of modeling were run to simulate the steered B_1^+ maps. Figure 22 shows the simulation model built in Remcom xFdtd 7.4. An almond shape uniform phantom (inside dimensions of 35.5cm by 26cm by 40cm) was modeled, closely following the elliptical human model reported by Van Den Bergen²⁶. The phantom's conductivity was set to 0.31S/m, and relative permeability was set to 45, which is close to the averaged human body' parameter reported by Leor Alon⁸³. An 8 channel dipole array was modeled around the phantom, following the design reported by Wiggins, GC⁸⁴. Each dipole element is modeled as a perfect electrical conductor of 37cm long, 1cm wide, and also fed at the center by a high impedance current source (1000 Ω , 1A). By using a current source with the source impedance much higher than the coil, the current flowing into the coil can be forced to be whatever the source output, therefore eliminating the coupling-induced current on each coil. Another way to explain this is high impedance source directly adds a big real impedance in series with the coil, therefore immediately damping the current induced by coupling. Thus, the ideal B_1^+ maps without the interference of dipole-to-dipole coupling can be acquired for the initial modeling study, shown around the phantom in Figure 22. Magnitude maps at the center plane of the phantom are plotted using MATLAB as examples, but phase maps were also acquired from the modeling.

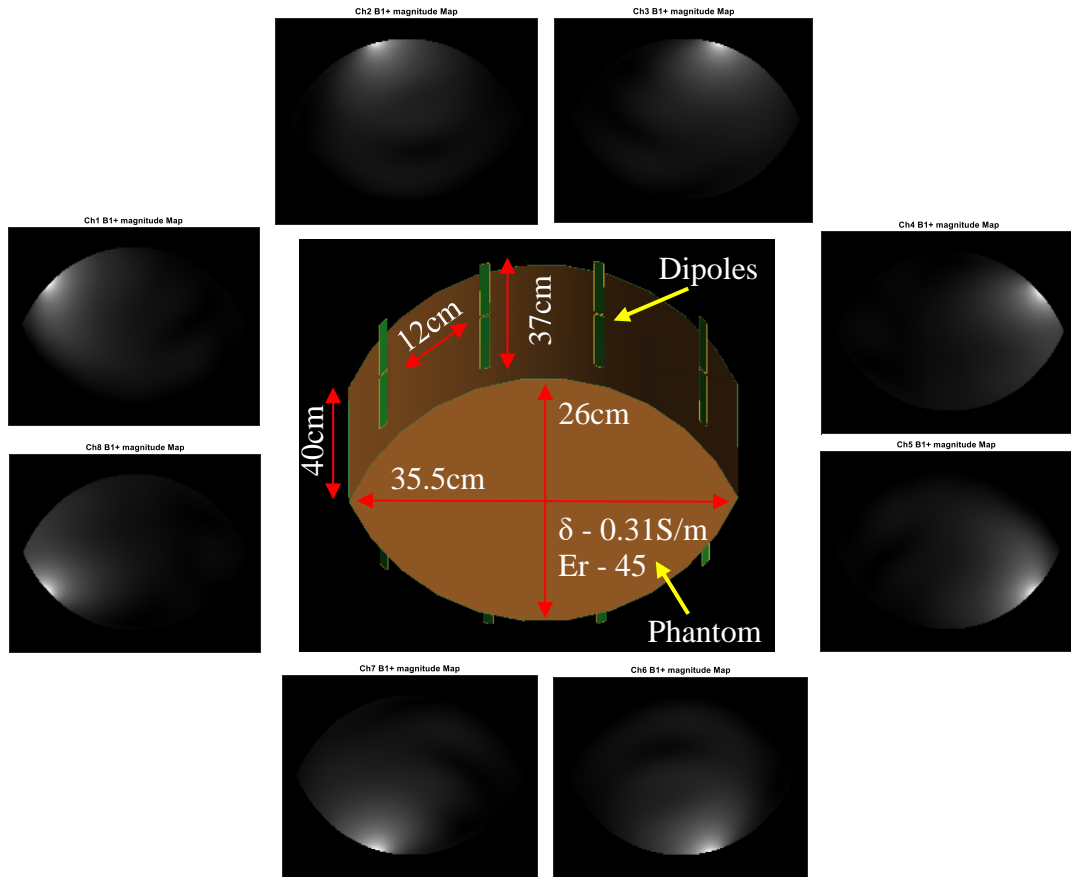


Figure 22. Overview of the simulation model in Remcom XFDTD. An almond shape uniform phantom (Major axis length of 35.5cm, Minor axis length of 26cm, Conductivity of 0.31 S/m, Permittivity of 45) was built for mimicking abdomen, and 8 dipoles were placed around the phantom as coil array. 8 simulated B⁺ magnitude maps from individual dipole are shown around the model.

In theory, for a parallel transmit coil array the total B_1^+ field is simply the summation of the B_1^+ field from individual coil element, assuming no coupling between each coil. Since we have acquired the clean individual B_1^+ maps with known input power from the modeling, any parallel-firing B_1^+ maps that combined from each coil with different magnitude and phase can be synthesized in post-processing.

An example of conventional birdcage excitation is shown in Figure 23. In birdcage excitation of an 8-coil array, the transmit pulse' phases on each channel are 0° , 45° , 90° , 135° , 180° , 225° , 270° , and 315° . In post-processing, this can be achieved by phase-shifting the B_1^+ maps from each coil and then adding them together. As you can see, in ultra-high-field (7T), the simulated transmit pattern of conventional birdcage is highly uniform where central brightening^{14,24,25,36} and undesired nulls and hot spot²⁶ can be observed everywhere. This is a long-standing issue in the high field and ultra-high-field MRI since the wavelength of the B1 field at high frequency (e.g., 298MHz is the Larmor frequency of 1H at 7T) has become comparable to the human body^{23,24}, the standing wave effect is inevitable for a large object like the human abdomen.

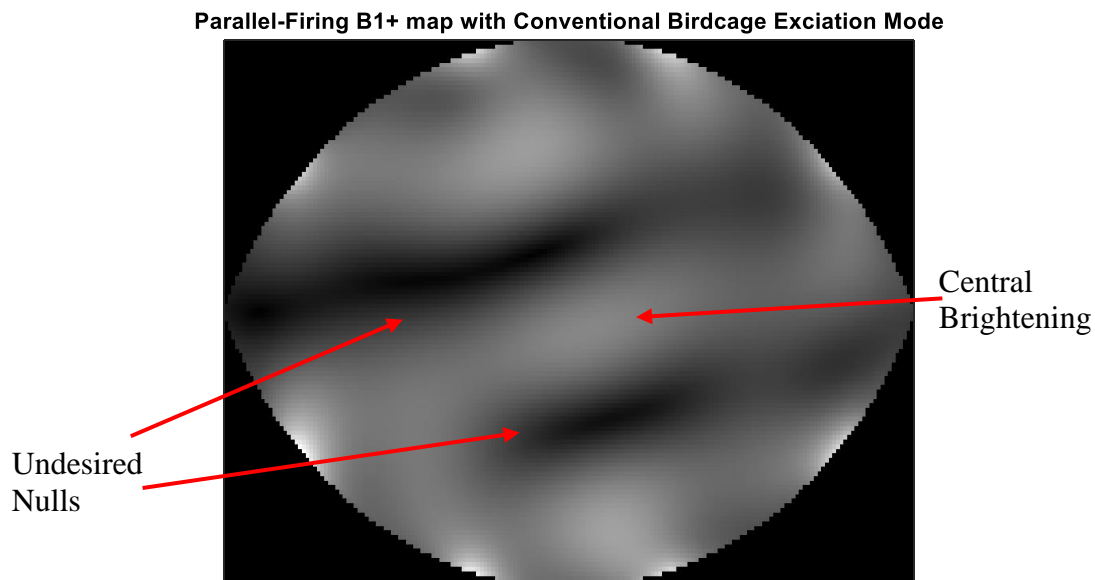


Figure 23. Simulated parallel-firing B_1^+ magnitude map with conventional birdcage excitation mode at 298MHz, where Tx pulse' phase of each coil element are 0° , 45° ... 315° degrees. Inhomogeneity of central brightening and undesired nulls can be observed due to the standing wave effect.

One advantage of using a parallel transmit coil array is the current distribution along the array need no longer be stationary like a fixed-tuned birdcage coil. Since each coil element has its feeding port, the magnitude and phase of transmit pulse on each element can be adjusted freely. The concept of B_1^+ shimming, or RF shimming, or the B_1^+ steering, is to adjust the amplitude and phase on each element to improve the transmit homogeneity^{25,26,36-41} and reduce the SAR²⁶, over a certain region of interest. Since the total B_1^+ map is the combination of individual coil's B_1^+ map, and at different places, the B_1^+ fields from each coil can be superposed both constructively and destructively and therefore resulting in nulls and hotspots, how to control the magnitude and phase on each element is the key to this method.

Scientists have reported many ways in terms of algorithms to practice B_1^+ shimming^{26,37-40}. But to validate our system in modeling, a simple conjugate-phase method that only the phase on each element was adjusted to optimize a single point on B_1^+ map is used, similar to the method reported by Metzger, G.J³⁷. Conjugate-phase means each coil's phase was set to the opposite of the measured phase at a selected point in its B_1^+ map. By applying the conjugate phase, all coil element's B_1^+ field will reach the same 0°-phase at the selected point, and therefore only add up but not cancel with each other only at this selective point.

9 simulated B_1^+ Steering results achieved using the conjugate-phase method targeted at different points are shown in Figure 24. For each case, phases from the different coil at the selected point (Red Marker) are first measured and then added back negatively to coils (realized by phase-shifting each B_1^+ field matrix). As we can see in

these results, an elliptical B_1^+ hotspot can be observed around the desired point.

However, nulls and hot regions still exist outside the hotspots, due to the nature of ultra-high-field.

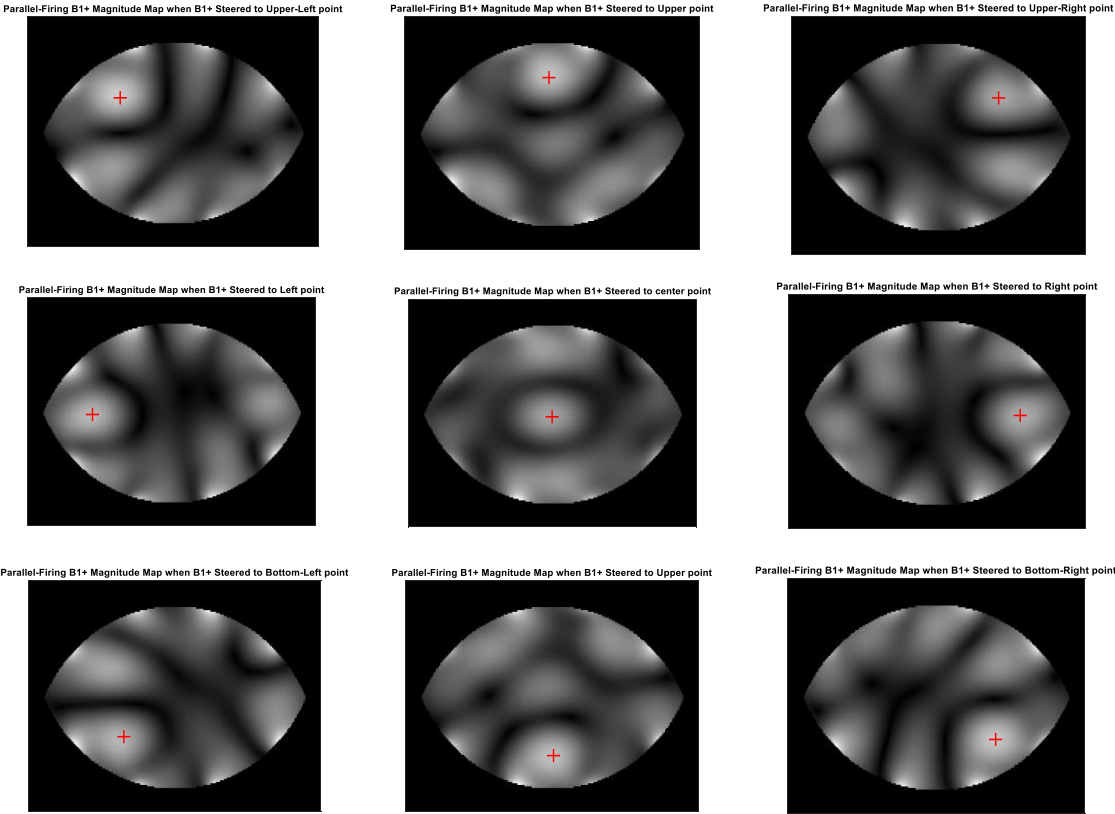


Figure 24. Simulated Parallel-Firing B_1^+ Magnitude Maps with different target points (Red Maker) of B_1^+ Steering.

4.6 Bench Validation

To test the system and the B_1^+ steering method, bench measurements are taken following the same workflow as in modeling. The bench measurement setup⁴³ is shown in the center of Figure 25. An almond shape phantom sitting on the side with the same dimension in simulation (35.5cm by 26cm by 40cm) was built for bench testing. The phantom is filled with corn syrup and distilled water with a ratio of 4:1 to achieve relative permittivity of 45, and added with salt to achieve conductivity of 0.31S/m⁸³. A cross-probe made of two shielded pickup probes⁸⁵ was inserted into the lid-open phantom to measure the B_1^+ field. The two-pickup probes are perpendicular so that both B_x and B_y can be measured first. And B_x and B_y were routed to a 90° hybrid coupler to form B_1^+ and B_1^- together, which are then measured by an HP4195A network analyzer. The cross probe is installed on a 2-dimensional positioner system so that it can be swept across the whole phantom region to map the B_1^+ and B_1^- fields. The $B_1^{+/-}$ acquisition on VNA and probe position moving are synchronized by a python program (done by Madavan).

8 B_1^+ maps were first acquired when each dipole transmits individually and other elements terminated by 50Ω-bit, shown in the peripheral of Figure 25. Again, each coil's B_1^+ magnitude map are shown as examples, but both magnitude and phase of B_1^+ and B_1^- were acquired,

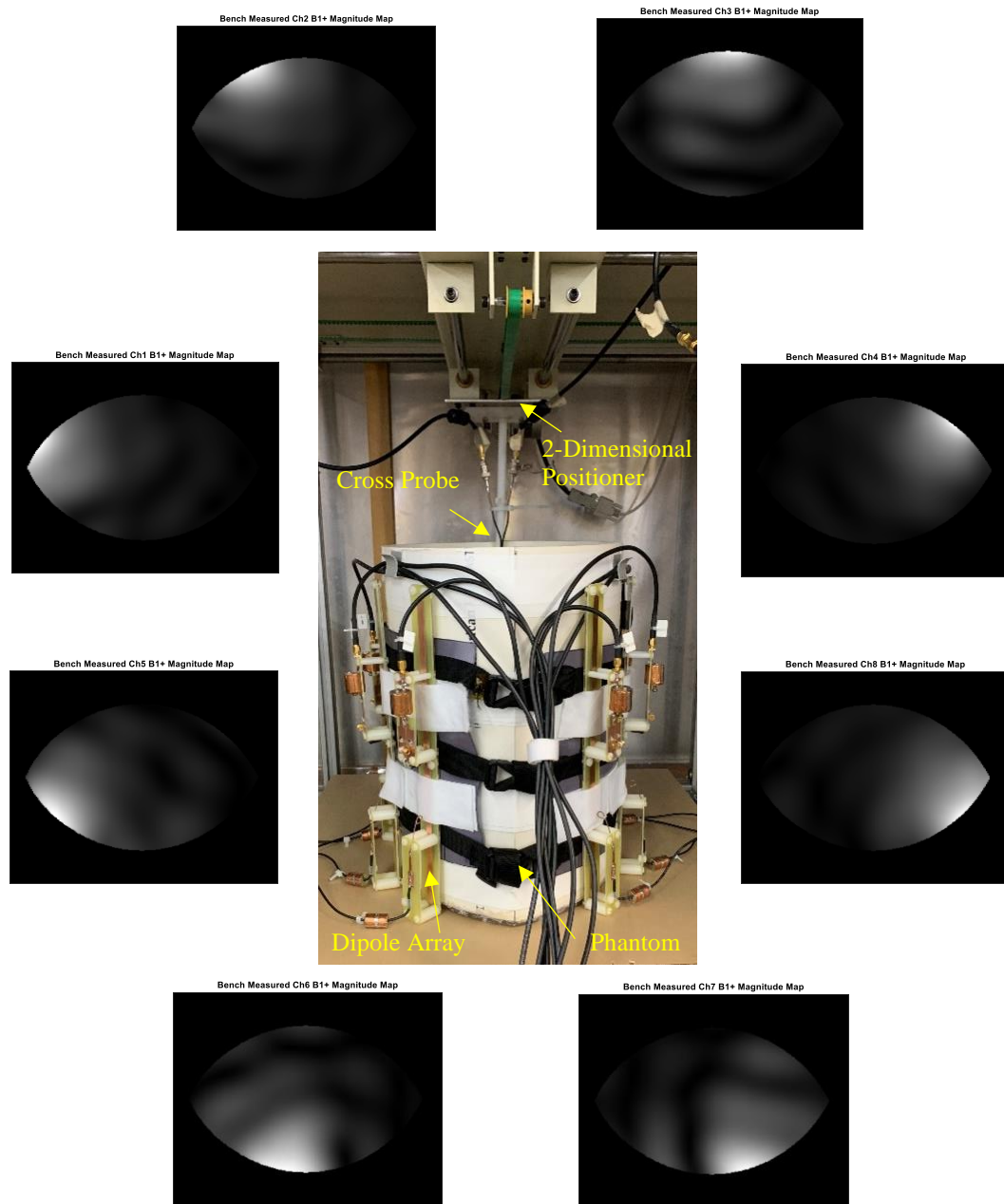


Figure 25. Overview of the bench measurement setup. A cross probe installed on a 2-dimensional positioner system is inserted into the phantom and can be moved around to map out the $B_{1\pm}$ field. Bench-measured B_1^+ magnitude maps from each coil are shown around the setup.

To B_1^+ steer to the target point on the bench, the same conjugate method with the simulation was used. Bench-measured phases on each target point from each coil's B_1^+ map were first extracted and applied back to each coil negatively so that a parallel firing B_1^+ map can be acquired for each targeted point. Some B_1^+ steering results focus on 4 different target points are shown in Figure 26. As we can see, hot spots are formed around the target point.

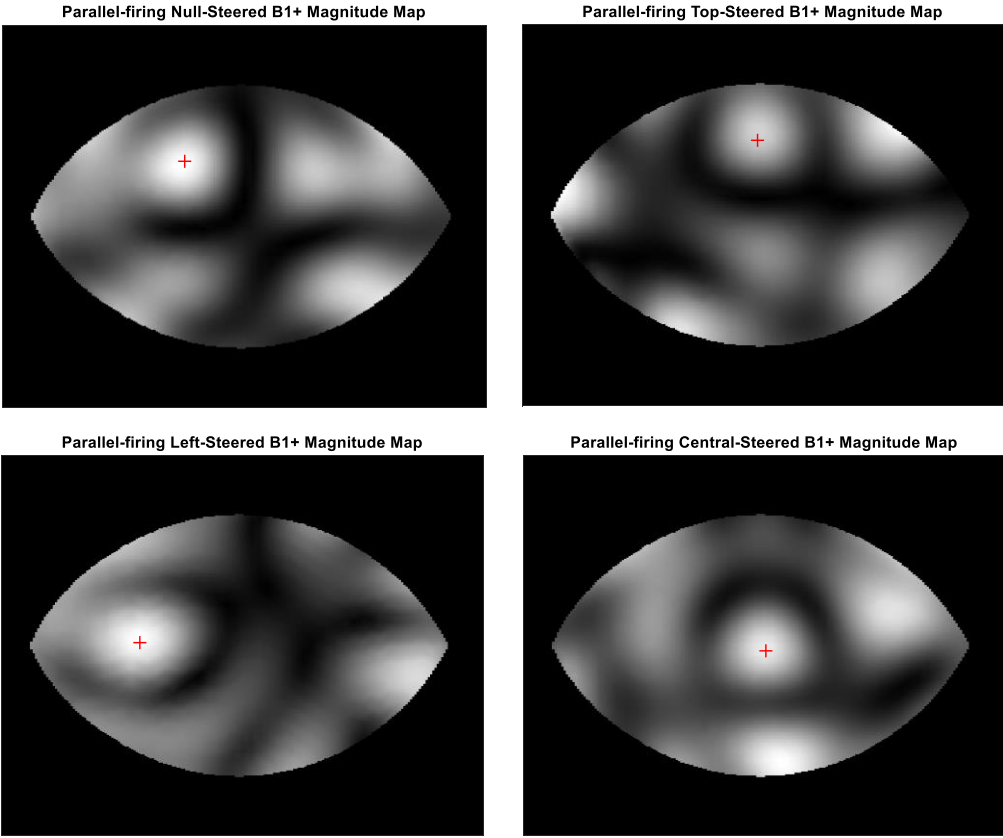


Figure 26. Bench-measured parallel-firing B_1^+ magnitude maps with different target points (Red Marker) of B_1^+ Steering.

4.7 Imaging on 7T Scanner

To test the performance of this system, the same B_1^+ steering method was used with the Phillip Achieva 7T scanner⁴³, shown in Figure 27. The phantom and dipole array was put on the patient table which can bring the load to the center of the bore automatically. The B_1^+ steering system is placed near the patient table to connect with the dipole array and scanner's interface box located on the patient table. The pulse sequence used for testing the system was a 3D gradient echo (T1FFE) with parameters as follow: anatomical plane of Transverse, FOV of 375 x 297 mm², matrix size of 96 x93, number of slices of 17, slice thickness of 40mm, slice gap of 20mm, echo time/pulse repetition time of 30/150ms.

B_1^+ Steering method in the manner analogous to the modeling and simulation was used on the scanner as well. 8 Images of individual dipole transmit/receive and others terminated were first acquired, shown in the peripheral of Figure 27. Phase information at the target point was extracted from these individual-transmit maps through the scanner's console and then applied back negatively to the phase-shifter system. The parallel-firing B_1^+ maps that B_1^+ steered to each target point were then acquired on the scanner, shown in Figure 28. As we can see, for all three target points good B_1^+ hotspots are formed, while the undesired nulls can still be observed as we expected.

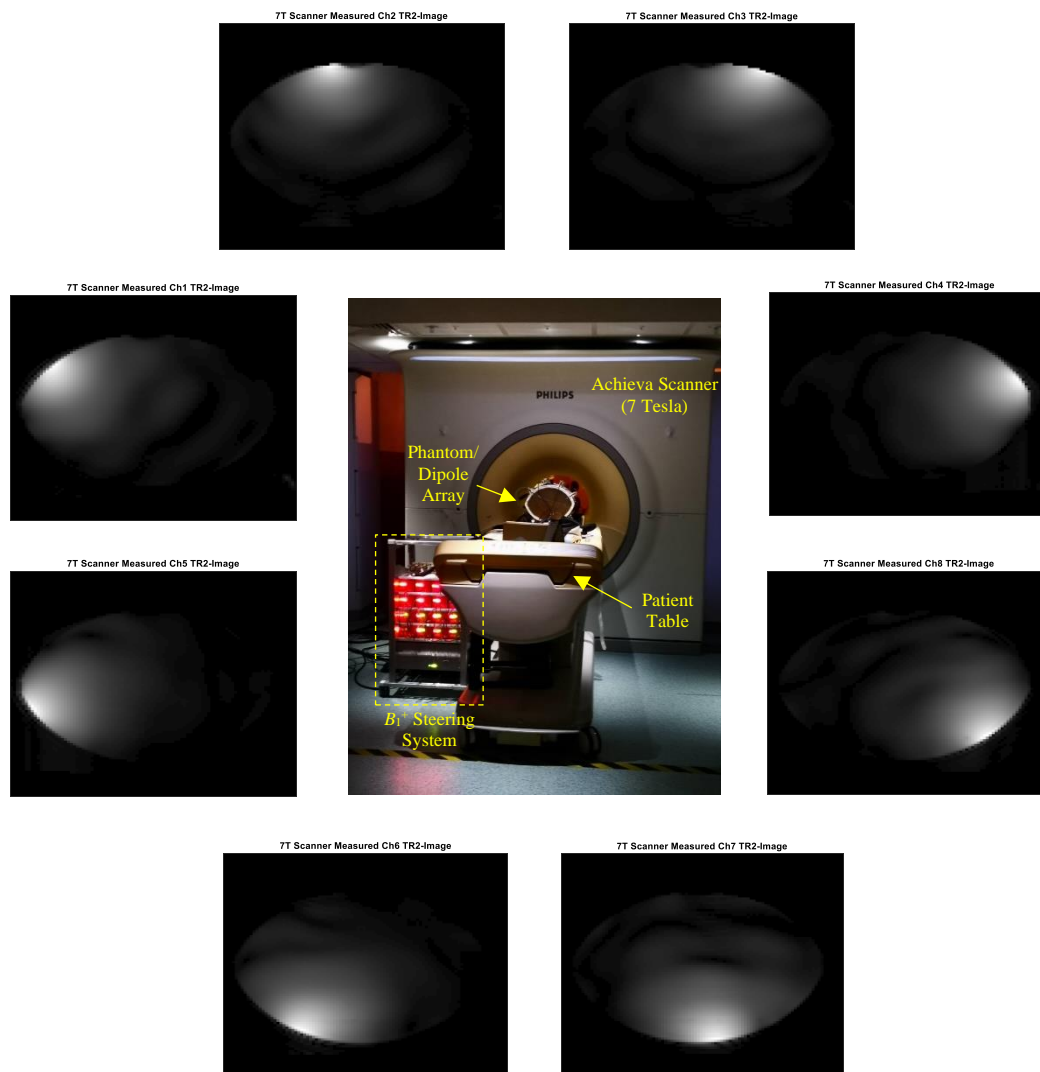


Figure 27. Overview of the system's setup when tested with 7T scanner. The phantom/dipole array was placed on the patient table, and the phase-shifter system was placed near the patient table to interface with the dipole array and scanner's I/O. 8 images of individual coil transmit/receive are shown on the peripheral.

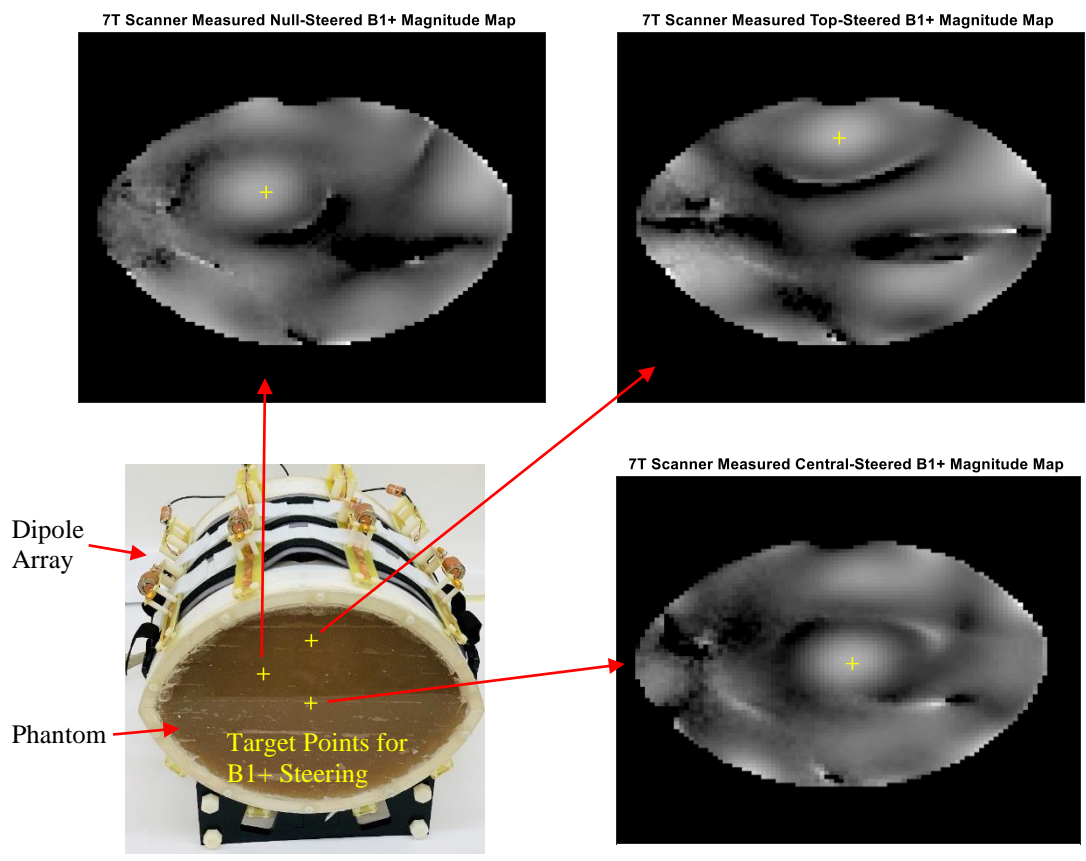


Figure 28. B_1^+ steering results acquired on 7T scanner that targeted at 3 different points. The yellow markers indicate where the targeted points locate.

4.8 B_1^+ Results Analysis and Discussion

B_1^+ Steering results acquired from simulation(A-C), bench-measurement(D-F), and 7T scanner(G-I) were compared in Figure 29⁴³. As we can see, a small region of increased B_1^+ intensity around the target point can be observed in all of the cases, due to the destructive cancellation between each coil's B_1^+ field being minimized. However, undesired nulls still exist at other places since B_1^+ fields out of the target point were not controlled in the B_1^+ steering method we were using. To quantify the B_1^+ steering results, the definition proposed by Mao³⁹ was used in this analysis: a very homogenous region has a relative standard deviation less than 5%, and a fairly homogenous region has a relative standard deviation less than 20%.

The measured sizes of very and fairly homogenous regions in different cases are shown in table 2. In the simulated B_1^+ steering maps, very homogenous regions around the target point are about 3.6 x 4.4 cm², 3.6 x 4.8 cm², and 3.6 x 4.4 cm² respectively for central focus, upper-left focus, and upper focus. Fairly homogenous regions around the target point are about 6.4 x 10.0 cm², 6.8 x 9.2 cm², and 7.2 x 10.0 cm², respectively. In the bench-measured B_1^+ steering maps, very homogenous regions around the target point are about 4.2 x 4.2 cm², 4.6 x 4.7 cm², and 4.2 x 4.2 cm², respectively. Fairly homogenous regions around the target point are about 8.1 x 8.6 cm², 8.6 x 9.2 cm², and 8.4 x 8.6 cm², respectively.

And most importantly in the 7T-scanner measured B_1^+ steering maps, very homogenous regions around the target point are about 2.6 x 3.9 cm², 2.6 x 3.9 cm², and

2.6 x 4.7 cm², respectively. Fairly homogenous regions around the target point are about f 5.7 x 7.8 cm², 5.7 x 8.6 cm², and 6.4 x 10.2 cm², respectively.

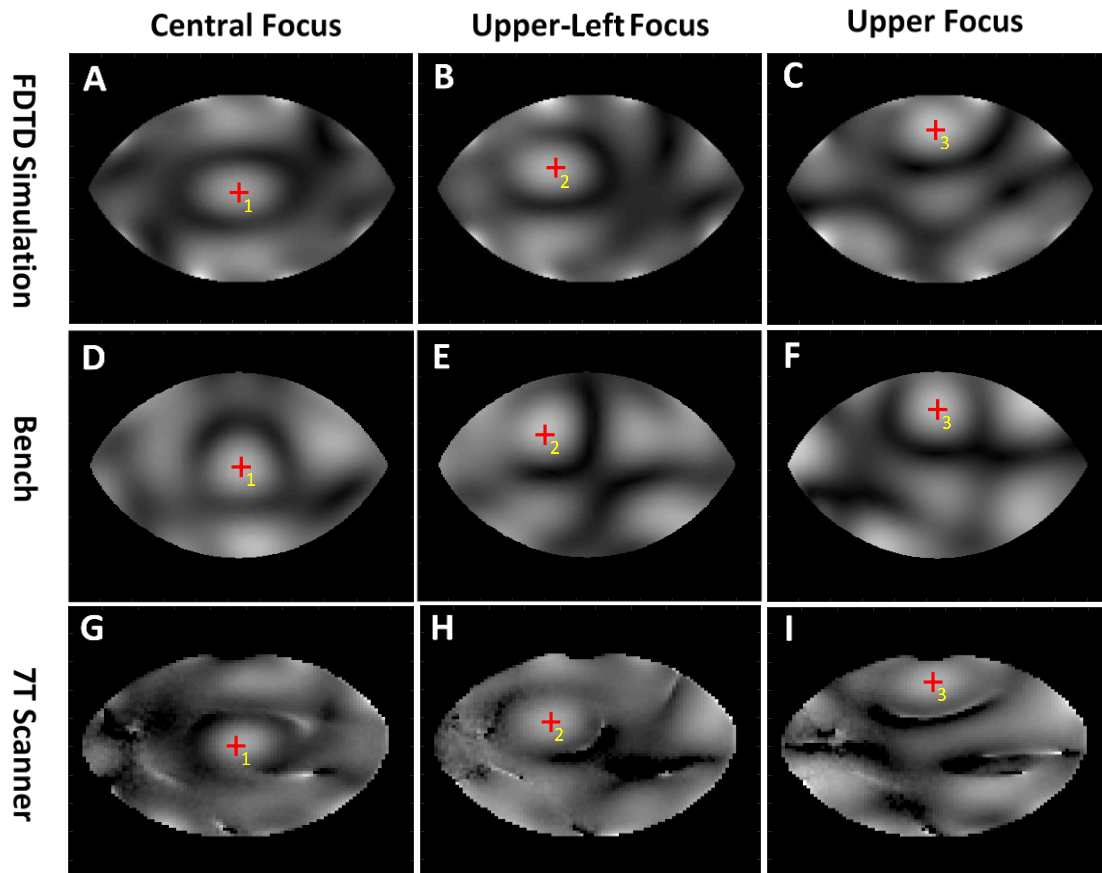


Figure 29. Comparison of B_1^+ steering results acquired from simulation (A-C), bench measurement (D-F), and 7T scanner (G-I). The red maker indicates the target point for B_1^+ steering. Figure courtesy⁴³.

The agreement can be found among all the B_1^+ maps acquired through both simulation, bench measurement, and 7T scanner that an elliptical region with homogenous B_1^+ field can be formed around the designated point using the conjugate-phase method. Based on results acquired on the 7T scanner, the average size of the very

homogenous region this method can achieve is approximately $2.6 \times 4.2 \text{ cm}^2$, and the average size of the fairly homogenous region this method can achieve is approximately $5.9 \times 8.9 \text{ cm}^2$. The demonstration of the conjugate-phase method validates the phase-manipulating ability of this system, and potentially more sophisticated B_1^+ steering methods can be implemented using this system.

Table 2. The measured sizes of very and fairly homogenous regions were generated when B_1^+ Steering to different target points, for both simulation, bench measurement, and 7T scanner.

	Homogenous Region	Central Focus	Upper-Left Focus	Upper Focus
Simulation	very homogeneous	$3.6 \times 4.4 \text{ cm}^2$	$3.6 \times 4.8 \text{ cm}^2$	$3.6 \times 4.4 \text{ cm}^2$
	Fairly homogenous	$6.4 \times 10 \text{ cm}^2$	$6.8 \times 9.2 \text{ cm}^2$	$7.2 \times 10.0 \text{ cm}^2$
Bench	very homogeneous	$4.2 \times 4.2 \text{ cm}^2$	$4.6 \times 4.7 \text{ cm}^2$	$4.2 \times 4.2 \text{ cm}^2$
	Fairly homogenous	$8.1 \times 8.6 \text{ cm}^2$	$8.6 \times 9.2 \text{ cm}^2$	$8.4 \times 8.6 \text{ cm}^2$
7T Scanner	very homogeneous	$2.6 \times 3.9 \text{ cm}^2$	$2.6 \times 3.9 \text{ cm}^2$	$2.6 \times 4.7 \text{ cm}^2$
	Fairly homogenous	$5.7 \times 7.8 \text{ cm}^2$	$5.7 \times 8.6 \text{ cm}^2$	$6.4 \times 10.2 \text{ cm}^2$

4.9 Summary

In general, a system was developed to perform B_1^+ Steering for 7T scanners without the need for a large parallel transmitter array⁴³. This system provides a new degree of freedom of phase on each Tx channel so that the parallel-firing B_1^+ maps can be controlled according to the B_1^+ steering method. A simple conjugate-phase method was used to successfully validate the feasibility of this system.

Frankly, the most efficient way to perform B_1^+ shimming is using the parallel transmitter, since it offers full magnitude and phase control with much finer resolution. But it comes with a very high associate cost, SAR issue, and complexity. The overall material cost of this system, including development, components, several prototypes, etc., is less than \$11,000⁴³. This is far less than a parallel transmitter with the same amount of channel.

Another advantage of this system is its add-on feature. With the similar concept to some previous work^{42,86,87}, this system is designed to be an add-on module to the scanner. When being used on the scanner, it doesn't cause permanent loss of CE-labeling⁴³. And the original clinical architecture of the scanner can be restored immediately after disconnecting the add-on system from the scanner. The simple conjugate-phase method was used in this work to validate the hardware of the system, so only point-focus B_1^+ patterns are shown as results. However, this system is capable of performing a more complex and dynamic B_1^+ shimming method both on phantom and potentially in-vivo. Also, the proposed system can be used as a general bench platform for developing steering or shimming method without a scanner, since the system has the ability to both generate and measure different field patterns of B_1^+ directly on the bench.

CHAPTER V
INVESTIGATION OF DECOUPLING MULTI-NUCLEI SURFACE COIL ARRAY
USING HIGH IMPEDANCE PREAMPLIFIER

5.1 Overview of Proposed Decoupling Strategy

For a single-channel MRI coil (such as a birdcage, saddle coil, or one surface coil), conjugate matching⁸⁸ is often used as the impedance matching strategy since the maximum RF power delivery between coil and preamplifier or between transmitter and the coil can be ensured in such case. As shown in Figure 30, a surface coil can be impedance matched to the conjugate of the preamplifier's input impedance (50Ω , standard impedance of RF device, usually the optimal NF impedance as well) by a two lumped element matching network. And the 50Ω input impedance of the preamplifier is also simultaneously matched to the conjugate of the coil impedance, which cancels out the coil's reactance and resonates with the coil. For a single-channel MRI coil, maximum RF current can be induced on the coil if the coil is properly resonated. For an array coil, however, resonating also means the cross-talk between each element cannot be avoided, which in reality degrades array coils' performance, such as coil sensitivity loss and noise transferring between coils⁷¹.

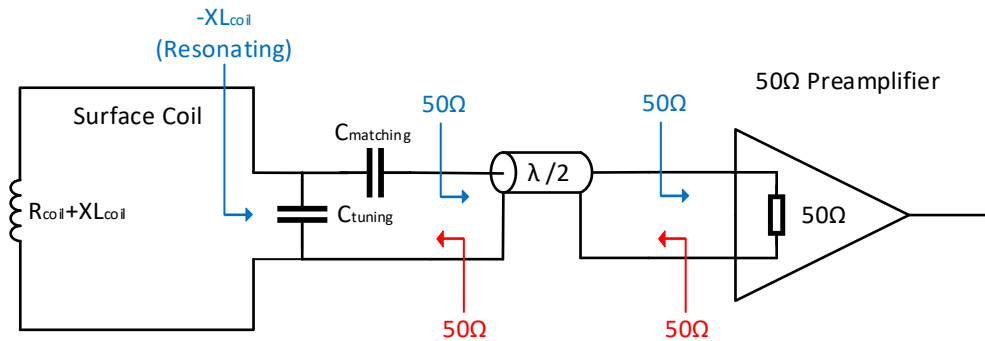


Figure 30. Conjugate Matching Configuration gives maximum RF power delivery between coil and preamplifier. In this configuration the coil's reactance is canceled thus maximum RF current can be induced on the coil and cause coupling.

To reduce the coupling between coils in an array, a low-impedance isolation preamplifier and matching network containing both capacitor and inductor are often used⁷¹. This configuration is shown in Figure 31. While the RF coil is matched and tuned to 50Ω through a capacitor and an inductor matching network so that the isolation preamplifier can see the optimal NF-matching source impedance (usually designed at 50Ω for preamplifier)⁸⁹, the low input impedance of the isolation preamplifier (around 0.5Ω) effectively parallel-resonate the LC matching network and creating a high-impedance block at the Larmor frequency that is directly in series with the coil. With the presence of this high impedance, the induced EMF in the coil does not generate an RF current and therefore the cross-talk between adjacent coils in an array can be reduced at the specific frequency. Typically, low impedance isolation preamplifier in this configuration can add more or less an additional 20dB of decoupling⁹⁰ to the surface coil beyond traditional decoupling methods such as overlapping and therefore can minimize the S11 shift of this coil as well as ensuring the clean receive pattern of the surface coil.

The penalty, however, is due to the nature of lumped element network in this decoupling configuration, the working frequency is limited to a narrow band (depending on the Q of the network). This decoupling configuration has proven to be effective for a single-nucleus coil array, and some researchers have built coil arrays with ever-increasing channel count based on this configuration^{7,8,91}. However, when the array coil needs to be operated at multiple frequencies, it becomes cumbersome to accomplish, since at each Larmor frequency a dedicated narrowband circuit network (coil/MN/preamplifier /switching) is both required. This means the multiple array coil using such an approach has to use multiple sets of the circuit but just work at different frequencies. The amount of complexity of decoupling multi-nuclei array coil solely based on low impedance isolation preamplifier is very high given the interference between each part of the array is usually very sensitive in reality. And the overall electrical design of such an array coil can be considered overwhelmingly bulky.

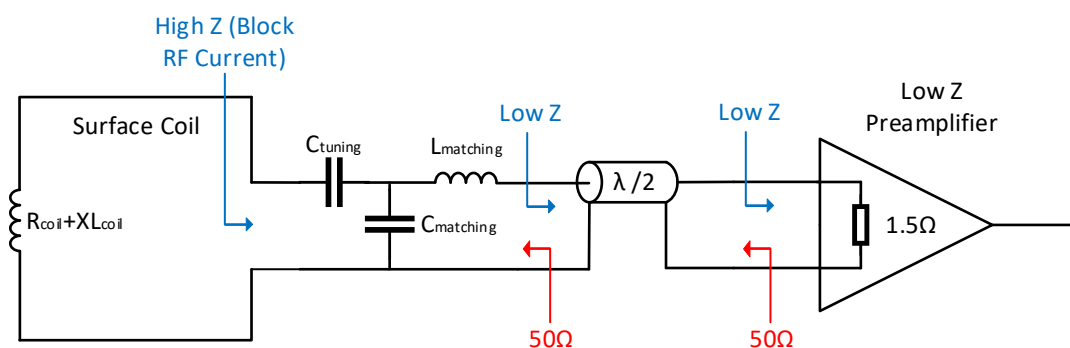


Figure 31. Roemer's Configuration, using LC and Low impedance preamplifier to create high Z on the coil for additional decoupling, but with a penalty of impedance mismatch as well as narrow operatable frequency

In general, the decoupling of Roemer's configuration is generated by a carefully-controlled impedance mismatch. Instead of matching the load impedance of 50Ω to the conjugate of the coil's source impedance (which resonates the coil), the short-circuit load impedance is mismatched to present a big impedance to the coil. And the mismatch can be used in different ways to decouple coils, such as shifting the resonant frequency away from the Larmor frequency⁹², and non-conventional impedance matching to higher than 50Ω with preamplifier holding inductive input impedance⁹³. For a multi-nuclei array coil, however, generating mismatch in a broadband manner for a surface coil (good decoupling) while maintaining good NF matching for preamplifier (good sensitivity) at the same time is still challenging.

In this study, we propose a novel decoupling strategy that could reduce the excessive complexity of decoupling multi-nuclei surface array coil. Instead of using an LC matching network and low impedance preamplifier to create a frequency-specific high-impedance parallel resonance, a preamplifier with a high input impedance itself can be utilized to suppress the induced RF current on MRI array coils directly, as shown in Figure 32. A series tuning element is firstly used to resonate the surface coil at multiple frequencies (could be achieved by multi-tuned LCC trap or varactor diode). A broadband impedance transformer is then used to match the low impedance of this coil closer to the preamplifier's optimal NF matching impedance, therefore the preamplifier can be operated with lower noise added. In the meanwhile, the very high input impedance of the preamplifier is brought down to the coil by the broadband transformer (down-

transformed but still high enough) to block the RF current and thus avoid coupling between adjacent elements.

Theoretically, since both high impedance preamplifier (e.g., a MOSFET) and transformer (RF transformer) are not frequency-specific, the decoupling can be achieved in a broad frequency range without the need of LC network as well as extra trap circuits operated at different nuclei. Therefore, if only one high impedance preamplifier and one transformer are needed to decouple a single resonator, the complexity of building a multi-nuclei array coil can be reduced significantly since multiple sets of LC networks/preamplifier/traps circuits are no longer needed. In practice, we observed the frequency bandwidth of this configuration is limited by the characteristic of the transformer. Therefore, infinite wideband decoupling is found difficult to achieve.

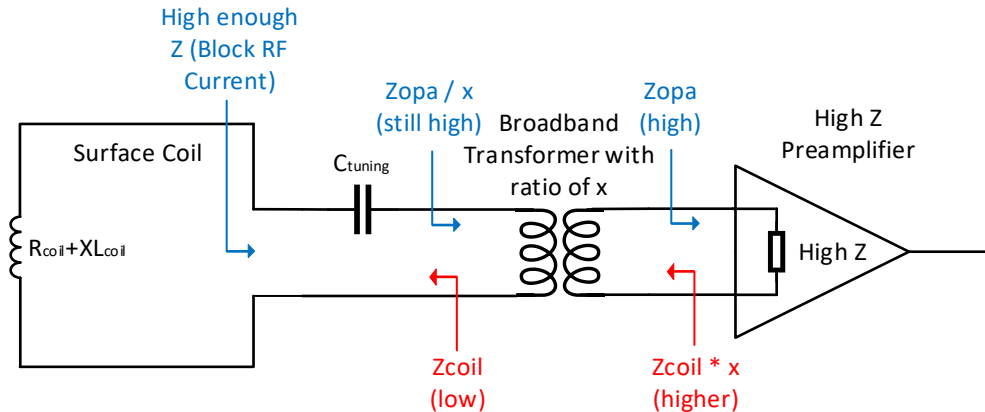


Figure 32. Proposed configuration using high impedance preamplifier to decouple coil and use a broadband transformer as the matching network between coil and preamplifier

5.2 High Impedance Preamplifier: Operational Amplifier

Many choices of high impedance amplifier units are available, such as a common MOSFET transistor or a dedicated ultra-low-noise SiGe RF transistor⁹⁴. Such a device could potentially deliver superior performance of NF, gain, etc. However, it requires expertise to design and build such circuits. In this work, we choose to use an operational amplifier to demonstrate the concept of high-impedance decoupling preamplifier because of its simplicity, low cost, and its broadband high input impedance. In general, the operational amplifier is commonly used for low-frequency applications. However, semiconductor companies, such as TI⁹⁵, provide a few products that can be used in MRI applications. After comparing different products, we decided to use LMH6629 (Texas Instruments) ultra-low-noise operational amplifier, since it has the lowest input noise ($0.69 \text{ nV}/\sqrt{\text{Hz}}$ and $2.6 \text{ pA}/\sqrt{\text{Hz}}$) and broad frequency range (GBWP of 4GHz). A non-inverting amplifier configuration was used in this work since it requires the minimum number of resistors (two resistors), which contribute thermal noises and reduce SNR. Additionally, the non-inverting amplifier type requires no resistor before the preamplifier, which helps preserve the cascaded NF as well as allows the high input impedance of OPA can be directly presented to the coil and matching network. The key parameter as an MRI preamplifier, the noise figure (NF), is modeled based on the specifications and supporting documents provided by the manufacturer^{95,96}. The calculation was done using MATLAB, and the script can be found in appendix C. The calculated OPA NF versus the resistor R_f and R_g 's value is investigated and shown in Figure 33. In calculation, a higher feedback resistance level effectively contributes to

no significant increment of the NF but can yield a higher gain. Therefore, the R_f should be chosen as high as possible in theory. And for the shunt resistor, the lower R_g leads to lower OPA NF in this calculation. Added with the benefit of even higher gain, the lowest possible R_g value should be chosen in theory.

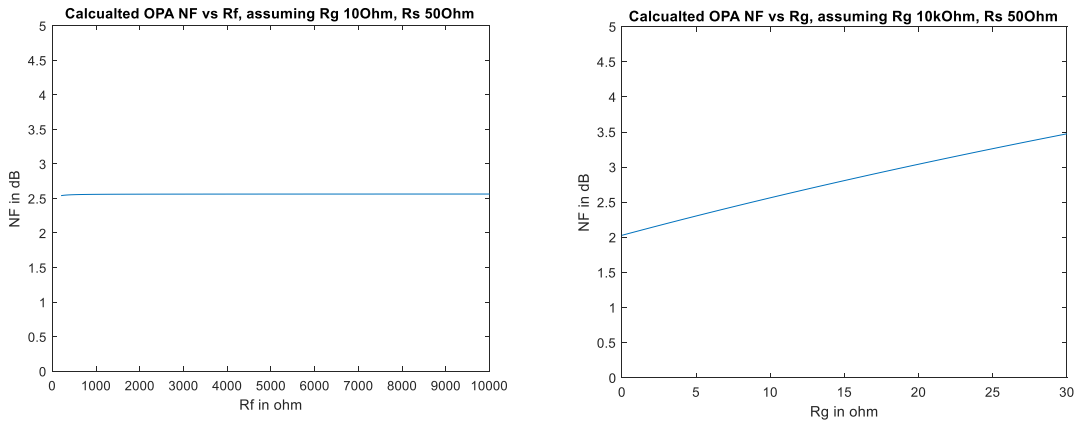


Figure 33. Calculated OPA NF with different R_f or R_g value for investigating optimal performance.

The calculated OPA NF versus the source resistance or impedance is investigated and shown in Figure 34, with the same value of R_f and R_g used in this calculation. The calculated ideal NF of OPA is optimally at about 0.99 dB when source resistance is around 306 Ohm. And between 40Ω to 2378Ω , this OPA design can maintain NF lower than 3dB, which theoretically gives us a broad source impedance range for the coil to be matched without too much sacrifice. When the ideal NF was plotted versus complex source impedance on the smith chart, the impedance area with NF lower than 3dB indicates the theoretical good-NF region for OPA.

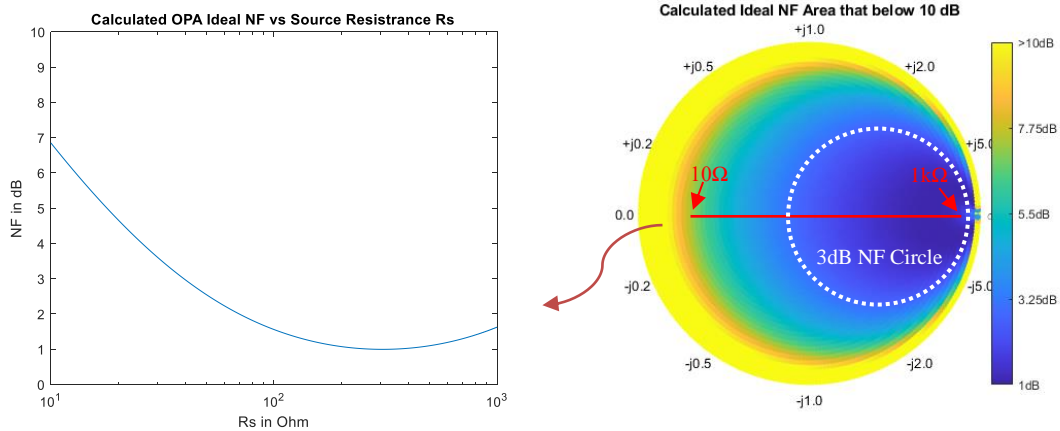


Figure 34. Calculated Ideal NF of OPA, versus pure real source resistance (Left), or complex source impedance (Right). The real source resistance in the left figure is plot as a red line on the smith chart as well.

Based on the calculated information, an OPA validation board is designed and built to test the OPA's performance, shown in Figure 35. A bias tee is used at the RF output port to bring in a positive 3.5 V DC supply, and another port is used to bring in the negative 3.5V DC supply. The simple non-inverting configuration is used with two resistors R_f and R_g for setting the gain and NF. RF filtering capacitors are used on the power rail to minimize the interface from the RF field. A pair of back-to-back Schottky diodes (Infineon Technologies, BAS 70-04W H6327) is used to protect the OPA in the case of sudden high input power level (such as MR transmit field). A series 50Ω RF resistor is used at output to match the OPA's low output impedance to the standard RF impedance of 50Ω. Since this resistor is at the later stage of the preamp, the overall cascaded NF is not degraded significantly according to the Friis formula.

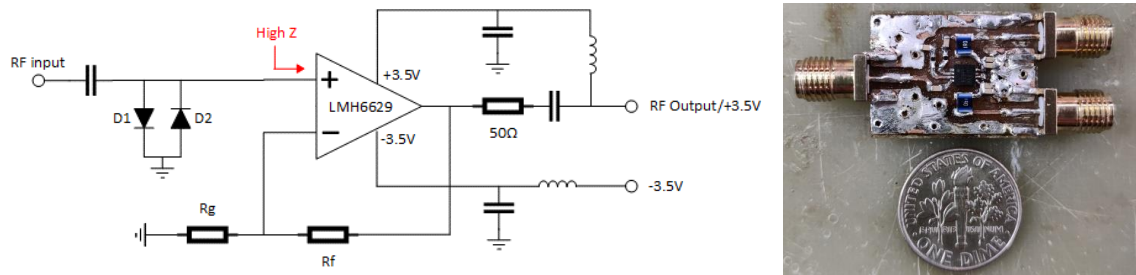


Figure 35. Schematic and picture of the validation OPA board.

The validation board was tested on the bench using the NF meter (HP8970B) with both 50Ω source and load impedance, and the results measured at 50MHz are shown in Figure 36. For a series of values of feedback resistance R_f tested on the bench (200, 300, 400, 500, 800, 1k, 3k, 5k and 10k Ω), the measured NF does not vary much, yet gain increase significantly with higher R_f level and reach a practical maximum around 5k Ω of R_f . In the same test for different values of R_g (0, 1, 3, 5, 7.5, 10, 20, and 30 Ω), the lower R_g value leads to both higher gain as well as lower NF. Good agreement can be found between the bench NF/Gain measurements and the calculation. Therefore, the R_g should be as small as it can (short-circuit) and the R_f should be infinite (open-circuit) since no penalty of using big R_f can be observed ideally. If the R_f and R_g 's value can be chosen to be optimal enough ($R_g=0\Omega$, $R_f=10k\Omega$), the measured gain and NF of the validation OPA board is 33.57dB and 2.58dB, respectively, when the source and load impedance are both 50Ω .

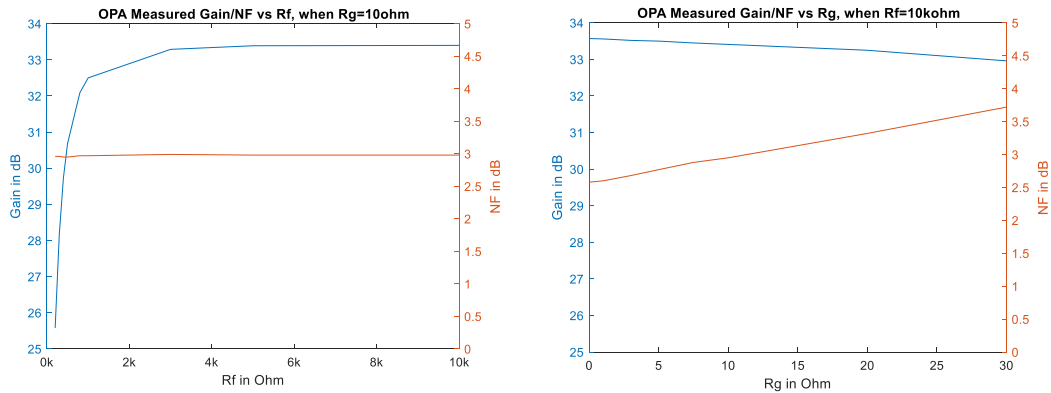
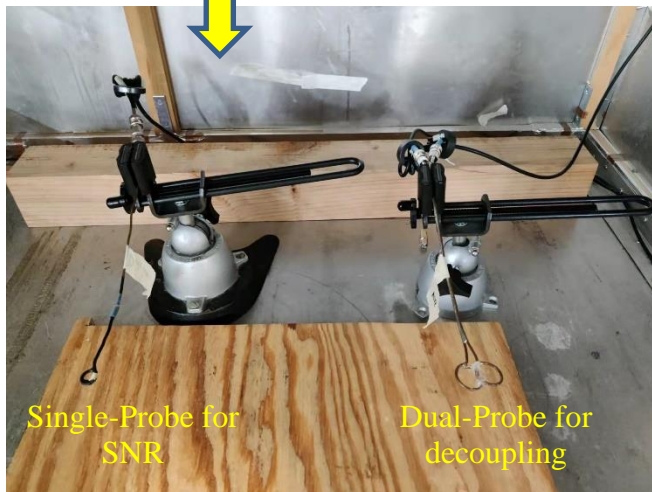
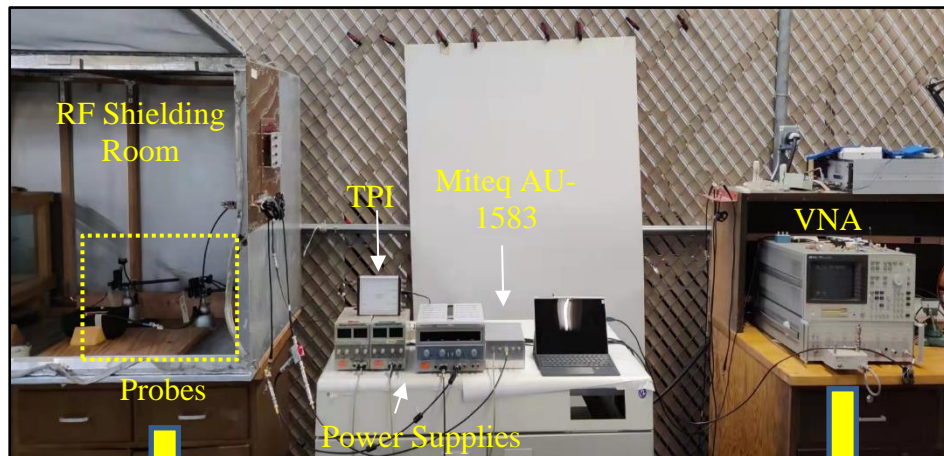
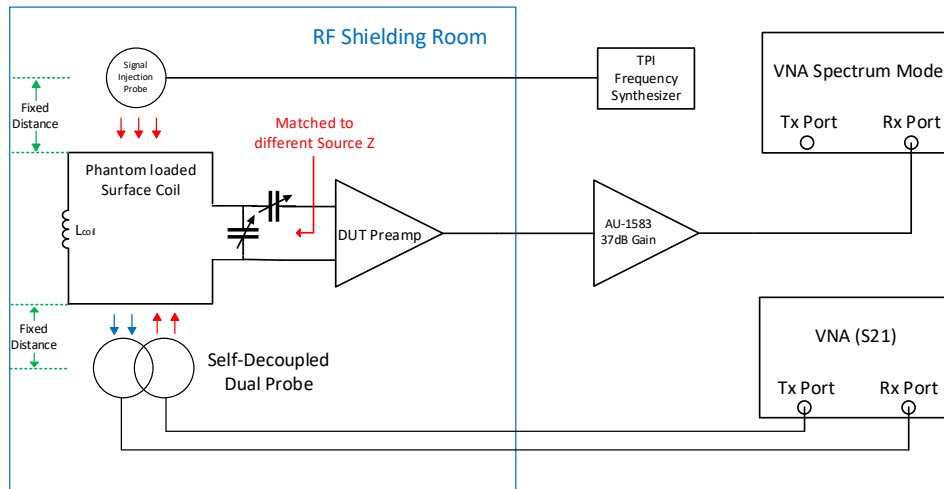


Figure 36. Bench measured OPA gain and NF for different values of Rf and Rg for validating the calculation.

However, the extremely low value of Rg easily causes the OPA to self-resonate when connected with a 4cm-coil matched to non-50 Ω impedance, and therefore cannot be used properly for any MRI experiments. Thus, the value of Rg is experimented with and chosen to be 10 Ω , which in combination with 10K of RF gives NF of 2.95dB measured on NF meter. Since 50 Ω of NF meter is not the optimal source impedance for OPA, this NF measurement is lower than the NF calculation at optimal. The NF vs source impedance analysis is shown in Figure 38 and Figure 40.

To validate the calculation of NF vs complex source impedance, a series of bench SNR experiments are conducted, as shown in figure 37. A 40cm loop coil is matched/tuned to different impedance using a conventional lumped element matching network and connects with the OPA board. The bench SNR of the combination of coil/MN/OPA is acquired and recorded with every different matched impedance. A signal injection probe is used to transmit a small signal at the targeted Larmor frequency to represent the sample signal, while the coil collects real sample noise from the

phantom loading beneath the coil. A TPI frequency synthesizer (TPI-1001-B, Trinity Power, Inc.) is used to generate a testing signal for the injection probe. A gain stage of Miteq AU-1583 is used after the first stage DUT preamp for boosting the noise level of this bench test, otherwise, the natural sample noise amplified only by the DUT preamp is lower than the machine noise floor of the VNA (around -95dBm with 20dB TEST ATT), and therefore too small to be detected. A VNA (HP4195) in spectrum mode is used to measure both the signal and noise level in dBm, thus the bench SNR can be accessed. The spectrum mode's parameters are set as: span of 0Hz (only measured at Larmor frequency), resolution bandwidth RBW of 30kHz (about the same order as scanner's spectrum width), test attenuation TEST ATT of 20dB (to protect the VNA in the case of sudden overflow). A python script is programmed to communicate with VNA to acquire measurements. Each of the spectrum readings (both for signal and noise) is the result of 4010 averages of the same measurement, to ensure measurement repeatability within a very small noise level 0.5dBm of fluctuation.



For Bench SNR	
VNA Mode	Spectrum T2
TEST ATT	20dB
RBW	30kHz
Span	0Hz
Center Frequency	Larmor Frequency
For Bench Decoupling	
VNA Mode	S21
Span	10-220MHz
T1 Power	10dB
TEST ATT	0dB
RBW	10kHz

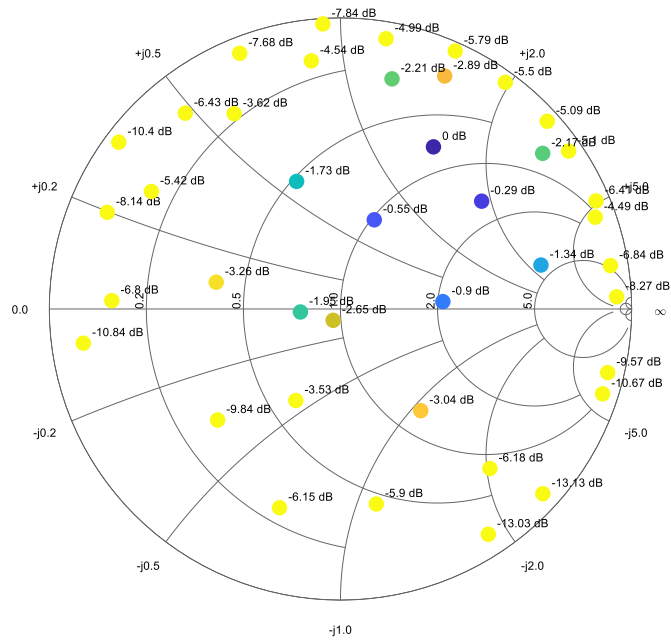
Figure 37. Overview and picture of the bench SNR and decoupling measurement setup.

The normalized bench SNR measurement versus the source impedance measured in this experiment is plotted in Figure 38. All the SNR measurements are normalized to the maximum value, to show the pattern of a good NF region.

As we can see at the Larmor frequency of 1H (200MHz at 4.7T), the higher SNR region is at the top right on the smith chart, different from the theoretical NF smith map in Figure 34. However, if the input parasitic capacitance of the OPA and the back-to-back Schottky diodes (in this case about 7pF together) is being considered here in the calculation, a good agreement of NF pattern can be found between the SNR measurement and NF modeling. For this configuration of OPA board (R_f 200 Ω , R_g 10 Ω), the best bench SNR is measured at source impedance of 38-j72 Ω , fairly centered inside modeled good NF region. The Reference SNR was measured using the same size coil, a conventional setup Roemer's MN, and Isolation preamp WanTcom WMA4R7A. Compared to the reference of isolation preamplifier at 50 Ω , the highest SNR found in this experiment using OPA is about 2.95dB lower at 1H.

Since the NF calculation method provided by the manufacture⁹⁶ is only based on the ideal scenario of the OPA, the extra loss introduced in the realistic condition, such as the back-to-back diodes, the parasitic parameter of the board design, as well as the 50 Ω output impedance matching resistor were not considered in the NF calculation. The loss introduced by these components are believed to cause the SNR difference.

1H (200MHz) Normalized Bench SNR in dB vs Source Impedance



1H OPA-NF vs Source Impedance, considering input parasitic

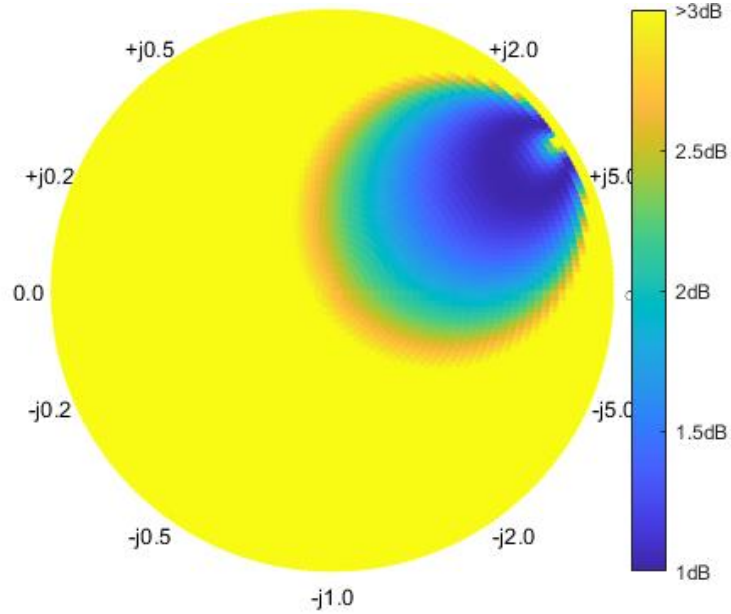


Figure 38. Bench-measured SNR at 1H (200MHz) versus different source impedance (Top). Calculated OPA NF when considering input parasitic capacitance. The agreement can be found between bench measurement and calculation.

At each measured impedance, the coil's decoupling in dB is also measured using a dual probe setup, as shown in Figure 39. Two overlapped pick-up probes maintaining more than -70dB decoupling (S21) are placed on top of the testing coil. One pickup probe excites a broadband signal into the testing coil, while the other pickup probe samples the RF current induced on the testing coil to measure the resonance condition at different frequencies. The decoupling of the testing coil is calculated as the difference between the dual-probe S21 measurement of the test coil against the same measurement of a conventional 50Ω match/tune coil at the Larmor frequency.

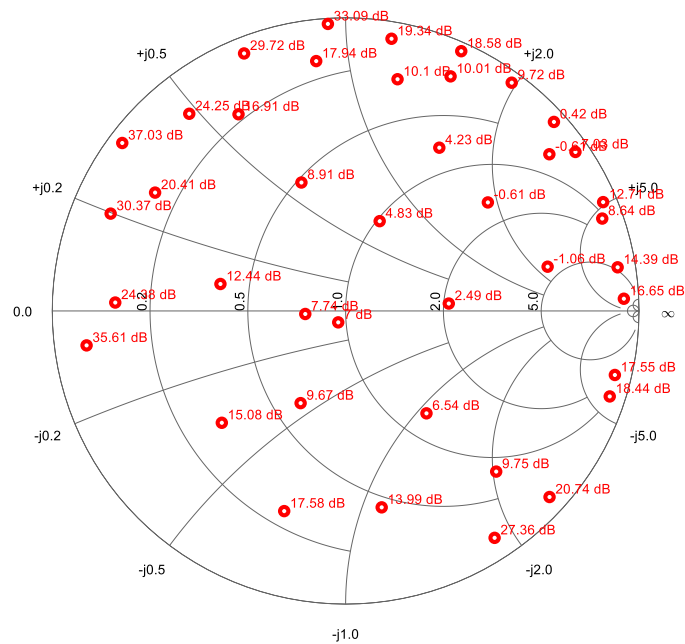


Figure 39. Measured decoupling of a test 4cm coil matched to different impedance and connected with OPA, at 1H Larmor frequency of 200.123MHz.

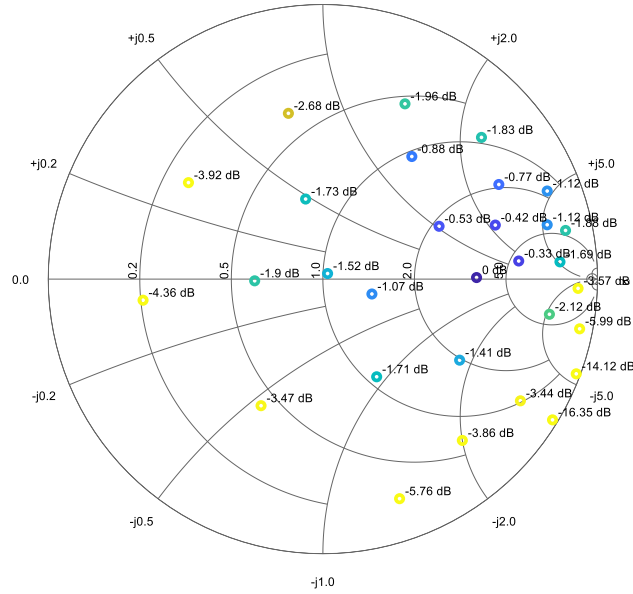
As we can see at 1H's Larmor frequency, the worst decoupling region aligns with the good SNR region. This is because the good NF region of OPA is close to the

conjugate of OPA's input impedance. To match the coil impedance to the good NF region, the near-conjugate matching condition (also good resonance condition) inevitably happens and thus leads to bad decoupling. If this configuration (conventional lumped element matching network) is used, the trade-off between decoupling and NF-matching will have to be considered.

The same experiments were conducted at ^{23}Na 's Larmor frequency (52.93MHz) as well, shown in Figure 40. Good agreement of pattern can be found between the NF modeling and SNR bench measurement. With the same input capacitance of the OPA and back-to-back diode, the lower operating frequency leads to the 3dB NF pattern at ^{23}Na (53MHz) to shift less than at ^1H (200MHz). The highest bench SNR is measured at $177+j2.9\Omega$, which is fairly centered inside the 3dB NF circle of modeling. The reference ^{23}Na SNR is acquired using the same size coil, a conventional Roemer matching network, and an isolation preamplifier (WanTcom, WMM50P), matched and tuned to 50Ω at ^{23}Na 's Larmor frequency. Compared to WanTcom, the highest SNR found in this experiment using OPA is 2.12dB lower.

At both ^1H and ^{23}Na , the bench-measured optimal SNR using an OPA is about 2-3dB lower than the reference of WanTcom, because of the OPA itself as well as some additional component loss from the circuit. However, a broadband high input impedance is provided by the OPA and therefore can be potentially used to decouple coil. And this SNR loss can be minimized in the future if a high impedance preamplifier design with lower NF is used.

23Na (53MHz) Normalized Bench SNR in dB vs Source Impedance



23Na OPA-NF vs Source Impedance, considering input parasitic

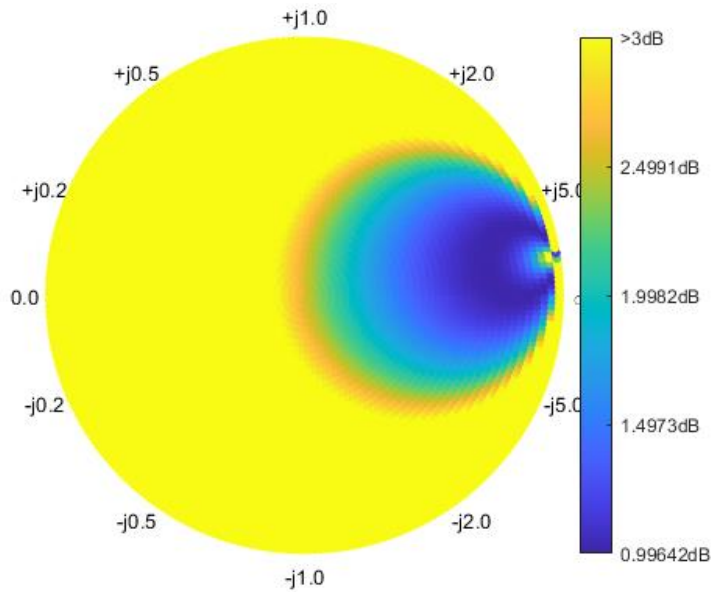


Figure 40. Bench-measured SNR at 23Na (53MHz) versus different source impedance (Top). Calculated OPA NF when considering input parasitic

capacitance. The agreement can be found between bench measurement and calculation.

Similar to the decoupling measurement at ^1H , decoupling versus the matched impedance with OPA is also measured at ^{23}Na 's Larmor frequency and shown in Figure 41.

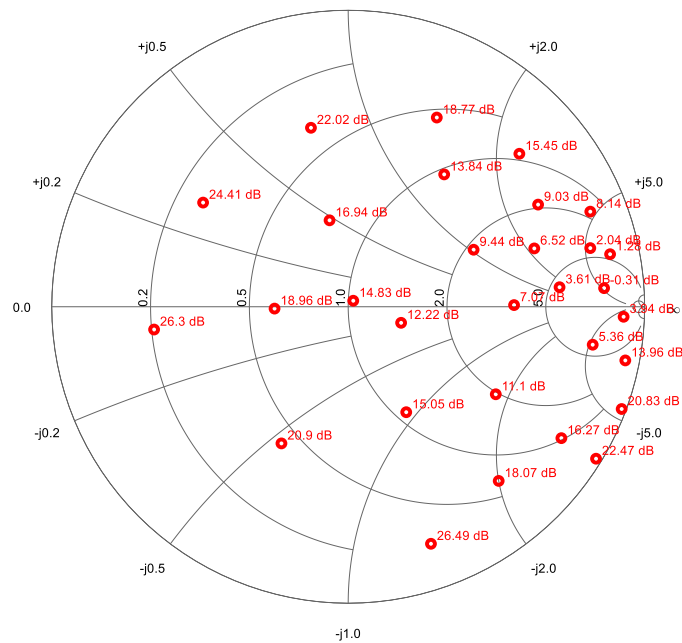


Figure 41. Measured decoupling of a test 4cm coil matched to different impedance and connected with OPA, at ^{23}Na Larmor frequency of 52.93MHz.

At 52.93MHz, the bad decoupling impedance area also overlapped with the best SNR area, because the 3dB NF area is naturally close to the conjugate of the OPA's input impedance therefore inevitably causing the coil to resonate. And the trade-off between good NF and bad decoupling has to be considered if a conventional lumped element matching network is used.

In general, at both ^1H and ^{23}Na 's Larmor frequency, a good agreement can be found between a good SNR pattern from bench measurement and a low NF pattern from modeling. However, the actual bench experiment NF of OPA is found to be not as ideal as it models (ideally about 1dB). Since reference WanTcom preamplifiers hold 0.5 and 0.4dB of NF (according to datasheet) at ^{23}Na and ^1H 's frequency respectively, the estimated NF of OPA at optimal impedance is approximately 2.62dB for ^{23}Na and 3.35dB for ^1H .

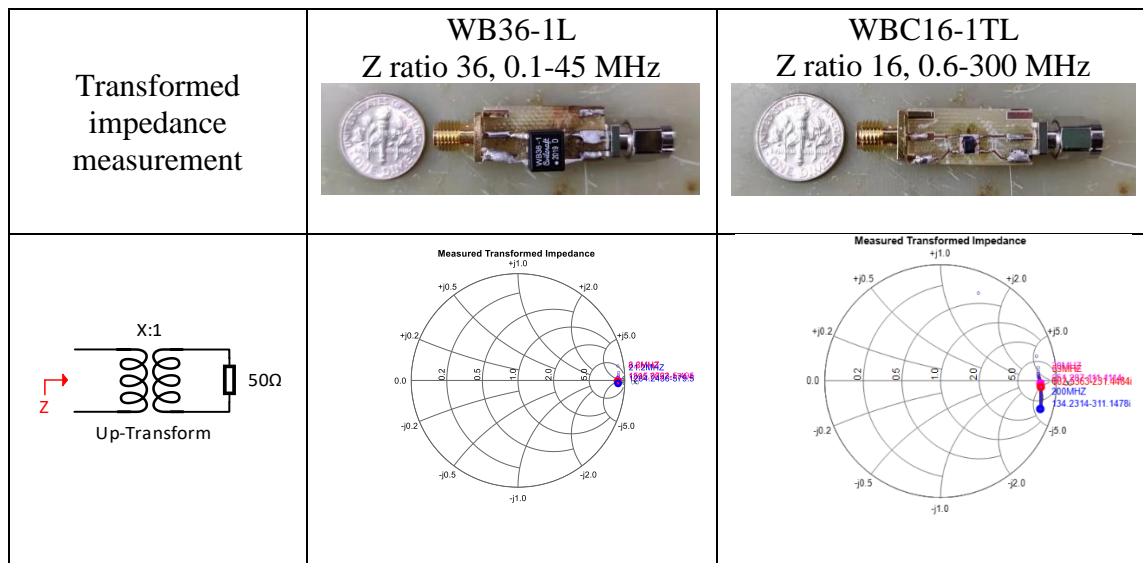
5.3 Matching Network with Ferrite Core Transformer

To utilize the broadband high input impedance of the preamplifier to decouple the loop coil, a true broadband match network is required to interface the coil (small impedance) and the preamplifier (high impedance). Instead of applying conjugate matching at a specific frequency that resonates the coil, the function of this broadband matching network should be matching the coil's small impedance to a reasonably high value so that preamplifier can see a source impedance with good NF matching while delivering the preamplifier's high impedance back to the coil to stop the induced RF current.

A transformer can be used to deliver for such performance. An ideal transformer is frequency-independent, and the impedance-transforming ratio only depends on the primary and secondary sides' winding number. Therefore, if a broadband transformer can transform the raw impedance of a series-tuned coil (usually $<10\Omega$ for 4cm loop coil) close to roughly 300Ω , the OPA can see the optimal NF impedance and therefore can

amplify the MR signals with minimum device noise added. And in the meanwhile, it can transform the OPA's high impedance down and delivered it to the tuned coil to destruct the resonance.

Two commercial RF transformers (Coilcraft, WB36-1L, WBC16-1TL) are first selected and tested to validate the idea of decoupling loop coil using a transformer and high impedance preamplifier. Product WB36-1L has the necessary high impedance transform ratio (1:36) but the frequency range is limited (0.1-45MHz) and WBC176-1TL has a proper frequency range (0.6-300MHz), yet the ratio (1:16) is compromised. Just like the vast majority of commercial RF transformers, these two products both use a ferrite core to minimize their leakage flux. Since the typical saturation flux density of ferrite material is under $0.4T^{97}$, these transformers are difficult to operate under the strong field strength of 4.7T MRI scanner. But we choose to test them on the bench to validate the concept. The testing board and results are shown in Figure 42.



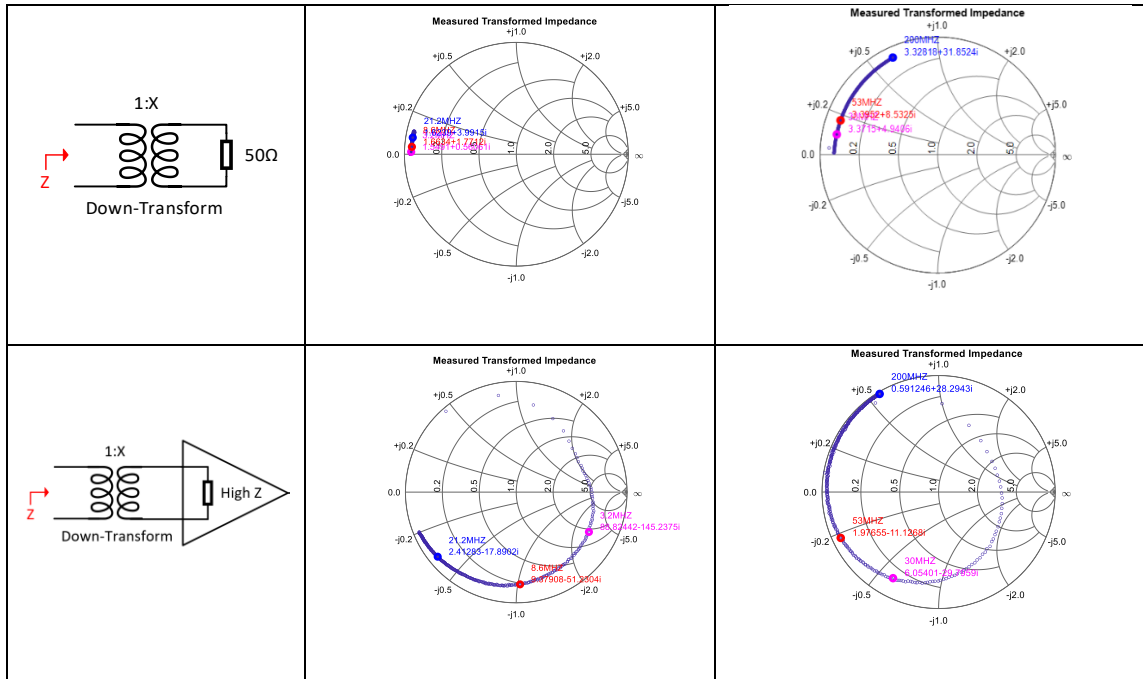
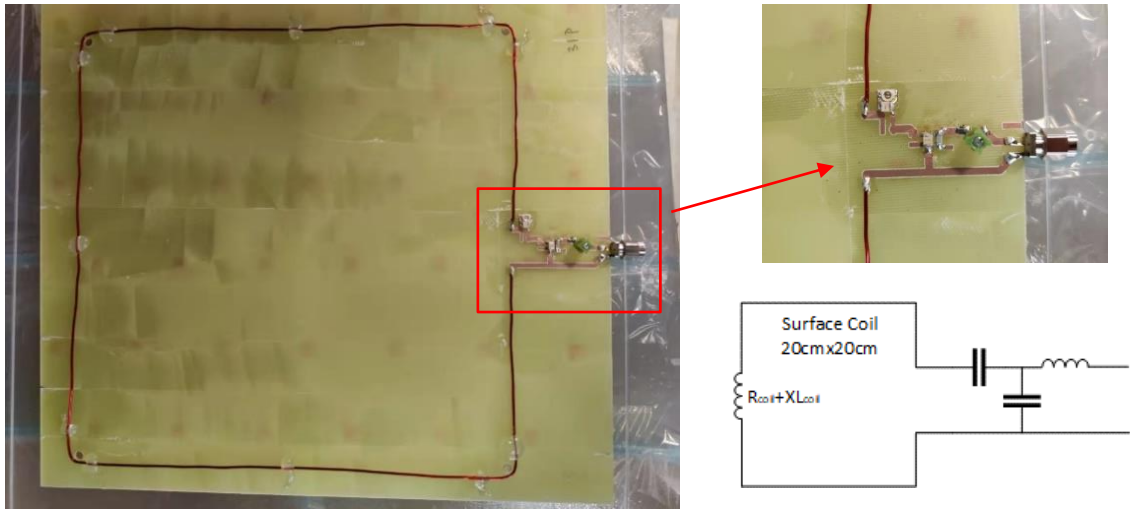


Figure 42. Bench testing performance of two commercial ferrite core transformers

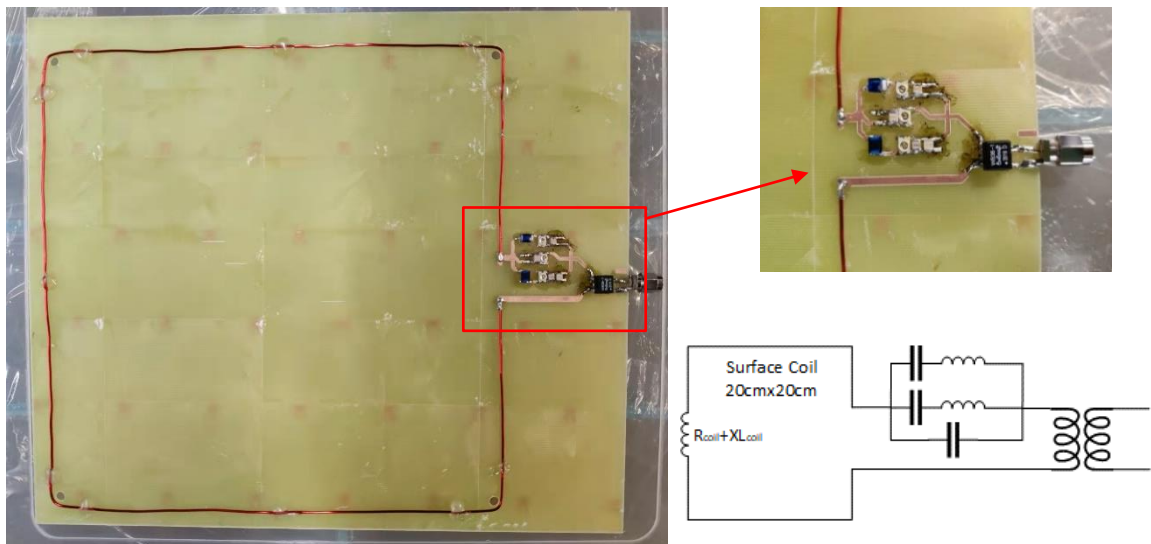
As we can see in these bench measurements, both two transformers work well when transforming up or down a 50Ω load with minor parasitic reactance added. Transforming up an open-circuit impedance (similar to the OPA) can also be achieved fairly well. However, when transforming down a high impedance of the OPA, the transformed results are far from desired potentially because of its parasitic parameters. Ideally, transforming down a very high impedance is still a fairly high impedance. However, in reality down-transformed results of a very high impedance are distorted with severe parasitic reactance. For the WBC16-1L with higher-rated bandwidth up to 300MHz, the down-transformed impedance at 2H, 23Na, and 1H's frequencies are $6-j29$, $1.9-j11$, and $0.59+j28\Omega$, respectively. Since only a fairly small extra impedance is required to decouple coil at a relatively lower frequency, the transformed-down

impedance at 2H and 23Na may be considered as barely enough. However, at 1H's higher Larmor frequency, only $0.59+j28\Omega$ is surely not enough to sufficiently decouple a loop coil. For the WB36-1L with rated bandwidth up to 45MHz, a similar performance of unideal parasitic reactance can be observed. At the frequencies of 2H, 31P, and 1H (assuming 0.5T since this product targets low frequency), the transformed down impedance is $88.8-j145$, $9.3-j51.2$, and $2.4-j17.8\Omega$. Similar to the other transformer, at the lower frequency it can provide fairly big impedance, yet at higher frequency, the transformed impedance is biased with severe reactance and honestly far away from high Z. However, since the coil at lower frequencies is easier to be decoupled (smaller coil raw impedance and transformer works better), the lower-frequency WB36-1L is selected to perform a further bench test to validate the concept.

With the limitation of max-frequency 45MHz and built-in ferrite core, a loop coil SNR/decoupling test comparing conventional Roemer's configuration and our proposed configuration is performed on the bench only and assuming at 0.5T. A popular choice of 20cm square coil at low field⁹⁸⁻¹⁰⁰ is used in this bench test since bigger reactance is needed to match/tune at the lower field. The 20cm coil is first matched and tuned using the conventional Roemer's configuration as references. Then the same size coil is tripled-tuned using a CLCLC network and matched using the proposed transformer WB-36-1L, shown in Figure 43.



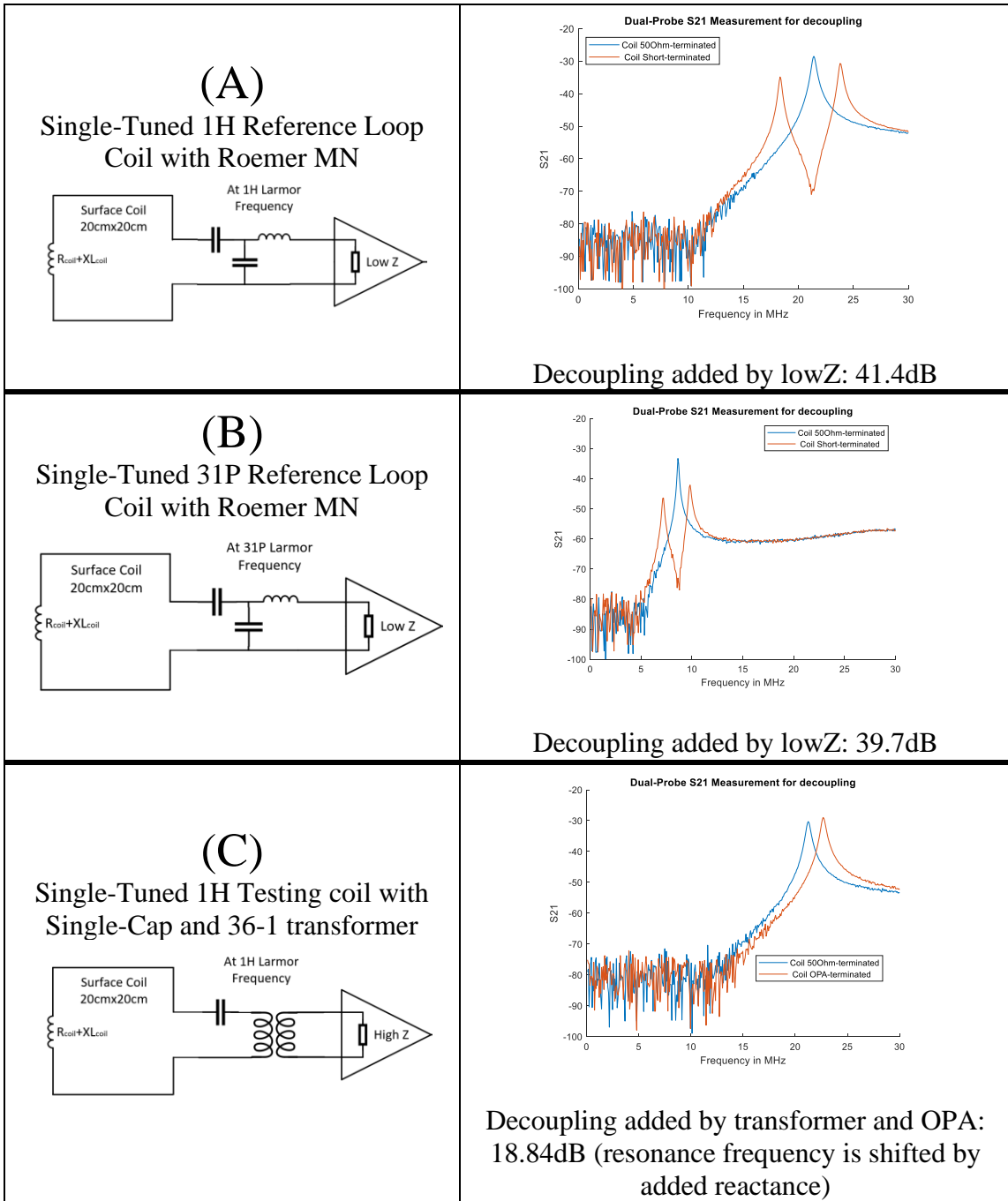
(a) 20cm loop coil with conventional Roemer's matching network, single-tuned



(b) 20cm loop coil with triple LCC as tuning and transformer WB36-1 as matching, triple-tuned.

Figure 43. Pictures of (a) reference coil with conventional matching network and (b) DUT coil with a single triple-tuned series matching network and transformer WB36-1L.

Bench SNR, decoupling of the coil are measured and compared using the same bench test setup described in section 5.2 and shown in Figure 44,45.



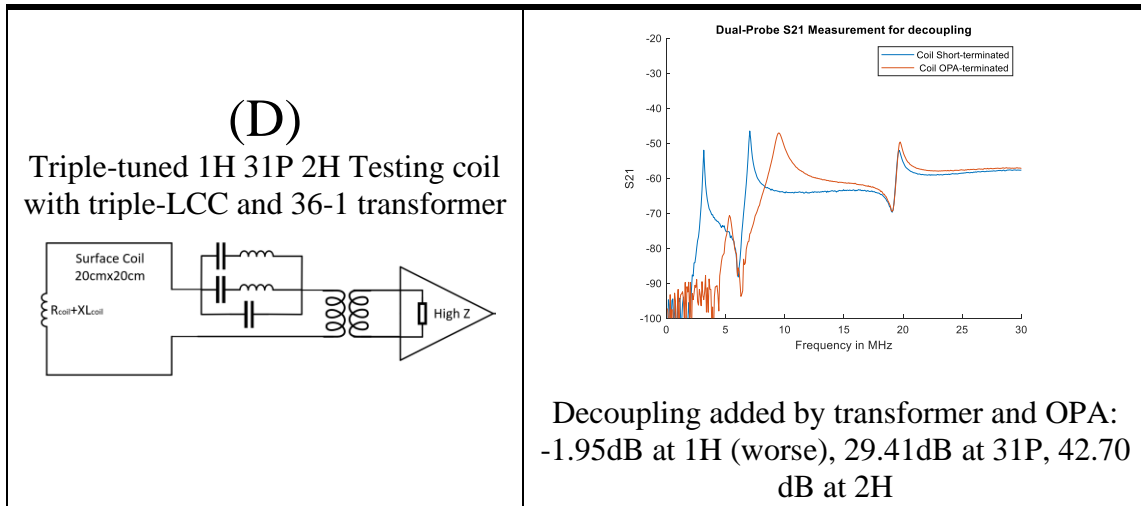
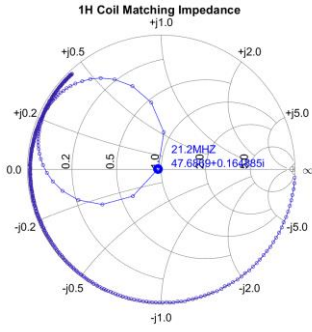


Figure 44. Bench decoupling measurement both for reference and DUT.

As we can see, conventional Roemer's MN and low impedance isolation preamp (in this test represented by a short terminator) can add a significant amount of decoupling (about 40dB at these frequencies) to the coil. However, due to the limitation of lumped element network, this high performance of decoupling can only happen at a narrow frequency band. A single-tuned testing coil and a triple-tuned test coil using our proposed decoupling method are then tested. Based on the previous down-transform impedance measurement, OPA and WB36-1L together can provide $2.4-j17.8\Omega$ at 1H, $9.3-51.2\Omega$ at 31P, and $88.8-j145.2\Omega$ of extra impedance back to the coil for decoupling. For the single-tuned test coil, as we can see that the added impedance of $2.4-j17.8\Omega$ shifts the resonance peak to a higher frequency with its extra reactance and thus lead to a better decoupling of 18.84dB (dual probe S21 decrease) at the Larmor frequency. However, the real part (2.4Ω) cannot suppress the resonance mode and honestly even make the peak higher compared to 50Ω load condition. For the triple-tuned testing coil,

the high impedance transformed back from OPA ($88.8-j145.2\Omega$) suppresses and shifts the resonance of the coil at 2H, providing 42.7dB of extra decoupling. The mediocre transformer impedance at 31P ($9.3-51.2\Omega$) manages to shift the resonance, thus leading to a fairly good 29.41dB decoupling improvement. However, at 1H, the small impedance ($2.4-j17.8\Omega$) cannot add extra decoupling to the coil yet make it 1.95dB worse. Different from the single-tuned testing coil, the triple-tuned has a higher raw impedance at 1H, since the complicated matching network (multiple sets of LC) added more loss. Therefore, the minor added impedance ($2.4-j17.8\Omega$) can only have less impact on the resonance peak compared to the single-tuned testing coil. Overall, as expected the WB36-1L and OPA together can introduce good decoupling at a relatively lower frequency range (2H, 31P at 0.5T), yet not performing well at 1H.

cases	Matched impedance that preamp sees	Measured Bench SNR and Q
<p style="text-align: center;">(A) Reference 1H Loop with Miteq AU-1583 (50Ohm)</p>		<p style="text-align: center;">SNR 57.516 dB at 1H</p>

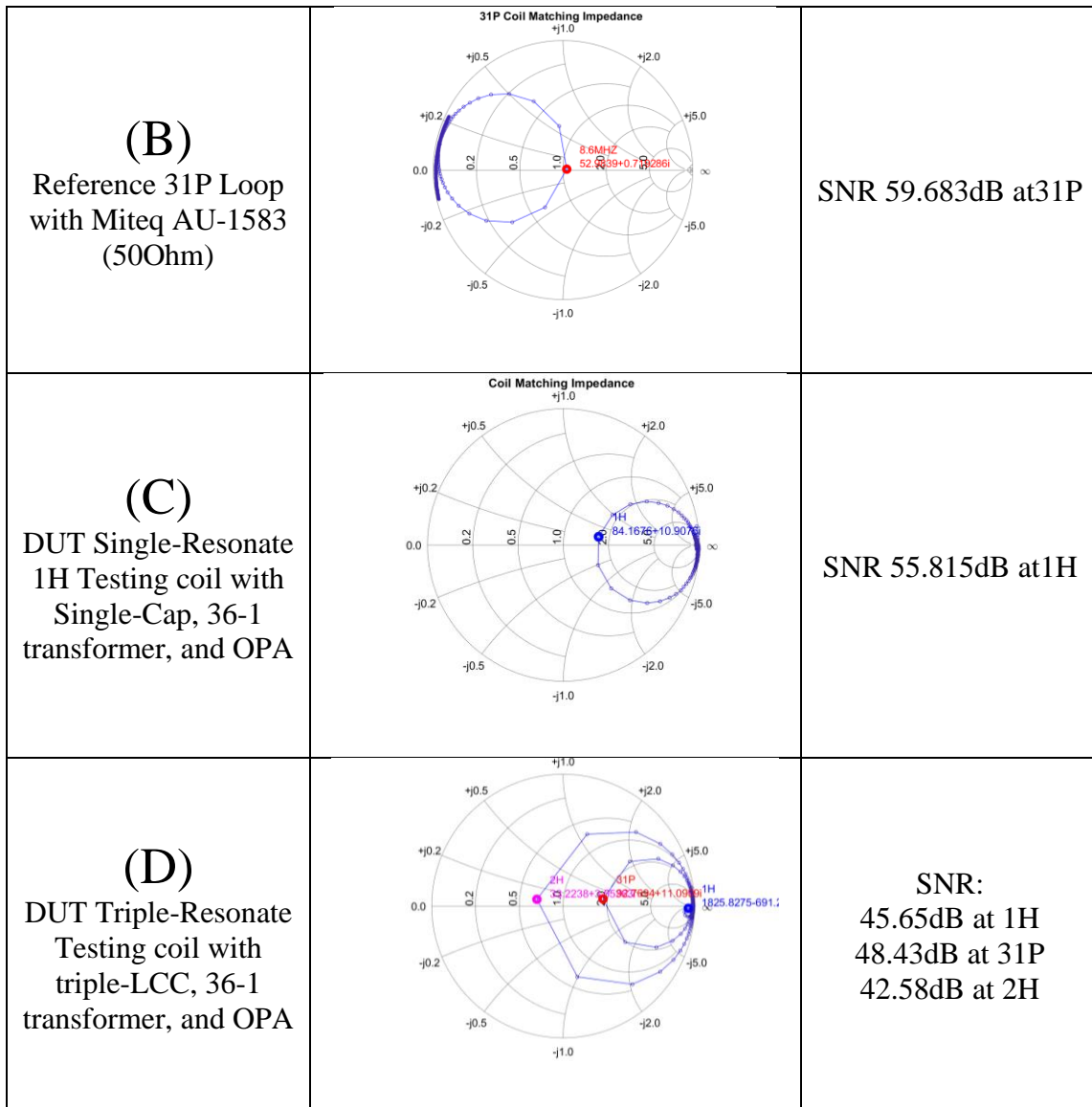


Figure 45. Bench SNR and coil Q measurement both for reference and DUT.

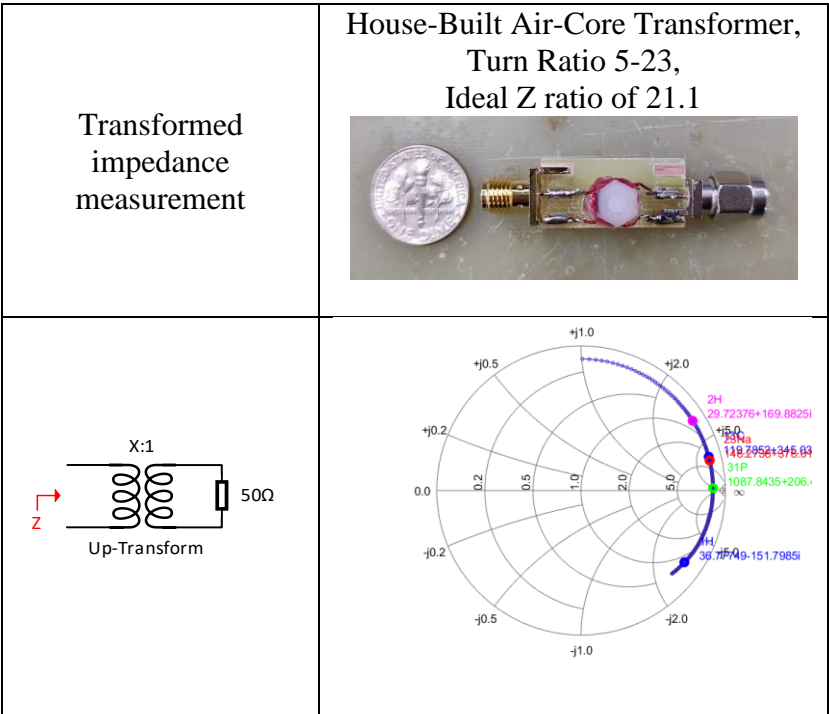
The bench SNR of testing are measured and compared against the reference case. In this particular setup, the reference coil (Roemer MN with 50Ω preamplifier) yield bench SNR of 57.5dB at 1H and 59.6dB at 31P. The single-tuned test coil (single capacitor as series-tuning, transformer WB36-1L as matching, and with OPA) can

provide a fairly good SNR of 55.8dB at 1H (1.7dB lower in power, 82.22% of reference SNR in Vpp). The matched coil impedance after the up transform is $84+j10\Omega$ and already reaches the 3dB good NF region although not at optimal. For the triple-tuned test coil, both SNR performance at each Larmor is far from ideal. The 20cm coil's raw resistance is 0.23Ω at 2H, 0.58Ω at 31P and 3.34Ω at 2H, and the ideal 36-times transform results are 8.28Ω , 20.88Ω , and 120.24Ω respectively. However, the matched coil impedances after up-transform are $33+j3\Omega$ for 2H, $92+j11\Omega$ and $1825-j691$ for 1H, both significantly higher than expected, which indicate some heavy loss has been added by the LC network (measured resistance of 2 inductors are 0.3Ω and 1.4Ω). This results in the 1H's matched impedance being way too far from the 3dB NF area, yet 2H's matched impedance is not enough. Matched impedance for 31P is relatively better, thus the bench SNR of 31P is slightly better than the other two, although SNR at both 3 nuclei is more than 10dB lower compared to the reference.

5.4 Matching Network with Air-Core transformer

Since the ferrite core transformer cannot be used inside the MRI scanner, a house-built air-core transformer is investigated and evaluated. In theory, the transformer's impedance ratio only depends on the winding number of the primary and secondary sides and is independent of the frequency. In practice, however, the performance of a transformer is subject to multiple parasitic parameters, such as leakage and magnetizing inductances, capacitances between each winding, capacitances between primary and second side, resistive loss, etc¹⁰¹. These stray and distributed elements are

frequency dependent¹⁰¹ and together limit the actual transformer's bandwidth. Dedicated researches have shown the potential of designing a non-ferrite transformer with an operating band wider than this multi-nuclei application requires^{102,103}. Such a transformer that met the requirement of this application can be achieved potentially. However, without expertise in designing and fabricating a state of art transformer with non-ferrite core, the leakage inductance and parasitic parameters are difficult to be minimized in this work. Therefore, a certain level of performance loss in both bandwidth, transform ratio, and insertion loss can be seen in this design and shown in Figure 46.



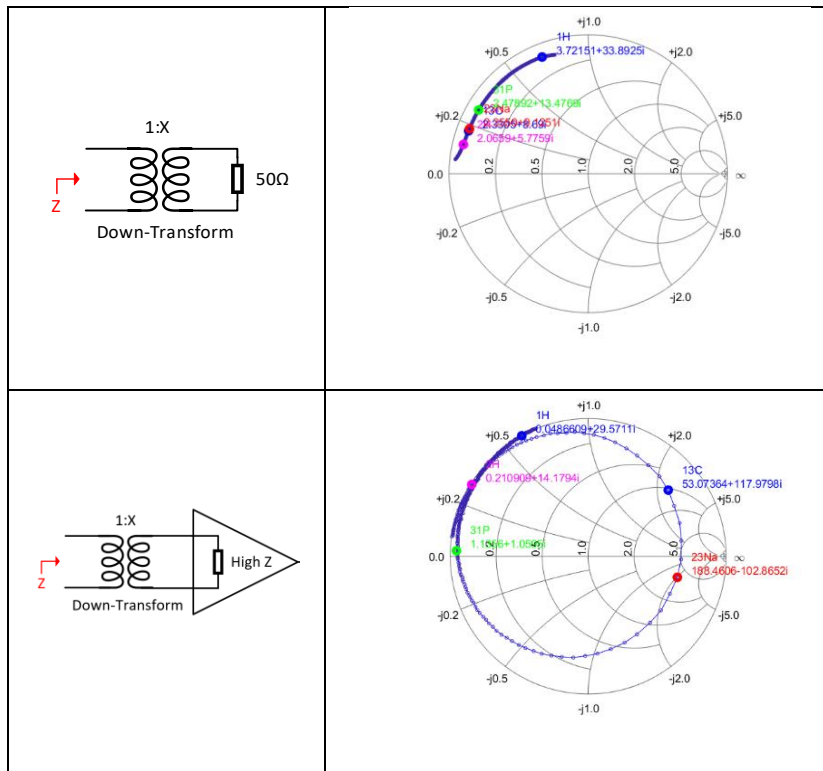


Figure 46. Bench testing performance of the house-built air core transformers

The transformer is wound around a piece of #4-40 threaded nylon rod with a length of ~9mm. Nylon nuts on both sides are used as end-stopper for resting the transformer's winding, which leaves about 5mm in length for wires to be wound. 26AWG magnet wire is used to wind both the primary side (5 turns) and secondary side (23 turns), leading to a theoretical impedance transform ratio of 21.16. Hot glue is used to secure the shape of the winding.

In general, as expected the frequency performance of this house-built transformer is relatively limited compared to the commercial ferrite core products. The up-transformed impedance of a 50Ω load at different frequencies is biased with either inductive or capacitive parasitic. When transforming down a 50Ω load, heavy inductive

parasitic bias can be observed as well at all frequencies, especially at 200MHz.

Unfortunately, the key performance of transforming down a high impedance (OPA) is limited to a fairly narrow band (about 10MHz wide around ^{23}Na 's frequency). At ^{23}Na and ^{13}C , a big transformed-down impedance ($188-j102\Omega$ and $53+j117\Omega$) can be considered sufficient enough to decouple a 4cm loop. However, the results at other frequencies are far from ideal.

To access the insertion loss of the house-built transformer, a simple add-on experiment is performed. A 4cm loop coil is matched to 50Ω using a two capacitors simple matching network and connected with a commercial preamplifier (WanTcom isolation preamplifier), and the bench SNR of this case is acquired as reference. Then using the matching network of two capacitors and the house-built transformer, the same coil is matched to 50Ω with the same preamplifier. And the bench SNR of this case (with an extra transformer) is acquired to compare with the reference. The SNR decrease can be considered as the insertion loss added by the transformer. At the frequency of 1H (200.123MHz), the bench SNR measured with the transformer is within the measurement setup's fluctuation when compared to the reference, therefore the transformer's insertion loss at 1H can be considered very low. However, at the frequency of ^{23}Na , the measured SNR with transformer is 1.8dB lower than the reference, which indicates some insertion loss is introduced and has to be considered.

A similar matching network using the LCC network for double-tuning and the house-built air core transformer for broadband matching is built, as shown in Figure 47.

4cm loop coil is used for the scanner's operation at 4.7T. Again, conventional decoupling configuration is used as a reference for comparing.

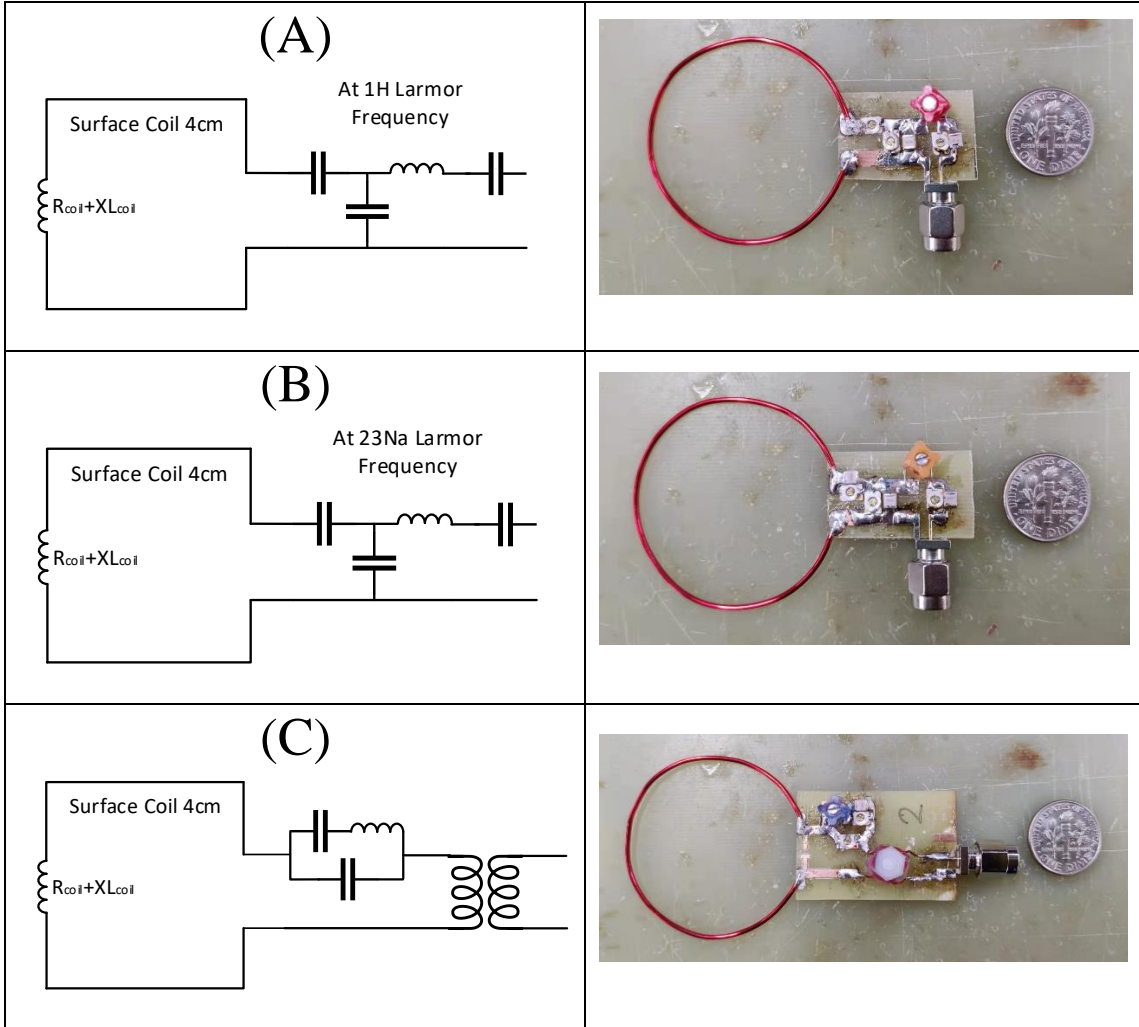
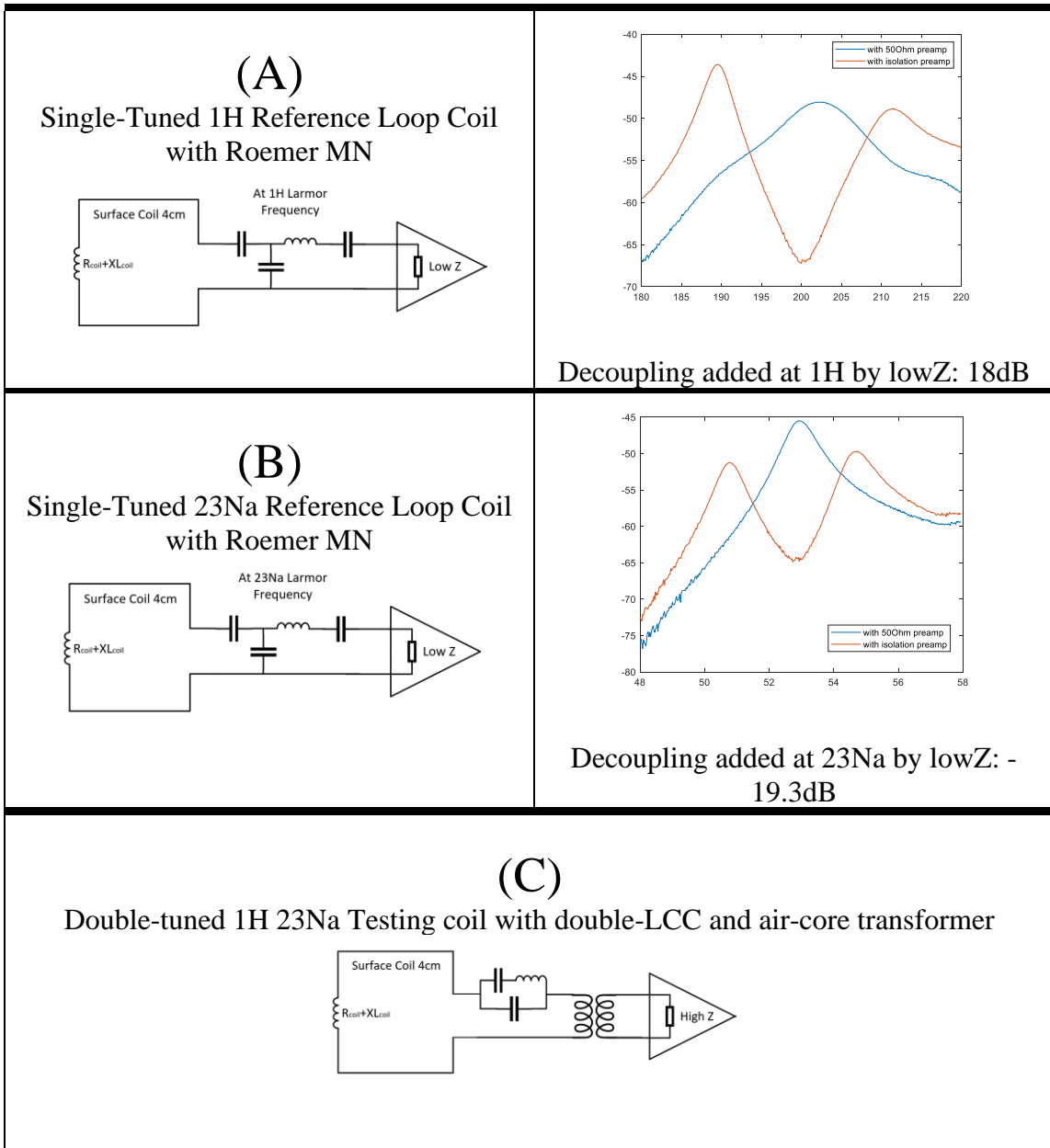


Figure 47. Schematic and picture of (AB) the reference coil and (C) the testing coil using LCC network and air-core transformer.

Bench SNR, decoupling are measured using the same setup, and the results of the reference coil and testing coil are shown in Figure 48,49.



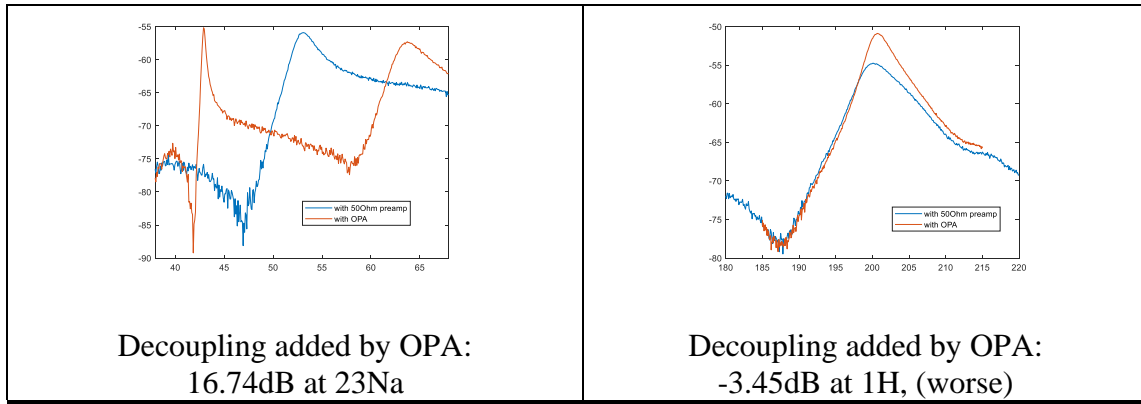


Figure 48. Bench decoupling measurement of reference coil and testing double-tuned coil using an air-core transformer and high impedance preamplifier.

As the reference, the conventional configuration using an isolation preamplifier can provide 18-19 dB of additional decoupling to the coil, which roughly agrees with the expectation of 20dB⁹⁰. For the dual-tuned testing coil, 16.74dB of decoupling at 23Na's frequency is added by using OPA, since from the previous bench measurement OPA and this transformer can provide big impedance($188-j102\Omega$) back to the coil. On top of this, a relatively broader frequency range of added decoupling can be overserved by using the proposed configuration. Between the range of 48.05 to 60.05MHz (12MHz), more than 14dB of decoupling is generated by the proposed configuration. While the conventional isolation preamplifier can only provide 14dB of decoupling for 5.5MHz range, given that the LC resonating network is used. The decoupling range provided by the proposed method depends on the performance of the transformer, as discussed in section 5.3. At the frequency of 1H (200MHz), the decoupling performance is far from ideal as expected, since at 1H this house-built transformer and OPA together can only provide $0.048+j29\Omega$ back to the coil. If an air-core transformer with better down-transforming bandwidth can be used, a better decoupling bandwidth can surely be achieved.

The coil match impedance and bench SNR are shown in Figure 49.

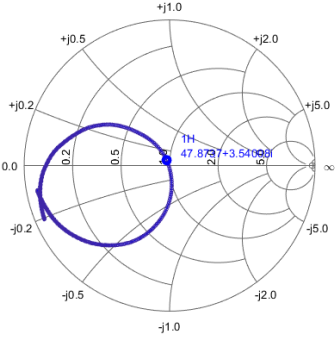
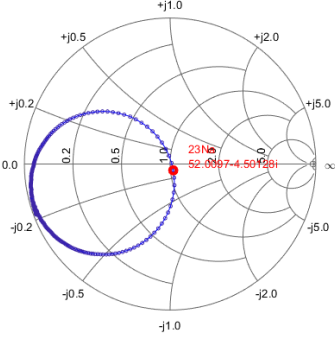
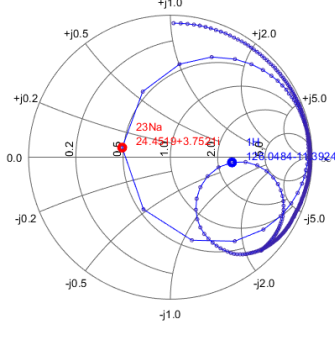
cases	Matched impedance that preamp sees	Measured Bench SNR and Q
<p>(A) Reference 1H coil with Roemer's MN and WanTcom Isolation preamplifier</p>		<p>SNR 66.39 dB</p>
<p>(B) Reference 23Na coil with Roemer's MN and WanTcom Isolation preamplifier</p>		<p>SNR 66.61dB</p>
<p>(C) DUT double-tune testing coil with LCC network, house-built air-core transformer, and OPA</p>		<p>SNR: 57.49dB at 1H 58.16dB at 23Na</p>

Figure 49. Bench SNR and matched impedance of both reference coil and testing coil.

Compared to the reference coil with a conventional Roemer matching network, the testing coil gives 8.9 dB lower SNR at 1H and 8.45 dB lower SNR at 23Na. One reason is that the matched impedances both for 1H and 23Na are away from the optimal NF matching point. According to the bench, SNR vs source impedance measurement reported in section 5.2, at the current matched points OPA is estimated to yield about 3~5dB lower SNR compared to the reference (WanTcom Isolation preamplifier). For 23Na, the transformed ratio of this current transformer is not high enough to match the small coil impedance (0.19Ω) close to the optimal point. For 1H, the transformed ratio is considered good enough since the coil at this frequency already has a higher impedance (5.27Ω) due to heavier sample loading. However, the added severe capacitive parasitic at this frequency biased the whole matching curve away from the optimal matching area. Once again, the NF matching condition of this method is limited by the up-transform performance of the house-built transformer. The matched impedance can be better for NF matching if a better transformer with a higher ratio at the lower frequency and less parasitic at higher frequency can be crafted. However, with limitations explained in the early section, such a better design unfortunately is hard to achieve currently. Another reason is the loss added by the LCC network. The measured ohm loss (measured by VNA4195A) of the inductor used in this network is about 0.8Ω at 1H's frequency. Along with the capacitor loss (between 135-195m Ω each at 1H's frequency), the calculated total equivalent resistance formed by this particular network (C1-14.2pF in parallel with C2-42.5pF and L3-80nH) is 6.73Ω at 1H's frequency, which decreases the sensitivity of the coil. The same at 23Na's frequency, the measured components' ohm

loss is 0.4Ω for inductor and neglectable for capacitors, therefore leading to a smaller total loss of 0.27Ω in the calculation. According to the formula of coil SNR¹⁰⁴:

$$SNR = \frac{\omega MVB\rho}{\sqrt{4T\Delta fR}}$$

The SNR is proportional to the reciprocal of the square root of the coil's noise resistance, which includes the coil's original resistance as well as the added resistance of the LCC network since it is in series with the coil directly. With the LCC network's loss (even more than the coil's original resistance) added, the SNR loss is estimated using this formula and then convert to dB (assuming 50Ω system for simple analysis). The calculation result reveals that 3.56dB at 1H and 3.77dB at ^{23}Na of SNR are lost because of the loss of the LCC matching network. Together with the 1.8dB SNR loss of transformer at ^{23}Na and the 3~5dB SNR loss due to undesired NF matching conditions at both frequencies, a total 8+ dB SNR loss can be understood.

Since the LCC double-tuning network is found to be lossy and harmful to the coil sensitivity. A single varactor diode (a voltage-controlled variable capacitor) is investigated as the tuning element since the variable capacitance it provides can be used to resonate the loop coil to different frequencies, therefore achieving multi-tuned yet not simultaneously. And in theory, since only one component is needed, excessive loss from the complicated network (especially inductors) can hopefully be avoided. Among the many available products, RF varactor BBY6602VH6327 (Infineon Technologies) is selected because of its non-magnetic package, which is necessary for an MRI application especially when it needs to be mounted on a coil. The capacitance tuning range of this

varactor diode is 10pF~70pF according to the datasheet. Since the capacitances needed for tuning a 4cm loop coil at 4.7T are vastly different for different nuclei, for example only 4.5pF is required at ^1H (200MHz), 83.4pF is required at ^{23}Na (53MHz) but 290.6pF is required at ^2H (30MHz). At this field strength, the dramatic difference in capacitance requirement at each frequency makes this varactor impossible to cover all the nuclei even with a biasing capacitor. Therefore, together with the bandwidth limitation from the transformer, only one targeting nucleus of ^{23}Na is selected to test the performance. However, the varactors in parallel can potentially be used to tune a coil to multiple Larmor frequencies at lower field strength, as discussed in section 5.6. The capacitance difference can be addressed if an RF switch circuit with different capacitors is applied on the coil to control the total tuning capacitance. However, similar to the LCC network, the additional loss introduced by the RF switching circuit can reduce the coil's sensitivity as well.

The schematic and picture of the testing board are shown in Figure 50. To best isolate the interference of varactor's biasing circuit from coil's resonating performance, both RF choke (1uH, Vishay, IMC1008ER1R0J), resistors (20k Ω , YAGEO, AC0402FR series), and high resistance wires (11.8k Ω per ft, NINJATEK, 3DEL0129010) are together used to supply the reverse-biased DC voltage to the varactor with minimum RF current can be induced to cause any issues (only 20nA is required for reverse biasing a varactor). A single DC blocking capacitor (0.01uF, Knowles, 060330630103KXT) is used to prevent DC short-circuit.

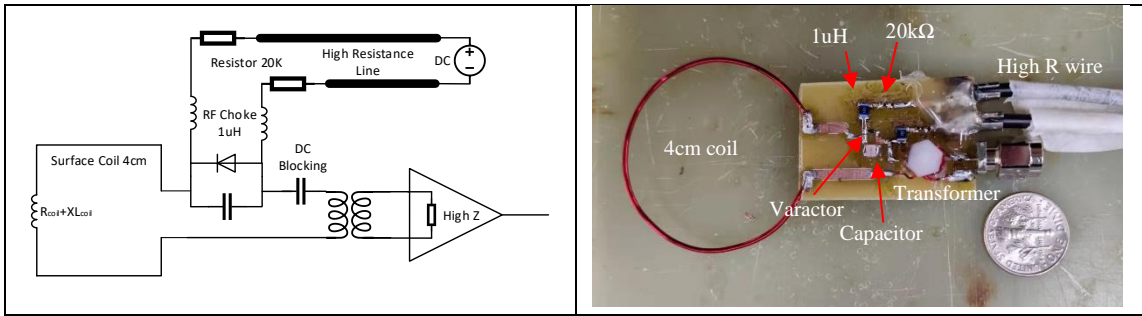
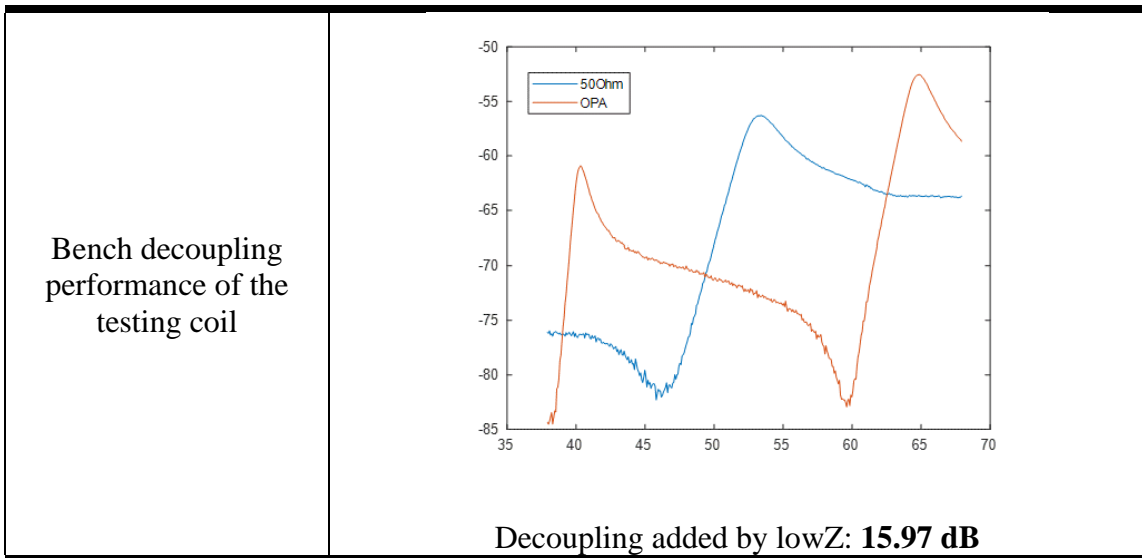


Figure 50. Schematic and picture of the testing coil using varactor for tuning and transformer for matching.

Similar bench measurement of SNR, decoupling, and loss analysis at only ^{23}Na is performed to test this coil since both transformer and capacitance range of a single varactor diode is limited. The results are shown in Figure 51.



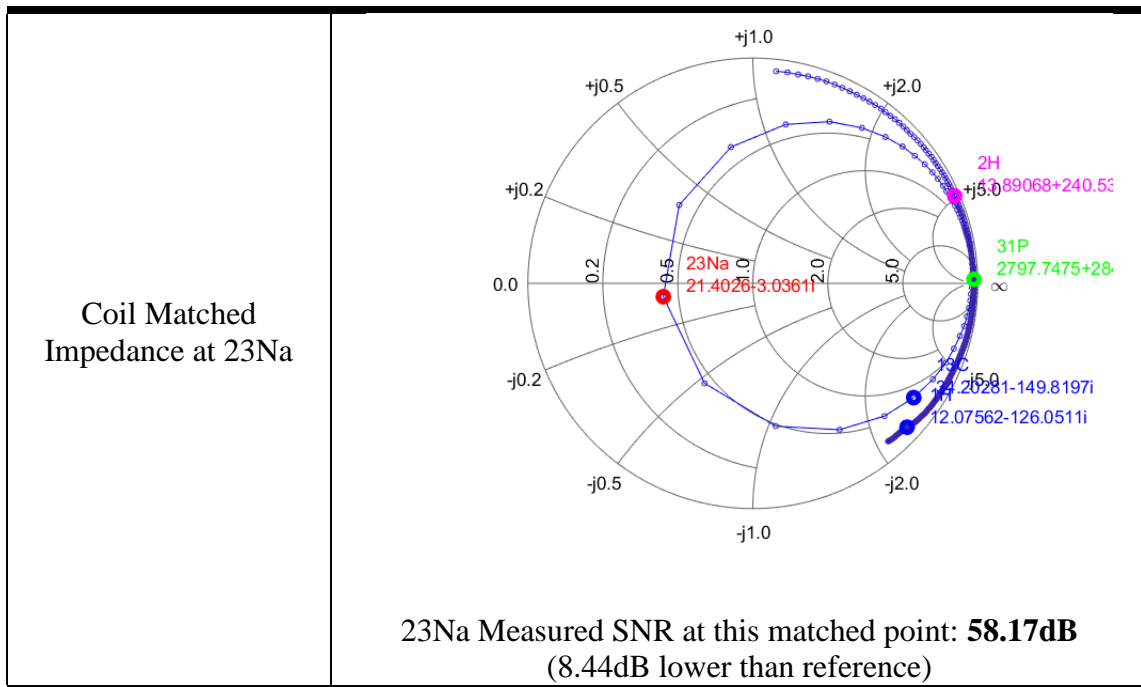


Figure 51. Bench measurement decoupling, matched impedance, and SNR performance of testing coil using varactor diode and transformer.

As expected, the decoupling achieved by this configuration is about 16dB since the transformer and OPA together provide fairly big impedance back to the coil. The matched impedance is again far from the optimal region since the transformer can't provide a high enough ratio as well as the coil resistance at 23Na is small. The measured bench SNR using the same setup is 58.17dB (8.44dB lower than the reference).

The ohm loss of the varactor with its biasing circuit is again measured to analyze the SNR cost. The total impedance of the varactor diode, biasing capacitor, and biasing circuit (with reverse biasing 3.9V supplied to resonate the coil at 23Na) is measured using HP4195A in different frequencies. And measured impedance results are shown in Figure 52.

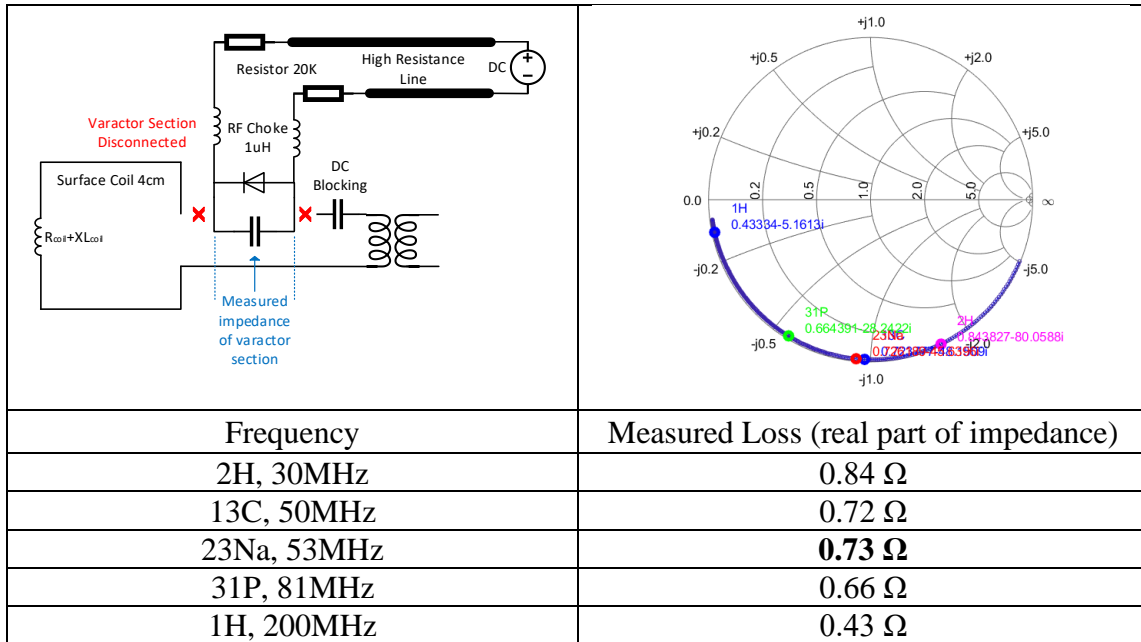


Figure 52. Measured loss of varactor diode at different frequencies.

As we can see at the operating frequency of 23Na 53MHz, the measured ohm loss of the varactor is 0.73 Ω . Compared to the coil resistance (0.19 Ω) at this frequency, 0.73 Ω of added loss results in a 6.7dB of SNR loss calculated based on the SNR formula. Since the coil's resistance is relatively small compared to the added impedance, the SNR loss in dB is high. If the resistance of the coil can be more sample-dominated, such as in 1H, the impact of added element loss can be reduced. Together with 1.8dB SNR loss from the transformer, and 3-5dB SNR loss from non-optimal NF matching, a big total SNR loss can be understood. Although fairly heavy loss can be found in the current setup, improvements can be made in the future, such as using a parallel varactor network as field broadband tuning and using a better preamplifier that requires smaller impedance as optimal NF point (discussed in section 5.6).

5.5 Imaging Validation

To further test the proposed decoupling setup, a series of images were acquired on the scanner for both the reference setup (conventional Roemer MN and isolation preamplifier) and the tested setup (air-core transformer and OPA. The LCC trap, double-tuned at ^{23}Na (52.93MHz) and ^1H (200.123MHz), is used in the scanner test. In comparison, reference coils operated at these two frequencies are used. All the images for both nuclei of ^1H and ^{23}Na are acquired using Varian 4.7T scanner, with single-tune volume birdcage coils as transmit, and loop coils as receive. A 3D printed phantom with a pin cushion printed on one side is used for showing resolution. The bulk solution is composed of water with 6.26g/L of NaCl and 1g/L of CuSO_4 so that both ^1H and ^{23}Na can be detected from the phantom. The general setup of birdcage, phantom, and loop coil is shown in Figure 53.

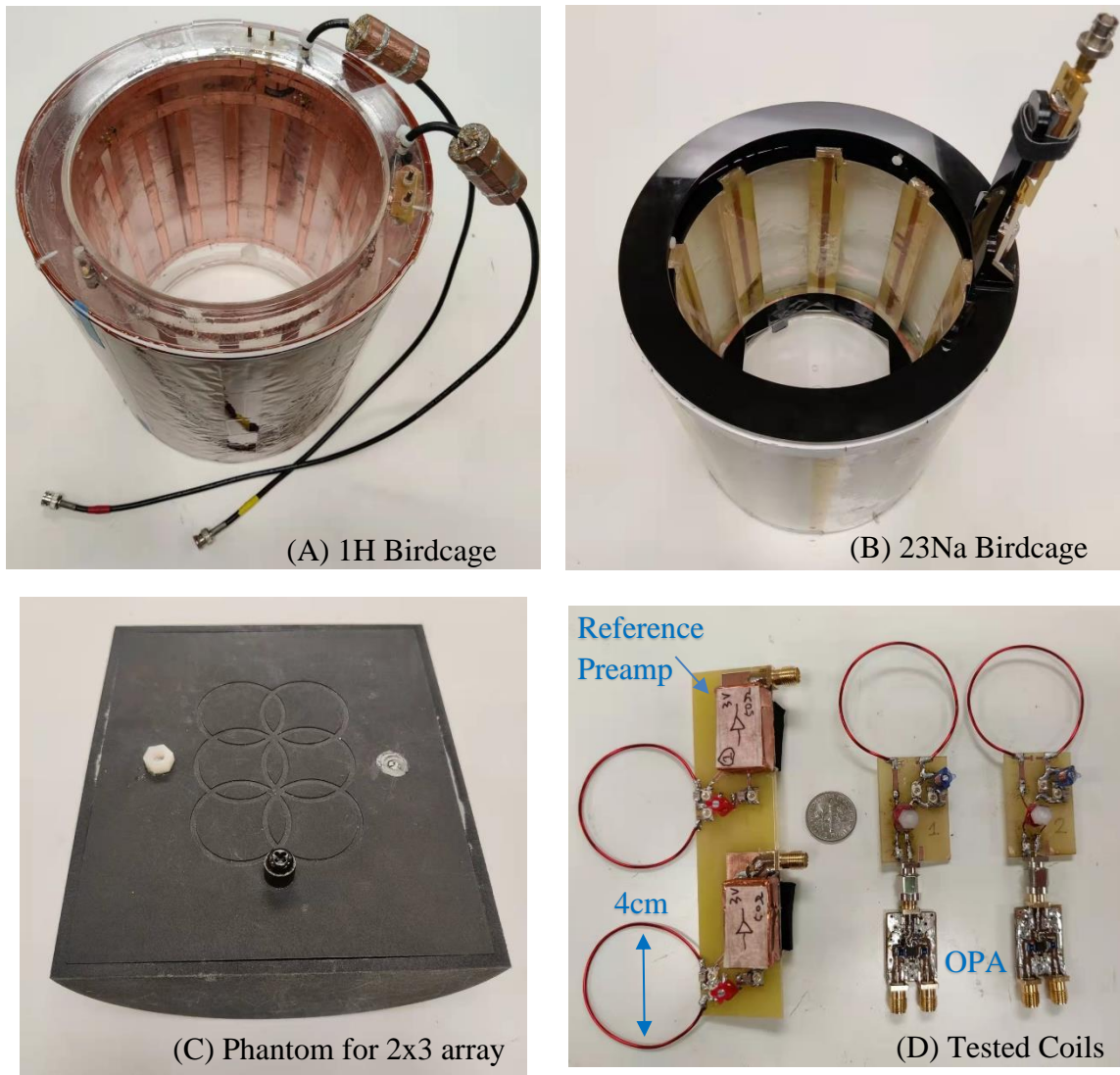


Figure 53. Pictures of scanner testing setup. (A) Transmit-only 1H birdcage coil. (B) Transmit-only 23Na birdcage coil. (C) Testing phantom for 2x3 loop coil array. (D) Receive-only loop coils/preamplifiers setup of reference coils (left) and testing coils (right).

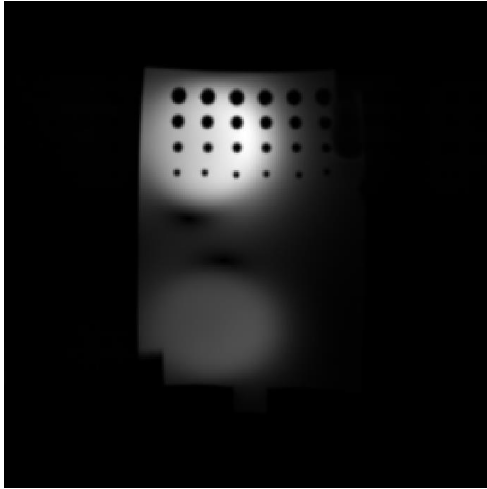
For both reference and testing setup, a two-coil array is used to simplify the experiment, yet still capable of showing the SNR and decoupling performance. For each case, two separate images were acquired with one channel on receive and the other channel 50 Ω -terminated. Since the signal measured on the terminated channel can show

the decoupling performance, both sensitivity (measured from the channel on receive) and decoupling (measured from the channel on termination) can be assessed at the same time. The testing coil's decoupling performance at ^{23}Na (52.93MHz) is provided by the high impedance OPA and the transformer. However, these two failed to provide a high enough impedance to decouple the coil at ^1H (200.123MHz) because of the transformer's frequency limitation. Therefore, the decoupling of the testing coil at ^1H is achieved by tuning the resonant frequency off to the side, leading to a lower dual-probe S_{21} measurement at the ^1H 's Larmor frequency⁹². The measured decoupling of the testing coil is 15.43dB at ^1H and 27.33dB at ^{23}Na .

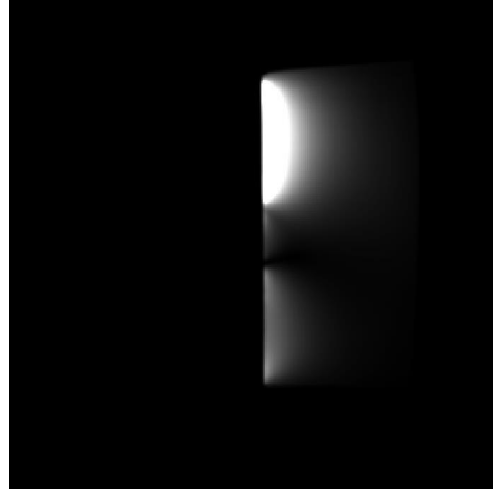
The MR sequence used for imaging ^1H is spin echo (sems, TR = 1000ms, TE = 30ms, average = 1, resolution = 256x256, FOV = 160x160mm, slice thickness = 2mm, flip angle = 90° , spectral width = 55.286 kHz, acquisition time = 4.63ms, imaging time = 4m 16s). The MR sequence used for imaging ^{23}Na is gradient echo (gems, TR = 100ms, TE = 5ms, average = 64, resolution = 64x64, FOV = 160x160mm, slice thickness = 10mm, flip angle = 65° , spectral width = 44.742 kHz, acquisition time = 1.43ms, imaging time = 6m 49s). The same MR sequences are used for imaging both the reference setup and the testing setup, and the imaging results acquired on scanner are reconstructed using MATLAB. The Hamming window¹⁰⁵ is applied on all the images. The imaging results are shown in Figure 54-61.

**1H Proton Imaging,
reference 50Ω Rx coils with 50Ω preamplifiers**

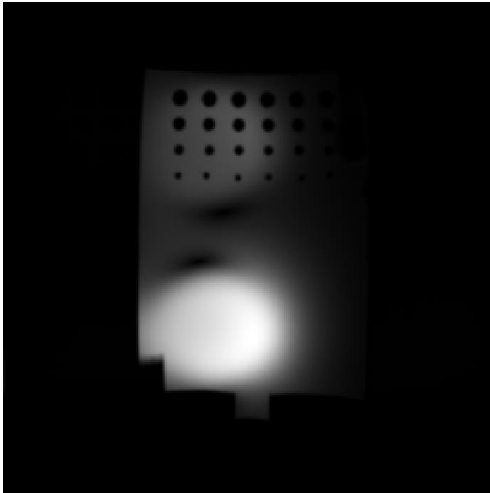
Coronal Plane, Ch1 Rx, Ch2 50Ωm-terminated



Sagittal Plane, Ch1 Rx, Ch2 50Ωm-terminated



Coronal Plane, Ch2 Rx, Ch1 50Ωm-terminated



Sagittal Plane, Ch2 Rx, Ch1 50Ωm-terminated

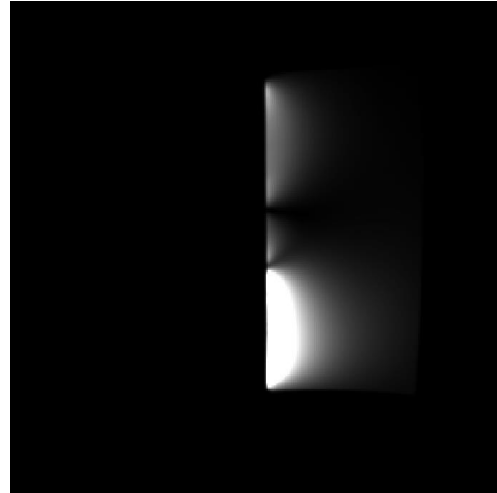


Figure 54. 1H imaging results acquired using two reference 50Ω loop coils with standard 50Ω preamplifier.

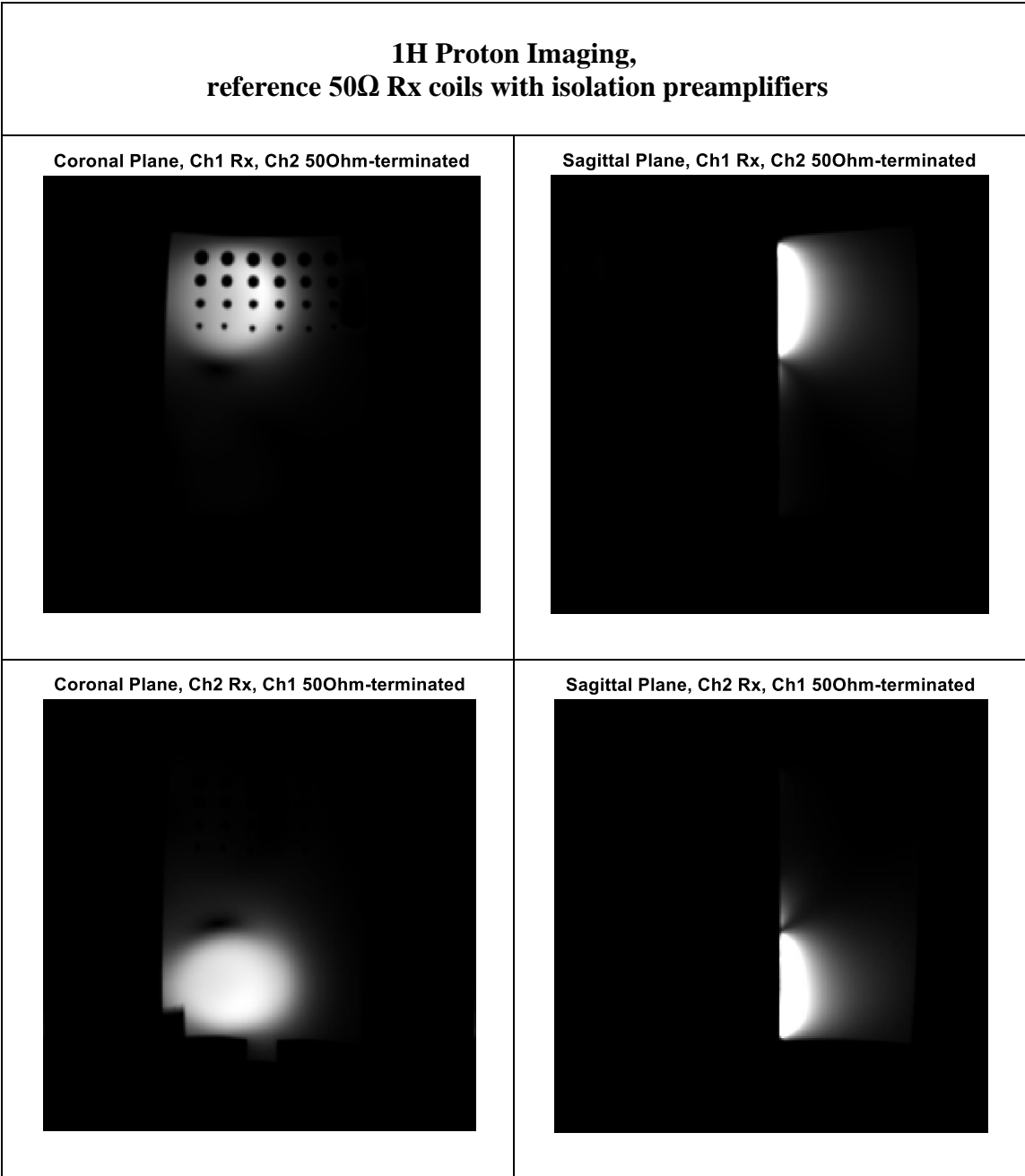


Figure 55. 1H imaging results acquired using two reference 50Ω loop coils with isolation preamplifier.

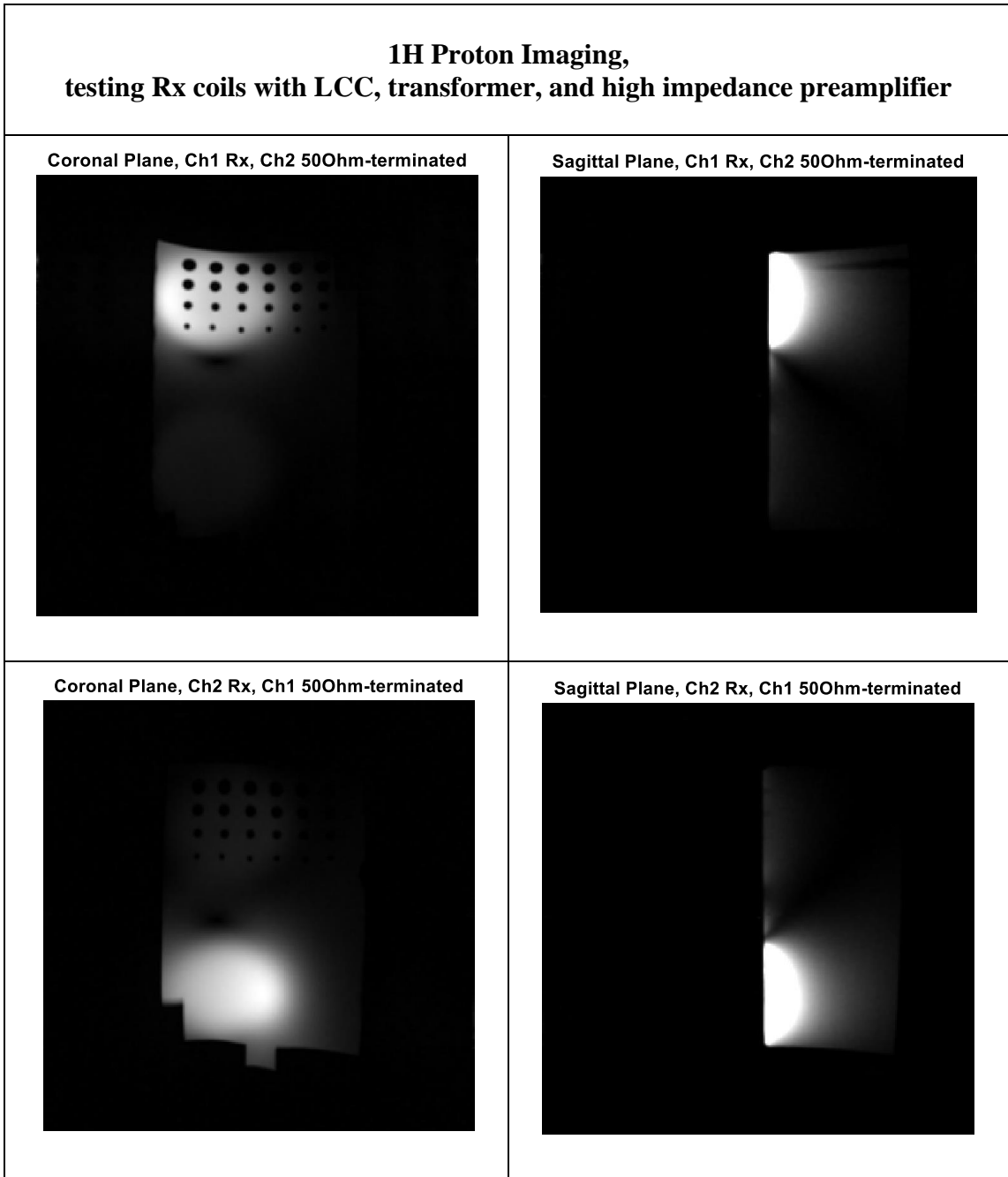


Figure 56. 1H imaging results acquired using two testing loop coils with LCC and transformer as matching network, and high impedance OPA as the preamplifier. The coupling between the two coils is reduced, however a minor residual pattern can still be observed.

1H SNR comparison

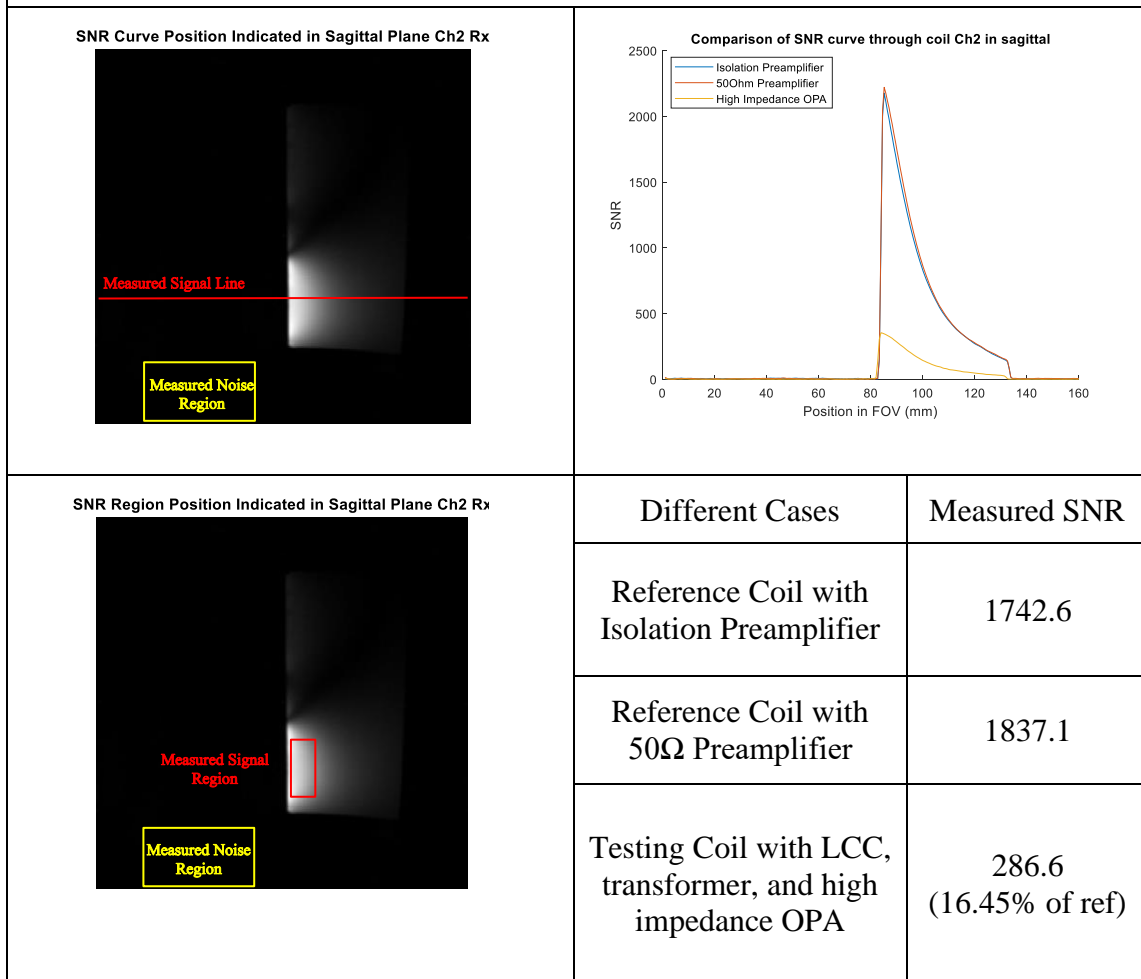
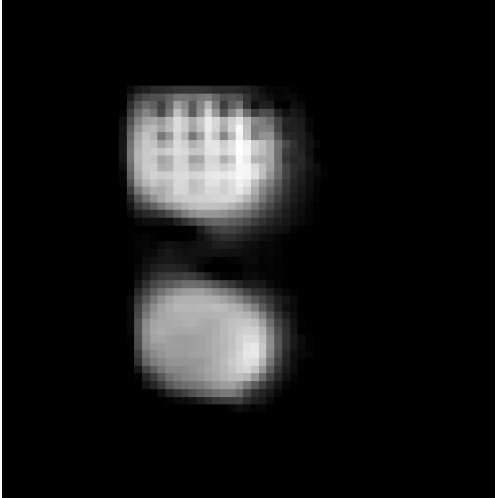


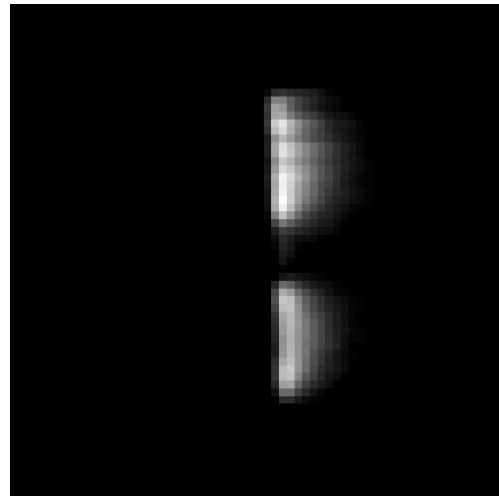
Figure 57. 1H SNR comparison between the reference coil in figure 47 (A) with isolation preamplifier or with 50Ω preamplifier, and the testing coil with LCC, transformer in figure 47 (C), and high impedance OPA.

**^{23}Na Imaging,
reference 50Ω Rx coils with 50Ω preamplifiers**

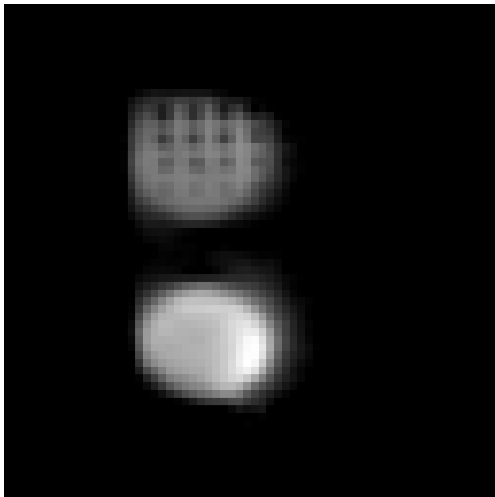
Coronal Plane, Ch1 Rx, Ch2 50Ω -terminated



Sagittal Plane, Ch1 Rx, Ch2 50Ω -terminated



Coronal Plane, Ch2 Rx, Ch1 50Ω -terminated



Sagittal Plane, Ch2 Rx, Ch1 50Ω -terminated

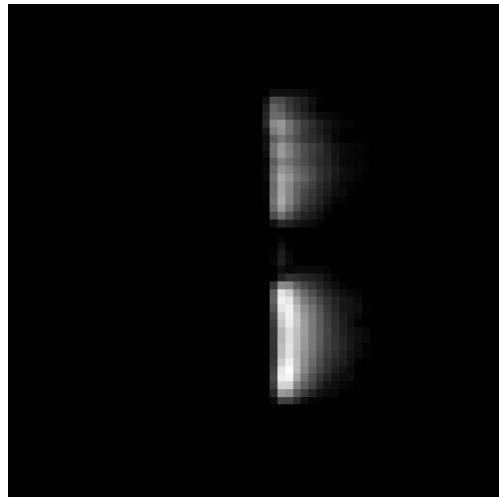
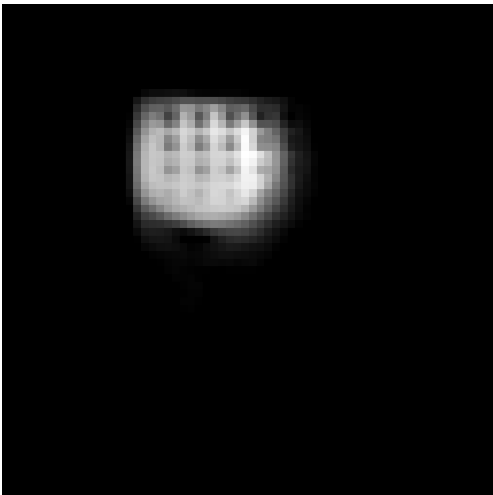


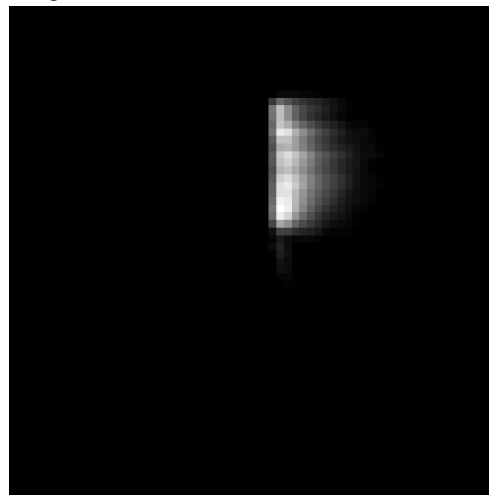
Figure 58. ^{23}Na imaging results acquired using two reference 50Ω loop coils with standard 50Ω preamplifier.

**^{23}Na Imaging,
reference 50Ω Rx coils with isolation preamplifiers**

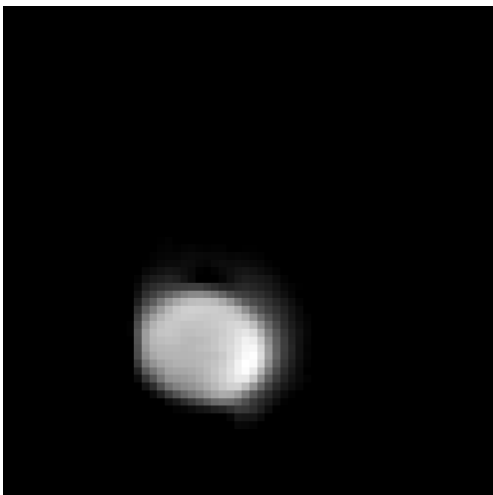
Coronal Plane, Ch1 Rx, Ch2 50Ohm-terminated



Sagittal Plane, Ch1 Rx, Ch2 50Ohm-terminated



Coronal Plane, Ch2 Rx, Ch1 50Ohm-terminated



Sagittal Plane, Ch2 Rx, Ch1 50Ohm-terminated

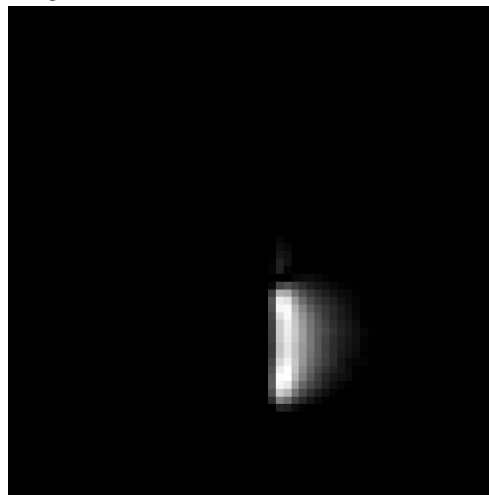


Figure 59. ^1H imaging results acquired using two reference 50Ω loop coils with isolation preamplifier.

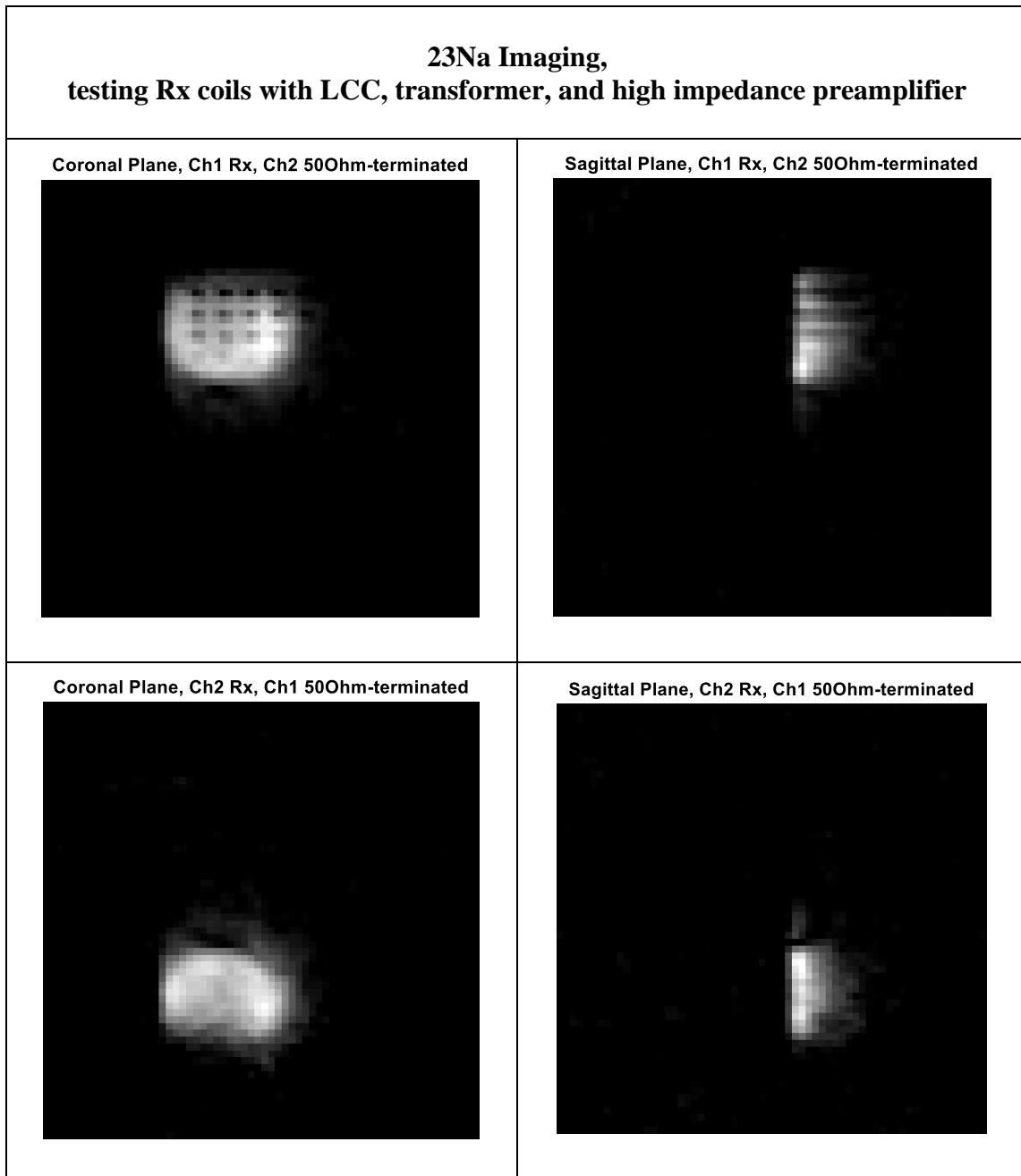


Figure 60. ^{23}Na imaging results acquired using two testing loop coils with LCC and transformer as matching network, and high impedance OPA as the preamplifier. The coupling between the two coils is reduced.

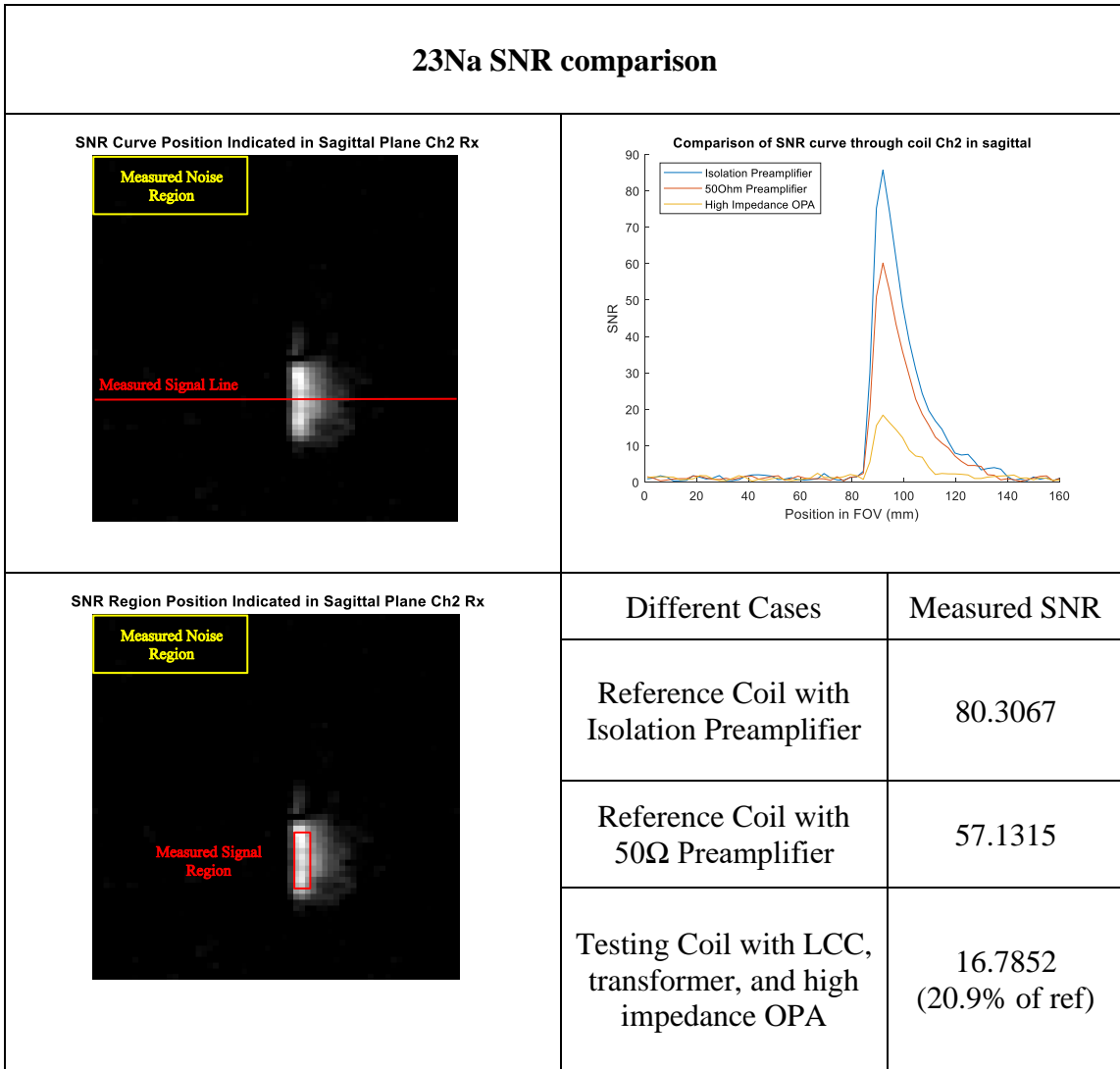


Figure 61. ^{23}Na SNR comparison between the reference coil in figure 48 (B) with isolation preamplifier or with 50Ω preamplifier, and the testing coil with LCC, transformer in figure 47 (C), and high impedance OPA.

As we can see that at both 1H and 23Na, coil decoupling is achieved by the testing coil. At 23Na, with the help of high impedance generated by the OPA and the transformer, the imaging results show no residual pattern on the 50 Ω -terminated coil while the other coil is on receive. It agrees with the bench measured of 27dB decoupling achieved at 23Na. At 1H, however, some minor residual pattern on the 50 Ω -terminated coil can still be observed, since only about 15dB of decoupling is achieved by moving the resonant peak away from Larmor frequency⁹². As discussed in section 5.4, with the bandwidth limitation of the hand-wind transformer, the matching network tested in this work can't bring the impedance back to decouple the coil.

At both 1H and 23Na, the SNR of the testing coil are relatively low compared to the reference coil. At 1H, the testing coil using OPA yields about 16.45% of the SNR of the reference coil with an isolation preamplifier. At 23Na, the testing coil using OPA yields about 20.9% of the SNR of the reference coil with an isolation preamplifier. As discussed in section 5.4, the heavy loss introduced by the first tuning element (LCC) as well as the insufficient impedance matching ratio of the transformer together lower the SNR of the testing configuration.

A summary of measured SNR for both bench and imaging experiments are shown in table 3. As discussed in section 5.4, since the amplified ohm loss from the LCC tuning network, the house-built transformer and undesired NF matching condition lead to the SNR reduction, the dual-tuned testing coil at 4.7T using a double-tuned LCC, the air-core transformer, and an OPA yield lower bench SNR at both frequencies. On the bench, the single-tuned reference coils with WanTcom isolation preamplifiers can yield

SNR of 66.61dB and 66.39dB at ^{23}Na and ^1H , respectively. The dual-tuned testing coil with house-built transformer and OPA can yield bench SNR of 58.16dB and 57.49dB at ^{23}Na and ^1H , which is 8.45dB and 8.9dB lower at ^{23}Na and ^1H when compared to WanTcom. The linear SNR is calculated and normalized based on the raw SNR in dB assuming a 50Ohm system for simplifying calculation, as shown in Table 3. Compared to the normalized SNR of the reference coils (100%), the dual-tuned testing coil with transformer and OPA can yield 37.8% and 35.89% of liner SNR at ^{23}Na and ^1H . In the imaging results, the reference coils with WanTcom isolation preamplifiers can yield 80.31 and 1742.6 SNR on the scanner at ^{23}Na and ^1H , respectively. However, the testing coil with transformer and OPA can only generate 16.79 and 16.45 imaging SNR at ^{23}Na and ^1H , respectively. The scanner-measured SNR of the testing coil are also normalized to their reference case and shown in Table 3. Compared to the normalized reference SNR (100%), the testing coil with transformer and OPA can generate 20.9% and 16.45% of the liner SNR at ^{23}Na and ^1H . Since the linear bench SNR is calculated based on raw SNR in dB assuming a 50Ω system, and the investigated approach using transformer and high impedance preamplifier is not standard 50Ω system, the normalized bench and imaging SNR are hard to compare directly.

The bench-measured reference decoupling generated by the WanTcom isolation preamplifier is 19.3dB at ^{23}Na and 18dB at ^1H . And the bench-measured decoupling generated by the testing setup using house-built transformer and OPA is 27.33 dB at ^{23}Na and 15.43 dB at ^1H . At ^{23}Na , this testing setup can generate relatively higher decoupling compared to the WanTcom, since this air-core transformer and OPA together

can together provide high impedance to the coil around this frequency. At 1H, however, due to the narrow frequency limitation of the transformer, decoupling of 15 dB is achieved by shifting the resonance away from Larmor frequency.

The decoupling based on the acquired images is quantified using the equation below.

$$Imaging Decoupling (dB) = 20 * \log_{10} \left(\frac{I_{Testing Coil On}}{I_{Testing Coil Off}} \bigg/ \frac{I_{50\Omega Coil On}}{I_{50\Omega Coil Off}} \right)$$

Where the $I_{Testing Coil on}$ is the signal intensity measured at a certain position near the testing coil that is on receive, and the $I_{Testing Coil off}$ is the signal intensity measured at the same relative position near the testing coil that is terminated. The $I_{50\Omega Coil on}$ and the $I_{Testing Coil off}$ are the same measurement of signal intensity at their positions but with two 50Ω matched and tuned coils.

The decoupling measured on imaging using reference WanTcom preamplifier is 19.69dB at 23Na and 19.91dB at 1H, which agree with the bench decoupling measurement. The decoupling measured on imaging using the testing setup of transformer and OPA is 23.55dB at 23Na and 10.73dB at 1H. Compared to the bench measurement, the imaging decoupling is relatively lower. Since the testing setup using OPA has lower SNR compared to the WanTcom, the decoupling measured on imaging is more affected by the noise in the imaging.

Table 3. Summary of the measured SNR and decoupling for both ^{23}Na and ^1H at 4.7T. The linear SNR of the testing coil is calculated based on the raw SNR and then normalized to the reference case acquired with WanTcom isolation preamplifier.

		^{23}Na			^1H		
Case		Raw SNR	Normalized Linear SNR	Decoupling	Raw SNR	Normalized Linear SNR	Decoupling
Bench	WanTcom	66.61dB	100%	19.3 dB	66.39 dB	100%	18 dB
	OPA	58.16 dB	37.8%	27.33 dB	57.49 dB	35.89%	15.43 dB
Imaging	WanTcom	80.31	100%	19.69 dB	1742.6	100%	19.91 dB
	OPA	16.79	20.90%	23.55 dB	286.6	16.45%	10.73 dB

5.6 Discussion and Future Potential

As shown here, this investigated configuration (transformer and OPA) is able to decouple surface coils at multiple Larmor frequencies, using only 1 set of matching network and preamplifier. Compared to the existing configurations that have to use multiple sets of preamplifier decoupling circuit, such as nested-type array coil or PIN diode switching array coil, the simplicity of this configuration to decouple a multi-nuclei

array coil is improved. And it can potentially allow a large channel-count multi-nuclei array coil to be built with the same level of complexity as the existing big single-tuned array coil⁷, while the amount of circuit and cabling will have to be multiplied if a conventional multi-nuclei configuration is used.

Within the good bandwidth of the house-built air-core transformer, the decoupling generated by this setup (27dB at ^{23}Na) sufficient reduces the undesired MR signal pattern caused by the coil crosstalk, resulting in a clean coil profile. This result validates the feasibility of using transformer and high impedance preamplifier to potentially decouple surface coil array in a more broadband way if a better transformer can be found. Without the help of the transformer and OPA, the decoupling at the highest frequency of ^1H is achieved by shifting the resonance away from the Larmor frequency. However, the operation of ^1H is considered less important in a multi-nuclei array coil design, since the relatively abundant SNR at ^1H allows the proton images to be acquired with a conventional volume coil, which most clinical scanners are equipped with. Instead, the performance of the X-nuclei (^{23}Na) is more focused in this work. The sensitivity of this investigated approach is undeniably far away from ideal in this prototype. The reason for the SNR loss is due to the inadequate ratio of the transformer (non-optimal NF matching for OPA) as well as the ohm loss introduced by the transformer and the first tuning element (total noise resistance added). Again, if a better air-core transformer can be realized the SNR cost of this investigated configuration could be reduced.

In theory, the transformer's impedance ratio only depends on the winding number of the primary and secondary sides and is independent of the frequency. In practice, however, the performance of a transformer is subject to multiple parasitic parameters, such as leakage and magnetizing inductances, capacitances between each winding, capacitances between primary and second side, resistive loss, etc¹⁰¹. These stray and distributed elements are frequency dependent¹⁰¹ and together limit the actual transformer's bandwidth. Dedicated researches have shown the potential of designing a non-ferrite transformer with an operating band wider than this multi-nuclei application requires^{102,103}. An improved transformer can potentially be realized if a more dedicated and thorough study on the air-core transformer can be done.

The recent development of hyperpolarization has shown great potential in X-nuclei signals enhancement¹⁰⁶⁻¹⁰⁸, yet still with the limitation of fast decay time¹⁰⁹. The potential use of hyperpolarization and the multi-tuned array coil could allow the good sensitivity of X-nuclei and fast acquisition to be achieved simultaneously. Although the significant SNR loss is a limitation for the current prototype design, the ability to construct large arrays with simplicity could allow parallel imaging to be done simultaneously at multiple nuclei, which could be valuable for metabolic studies using hyperpolarization media¹¹⁰⁻¹¹² since fast acquisition time potentially is more important than coil sensitivity in this case.

One possible approach to mitigate the tuning element's loss in this configuration is using a parallel network of multiple varactors¹¹³. The parallel of multiple varactors allows the total series resistance to be reduced and the total equivalent capacitance range

to be extended at the same time. Since at lower frequency, the capacitance required to tune a coil is generally bigger than the high frequency, a parallel varactor network potentially could be used to tune a low-field surface coil to multiple Larmor frequencies. For example, to series resonate a 6.4cm loop coil at 1.5T¹¹⁴ between 13C's Larmor frequency (16.06MHz) to 1H's Larmor frequency (63.85MHz), the calculated capacitance needed is between 36.5pF (for 1H) to 576pF (for 13C) with a max/min cap ratio of 15.80. Therefore, multiple varactors with a capacitance ratio higher than 15.8 can be paralleled together to achieve the needed capacitance range. And the equivalent loss of these varactors can be decreased at the same time. In theory, the lower the field strength (lower Larmor frequency), the higher capacitance is needed. And the requirement of more numbers of varactors to achieve a broader capacitance range in parallel could lead to even lower series loss in total.

A varactor with the capacitance ratio of 22.62 (BB640, Infineon) and a non-magnetic package is selected to validate the feasibility of resistance reduction, as well as the extended tuning range. A 6.4cm loop coil at 1.5T¹¹⁴ was built to experiment with different numbers of varactors, as shown in Figure 62. The measured series resistance (real part of the measured impedance) with a different number of varactors in parallel is shown in Figure 62.

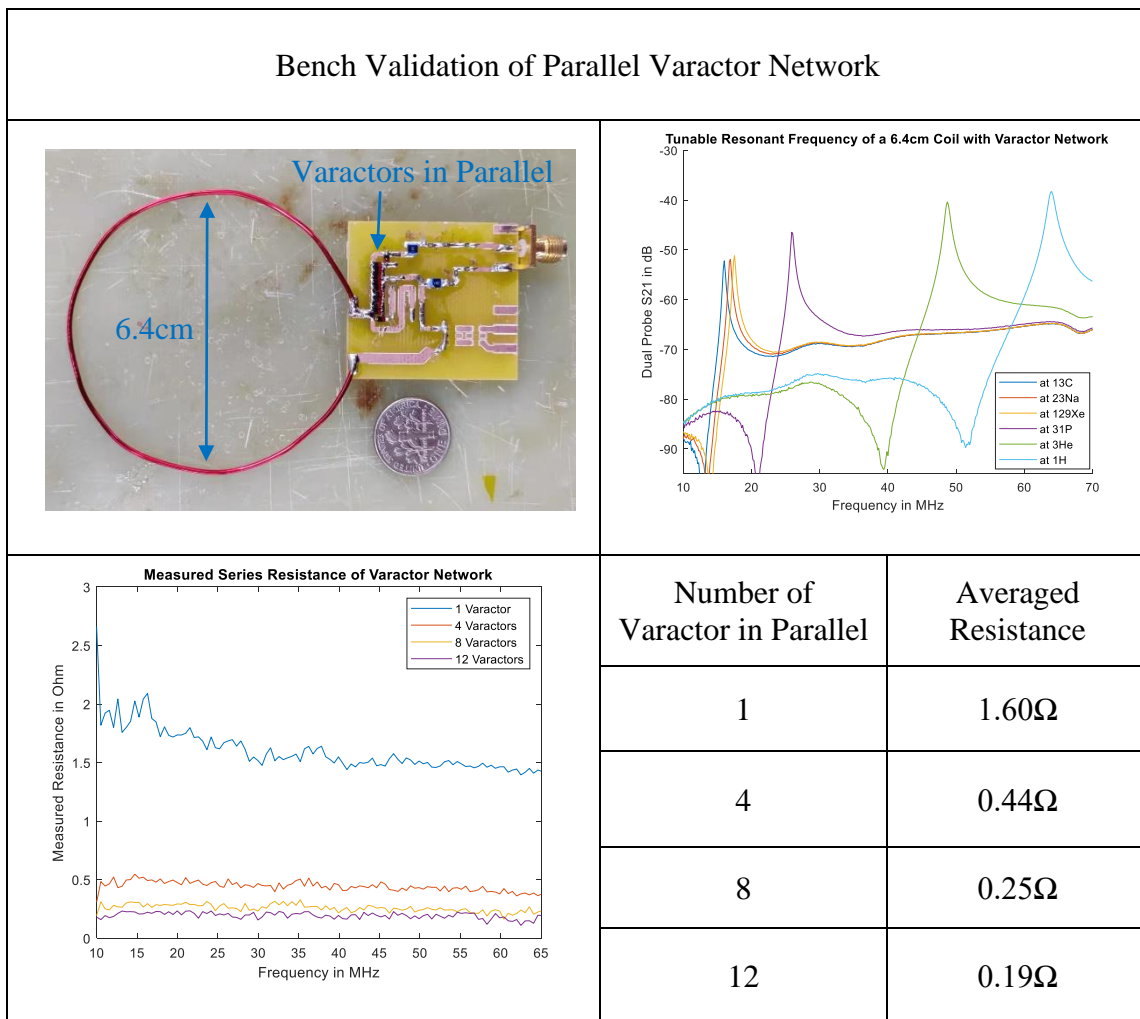


Figure 62. Bench validation of parallel varactor network as the possible multi-nuclei tuning element.

The measured resistances of the parallel network (averaged between 10 to 65MHz) are 1.60Ω for 1 varactor, 0.44Ω for 4 varactors, 0.25Ω for 8 varactors and 0.19Ω for 12 varactors. As we can see that with more varactors in parallel, the series resistance is significantly reduced. The capacitance range of the parallel network was tested by tuning the 6.4cm loop to the possible highest and lowest Larmor frequencies. As we can see, the tested varactor bank is capable of resonating the coil at any frequency

between 13C (16.06MHz) to 1H (63.85MHz) at 1.5T. If a good transformer with a high enough ratio and reasonable wide-enough bandwidth can be realized in the future, this approach of parallel varactor network can potentially be used to decouple low-field multi-nuclei surface coil array with much lower loss added compared to the LCC network.

As discussed in section 5.2, for OPA the good NF source impedance region is close to the conjugate of its input impedance, therefore the trade-off between good NF matching and good decoupling is hard to be avoided. For the same reason, the conventional matching network, such as double-tuned double matched lumped element network, or combination of transmission line and lumped element network is also difficult to achieve good NF and good decoupling at the same time. One possible approach to address this issue is using a high impedance preamplifier with an optimal NF matching area far away from the conjugate of its input impedance, such as a commercial LNA of Elcry¹¹⁵. Since the optimal NF source impedance of the Elcry preamp is around 50Ω , but the input impedance is close to the open circuit, this trade-off can be avoided potentially.

5.7 Summary

In this work, a novel approach aimed at simplifying the decoupling of multi-nuclei array coil is investigated. Instead of using multiple sets of isolation preamplifiers or trap circuits, which are often practiced on overlap/co-register or pin diode switching type of multi-nuclei array, transformer and high impedance preamplifier are tested and

compared with the conventional approach. The preliminary results indicate sufficient decoupling can be generated with this configuration, however the operating bandwidth is limited by the characteristic of the house-built transformer. The sensitivity of this prototype design is relatively lower when compared to the conventional single-tuned decoupling approach, because of the loss introduced by the double-tuning element of LCC, as well as the inadequate impedance ratio provided by the house-built transformer. However, a parallel varactor network shows the potential of multi-tuning a low field array coil with relatively much lower loss added. If a better air-core transformer with wider frequency bandwidth and higher impedance ratio can be realized, this investigated approach can be used to truly decouple array coil in a broadband way.

In general, by using only one set of elements (coil, MN, and preamplifier), decoupling at two Larmor frequencies can be achieved with this approach. Compared to the conventional way of overlapping multiple sets of array coil at different frequencies, great simplicity is found in the investigated approach. With the future development of non-ferrite transformer design, this configuration potentially can be used as a much simpler way to construct a multi-nuclei array coil.

CHAPTER VI

CONCLUSIONS

In this dissertation, several research works regarding different aspects of MRI parallel imaging are described. An 8-channel 9.4T head coil array using the serial transmit parallel receive (STxPRx) pulse sequence was modeled and analyzed. Compared to the conventional parallel transmit mode where all elements excite simultaneously and thus could form SAR hotspots, the STxPRx sequence excites each element sequentially and avoid the possibility of E fields aligning up (causing SAR hot spot). The hexagonal head array was first modeled in Remcom XFDTD, and the simulated B_1^+ /SAR maps were then post-processed in MATLAB according to the STxPRx sequence. With the same flip angle generated at the brain center, the calculation results show a benefit of 25.7% local maximum SAR reduction using STxPRx mode compared to the parallel transmit mode. This work provides a possible approach for the MRI application with significant SAR concerns, such as lower-gamma nuclei imaging or patients with an implanted medical device.

An add-on 7T B_1^+ steering system was constructed to enable 8-channel phase-steering capability with only two-channel transmitters required from the scanner. Wilkinson power dividers were first used to split the scanner's two transmit channels into equally into 8 RF channels, house-built phase shifter modules were then applied on each channel to enable independent phase control with the resolution of 22.5° . Finally, the 8 phase-conditioned channels were routed through a house-built TR switch array and got to the transmit coil array. With this add-on system, 8 RF channels with independent

phase control are generated to drive an 8-channel transmit coil array, with only two power amplifiers needed from the scanner. To validate the functionality of the system, the conjugate-phase steering method was used. By compensating each channel's phase accordingly, an elliptical B_1^+ hotspot with a very homogenous region of $2.6 \times 4.2 \text{ cm}^2$ and a fairly homogenous region of $5.9 \times 8.9 \text{ cm}^2$ can be generated at any targeting point in phantom. This work provides a novel and inexpensive hardware solution to gain the freedom of controllable B_1^+ pattern in parallel transmit, without the need for a large transmitter array. The modular design of this work allows the easy expansion of both the channel count as well as the finest phase resolution. Although only a point-focus steering method was used to validate the feasibility, this system is capable of studying more sophisticated steering or shimming approaches both with phantom and in-vivo. Since the system can manipulate and map the B_1^+ pattern at the same time without the actual scanner, it could be used as a handy bench platform for developing transmit pulse sequence.

A novel decoupling strategy aimed at simplifying multi-nuclei array coil design is investigated in this work. Instead of using conventional isolation preamplifiers and trap circuits to decouple overlapping type or PIN diode switching type of multi-nuclei array coil, transformer and high impedance preamplifier is tested to deliver decoupling at multiple Larmor frequency. Different types of tuning elements and transformers were tested and compared. The preliminary results validate the feasibility of achieving broadband decoupling using this configuration. The bandwidth of decoupling is found to be limited by the characteristic of the house-built transformer, and the achievable

sensitivity is also limited by the loss of the matching network and the inadequate ratio of the transformer. However, this approach can be potentially used at low field MRI with relatively less SNR sacrifice, if a better transformer can be developed in the future.

REFERENCES

1. Lauterbur PC. Image formation by induced local interactions: examples employing nuclear magnetic resonance. *nature*. 1973;242(5394):190-191.
2. Morrow G. Progress in MRI magnets. *IEEE transactions on applied superconductivity*. 2000;10(1):744-751.
3. Snyder CJ, DelaBarre L, Metzger GJ, et al. Initial results of cardiac imaging at 7 Tesla. *Magn Reson Med*. 2009;61(3):517-524.
4. Herrera VL, Viereck JC, Lopez-Guerra G, et al. 11.7 Tesla magnetic resonance microimaging of laryngeal tissue architecture. *Laryngoscope*. 2009;119(11):2187-2194.
5. McNab JA, Edlow BL, Witzel T, et al. The Human Connectome Project and beyond: initial applications of 300 mT/m gradients. *Neuroimage*. 2013;80:234-245.
6. Schmitt F. The gradient system. Paper presented at: Proc. Intl. Soc. Mag. Res. Med2013.
7. Wiggins GC, Polimeni JR, Potthast A, Schmitt M, Alagappan V, Wald LL. 96-Channel receive-only head coil for 3 Tesla: design optimization and evaluation. *Magn Reson Med*. 2009;62(3):754-762.
8. Lee R, Chang H, Stefanescu C, et al. A 128-channel helium-3 phased array at 3T for highly accelerated parallel imaging in hyperpolarized gas MRI. Paper presented at: Proceedings of the 16th Annual Meeting of ISMRM2008.
9. Graessl A, Renz W, Hezel F, et al. Modular 32-channel transceiver coil array for cardiac MRI at 7.0T. *Magn Reson Med*. 2014;72(1):276-290.
10. Hoult DI, Richards RE. The signal-to-noise ratio of the nuclear magnetic resonance experiment. 1976. *J Magn Reson*. 2011;213(2):329-343.

11. Hamilton J, Franson D, Seiberlich N. Recent advances in parallel imaging for MRI. *Prog Nucl Magn Reson Spectrosc.* 2017;101:71-95.
12. Meyerspeer M, Magill AW, Kuehne A, Gruetter R, Moser E, Schmid AI. Simultaneous and interleaved acquisition of NMR signals from different nuclei with a clinical MRI scanner. *Magn Reson Med.* 2016;76(5):1636-1641.
13. Bottomley PA, Andrew ER. RF magnetic field penetration, phase shift and power dissipation in biological tissue: implications for NMR imaging. *Phys Med Biol.* 1978;23(4):630-643.
14. Van de Moortele PF, Akgun C, Adriany G, et al. B(1) destructive interferences and spatial phase patterns at 7 T with a head transceiver array coil. *Magn Reson Med.* 2005;54(6):1503-1518.
15. Collins CM, Liu W, Schreiber W, Yang QX, Smith MB. Central brightening due to constructive interference with, without, and despite dielectric resonance. *J Magn Reson Imaging.* 2005;21(2):192-196.
16. Glover G, Hayes C, Pelc N, et al. Comparison of linear and circular polarization for magnetic resonance imaging. *J Magn Reson.* 1985;64(2):255-270.
17. Yang QX, Wang J, Zhang X, et al. Analysis of wave behavior in lossy dielectric samples at high field. *Magn Reson Med.* 2002;47(5):982-989.
18. Kangarlu A, Baertlein BA, Lee R, et al. Dielectric resonance phenomena in ultra high field MRI. *J Comput Assist Tomogr.* 1999;23(6):821-831.
19. van den Bergen B, van den Berg CA, Klomp DW, Lagendijk JJ. SAR and power implications of different RF shimming strategies in the pelvis for 7T MRI. *J Magn Reson Imaging.* 2009;30(1):194-202.
20. Wolf S, Diehl D, Gebhardt M, Mallow J, Speck O. SAR simulations for high-field MRI: how much detail, effort, and accuracy is needed? *Magn Reson Med.* 2013;69(4):1157-1168.

21. Jin J. *Electromagnetic analysis and design in magnetic resonance imaging*. Routledge; 2018.
22. Thulborn KR, Ma C, Sun C, et al. SERIAL transmit - parallel receive (ST(x)PR(x)) MR imaging produces acceptable proton image uniformity without compromising field of view or SAR guidelines for human neuroimaging at 9.4 Tesla. *J Magn Reson*. 2018;293:145-153.
23. Vaughan JT, Snyder CJ, DelaBarre LJ, et al. Whole-body imaging at 7T: preliminary results. *Magn Reson Med*. 2009;61(1):244-248.
24. Vaughan JT, Garwood M, Collins CM, et al. 7T vs. 4T: RF power, homogeneity, and signal-to-noise comparison in head images. *Magn Reson Med*. 2001;46(1):24-30.
25. Adriany G, Van de Moortele PF, Wiesinger F, et al. Transmit and receive transmission line arrays for 7 Tesla parallel imaging. *Magn Reson Med*. 2005;53(2):434-445.
26. van den Bergen B, Van den Berg CA, Bartels LW, Lagendijk JJ. 7 T body MRI: B1 shimming with simultaneous SAR reduction. *Phys Med Biol*. 2007;52(17):5429-5441.
27. Liu W, Collins CM, Smith MB. Calculations of B(1) Distribution, Specific Energy Absorption Rate, and Intrinsic Signal-to-Noise Ratio for a Body-Size Birdcage Coil Loaded with Different Human Subjects at 64 and 128 MHz. *Appl Magn Reson*. 2005;29(1):5-18.
28. Balchandani P, Glover G, Pauly J, Spielman D. Improved slice-selective adiabatic excitation. *Magn Reson Med*. 2014;71(1):75-82.
29. Eryaman Y, Guerin B, Keil B, et al. SAR reduction in 7T C-spine imaging using a "dark modes" transmit array strategy. *Magn Reson Med*. 2015;73(4):1533-1539.

30. Orzada S, Maderwald S, Poser BA, Bitz AK, Quick HH, Ladd ME. RF excitation using time interleaved acquisition of modes (TIAMO) to address B1 inhomogeneity in high-field MRI. *Magn Reson Med.* 2010;64(2):327-333.
31. Orzada S, Johst S, Maderwald S, Bitz AK, Solbach K, Ladd ME. Mitigation of B1(+) inhomogeneity on single-channel transmit systems with TIAMO. *Magn Reson Med.* 2013;70(1):290-294.
32. Brunner DO, De Zanche N, Fröhlich J, Paska J, Pruessmann KP. Travelling-wave nuclear magnetic resonance. *Nature.* 2009;457(7232):994-998.
33. Alsop DC, Connick TJ, Mizsei G. A spiral volume coil for improved RF field homogeneity at high static magnetic field strength. *Magn Reson Med.* 1998;40(1):49-54.
34. Vaughan JT, Hetherington HP, Otu JO, Pan JW, Pohost GM. High frequency volume coils for clinical NMR imaging and spectroscopy. *Magn Reson Med.* 1994;32(2):206-218.
35. Padormo F, Beqiri A, Hajnal JV, Malik SJ. Parallel transmission for ultrahigh-field imaging. *NMR Biomed.* 2016;29(9):1145-1161.
36. Vaughan JT, Adriany G, Snyder CJ, et al. Efficient high-frequency body coil for high-field MRI. *Magn Reson Med.* 2004;52(4):851-859.
37. Metzger GJ, Snyder C, Akgun C, Vaughan T, Ugurbil K, Van de Moortele PF. Local B1+ shimming for prostate imaging with transceiver arrays at 7T based on subject-dependent transmit phase measurements. *Magn Reson Med.* 2008;59(2):396-409.
38. Curtis AT, Gilbert KM, Klassen LM, Gati JS, Menon RS. Slice-by-slice B1+ shimming at 7 T. *Magn Reson Med.* 2012;68(4):1109-1116.
39. Mao W, Smith MB, Collins CM. Exploring the limits of RF shimming for high-field MRI of the human head. *Magn Reson Med.* 2006;56(4):918-922.

40. Pfaffenrot V, Brunheim S, Rietsch SHG, et al. An 8/15-channel Tx/Rx head neck RF coil combination with region-specific B(1) + shimming for whole-brain MRI focused on the cerebellum at 7T. *Magn Reson Med.* 2018;80(3):1252-1265.
41. Abraham R, Ibrahim TS. Proposed radiofrequency phased-array excitation scheme for homogenous and localized 7-Tesla whole-body imaging based on full-wave numerical simulations. *Magn Reson Med.* 2007;57(2):235-242.
42. Yan X, Cao Z, Grissom WA. Experimental implementation of array-compressed parallel transmission at 7 tesla. *Magn Reson Med.* 2016;75(6):2545-2552.
43. Sun C, Patel K, Wilcox M, et al. A retrofit to enable dynamic B1+ steering for transmit arrays without multiple amplifiers. *Magn Reson Med.* 2021;85(6):3497-3509.
44. Ladd ME, Bachert P, Meyerspeer M, et al. Pros and cons of ultra-high-field MRI/MRS for human application. *Prog Nucl Magn Reson Spectrosc.* 2018;109:1-50.
45. Hu R, Kleimaier D, Malzacher M, Hoesl MAU, Paschke NK, Schad LR. X-nuclei imaging: Current state, technical challenges, and future directions. *J Magn Reson Imaging.* 2020;51(2):355-376.
46. Niesporek SC, Nagel AM, Platt T. Multinuclear MRI at Ultrahigh Fields. *Top Magn Reson Imaging.* 2019;28(3):173-188.
47. Choi CH, Hong SM, Felder J, Shah NJ. The state-of-the-art and emerging design approaches of double-tuned RF coils for X-nuclei, brain MR imaging and spectroscopy: A review. *Magn Reson Imaging.* 2020;72:103-116.
48. Zöllner FG, Kalayciyan R, Chacón-Caldera J, Zimmer F, Schad LR. Pre-clinical functional Magnetic Resonance Imaging Part I: The kidney. *Z Med Phys.* 2014;24(4):286-306.
49. Zöllner FG, Konstandin S, Lommen J, et al. Quantitative sodium MRI of kidney. *NMR Biomed.* 2016;29(2):197-205.

50. Shah NJ, Worthoff WA, Langen KJ. Imaging of sodium in the brain: a brief review. *NMR Biomed.* 2016;29(2):162-174.
51. Bottomley PA. Sodium MRI in human heart: a review. *NMR Biomed.* 2016;29(2):187-196.
52. Guermazi A, Alizai H, Crema MD, Trattnig S, Regatte RR, Roemer FW. Compositional MRI techniques for evaluation of cartilage degeneration in osteoarthritis. *Osteoarthritis Cartilage.* 2015;23(10):1639-1653.
53. Petracca M, Fleysher L, Oesingmann N, Inglese M. Sodium MRI of multiple sclerosis. *NMR Biomed.* 2016;29(2):153-161.
54. Petracca M, Vancea RO, Fleysher L, Jonkman LE, Oesingmann N, Inglese M. Brain intra- and extracellular sodium concentration in multiple sclerosis: a 7 T MRI study. *Brain.* 2016;139(Pt 3):795-806.
55. Dani KA, Warach S. Metabolic imaging of ischemic stroke: the present and future. *AJNR Am J Neuroradiol.* 2014;35(6 Suppl):S37-43.
56. Mellon EA, Pilkinton DT, Clark CM, et al. Sodium MR imaging detection of mild Alzheimer disease: preliminary study. *AJNR Am J Neuroradiol.* 2009;30(5):978-984.
57. Hilal SK, Maudsley AA, Simon HE, et al. In vivo NMR imaging of tissue sodium in the intact cat before and after acute cerebral stroke. *AJNR Am J Neuroradiol.* 1983;4(3):245-249.
58. Fain S, Schiebler ML, McCormack DG, Parraga G. Imaging of lung function using hyperpolarized helium-3 magnetic resonance imaging: Review of current and emerging translational methods and applications. *J Magn Reson Imaging.* 2010;32(6):1398-1408.
59. Avdievich NI, Ruhm L, Dorst J, Scheffler K, Korzowski A, Henning A. Double - tuned ³¹P/¹H human head array with high performance at both frequencies for spectroscopic imaging at 9.4 T. *Magnetic resonance in medicine.* 2020;84(2):1076-1089.

60. Lakshmanan K, Brown R, Madelin G, Qian Y, Boada F, Wiggins GC. An eight - channel sodium/proton coil for brain MRI at 3 T. *NMR in Biomedicine*. 2018;31(2):e3867.
61. Malzacher M, Chacon-Caldera J, Paschke N, Schad LR. Feasibility study of a double resonant 8-channel ¹H/8-channel ²³Na receive-only head coil at 3 Tesla. *Magnetic resonance imaging*. 2019;59:97-104.
62. Shajan G, Mirkes C, Buckenmaier K, Hoffmann J, Pohmann R, Scheffler K. Three-layered radio frequency coil arrangement for sodium MRI of the human brain at 9.4 Tesla. *Magn Reson Med*. 2016;75(2):906-916.
63. Brown R, Lakshmanan K, Madelin G, et al. A flexible nested sodium and proton coil array with wideband matching for knee cartilage MRI at 3T. *Magn Reson Med*. 2016;76(4):1325-1334.
64. Brown R, Madelin G, Lattanzi R, et al. Design of a nested eight-channel sodium and four-channel proton coil for 7T knee imaging. *Magn Reson Med*. 2013;70(1):259-268.
65. Kim JH, Moon CH, Park BW, Furlan A, Zhao T, Bae KT. Multichannel transceiver dual-tuned RF coil for proton/sodium MR imaging of knee cartilage at 3 T. *Magn Reson Imaging*. 2012;30(4):562-571.
66. Avdievich NI. Transceiver-Phased Arrays for Human Brain Studies at 7 T. *Appl Magn Reson*. 2011;41(2-4):483-506.
67. Ha S, Hamamura MJ, Nalcioglu O, Muftuler LT. A PIN diode controlled dual-tuned MRI RF coil and phased array for multi nuclear imaging. *Phys Med Biol*. 2010;55(9):2589-2600.
68. Han SD, Heo P, Kim HJ, et al. Double - layered dual - tuned RF coil using frequency - selectable PIN - diode control at 7 - T MRI. *Concepts in Magnetic Resonance Part B: Magnetic Resonance Engineering*. 2017;47(4):e21363.
69. Hurshkainen A, Nikulin A, Georget E, et al. A novel metamaterial-inspired RF-coil for preclinical dual-nuclei MRI. *Scientific reports*. 2018;8(1):1-13.

70. Hernandez D. Design of a Coplanar Interlayer Gapped Microstrips Arrangement for Multi-Nuclei (^1H , ^{19}F , ^{31}P , and ^{23}Na) Applications in 7T MRI. *Applied Sciences*. 2021;11(3):957.
71. Roemer PB, Edelstein WA, Hayes CE, Souza SP, Mueller OM. The NMR phased array. *Magnetic resonance in medicine*. 1990;16(2):192-225.
72. Wu B, Wang C, Krug R, et al. 7T human spine imaging arrays with adjustable inductive decoupling. *IEEE Trans Biomed Eng*. 2010;57(2):397-403.
73. Von Morze C, Tropp J, Banerjee S, et al. An eight - channel, nonoverlapping phased array coil with capacitive decoupling for parallel MRI at 3 T. *Concepts in Magnetic Resonance Part B: Magnetic Resonance Engineering: An Educational Journal*. 2007;31(1):37-43.
74. Oh S, Webb AG, Neuberger T, Park B, Collins CM. Experimental and numerical assessment of MRI-induced temperature change and SAR distributions in phantoms and in vivo. *Magn Reson Med*. 2010;63(1):218-223.
75. Collins CM. Numerical field calculations considering the human subject for engineering and safety assurance in MRI. *NMR Biomed*. 2009;22(9):919-926.
76. Jin J, Liu F, Weber E, Crozier S. Improving SAR estimations in MRI using subject-specific models. *Phys Med Biol*. 2012;57(24):8153-8171.
77. Homann H, Graesslin I, Nehrke K, Findelee C, Dössel O, Börnert P. Specific absorption rate reduction in parallel transmission by k - space adaptive radiofrequency pulse design. *Magnetic resonance in medicine*. 2011;65(2):350-357.
78. Shen GX, Boada FE, Thulborn KR. Dual - frequency, dual - quadrature, birdcage RF coil design with identical B1 pattern for sodium and proton imaging of the human brain at 1.5 T. *Magnetic resonance in medicine*. 1997;38(5):717-725.

79. Schnall M, Subramanian VH, Leigh Jr J, Chance B. A new double-tuned probed for concurrent ^1H and ^{31}P NMR. *Journal of Magnetic Resonance (1969)*. 1985;65(1):122-129.
80. Wilkinson EJ. An N-way hybrid power divider. *IRE Trans Microw Theory Tech*. 1960;8(1):116-118.
81. White JF. *Microwave semiconductor engineering*. Netherlands: Springer Science & Business Media; 2012.
82. Unknown. UsetwoAD8302tomeasure360degrees-RevA.
83. Alon L, Lattanzi R, Lakshmanan K, et al. Transverse slot antennas for high field MRI. *Magn Reson Med*. 2018;80(3):1233-1242.
84. Wiggins G, Zhang B, Cloos M, et al. Mixing loops and electric dipole antennas for increased sensitivity at 7 Tesla. In Proceedings of the 21st Annual Meeting of ISMRM, Salt Lake City, UT, USA, 2013. p. 2737.
85. Stensgaard A. Optimized design of the shielded-loop resonator. *Journal of Magnetic Resonance, Series A*. 1996;122(2):120-125.
86. Cao Z, Yan X, Grissom WA. Array-compressed parallel transmit pulse design. *Magn Reson Med*. 2016;76(4):1158-1169.
87. Yan X, Cao Z, Grissom WA. Ratio-adjustable power splitters for array-compressed parallel transmission. *Magn Reson Med*. 2018;79(4):2422-2431.
88. Rahola J. Power waves and conjugate matching. *IEEE Transactions on Circuits and Systems II: Express Briefs*. 2008;55(1):92-96.
89. Johansen D, Sánchez-Heredia J, Zhurbenko V, Ardenkjær-Larsen J. Practical aspects of preamplifier designs for ^{13}C imaging. *ISMRM 25th*. 2017.

90. de Lara LN, Windischberger C, Sieg J, Moser E, Laistler E. P 212. A novel high sensitivity MR-device for combined TMS/fMRI experiments. *Clinical Neurophysiology*. 2013;124(10):e164-e165.
91. Wilcox M, Ogier S, Cheshkov S, et al. A 16-Channel 13 C Array Coil for Magnetic Resonance Spectroscopy of the Breast at 7T. *IEEE Transactions on Biomedical Engineering*. 2021;68(6):2036-2046.
92. Sun C, Bauer C, Busher J, McDougall MP, Wright SM. Investigation of Low-Cost Op-Amps as Decoupling Preamplifiers for MRI Array Coils. *Annu Int Conf IEEE Eng Med Biol Soc*. 2020;2020:1473-1476.
93. Sánchez-Heredia JD, Johansen DH, Hansen RB, et al. Improved decoupling for low frequency MRI arrays using non-conventional preamplifier impedance. *IEEE Transactions On Biomedical Engineering*. 2018;66(7):1940-1948.
94. Taunk B, Zaveri P. Design of Low Noise Amplifier using BFP 540 and BFP 640. Paper presented at: 2012 1st International Conference on Emerging Technology Trends in Electronics, Communication & Networking2012.
95. Instruments T. *LMH6629 Ultra-Low Noise, High-Speed Operational Amplifier with Shutdown*. Texas Instruments, Tech. Rep., 2016.[Online]. Available: [www.ti.com/lit/ds ...](http://www.ti.com/lit/ds...);2010.
96. Karki J. Calculating noise figure in op amps. *Analog Applic J Q*. 2003;4:31-37.
97. Coil Winding Specialist I. AppNotes - Magnetic and Transformers Design Consulting.
98. Anisimov N, Tarasova A, Pavlova O, et al. MRI Coils Optimized for Detection of 1 H and 23 Na at 0.5 T. *Applied Magnetic Resonance*. 2021;52(3):221-233.
99. Anisimov N, Sadykhov E, Pavlova O, Fomina D, Tarasova A, Pirogov YA. Whole Body Sodium MRI at 0.5 Tesla Using Surface Coil and Long Echo Time Sequence. *Applied Magnetic Resonance*. 2019;50(10):1149-1161.

100. Rousseau J, Lecouffe P, Marchandise X. A new, fully versatile surface coil for MRI. *Magnetic resonance imaging*. 1990;8(4):517-523.
101. Biernacki J, Czarkowski D. High frequency transformer modeling. Paper presented at: ISCAS 2001. The 2001 IEEE International Symposium on Circuits and Systems (Cat. No. 01CH37196)2001.
102. Long JR. Monolithic transformers for silicon RF IC design. *IEEE Journal of Solid-State Circuits*. 2000;35(9):1368-1382.
103. Hergt M, Oppelt R, Vester M, et al. Low noise preamplifier with integrated cable trap. Paper presented at: Proceedings of the 15th Annual Meeting of ISMRM, Berlin, Germany2007.
104. Wang J, Reykowski A, Dickas J. Calculation of the signal-to-noise ratio for simple surface coils and arrays of coils [magnetic resonance imaging]. *IEEE transactions on biomedical engineering*. 1995;42(9):908-917.
105. Aibinu AM, Salami M-JE, Shafie AA, Najeeb AR. MRI reconstruction using discrete Fourier transform: a tutorial. 2008.
106. Wang ZJ, Ohliger MA, Larson PE, et al. Hyperpolarized ¹³C MRI: state of the art and future directions. *Radiology*. 2019;291(2):273-284.
107. Mugler III JP, Altes TA. Hyperpolarized ¹²⁹Xe MRI of the human lung. *Journal of Magnetic Resonance Imaging*. 2013;37(2):313-331.
108. Olaru AM, Robertson TB, Lewis JS, et al. Extending the scope of ¹⁹F hyperpolarization through signal amplification by reversible exchange in MRI and NMR spectroscopy. *ChemistryOpen*. 2018;7(1):97-105.
109. Kovtunov KV, Truong ML, Barskiy DA, et al. Long - lived spin states for low - field hyperpolarized gas MRI. *Chemistry - A European Journal*. 2014;20(45):14629-14632.

110. Ma J, Pinho MC, Harrison CE, et al. Dynamic ¹³C MR spectroscopy as an alternative to imaging for assessing cerebral metabolism using hyperpolarized pyruvate in humans. *Magnetic resonance in medicine*. 2022;87(3):1136-1149.
111. Grist JT, Miller JJ, Zaccagna F, et al. Hyperpolarized ¹³C MRI: A novel approach for probing cerebral metabolism in health and neurological disease. *Journal of Cerebral Blood Flow & Metabolism*. 2020;40(6):1137-1147.
112. Golman K, Petersson JS, Magnusson P, et al. Cardiac metabolism measured noninvasively by hyperpolarized ¹³C MRI. *Magnetic Resonance in Medicine: An Official Journal of the International Society for Magnetic Resonance in Medicine*. 2008;59(5):1005-1013.
113. Raab FH. Electronically tuned UHF power amplifier. Paper presented at: 2011 IEEE MTT-S International Microwave Symposium2011.
114. Hardy CJ, Giaquinto RO, Piel JE, et al. 128 - channel body MRI with a flexible high - density receiver - coil array. *Journal of Magnetic Resonance Imaging: An Official Journal of the International Society for Magnetic Resonance in Medicine*. 2008;28(5):1219-1225.
115. Zhurbenko V, Sánchez-Heredia JD, Wang W, Ardenkjær-Larsen JH. Flexible Self-Resonant Detector Coil for Magnetic Resonance Imaging of Carbon-13. Paper presented at: 2020 50th European Microwave Conference (EuMC)2021.

APPENDIX A

SUPPLEMENTARY MATERIAL FOR HEAD COIL ARRAY ANALYSIS

The SAR analyzing MATLAB script is attached here. The original Remcom model files, simulated data, and a legacy subfunction are required to work with this code (contact smwright@tamu.edu).

```
function [] = Universal()
close all
clc
clear

global AngleFactor Slice DC_P DC_S DC_I center_Position BorE
AngleFactor = 2*pi*42.57e6*1e-3*180/pi;
Slice = 59;
DC_P = 0.004;%0.004; %Duty Cycle
DC_S = 0.004;
DC_I = 0.004;
center_Position = [198,186];
BorE = 0; %% 0 is for B1+, 1 is for E total Field
%center_Position = [202,193];
%% Get Raw B1+ or E and SAR data, then get scaling factor
[B1p,B3p,B5p,B7p,B9p,NorFacPower1,NorFacPower3,NorFacPower5,NorFacPower
7,NorFacPower9] = Get_B1_plus(); % also QUIVER plotting
[SAR1,SAR3,SAR5,SAR7] =
Get_SAR_Series(NorFacPower1,NorFacPower3,NorFacPower5,NorFacPower7);
[SAR9] = Get_SAR_Parallel(NorFacPower9);
[SF1,SF3,SF5,SF7,SF9] = Get_ScalingFactor(B1p,B3p,B5p,B7p,B9p);

%% Plot B1+ data or E before scaled and get same reference
[clims_B,clims_PS,clims_PS_Sq] = Get_Reference(B1p,B3p,B5p,B7p,B9p); %
Now this is data before second scaling
% Plot_individual_B1p(B1p,B3p,B5p,B7p,clims_B);
Plot_Series_B1P(B1p,B3p,B5p,B7p,clims_PS);
Plot_Parallel_B1p(B9p,clims_PS);
%
Plot_Series_Parallel_After_Scaled(B1p,B3p,B5p,B7p,B9p,SF1,SF3,SF5,SF7,S
F9);

Plot_Series_Parallel_Squared(clims_PS_Sq,B1p,B3p,B5p,B7p,B9p)
Plot_Series_Parallel_Squared_After_Scaled(B1p,B3p,B5p,B7p,B9p,SF1,SF3,S
F5,SF7,SF9)

%Find_Center(B1p,B3p,B5p,B7p);

%% Scale the SAR using Scaling factor
```

```

[SAR1,SAR3,SAR5,SAR7,SAR9] =
Scaling_SAR(SAR1,SAR3,SAR5,SAR7,SAR9,SF1,SF3,SF5,SF7,SF9);

%% plot SAR
% Plot_Individual_SAR(SAR1,SAR3,SAR5,SAR7) % Before Scaled,self
referenced

[clims_SAR_PS] = Get_SAR_Reference(SAR1,SAR3,SAR5,SAR7,SAR9);
Plot_Individual_SAR(SAR1,SAR3,SAR5,SAR7,clims_SAR_PS)

[Max_Parallel_SAR_AfterScaled] = Plot_Parallel_SAR(SAR9,clims_SAR_PS);
[Max_Series_SAR_AfterScaled] =
Plot_Series_SAR(SAR1,SAR3,SAR5,SAR7,clims_SAR_PS);
Calculate_Average_Individual_SAR(SAR1,SAR3,SAR5,SAR7,SAR9);

end

%% subroutine

function [B1p,B3p,B5p,B7p,B9p,Phase1,Phase3,Phase5,Phase7,Phase9] =
Get_B1_plus()
global AngleFactor BorE
%AngleFactor = 2*pi*42.57e6*1e-3*180/pi;

[cx1, cy1, cz1, gridVertices1, Bx1, By1, Bz1,
max10gSAR_06_1,Phase1]=readSurfaceFields_v1_fcn('D:\St_Pr_MRI_9th\St_Pr
_MRI_9th\000167\Run0001', 'MultiPoint_Upper_Axial_Sensor_8',0,BorE);
[cx3, cy3, cz3, gridVertices3, Bx3, By3, Bz3,
max10gSAR_06_3,Phase3]=readSurfaceFields_v1_fcn('D:\St_Pr_MRI_9th\St_Pr
_MRI_9th\000168\Run0001', 'MultiPoint_Upper_Axial_Sensor_8',0,BorE);
[cx5, cy5, cz5, gridVertices5, Bx5, By5, Bz5,
max10gSAR_06_5,Phase5]=readSurfaceFields_v1_fcn('D:\St_Pr_MRI_9th\St_Pr
_MRI_9th\000169\Run0001', 'MultiPoint_Upper_Axial_Sensor_8',0,BorE);
[cx7, cy7, cz7, gridVertices7, Bx7, By7, Bz7,
max10gSAR_06_7,Phase7]=readSurfaceFields_v1_fcn('D:\St_Pr_MRI_9th\St_Pr
_MRI_9th\000170\Run0001', 'MultiPoint_Upper_Axial_Sensor_8',0,BorE);

[cx9, cy9, cz9, gridVertices9, Bx9, By9, Bz9,
max10gSAR_06_9,Phase9]=readSurfaceFields_v1_fcn('D:\St_Pr_MRI_9th\St_Pr
_MRI_9th\000166\Run0001', 'MultiPoint_Upper_Axial_Sensor_8',0,BorE);

if BorE == 0
    B1p = (Bx1+1i*By1)/2;
    B3p = (Bx3+1i*By3)/2;
    B5p = (Bx5+1i*By5)/2;
    B7p = (Bx7+1i*By7)/2;

    B9p = (Bx9+1i*By9)/2;
    B9p = B9p*sqrt(4/1); %Scale parallel to 4 W
else
    B1p = sqrt(Bx1.^2+By1.^2+Bz1.^2);
    B3p = sqrt(Bx3.^2+By3.^2+Bz3.^2);
    B5p = sqrt(Bx5.^2+By5.^2+Bz5.^2);

```

```

B7p = sqrt (Bx7.^2+By7.^2+Bz7.^2);

B9p = sqrt (Bx9.^2+By9.^2+Bz9.^2);
B9p = B9p*sqrt(4/1); %Scale parallel to 4 W

Bx_Total = Bx1+Bx3+Bx5+Bx7;
By_Total = By1+By3+By5+By7;
Bz_Total = Bz1+Bz3+Bz5+Bz7;
Blp_VecAdding = sqrt (Bx_Total.^2 + By_Total.^2 + Bz_Total.^2);

end
%%%%%%%%%%%%%%%%%%%%%%%%%%%%%%%%%%%%%%%%%%%%%%%%%%%%%%%%%%%%%%%%%%%%%%%%
%   Quiver plotting
%%%%%%%%%%%%%%%%%%%%%%%%%%%%%%%%%%%%%%%%%%%%%%%%%%%%%%%%%%%%%%%%%%%%%%%%
%   if BorE == 1
%       SamplingRate = 12;
%       Bz1 = Bz1(1:SamplingRate:end,1:SamplingRate:end,1);
%       SIZE = size(Bz1);
%       [X,Y] = meshgrid(1:SIZE(1,1),1:SIZE(1,2));
%       Z = Bz1;
%       surf(X,Y,abs(Z'));
%       quiver3(Z',U,V,W)
%
%
% x = 1:400;
% y = 1:366;
% surf(y,x,ones(400,366))
%
quiver3(zeros(366,400),flip(abs(Bx1')),flip(abs(By1')),flip(abs(Bz1')))
%
%
%
%       Bx1 = Bx1(1:SamplingRate:end,1:SamplingRate:end,1);
%       By1 = By1(1:SamplingRate:end,1:SamplingRate:end,1);
%       Bz1 = Bz1(1:SamplingRate:end,1:SamplingRate:end,1);
%       SIZE = size(Bx1);
%       x = 1:SIZE(1,1);
%       y = 1:SIZE(1,2);
%       z = ones(1,1);
%       %figure
%       X = zeros(SIZE(1,1),SIZE(1,2),1);
%       %quiver3(x,y,z,flip(abs(Bx1')),flip(abs(By1')),flip(abs(Bz1')))
%       quiver3(y,x,z,X,X,flip(abs(Bz1)))
%       title(['E field in Vector of Coil ',num2str(NumofCoil)])
%
%
%
%
%       Plot_Vector(SamplingRate,Bx1,By1,3);
%       Plot_Vector(SamplingRate,Bx3,By3,4);
%       Plot_Vector(SamplingRate,Bx5,By5,1);
%       Plot_Vector(SamplingRate,Bx7,By7,2);
%       Plot_Vector(SamplingRate,Bx9,By9,'all in parallel');

```

```

% end
end
%%%%%%%%%%%%%%%%%%%%%%%%%%%%%%%%%%%%%%%%%%%%%%%%%%%%%%%%%%%%%%%%%%%%%%%%
%%%
function [DataGet1,DataGet2,DataGet3,DataGet4] =
Get_SAR_Series (NorFacPower1,NorFacPower3,NorFacPower5,NorFacPower7)
global Slice

syms DataGet
load('167_10g.mat')
%load('161_raw.mat')
Size = size(Sar);
DataGet1 = zeros (Size(1,2),Size(1,3));
for i = 1:Size(1,2)
    for j = 1:Size(1,3)
        DataGet1(i,j) = Sar(Slice,i,j);
    end
end
DataGet1 = DataGet1*NorFacPower1;

load('168_10g.mat')
% load('162_raw.mat')
DataGet2 = zeros (Size(1,2),Size(1,3));
for i = 1:Size(1,2)
    for j = 1:Size(1,3)
        DataGet2(i,j) = Sar(Slice,i,j);
    end
end
DataGet2 = DataGet2*NorFacPower3;

load('169_10g.mat')
% load('163_raw.mat')
DataGet3 = zeros (Size(1,2),Size(1,3));
for i = 1:Size(1,2)
    for j = 1:Size(1,3)
        DataGet3(i,j) = Sar(Slice,i,j);
    end
end
DataGet3 = DataGet3*NorFacPower5;

load('170_10g.mat')
% load('164_raw.mat')
DataGet4 = zeros (Size(1,2),Size(1,3));
for i = 1:Size(1,2)
    for j = 1:Size(1,3)
        DataGet4(i,j) = Sar(Slice,i,j);
    end
end
DataGet4 = DataGet4*NorFacPower7;

end
%%%%%%%%%%%%%%%%%%%%%%%%%%%%%%%%%%%%%%%%%%%%%%%%%%%%%%%%%%%%%%%%%%%%%%%%
%%%

```

```

function [DataGet5] = Get_SAR_Parallel(NorFacPower9)
global Slice

syms DataGet
load('166_10g.mat')
% load('165_raw.mat')
Size = size(Sar);
DataGet5 = zeros(Size(1,2),Size(1,3));
for i = 1:Size(1,2)
    for j = 1:Size(1,3)
        DataGet5(i,j) = Sar(Slice,i,j);
    end
end
DataGet5 = DataGet5*NorFacPower9; % Scale to 1 W first, auto
DataGet5 = DataGet5*4; % Scale to 4W

end
%%%%%%%%%%%%%%%%%%%%%%%%%%%%%%%%%%%%%%%%%%%%%%%%%%%%%%%%%%%%%%%%%%%%%%%%
%%%
function [SF1,SF3,SF5,SF7,SF9] = Get_ScalingFactor(B1p,B3p,B5p,B7p,B9p)
global AngleFactor center_Position BorE
y = center_Position(1,1);
x = center_Position(1,2); %% 200,183 currently

if BorE == 0
%     SF1 = 22.5/(abs(B1p(y,x))*AngleFactor);
%     SF3 = 22.5/(abs(B3p(y,x))*AngleFactor);
%     SF5 = 22.5/(abs(B5p(y,x))*AngleFactor);
%     SF7 = 22.5/(abs(B7p(y,x))*AngleFactor);
    SF1 = 90/ ( (
abs(B1p(y,x))+abs(B3p(y,x))+abs(B5p(y,x))+abs(B7p(y,x)) ) *AngleFactor )
;
    SF3 = 0;
    SF5 = 0;
    SF7 = 0;
    SF9 = 90/(abs(B9p(y,x))*AngleFactor);
else
    SF1 = 6.6521; % Get these two numbers from BorE=0 first,then
    SF3 = 1;      % apply to here
    SF5 = 1;
    SF7 = 1;
    SF9 = 7.2565;
end
end
%%%%%%%%%%%%%%%%%%%%%%%%%%%%%%%%%%%%%%%%%%%%%%%%%%%%%%%%%%%%%%%%%%%%%%%%
%%%
function [clims_B,clims_PS,clims_PS_Sq] =
Get_Reference(B1p,B3p,B5p,B7p,B9p)

MAX1_B = max(max(abs(B1p)));
MAX3_B = max(max(abs(B3p)));
MAX5_B = max(max(abs(B5p)));

```

```

MAX7_B = max(max(abs(B7p)));
MAXall_B = max([MAX1_B,MAX3_B,MAX5_B,MAX7_B]);
clims_B = [0,MAXall_B];

MAX_P = max(max(abs(B9p)));
B1p_total = abs(B1p)+abs(B3p)+abs(B5p)+abs(B7p);
MAX_S = max(max(B1p_total));
MAXall_PS = max([MAX_P,MAX_S]);
clims_PS = [0,MAXall_PS];

MAX_P_Sq = max(max(abs(B9p).^2));
B1p_total_Sq = abs(B1p).^2+abs(B3p).^2+abs(B5p).^2+abs(B7p).^2;
MAX_S_Sq = max(max(B1p_total_Sq));
MAXall_PS_Sq = max([MAX_P_Sq,MAX_S_Sq]);
clims_PS_Sq = [0,MAXall_PS_Sq];

end
%%%%%%%%%%%%%%%%%%%%%%%%%%%%%%%%%%%%%%%%%%%%%%%%%%%%%%%%%%%%%%%%%%%%%%%%
%%%
function [] = Plot_individual_B1p(B1p,B3p,B5p,B7p,clims_B)
global AngleFactor BorE

if BorE == 0
figure
imagesc(abs(B1p'),clims_B)
colorbar
title('Coil 3 B1+ field After 1st scaling')
figure
imagesc(abs(B1p')*AngleFactor,clims_B*AngleFactor);
colorbar
title('Coil 3 tip angle map After 1st scaling')
%SF1 = 22.5/(abs(B1p(y,x))*AngleFactor);

figure
imagesc(abs(B3p'),clims_B)
colorbar
title('Coil 4 B1+ field After 1st scaling')
figure
imagesc(abs(B3p')*AngleFactor,clims_B*AngleFactor);
colorbar
title('Coil 4 tip angle map After 1st scaling')
%SF3 = 22.5/(abs(B3p(y,x))*AngleFactor);

figure
imagesc(abs(B5p'),clims_B)
colorbar
title('Coil 1 B1+ field After 1st scaling')
figure
imagesc(abs(B5p')*AngleFactor,clims_B*AngleFactor);
colorbar
title('Coil 1 tip angle map After 1st scaling')
%SF5 = 22.5/(abs(B5p(y,x))*AngleFactor);

```

```

figure
imagesc(abs(B7p'),clims_B)
colorbar
title('Coil 2 B1+ field After 1st scaling')
figure
imagesc(abs(B7p')*AngleFactor,clims_B*AngleFactor);
colorbar
title('Coil 2 tip angle map After 1st scaling')
%SF7 = 22.5/(abs(B7p(y,x))*AngleFactor);

else
    figure
    imagesc(abs(B1p'),clims_B)
    colorbar
    title('Coil 3 E field After 1st scaling')

    figure
    imagesc(abs(B3p'),clims_B)
    colorbar
    title('Coil 4 E field After 1st scaling')

    figure
    imagesc(abs(B5p'),clims_B)
    colorbar
    title('Coil 1 E field After 1st scaling')

    figure
    imagesc(abs(B7p'),clims_B)
    colorbar
    title('Coil 2 E field After 1st scaling')

end

end
%%%%%%%%%%%%%%%%%%%%%%%%%%%%%%%%%%%%%%%%%%%%%%%%%%%%%%%%%%%%%%%%%%%%%%%%
%%%
function [] = Plot_Series_B1P(B1p,B3p,B5p,B7p,clims_PS)
global AngleFactor BorE

if BorE == 0
B1p_total = abs(B1p')+abs(B3p')+abs(B5p')+abs(B7p');
figure
imagesc(B1p_total,clims_PS)
colorbar
title('Series mode B1+ field After 1st scaling')
figure
imagesc(B1p_total*AngleFactor,clims_PS*AngleFactor)
title('Series mode Tip angle map After 1st scaling')
colorbar
else
    B1p_total = abs(B1p')+abs(B3p')+abs(B5p')+abs(B7p');
    figure
    imagesc(B1p_total,clims_PS)

```



```

colorbar
title('Series mode E field After 1st scaling')

%%%%%%%%%%%%%%%%%%%%%%%%%%%%%%%%%%%%%%%%%%%%%%%%%%%%%%%%%%%%%%%%%%%%%%%%
%
% figure
% imagesc(abs(B1p_VecAdding'))
% colorbar
% title('E field using vector adding based on E1 E2 E3 and E4
before scaling')

% figure
% imagesc(log10(B1p_total),clims_PS)
% colorbar
% title('Series mode E field before scaled')
end

end

%%%%%%%%%%%%%%%%%%%%%%%%%%%%%%%%%%%%%%%%%%%%%%%%%%%%%%%%%%%%%%%%%%%%%%%%
%%%
function [] = Plot_Parallel_B1p(B9p,clims_PS)
global AngleFactor BorE
if BorE == 0
figure
imagesc(abs(B9p'),clims_PS)
colorbar
title('Parallel mode B1+ field After 1st scaling')
figure
imagesc(abs(B9p')*AngleFactor,clims_PS*AngleFactor);
colorbar
title('Parallel mode Tip angle map After 1st scaling')
else
figure
imagesc(abs(B9p'),clims_PS)
colorbar
title('Parallel mode E field After 1st scaling')

end
end

%%%%%%%%%%%%%%%%%%%%%%%%%%%%%%%%%%%%%%%%%%%%%%%%%%%%%%%%%%%%%%%%%%%%%%%%
%%%
function [SAR1_New,SAR3_New,SAR5_New,SAR7_New,SAR9_New] =
Scaling_SAR(SAR1,SAR3,SAR5,SAR7,SAR9,SF1,SF3,SF5,SF7,SF9)
%global DC_P DC_S
SAR1_New = SAR1*(SF1^2);
SAR3_New = SAR3*(SF1^2);
SAR5_New = SAR5*(SF1^2);
SAR7_New = SAR7*(SF1^2);
SAR9_New = SAR9*(SF9^2);
end

%%%%%%%%%%%%%%%%%%%%%%%%%%%%%%%%%%%%%%%%%%%%%%%%%%%%%%%%%%%%%%%%%%%%%%%%
%%%

```

```

function [] = Plot_Individual_SAR(SAR1,SAR3,SAR5,SAR7,clims_SAR_PS)
global DC_I

MAX = max([ max(max(SAR1)), max(max(SAR3)), max(max(SAR5)),
max(max(SAR7))] );
% clims = [0,MAX*DC_I];
%%
clims = [0,MAX*DC_I];
SAR1 = padarray(SAR1,[45 19]);
figure
imagesc(SAR1*DC_I,clims_SAR_PS);
colorbar
title(['Coil 3 SAR using duty cycle ',num2str(DC_I)])

SAR3 = padarray(SAR3,[45 19]);
figure
imagesc(SAR3*DC_I,clims_SAR_PS);
colorbar
title(['Coil 4 SAR using duty cycle ',num2str(DC_I)])

SAR5 = padarray(SAR5,[45 19]);
figure
imagesc(SAR5*DC_I,clims_SAR_PS);
colorbar
title(['Coil 1 SAR using duty cycle ',num2str(DC_I)])

SAR7 = padarray(SAR7,[45 19]);
figure
imagesc(SAR7*DC_I,clims_SAR_PS);
colorbar
title(['Coil 2 SAR using duty cycle ',num2str(DC_I)])

%%
% SAR1 = padarray(SAR1,[45 19]);
% figure
% imagesc(SAR1*DC_I,clims);
% colorbar
% title(['Coil 3 SAR using duty cycle ',num2str(DC_I)])
%
% SAR3 = padarray(SAR3,[45 19]);
% figure
% imagesc(SAR3*DC_I,clims);
% colorbar
% title(['Coil 4 SAR using duty cycle ',num2str(DC_I)])
%
% SAR5 = padarray(SAR5,[45 19]);
% figure
% imagesc(SAR5*DC_I,clims);
% colorbar
% title(['Coil 1 SAR using duty cycle ',num2str(DC_I)])
%
% SAR7 = padarray(SAR7,[45 19]);
% figure

```

```

% imagesc(SAR7*DC_I,clims);
% colorbar
% title(['Coil 2 SAR using duty cycle ',num2str(DC_I)])
end
%%%%%%%%%%%%%%%%%%%%%%%%%%%%%%%%%%%%%%%%%%%%%%%%%%%%%%%%%%%%%%%%%%%%%%%%
%%%
function [clims_SAR_PS] = Get_SAR_Reference(SAR1,SAR3,SAR5,SAR7,SAR9)
global DC_P DC_S
SAR_Total = (SAR1 + SAR3 +SAR5 +SAR7);
MAX = max([ max(max(SAR9))*DC_P , max(max(SAR_Total))*DC_S]);
clims_SAR_PS = [0,MAX];
end
%%%%%%%%%%%%%%%%%%%%%%%%%%%%%%%%%%%%%%%%%%%%%%%%%%%%%%%%%%%%%%%%%%%%%%%%
%%%
function
[Max_Parallel_SAR_AfterScaled]=Plot_Parallel_SAR(SAR9,clims_SAR_PS)
global DC_P
SAR9 = padarray(SAR9,[45 19]);
% Size = size(SAR9);
% for i=1:Size(1,1)
%     for j = 1:Size(1,2)
%         if SAR9(i,j)*DC_P > 2
%             SAR9(i,j) = 0;
%         end
%     end
% end
figure
imagesc(SAR9*DC_P,clims_SAR_PS)
colorbar
title('Parallel Mode SAR after scaled')

Max_Parallel_SAR_AfterScaled = max(max(SAR9*DC_P));

end
%%%%%%%%%%%%%%%%%%%%%%%%%%%%%%%%%%%%%%%%%%%%%%%%%%%%%%%%%%%%%%%%%%%%%%%%
%%%
function
[Max_Series_SAR_AfterScaled]=Plot_Series_SAR(SAR1,SAR3,SAR5,SAR7,clims_
SAR_PS)
global DC_S
SAR_Total = (SAR1 + SAR3 +SAR5 +SAR7)*DC_S;
SAR_Total = padarray(SAR_Total,[45 19]);
figure
imagesc(SAR_Total,clims_SAR_PS)
colorbar
title('Series Mode SAR after scaled')

Max_Series_SAR_AfterScaled = max(max(SAR_Total));

end
%%%%%%%%%%%%%%%%%%%%%%%%%%%%%%%%%%%%%%%%%%%%%%%%%%%%%%%%%%%%%%%%%%%%%%%%
%%%
function [Optimal] = Find_Center(B1p,B3p,B5p,B7p)

```

```

A1 = B1p(170:230,150:210);
A3 = B3p(170:230,150:210);
A5 = B5p(170:230,150:210);
A7 = B7p(170:230,150:210);

C = cat(3,A1,A3,A5,A7);
A = std(C,0,3)*1e7;
[B,J] = min(A);
[C,I] = min(min(A));
Optimal = [170+J(1,I),150+I];
end
%%%%%%%%%%%%%%%%%%%%%%%%%%%%%%%%%%%%%%%%%%%%%%%%%%%%%%%%%%%%%%%%%%%%%%%%%%%%%%
%%%
function [] =
Plot_Series_Parallel_After_Scaled(B1p,B3p,B5p,B7p,B9p,SF1,SF3,SF5,SF7,S
F9)
global AngleFactor BorE
% Same reference clims_PS
%B1p_total = abs(B1p')*SF1+abs(B3p')*SF3+abs(B5p')*SF5+abs(B7p')*SF7;

B1p_total = (abs(B1p')+abs(B3p')+abs(B5p')+abs(B7p'))*SF1;
%B1p_total = (abs(B7p'))*SF1;
MAX = max([ max(max(B1p_total)) , max(max(abs(B9p)*SF9)) ]);
clims_PS = [0,MAX];
if BorE == 0
%Series
%B1p_total = abs(B1p')*SF1+abs(B3p')*SF3+abs(B5p')*SF5+abs(B7p')*SF7;
figure
imagesc(B1p_total,clims_PS)
colorbar
title('Series mode B1+ field after 2nd scaling')
figure
imagesc(B1p_total*AngleFactor,clims_PS*AngleFactor)
%imagesc(B1p_total*AngleFactor)
title('Series mode Tip angle map after 2nd scaling')
colorbar

%Parallel
figure
imagesc(abs(B9p'*SF9),clims_PS)
colorbar
title('Parallel mode B1+ field after 2nd scaling')
figure
imagesc(abs(B9p'*SF9)*AngleFactor,clims_PS*AngleFactor);
colorbar
title('Parallel mode Tip angle map after 2nd scaling')

else
figure
imagesc(B1p_total,clims_PS)
colorbar
title('Series mode E field after 2nd scaling')

```

```

    figure
    imagesc(abs(B9p'*SF9),clims_PS)
    colorbar
    title('Parallel mode E field after 2nd scaling')
end

end

function [] = Plot_Vector(SamplingRate,Bx1,By1,NumofCoil)
global BorE
if BorE == 1
    Bx1 = Bx1(1:SamplingRate:end,1:SamplingRate:end);
    By1 = By1(1:SamplingRate:end,1:SamplingRate:end);
    SIZE = size(Bx1);
    x = 1:SIZE(1,1);
    y = 1:SIZE(1,2);
    figure
    quiver(x,y,flip(abs(Bx1')),flip(abs(By1')))
    title(['E field in Vector of Coil ',num2str(NumofCoil)])
end
end
%%%%%%%%%%%%%%%%%%%%%%%%%%%%%%%%%%%%%%%%%%%%%%%%%%%%%%%%%%%%%%%%%%%%%%%%
%%
function [] =
Plot_Series_Parallel_Squared(clims_PS_Sq,B1p,B3p,B5p,B7p,B9p)
global BorE
if BorE == 1
    clims = [-3.5,0];

    B1p_total_square =
abs(B1p').^2+abs(B3p').^2+abs(B5p').^2+abs(B7p').^2;
    figure
    imagesc(B1p_total_square,clims_PS_Sq)
    colorbar
    title('Series mode E1^2+E2^2+E3^2+E4^2 before scaled')

    figure
    B1p_total_square_log = log10(B1p_total_square/clims_PS_Sq(1,2));
    imagesc(B1p_total_square_log,clims)
    colorbar
    title({'E1^2+E2^2+E3^2+E4^2 in dB before scaled',' reference at ',
num2str(clims_PS_Sq(1,2))})

    figure
    imagesc(abs(B9p').^2,clims_PS_Sq)
    colorbar
    title('Parallel mode Eparallel^2 before scaled')

    figure
    B9p_square_log = log10( (abs(B9p').^2)/clims_PS_Sq(1,2) );
    imagesc(B9p_square_log,clims)
    colorbar

```

```

        title({'Parallel mode Eparallel^2 in dB before scaled', 'reference
at ', num2str(clims_PS_Sq(1,2))})

end
end
%%%%%%%%%%%%%%%%%%%%%%%%%%%%%%%%%%%%%%%%%%%%%%%%%%%%%%%%%%%%%%%%%%%%%%%%
%%%
function [] =
Plot_Series_Parallel_Squared_After_Scaled(B1p,B3p,B5p,B7p,B9p,SF1,SF3,S
F5,SF7,SF9)
global BorE
if BorE == 1
    B1p = B1p*SF1;B3p = B3p*SF1;B5p = B5p*SF1;B7p = B7p*SF1;B9p =
B9p*SF9;

    B1p_total_square =
abs(B1p').^2+abs(B3p').^2+abs(B5p').^2+abs(B7p').^2;
    MAX = max([ max(max(B1p_total_square)) , max(max(abs(B9p.^2))) ]);
    clims_PS_Scaled_Sq = [0,MAX];

%     MAX_P_Sq = max(max(abs(B9p).^2));
%     B1p_total_Sq = abs(B1p).^2+abs(B3p).^2+abs(B5p).^2+abs(B7p).^2;
%     MAX_S_Sq = max(max(B1p_total_Sq));
%     MAXall_PS_Sq = max([MAX_P_Sq,MAX_S_Sq]);
%     clims_PS_Sq = [0,MAXall_PS_Sq];

    clims = [-3.5,0];

    figure
    imagesc(B1p_total_square,clims_PS_Scaled_Sq)
    colorbar
    title('Series mode E1^2+E2^2+E3^2+E4^2 after scaled')

    figure
    B1p_total_square_log =
log10(B1p_total_square/clims_PS_Scaled_Sq(1,2));
    imagesc(B1p_total_square_log,clims)
    colorbar
    title({'E1^2+E2^2+E3^2+E4^2 in dB after scaled',' reference at ',
num2str(clims_PS_Scaled_Sq(1,2))})

    figure
    imagesc(abs(B9p').^2,clims_PS_Scaled_Sq)
    colorbar
    title('Parallel mode Eparallel^2 after scaled')

    figure
    B9p_square_log = log10( (abs(B9p')).^2/clims_PS_Scaled_Sq(1,2) );
    imagesc(B9p_square_log,clims)
    colorbar
    title({'Parallel mode Eparallel^2 in dB before scaled', 'reference
at ', num2str(clims_PS_Scaled_Sq(1,2))})

```

```

end
end

function [] = Calculate_Average_Individual_SAR(SAR1,SAR3,SAR5,SAR7,SAR9)
global DC_I DC_P DC_S
Average_SAR1 = mean(mean(SAR1*DC_I, 'omitnan'), 'omitnan');
Average_SAR3 = mean(mean(SAR3*DC_I, 'omitnan'), 'omitnan');
Average_SAR5 = mean(mean(SAR5*DC_I, 'omitnan'), 'omitnan');
Average_SAR7 = mean(mean(SAR7*DC_I, 'omitnan'), 'omitnan');

Average_Parallel = mean(mean(SAR9*DC_P, 'omitnan'), 'omitnan');
Average_Series =
mean(mean((SAR1+SAR3+SAR5+SAR7)*DC_S, 'omitnan'), 'omitnan');

end

```

APPENDIX B

SUPPLEMENTARY MATERIAL FOR B1+ STEERING SYSTEM

B.1 Drawing of PIN Diode Driver Board.

Schematic, layout, BOM, and pictures of the PIN diode driver boards are shown in this section.

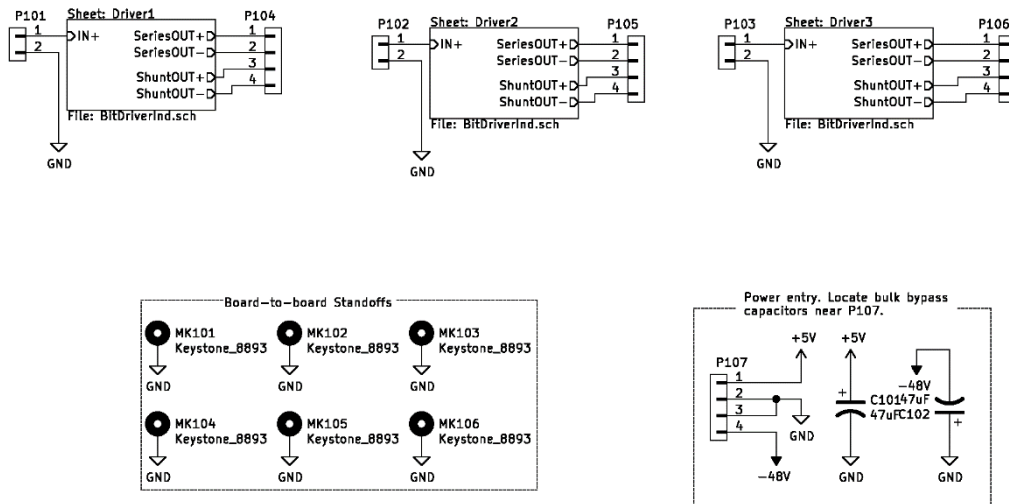


Figure 63. Overview of the PIN diode driver board. Each PCB contains 3 identical driver circuit that controls each bit of the phase shifter individually.

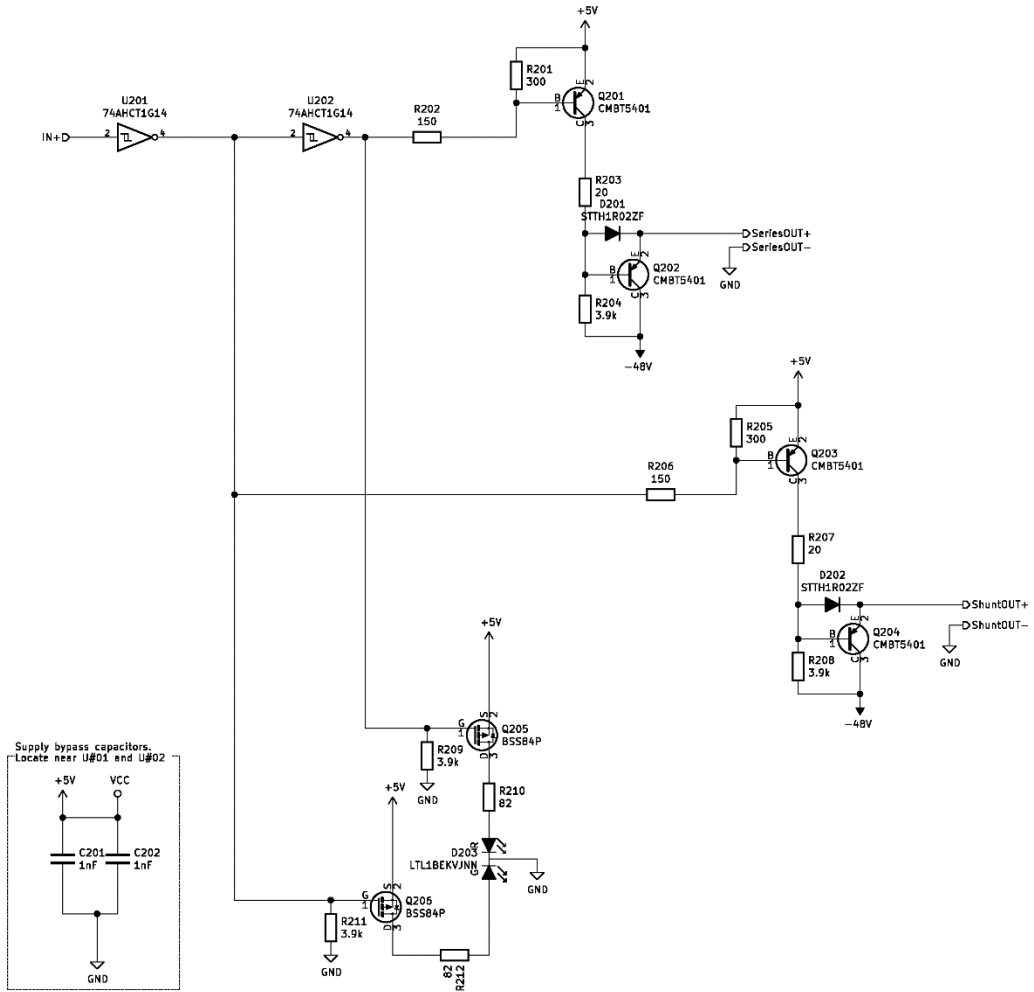


Figure 64. One of the three PIN diode driver circuits. The rest two are the same.

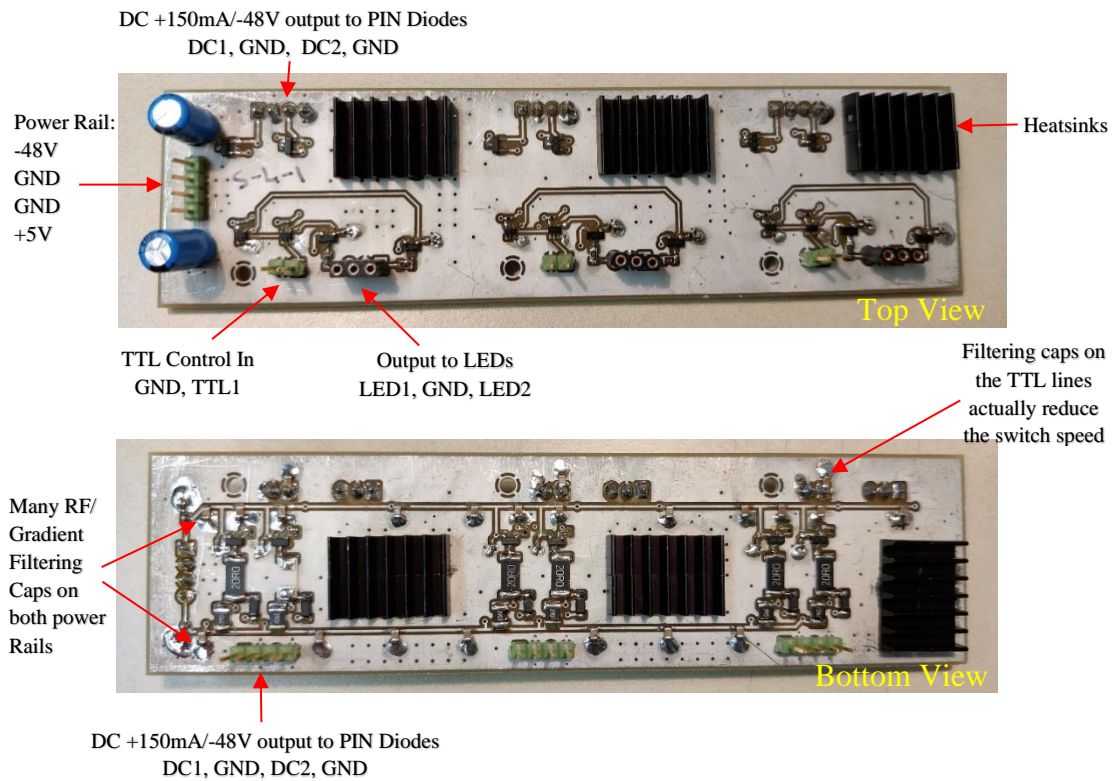


Figure 67. Pictures of the assembled Pin diode driver board.

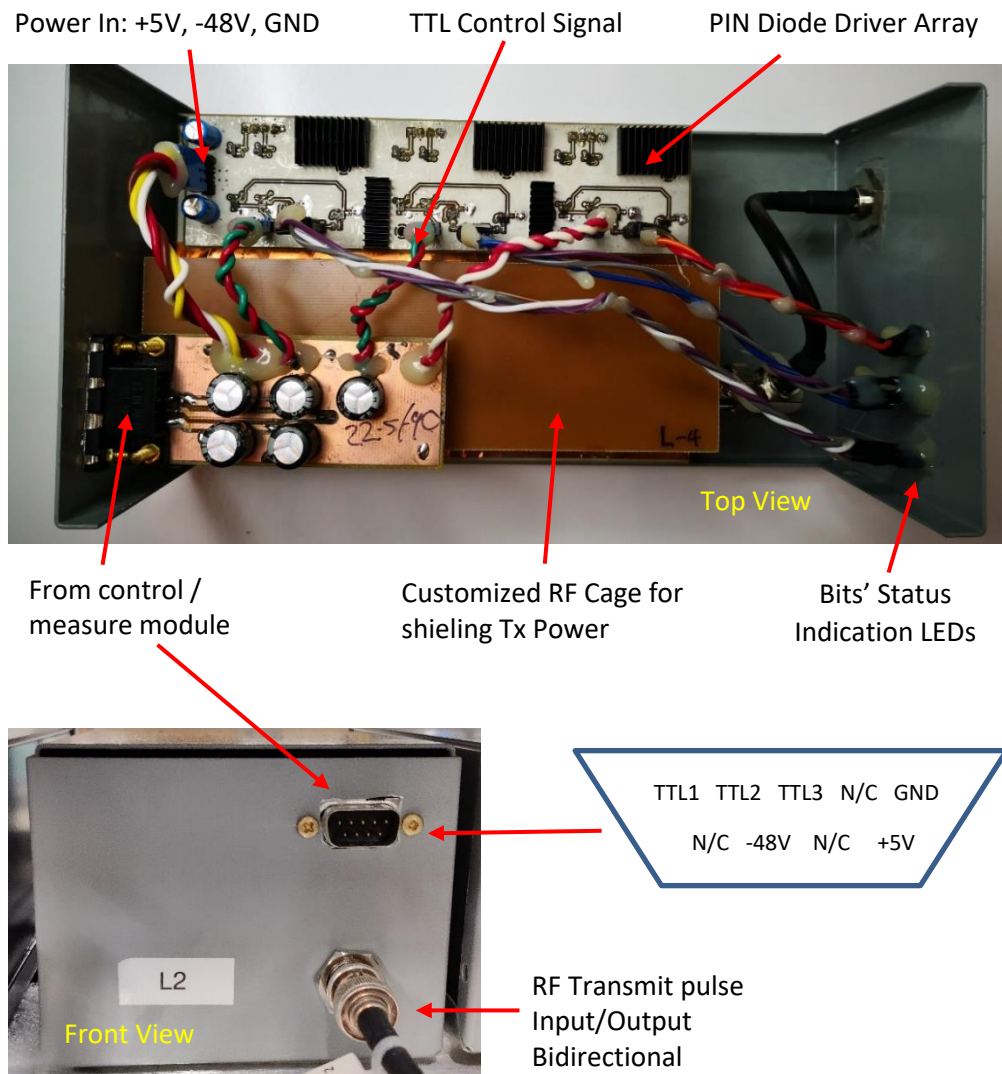


Figure 68. Pictures of the Pin diode driver board inside the RF shield case, with indications of connection.

Table 4. Bill of materials for PIN diode driver circuit.

Ref	Qty	Value	MFR	MPN
C101 C102	2	47uF	Lelon	REA100M2ABK-0611P
C201 C202 C301 C302 C401 C402	6	1nF	Murata	GRM155R61C104KA88J
D203 D303 D403	3	LTL1BEKVJN N	Lite-On	LTL1BEKVJNN
D202 D201 D302 D301 D402 D401	6	STTH1R02ZF	STMicroelectronics	STTH1R02ZF
MK102 MK105 MK103 MK106 MK101 MK104	6	Keystone_8893	Keystone Electronics	8891
P101 P102 P103	3	KK 0.254 2 Pin RA	Molex	171857-0002
P107	1	KK 0.254 4 Pin RA	Molex	171857-0004
P106 P105 P104	3	Four pin	Preci-dip	801-87-004-10-001101
Q201 Q202 Q203 Q204 Q301 Q302 Q303 Q304 Q401 Q402 Q403 Q404	12	CMBT5401	Rectron	CMBT5401
Q205 Q206 Q305 Q306 Q405 Q406	6	BSS84P	Infineon Technologies	BSS84P H6433
R201 R205 R301 R305 R401 R405	6	300Ω	Yageo	RC0402JR-07300RL
R203 R207 R303 R307 R403 R407	6	20 Ω	TE Connectivity	352120RFT
R202 R206 R302 R306 R402 R406	6	150 Ω	Yageo	RC0403RF-07150RP

R204 R208 R209 R211 R304 R308 R309 R311 R404 R408 R409 R411	12	3.9k Ω	Yageo	RC0402JR-073K9L
R210 R212 R310 R312 R410 R412	6	82 Ω	Rohm	ESR10EZPJ820
U201 U202 U301 U302 U401 U402	6	74AHCT1G14	Nexperia	74AHCT1G14GW 125

B.2 Drawing of Phase Shifter Board.

Schematic, layout, and pictures of the phase shifter boards are shown in this section.

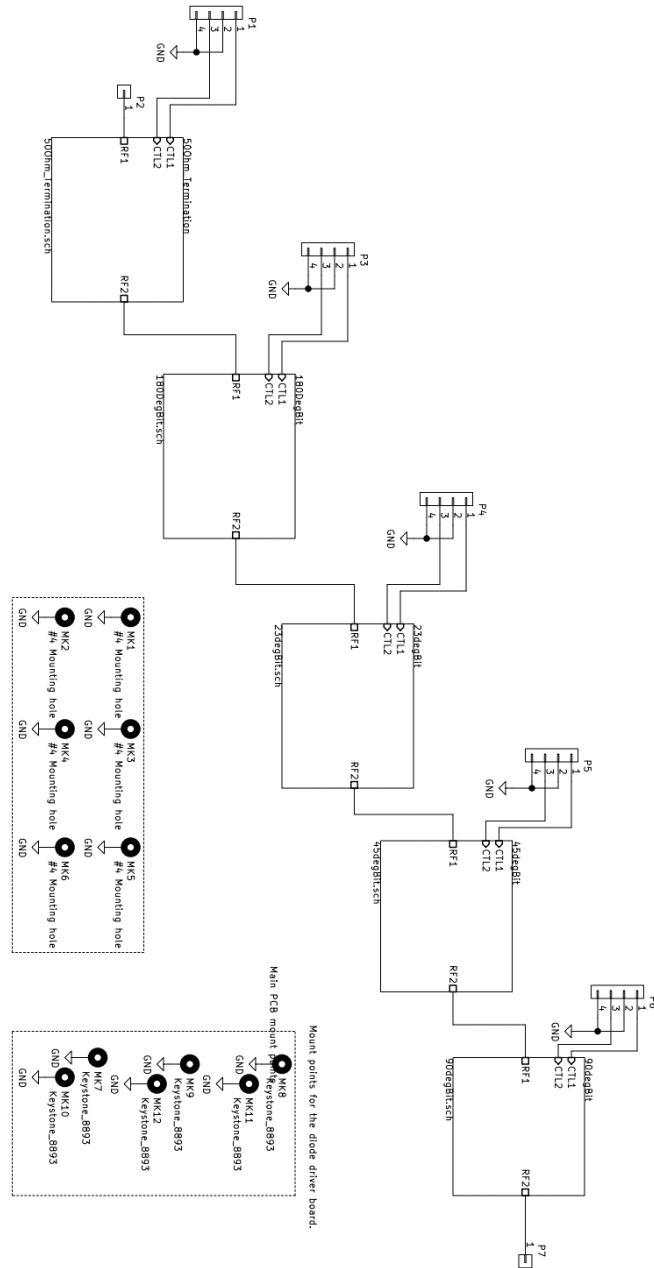


Figure 69. Overview of the phase shifter circuit, which consists of 5 different bits in series.

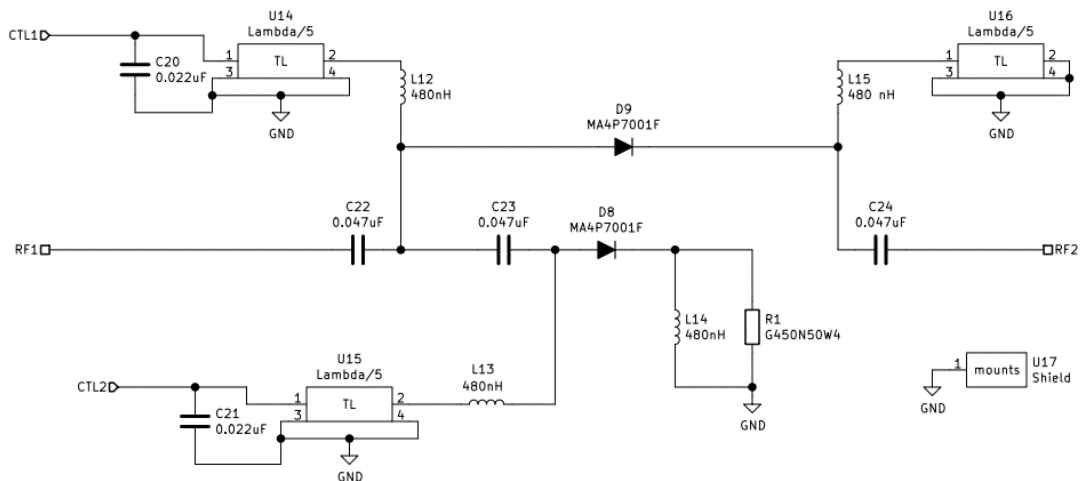


Figure 70. Schematic of 50Ω termination bit.

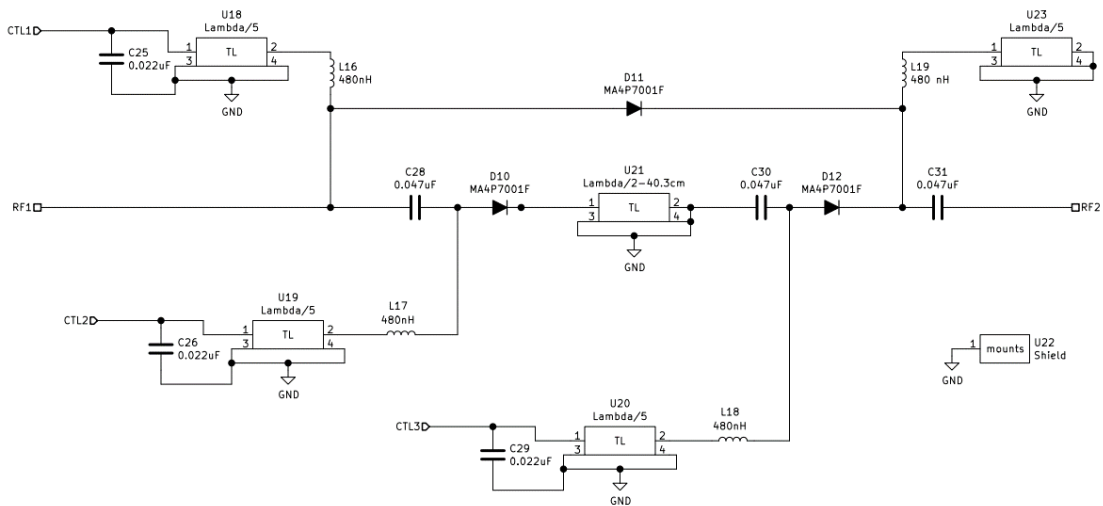


Figure 71. Schematic of 180°-bit.

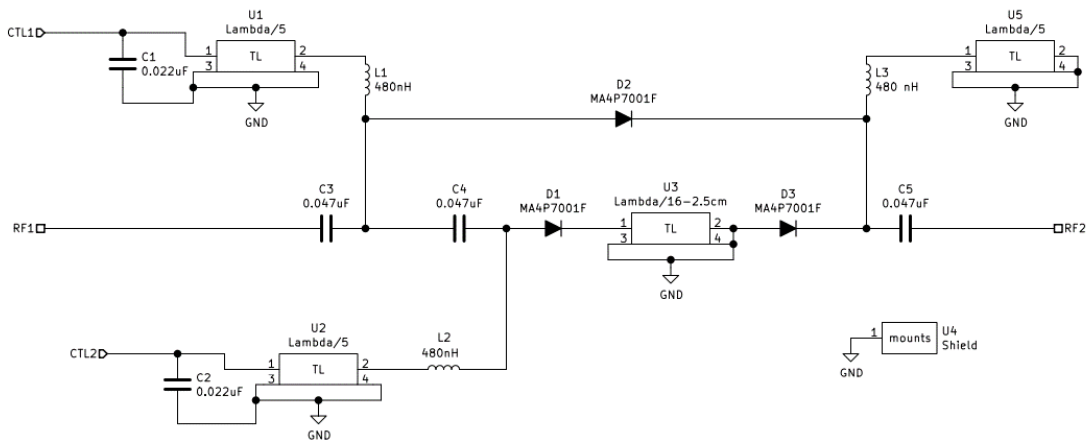


Figure 72. Schematic of 22.5° bit.

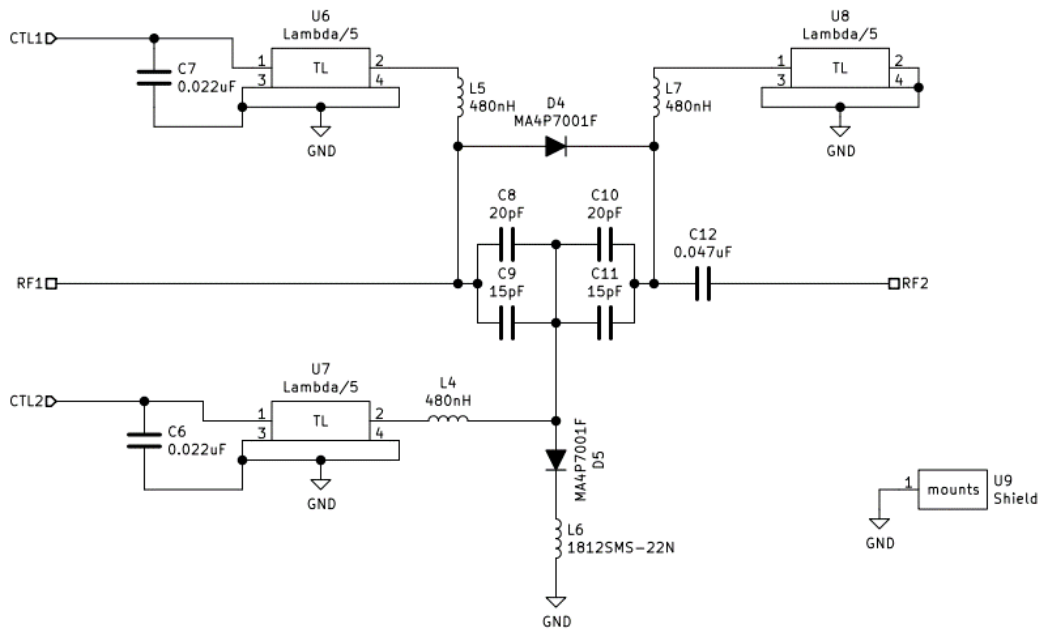


Figure 73. Schematic of 45°-bit.

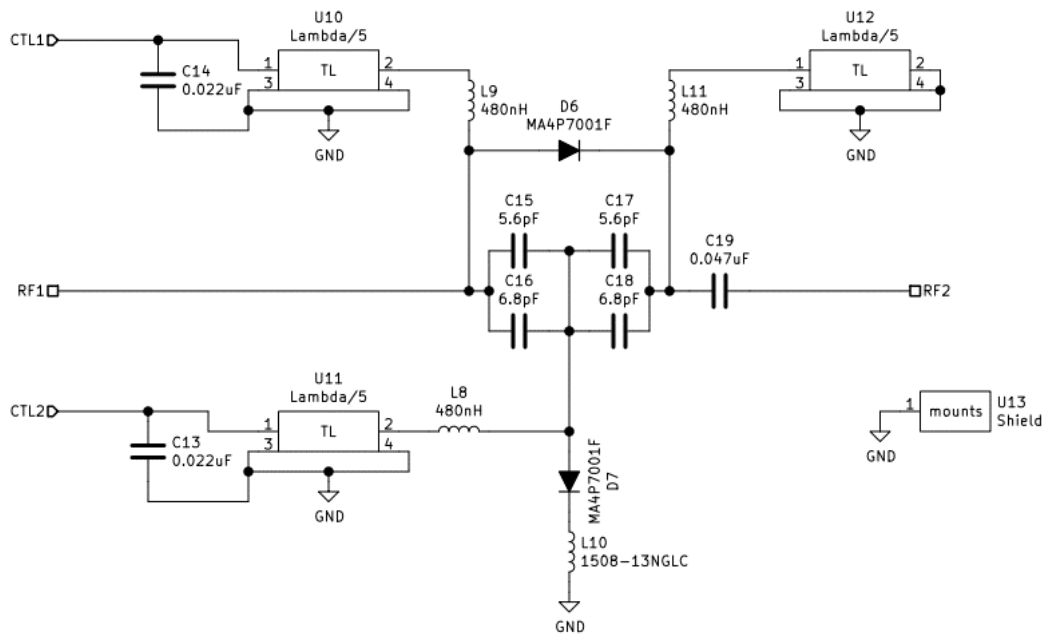


Figure 74. Schematic of 90°-bit.

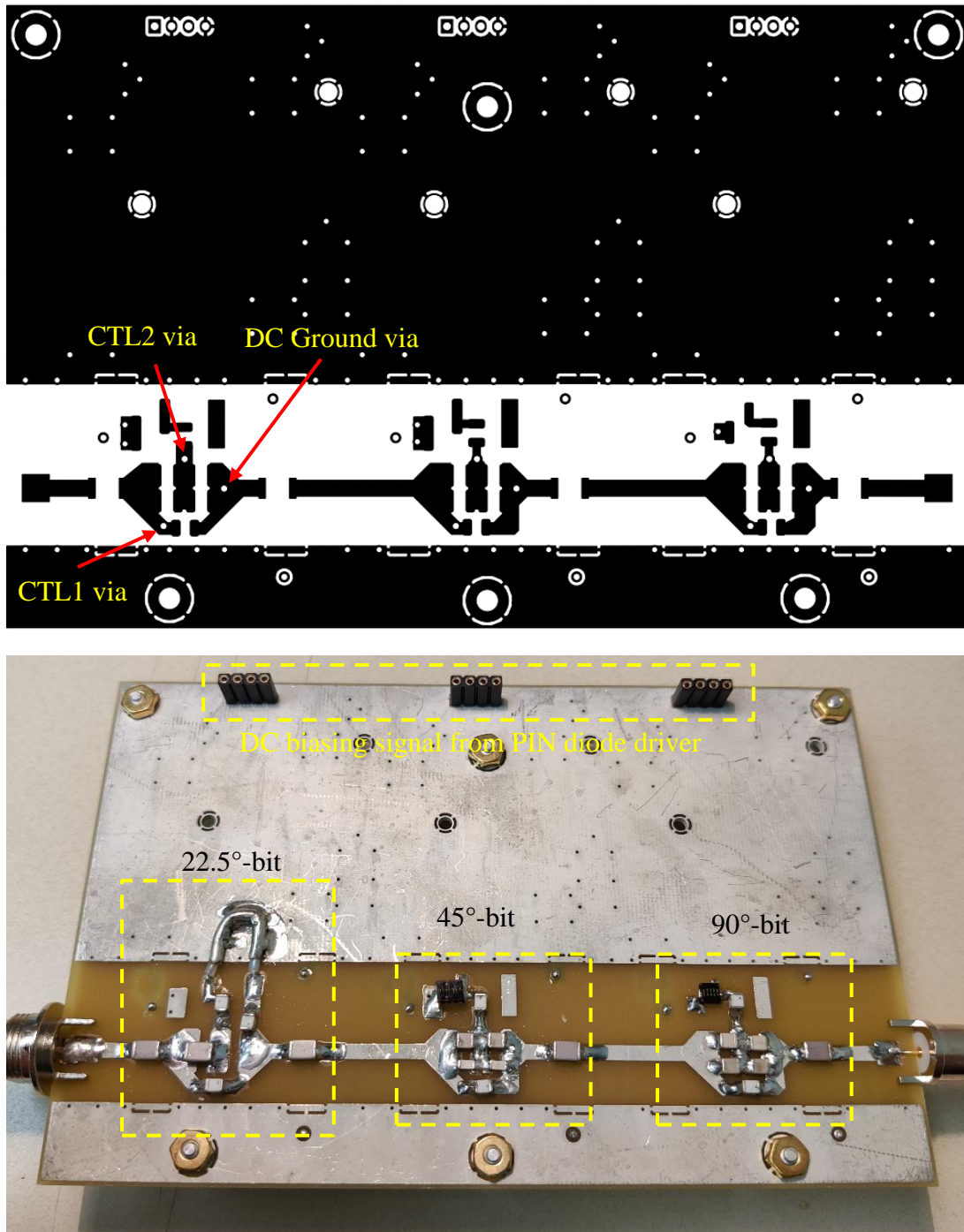


Figure 75. Top view of layout and picture of an assembled board containing 22.5°-bit, 45°-bit, and 90°-bit.

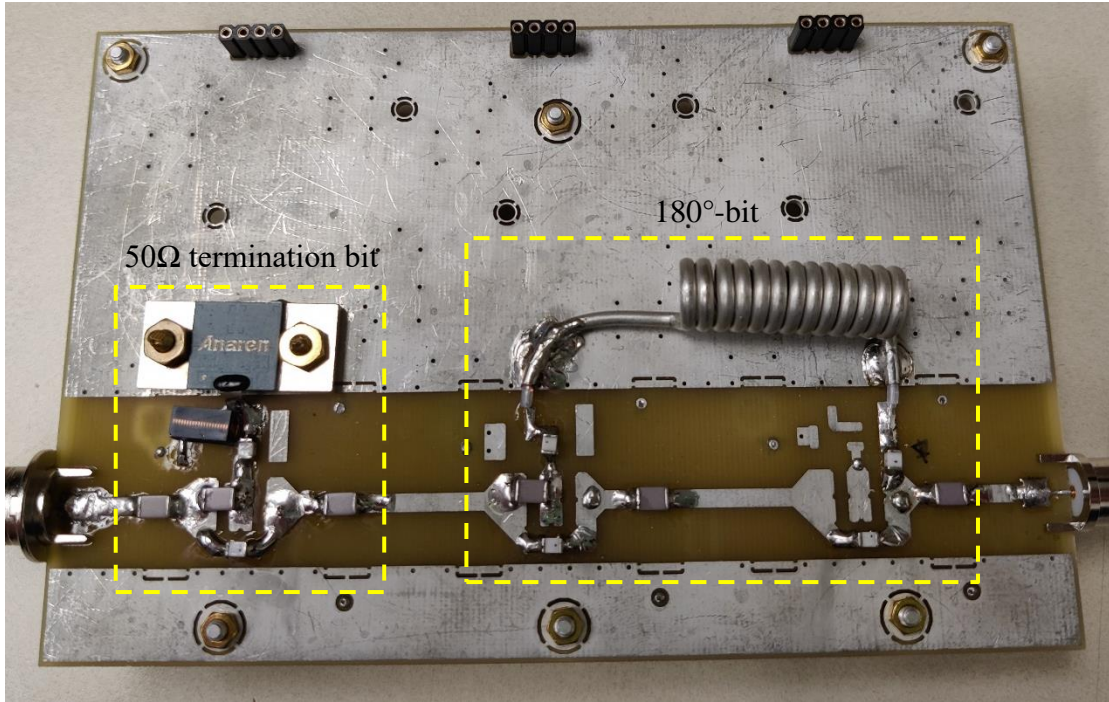


Figure 76. Top view of layout and picture of an assembled board containing 50Ω termination bit and 180°-bit.

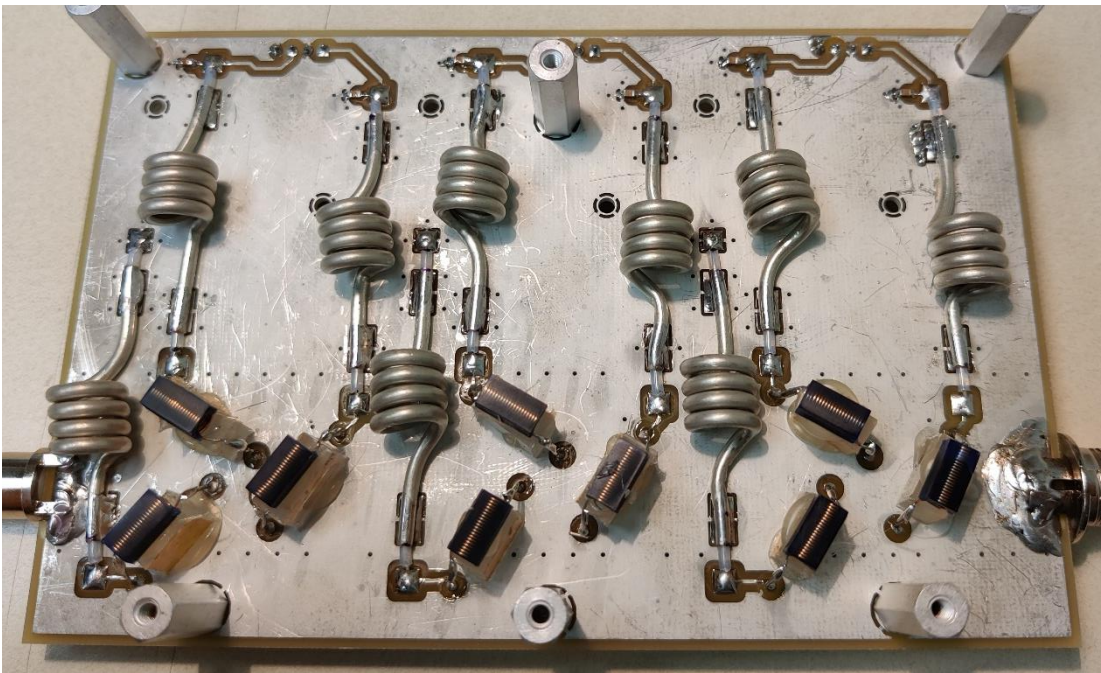
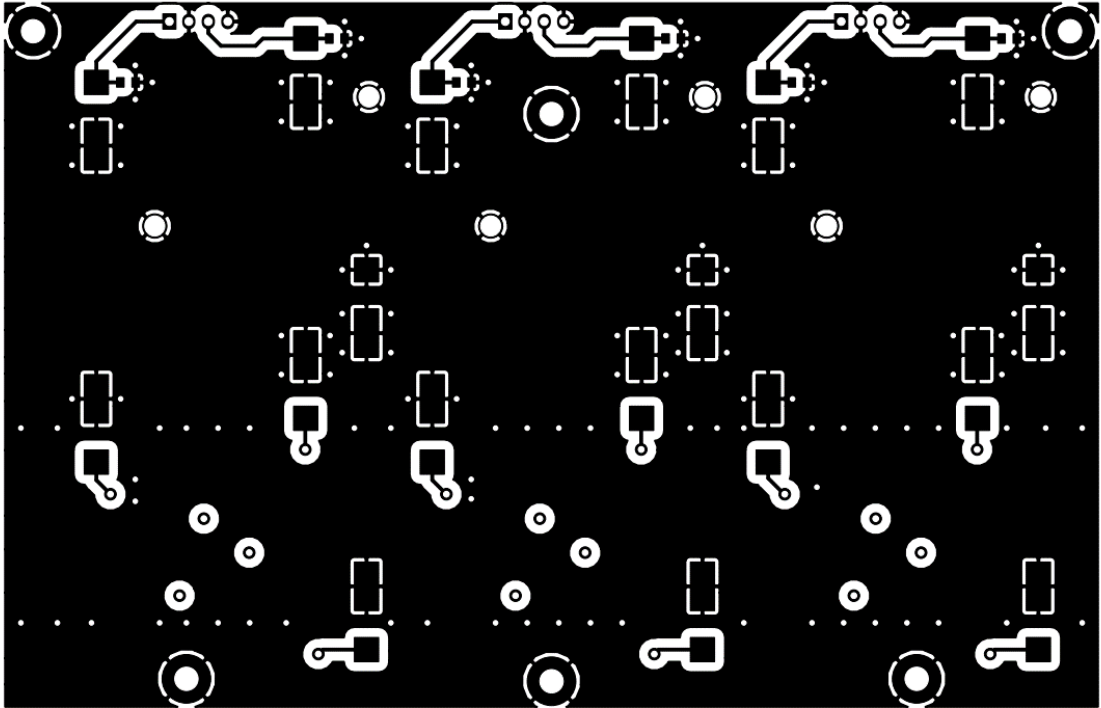


Figure 77. Bottom view of layout and picture of an assembled board.

Table 5. Bill of materials for phase shifter circuit.

Qty	Reference(s)	Value	MFR	MPN
11	C1, C2, C6, C7, C13, C14, C20, C21, C25, C26, C29	0.022uF	Kemet	C0805C223K5RAC7800
11	C3, C4, C5, C12, C19, C22, C23, C24, C28, C30, C31	0.047uF	TDK	CGA8N4NP02W473J230KA
2	C8, C10	20pF	PPI	1111C Series - 1500V
2	C9, C11	15pF	PPI	1111C Series - 1500V
2	C15, C17	5.6pF	PPI	1111C Series - 1500V
2	C16, C18	6.8pF	PPI	1111C Series - 1500V
12	D1, D2, D3, D4, D5, D6, D7, D8, D9, D10, D11, D12	MA4P7001F	MACOM	MA4P7001F-1072-T
17	L1, L2, L3, L4, L5, L7, L8, L9, L11, L12, L13, L14, L15, L16, L17, L18, L19	480nH	Abracon	x
1	L6	1812SMS-22N	CoilCraft	1812SMS-22NJLB
1	L10	1508-13NGLC	CoilCraft	A05TJLB
6	MK1, MK2, MK3, MK4, MK5, MK6	#4 Mounting hole	x	x
6	MK7, MK8, MK9, MK10, MK11, MK12	Keystone_8893	x	x
5	P1, P3, P4, P5, P6	01X04	Würth Electronics	61300411121
2	P2, P7	01X01	Amphenol RF	172117
1	R1	50Ω	Anaren	G450N50W4
16	U1, U2, U5, U6, U7, U8, U10, U11, U12, U14,	Lambda/5	EZ From	EZ-86-CU

	U15, U16, U18, U19, U20, U23			
1	U3	Lambda/16- 2.5cm	EZ From	EZ-86-CU
5	U4, U9, U13, U17, U22	Shield	x	x
1	U21	Lambda/2- 40.3cm	EZ From	EZ-86-CU

APPENDIX C

SUPPLEMENTARY MATERIAL FOR HIGH IMPEDANCE DECOUPLING

PREAMPLIFIER

The MATLAB scripts, including OPA NF analysis, coil decoupling calculation, matching network modeling, etc., are attached here.

C.1 Main Function

```
clear
close all
clc
tic % timer

%% Part 1. Constant & initial Setup
% setup gammas for smith chart
% Nrings = 20; %36
% dfactor = 120; %200
markersize = 4; %4 size of each dot on Smith chart
Cres = 256; % numbers of color scale
Nrings = 36; %36 number of rings on Smith Chart
dfactor = 300; %200

% Admittance Matrix uniformly disturbed around Smith map
Gammas = Gamma_Setup(Nrings,dfactor);

Rf = 200;
Rg = 0.01;

% Measured Impedance of different devices%
%%%%%%%%%%%%%%%%%%%%%%%%%%%%%%%%%%%%%%%%%%%%%%%%%%%%%%%%%%%%%%%%%%%%%%%%
% Impedance measurements are done using Left 4195A, 10MHz to 220MHz,
401 points
% RBW 1kHz, default pwr and Rx attenuation
%%%%%%%%%%%%%%%%%%%%%%%%%%%%%%%%%%%%%%%%%%%%%%%%%%%%%%%%%%%%%%%%%%%%%%%%
% Freq(:,1) is the specific frequency for different points measured in
VNA
% Z(:,3) is the OPA's measured input impedance from 10MHz to 220MHz
% Z(:,5) is the loaded 4cm-coil's measured raw impedance from 10MHz to
220MHz
% There are other data as well but doesn't matter for this study
% case 1: 50ohm load -> 1:4 transformer -> measured impedance
```



```

% case 2: measured impedance <- 1:4 transformer <- 50Ohm load, and so
on
% details are in docs

%frequency index
Freq_27MHZ_Index = 34; %17O 27.1284MHz
Freq_30MHZ_Index = 40; %2H 30.7192 MHz
Freq_50MHZ_Index = 78; %13C, 50.3294MHZ
Freq_53MHZ_Index = 83; %23Na
Freq_81MHZ_Index = 136; %31P, 81.0045MHZ
Freq_188MHZ_Index = 341; %19F, 188.24MHZ
Freq_200MHZ_Index = 363; %1H

for i = 1:10
T = readtable(['Z',num2str(i) , '_3nd.csv'], 'HeaderLines',1);
T = T{:, :};
Freq = T(:,1);
Gammas_Z(:,i) = T(:,2) .* exp(1i*T(:,3)*pi/180) ;
Z(:,i) = gamma2z(Gammas_Z(:,i));
end
Data(1:401,1) = 1;

%% plot Loaded Coil impedance and OPA impedance
i = 5;
figure
SmithPlot2(Z(:,i),Data,256,0,0,"None",3, "NF_Area_Off", "Nuclei_On",0
);
title({'Loaded Coil, Raw Impedance', ' ' })
i = 3;
% Z(:,i) = 50; % if assuming 50 Ohm load of preamp
figure
SmithPlot2(Z(:,i),Data,256,0,0,"None",3, "NF_Area_Off", "Nuclei_On",0
);
title({'Op Amp, Input Impedance ', ' ' })

%% Plot NF vs Rs, single Curve

Rs = linspace(10,10000,10000);
[NFs] = NF_Calculation_LMH6629_NonInverting(Rf,Rg,Rs);
figure
semilogx(Rs, NFs)
title('Calculated OPA Ideal NF vs Source Resistance Rs, Assuming
Rf=200 Rg=10')
xlabel('Rs in Ohm')
ylabel('NF in dB')

stophere=1;
%

%% Plot Gain/NF vs Rf

Rf = linspace(200,10000,1000);

```

```

Rg = 10;
Rs = 50;
[NFs_Rf] = NF_Calculation_LMH6629_NonInverting(Rf,Rg,Rs);
Gain_Rf = 20*log10( 1+(Rf./Rg) ) ;

figure
plot(Rf, NFs_Rf)
ylim([0 5])
title('Calculated OPA NF vs Rf, assuming Rg 100ohm, Rs 500hm')
xlabel('Rf in ohm')
ylabel('NF in dB')
%% Plot Gain/NF vs Rg

Rf = 10000;
Rg = linspace(1,30,100);
Rs = 50;
[NFs_Rg] = NF_Calculation_LMH6629_NonInverting(Rf,Rg,Rs);
Gain_Rg = 20*log10( 1+(Rf./Rg) ) ;

figure
plot(Rg, NFs_Rg)
ylim([0 5])
title('Calculated OPA NF vs Rg, assuming Rg 10kOhm, Rs 500hm')
xlabel('Rg in ohm')
ylabel('NF in dB')

stophere = 1;
%% Part 2.1 Ideal Calculated NF based on Gammas RL
%calculate OPA's NF based on Source Resistance(Rs), Feedback
Resistance(Rf) and
%Shunt Resistance(Rs), in theoretical case (No parasitic capacitance)
Rf = 200;
Rg = 10;

Rs = real( gamma2z(Gammas) );
%Rs is a impedance matrix uniformly disturbed across the smith chart
[NFs] = NF_Calculation_LMH6629_NonInverting(Rf,Rg,Rs);
%Therefore the calculated NFs is also a NF matrix according to the
impedance matrix

Dmax = 3;% plot on smith
Dmin = 0;
figure
SmithPlot( Gammas ,NFs,Cres,Dmax,Dmin,"Higher",markersize)
title({ ['Calculated Ideal NF Area that below ', num2str(Dmax), ' dB'],
' ' })
DATA = NFs;
colorbar('ticks', [0,0.25,0.5,0.75,1], 'TickLabels', ...
{ [ num2str( round(min(DATA),2) ) 'dB' ], [ num2str(
round((min(DATA)+(min(DATA)+Dmax)/2))/2 ,2) ) 'dB' ],...
[ num2str( round((min(DATA)+Dmax)/2),2) ) 'dB' ], [ num2str(
round(((min(DATA)+Dmax)/2)+Dmax)/2,2) ) 'dB' ],...

```

```

    ['>' num2str(Dmax) 'dB' ])

stophere = 1;
%% Part 2.2 Calculate NF Considering input capacitance 4.8 pF for 1H
% calculate OPA's NF, adding the input parasitic caps of ~4.8pF
% Simply by paralling the orgianl source Z with a shunt cap 4.8pF, and
% transform to a new equivelent Z that OPA sees.

% Rf = 200; % resistor values
% Rg = 10;
Z_original = gamma2z(Gammas); % Original source Z for OPA
Z_Cap = 1/(1i*2*pi*Freq(Freq_200MHZ_Index)*4.8e-12); %input parasitic
cap's impedance
R_withCap = 1 ./ ( (1./Z_original) + (1./Z_Cap) );
%this is the equivelent impedance, paralleled from original source Z and
input
%cap
Rs = real( R_withCap ); %take the real part, only resistive part
[NFs_1H] = NF_Calculation_LMH6629_NonInverting(Rf,Rg,Rs);

Dmax = 3;% plot on smith
Dmin = 0;
figure
SmithPlot(Gammas,NFs_1H,Cres,Dmax,Dmin,"Higher",markersize)
% title({ ['1H OPA-NF vs Source Impedance, threshold at ',
num2str(Dmax), ' dB'], ' ' })
title({ '1H OPA-NF vs Source Impedance, considering input parasitic
capacitance ', ' ' })
% colorbar('ticks', [0,0.25,0.5,0.75,1], 'TickLabels', ...
% { [ num2str(min(NFs_1H)) 'dB' ], [ num2str(
(min(NFs_1H)+((min(NFs_1H)+Dmax)/2))/2 ) 'dB' ],...
% [ num2str( ((min(NFs_1H)+Dmax)/2) ) 'dB'],[ num2str(
(((min(NFs_1H)+Dmax)/2)+Dmax)/2 ) 'dB' ],...
% ['>' num2str(Dmax) 'dB' ]})
DATA = NFs_1H;
colorbar('ticks', [0,0.25,0.5,0.75,1], 'TickLabels', ...
% { [ num2str( round(min(DATA),2) ) 'dB' ], [ num2str(
round((min(DATA)+((min(DATA)+Dmax)/2))/2 ,2) ) 'dB' ],...
% [ num2str( round(((min(DATA)+Dmax)/2),2) ) 'dB'],[ num2str(
round(((min(DATA)+Dmax)/2)+Dmax)/2,2) ) 'dB' ],...
% ['>' num2str(Dmax) 'dB' ]})
%
figure
[lines, hsm] = smithchart();
BenchSNR_1H_Measurement_Validation
stophere = 1;
%% Part 2.3 Calculate NF Considering input capacitance 4.8 pF for Na23
% same thing as before, only at 23Na frequency
Rf = 200; % resistor values
Rg = 10;
Z_original = gamma2z(Gammas); % ideal source Z for OPA
Z_Cap = 1/(1i*2*pi*Freq(Freq_53MHZ_Index)*4.8e-12); %input parasitic cap
R_withCap = 1 ./ ( (1./Z_original) + (1./Z_Cap) );

```

```

Rs = real( R_withCap ); %
[NFs_23Na] = NF_Calculation_LMH6629_NonInverting(Rf,Rg,Rs);

Dmax = 3;% plot on smith
Dmin = 0;
% figure
SmithPlot(Gammas,NFs_23Na,Cres,Dmax,Dmin,"Higher",markersize)
title({ ['23Na, With input Cap, NF Area that below ', num2str(Dmax), '
dB'], ' ' })
DATA = NFs_23Na;
colorbar('ticks', [0,0.25,0.5,0.75,1], 'TickLabels', ...
{ [ num2str(min(DATA)) 'dB' ], [ num2str(
(min(DATA)+((min(DATA)+Dmax)/2))/2 ) 'dB' ],...
[ num2str( ((min(DATA)+Dmax)/2) ) 'dB'],[ num2str(
(((min(DATA)+Dmax)/2)+Dmax)/2 ) 'dB' ],...
['>' num2str(Dmax) 'dB' ] })

BenchSNR_23Na_Measurement_Validation
stosphere = 1;

%% Part 3.1 EMBC Paper modelling. (Lambda/4 TL setup)
% % This part is for simulating the 1H OPA setup published in EMBC 2020
% % Setup simply as: Loaded Coil(1H) -> Series Cap -> Lambda/4 TL ->
OPA
% % Series cap is for resonating the coil, Lambda/4 TL then transform
the Z
% % from near-short to near-open, therefore land inside good NF
reagion.
% % Decoupling was achieved by tuning the series cap, off-resonate the
coil
% %%%%%%%%%%%%%%%%%%%%%%%%%%%%%%%%%%%%%%%%%%%%%%%%%%%%%%%%%%%%%%%%%%%%%%%%%
% % This part show the OPA's NF vs matched-to impedance, as well as the
% % coil's decoupling vs matched-to impedance, so that we can clearly
see
% % the trade off between decoupling and NF.
% %%%%%%%%%%%%%%%%%%%%%%%%%%%%%%%%%%%%%%%%%%%%%%%%%%%%%%%%%%%%%%%%%%%%%%%%%
%
% % Here first plot the OPA's NF vs source impedance it see, just like
previous.
% Dmax = 3;% plot on smith
% Dmin = 0;
%
% figure
% SmithPlot(Gammas,NFs_1H,Cres,Dmax,Dmin,"Higher",markersize)
% title({ 'NF vs Matched-to Impedance at 1H 200MHZ', ' ' })
%
% %Here plot the
% f = Freq(Freq_200MHZ_Index);
% Zcoil_1H = Z(Freq_200MHZ_Index,5); % 1+178i;
% Zopa_1H = Z(Freq_200MHZ_Index,3); % 9.5-152i;
%

```

```

% Ztrans = (50^2)./Zopa_1H ;% Transformed Z <- Lambda/4 TL <- OPA's
Impedance
% CAP = 0.1 : 0.01 : 30; % series cap in pF
% Zcap = 1./(1i*2*pi*f*CAP*1e-12) ; %impedance of the series cap
% Ztotal_1 = Zcap+Ztrans; % impedance that coil sees:
% % Total Z <- Series Cap <- Lambda/4 TL <- OPA's Impedance
% Gammas_1 = z2gamma( Ztotal_1 ); % from impedace to admittance, same
thing different form
% %calculate decoupling in dB, give the Coil impedance and total
impedance it sees.
% Decoupling_EMBC = Decoupling_Calculation(Zcoil_1H,Gammas_1);
%
% Ztotal_2 = (50^2)./ (Zcoil_1H+Zcap);
% Gammas_2 = z2gamma(Ztotal_2);
% % Total impedance on the other side, total Z that OPA sees.
%
% Dmax = -14; %threthold of -14dB decoupling
% Dmin = -14;
% figure
%
SmithPlot(Gammas_2,Decoupling_EMBC,Cres,Dmax,Dmin,"2color",markersize);
% title( { ['Z that OPA see, Decoupling, y > ', num2str(Dmax), ' dB', '
and b < ', num2str(Dmax), ' dB'], ' ' } )
% hold on
% %here is to mark the most well-resonating impedance point.
% [M,I] = max(Decoupling_EMBC');
% plot(real( Gammas_2(I)
),imag(Gammas_2(I)),'ro','LineWidth',3,'Color', 'r');
% text(real( Gammas_2(I) )+0.1,imag(Gammas_2(I))+0.1,num2str( gamma2z(
Gammas_2(I) ) ),'Color', 'r');

%% Part 3.2 Same Lambda/4 TL setup modelling for 23Na,
% Zcoil_23Na = Z(Freq_53MHZ_Index,5);
% Zopa_23Na = Z(Freq_53MHZ_Index,3);
%
% Dmax = 3;% plot on smith
% Dmin = 0;
% figure
% SmithPlot(Gammas,NFs_23Na,Cres,Dmax,Dmin,"Higher",markersize)
% title({'NF vs Matched-to Impedance at 23Na 53MHz', ' ' })
% hold on
% f = 53e6;
% Ztrans = (50^2)./Zopa_23Na ;
% CAP = 0.1 : 0.1 : 100; %pF
% Zcap = 1./(1i*2*pi*f*CAP*1e-12) ;
% Ztotal_1 = Zcap+Ztrans;
% Gammas_1 = z2gamma( Ztotal_1 );
% Decoupling_EMBC = Decoupling_Calculation(Zcoil_23Na,Gammas_1);
% Ztotal_2 = (50^2)./ (Zcoil_23Na+Zcap);
% Gammas_2 = z2gamma(Ztotal_2);
%
% Dmax = -14;

```

```

% Dmin = -14;
% figure
%
SmithPlot(Gammas_2,Decoupling_EMBC,Cres,Dmax,Dmin,"2color",markersize);
% title( { ['Z that OPA see, Decoupling, y > ', num2str(Dmax), ' dB', '
and b < ', num2str(Dmax), ' dB'], ' ' } )
% hold on
% [M,I] = max(Decoupling_EMBC');
% plot(real( Gammas_2(I)
),imag(Gammas_2(I)),'ro','LineWidth',3,'Color', 'r');
% text(real( Gammas_2(I) )+0.1,imag(Gammas_2(I))+0.1,num2str( gamma2z(
Gammas_2(I) ) ),'Color', 'r');
%

%% Part 4. Calculating Stability Map
% % S-parameter measured by VNA4195A, 10-220MHz.
% % S-para have be measured in linear |Gamma|/Phase mode#2,
% % VNA Port1 -> Btb Diodos + OPA(Rf100Rg10) <- VNA Port 2
%
% % Read S para matrix
% [Raw_S21,S11,S22,S21,S12] = Read_Sparameter('PwrOn');
% %Calculate Stability Circle, plotted inside this function
% [CL,RL,CS,RS] =
Stability_Circle(Freq,markersize,Cres,Gammas,S11,S22,S21,S12,Freq_200MH
Z_Index);
% % Here add the actual bench measurement to validate the calculatoin
% Stability_Measurement_Validation; %optional
%
%
%
%% Part 5. Calculated Induced Voltage Map for 1H 200MHz using Matlab's
MN design
%
% Z_Coil = Z(Freq_200MHZ_Index,5);
%
% Components_Matrix =
Gamma2MN_pCsC(Z_Coil,Gammas,Freq(Freq_200MHZ_Index));
%
% for vt = 1:size(Gammas,2)
%     if vt == 1028
%         stophere = 1;
%     end
%     [Z_right,Z_left,VI2] = AfterMatching( Freq(Freq_200MHZ_Index),
Z(Freq_200MHZ_Index,5), Z(Freq_200MHZ_Index,3)
,Components_Matrix(:, :, vt));
%     Z_Obs(1,vt) = Z_right;
%     Induced_Voltage(1,vt) = abs(VI2(1,1));
%     Decpl(1,vt) = Decoupling_Calculation(
Z(Freq_200MHZ_Index,5),z2gamma( Z_left ));
%         if Induced_Voltage(1,vt) >= 2.17 && NFs_1H(1,vt)<=1.5 % &&
Decpl(1,vt)<=-14
%             Flag_V_D(1,vt) = 1 ;
%         else

```

```

%             Flag_V_D(1,vt) = 0 ;
%         end
% end
%
% Gammas1 = z2gamma(Z_Obs);
% % induced voltage
% Dmax = 0; % plot on smith
% Dmin = 2.17;
% figure
% SmithPlot(Gammas,abs(
Induced_Voltage),Cres,Dmax,Dmin,"Lower",markersize);
% title({'1H Induced Voltage vs Matched-to impedance, threshold at',
num2str(Dmin), ' ' })
% % DATA = abs( Induced_Voltage);
% % colorbar('ticks', [0,0.25,0.5,0.75,1], 'TickLabels', ...
% %     { ['<' num2str(Dmin) 'V' ], [ num2str( (
Dmin+((max(DATA)+Dmin)/2) )/2 ) 'V' ],...
% %     [ num2str( ((max(DATA)+Dmin)/2) ) 'V'],[ num2str( (
max(DATA)+((max(DATA)+Dmin)/2) )/2 ) 'V' ],...
% %     [ num2str(max(DATA)) 'V' ] })
%
% %Add some induced voltage measurement for validation
% Ind_Voltage_Measurement_Validation;
%
% Dmax = -10; % plot on smith
% Dmin = -10;
% figure
% SmithPlot(Gammas,Decpl,Cres,Dmax,Dmin,"Lower",markersize);
% title({'1H Decoupling vs Matched-to impedance, threshold at',
num2str(Dmin), ' ' })

%% Part 6. Calculated Decoupling Map using LCC Trap circuit for 1H
% % Series cap ranging from 4.5-100pF, Shunt cap ranging from 0-80pF.
% % Z_Coil = Z(Freq_200MHZ_Index,5);
% Z_Coil = 2 + 178i;
% vt = 0; %impedance point count
% vt2 = 0;
% for C1 = linspace((4e-12),(7e-12),200) % logspace(log10(2.5e-
12),log10(6.5e-12),150)
%     for Cm = linspace( 3e-12,20e-12,200)
%
%         Components_Matrix = [
%             [ C1 6 1 20e-12 345e-9];
%             [Cm 1 0 0 0];
%             ];
%         [Z_right,Z_left,VI2] = AfterMatching(
Freq(Freq_200MHZ_Index), Z_Coil, Z(Freq_200MHZ_Index,3)
,Components_Matrix);
%         vt = vt+1;
%         Z_Obs(1,vt) = Z_right;
%         NFs_Here(1,vt) =
NF_Cal_withC(Rf,Rg,Z_right,Freq(Freq_200MHZ_Index),4.8e-12);
%         Induced_Voltage(1,vt) = VI2(1,1);

```

```

%         Induced_Currnet(1,vt) = VI2(2,1);
%         Decpl(1,vt) = Decoupling_Calculation( Z_Coil,z2gamma( Z_left
));
%         if abs(Induced_Voltage(1,vt)) >= 1.5 && Decpl(1,vt)<= -10 &&
NFs_Here(1,vt)<3
%             Flag_V_D(1,vt) = 1 ;
%             vt2 = vt2+1;
%             Value_Store(1,vt2) = C1;
%             Value_Store(2,vt2) = Cm;
%         else
%             Flag_V_D(1,vt) = 0 ;
%         end
%     end
% end
%
% Gammas1 = z2gamma(Z_Obs);
%
% % Decoupling
% Dmax = -10; % plot on smith
% Dmin = -10;
% figure
% SmithPlot(Gammas1,Decpl,Cres,Dmax,Dmin,"Lower",markersize);
% title( { ['1H Decoupling vs Matched-to impedance, dark blue <= ',
num2str(Dmin) , ' dB'], ' ' })
%
% stophere = 1;

%% Part 7. Applying Matching Components
%%Matching Network's matrix is defined here, every type is independent
and
%%can be cascaded.
%%%%%%%%%%%%%%%%%%%%%%%%%%%%%%%%%%%%%%%%%%%%%%%%%%%%%%%%%%%%%%%%%%%%%%%%
% 1st | 2nd | 3rd | 4th | 5th |
% H | 0-L | 0-Series | 0 | 0 |
% F | 1-C | 1-Shunt | 0 | 0 |
% Z Ratio | 2-Tsfr | 2-Tsfr | 0 | 0 |
% Z0 | 3-TL | 3-TL | Length(m) | 0 |
% Ohm | 4-R | 0 | 0 | 0 |
% C1-F | 5-LCC_type1 | 0 | C2-F | L-H |
% C1-F | 6-LCC_Type2 | 0 | C2-F | L-H |
%%%%%%%%%%%%%%%%%%%%%%%%%%%%%%%%%%%%%%%%%%%%%%%%%%%%%%%%%%%%%%%%%%%%%%%%
%%For example, a MN of :
% [ seriec C(5pF) -> Ideal Transformer(1:4) -> shunt C(10pF) ]
% can be defined as:
% Components_Matrix = [
%
%             [ 5e-12 1 0 0 0];
%             [4 2 2 0 0];
%             [ 10e-12 1 1 0 0];
%             ];

%%%%%%%%%%%%%%%%%%%%%%%%%%%%%%%%%%%%%%%%%%%%%%%%%%%%%%%%%%%%%%%%%%%%%%%%
%% Random Notes %%%%%%%%%%%%%%%%%%%%%%%%%%%%%%%%%%%%%%%%%%%%%%%%%%%%%%%%%%%%%%%%%%%%%%%%%
% 0.8255m is one lambda for 200Mhz, assuming Er3.3
% 3.1159m is one lambda for 53MHz,

```



```

% Measured ~25cm is 1/4 lambda for 200MHz
% Measured ~95cm is 1/4 lambda for 53MHz
% Means that calculated Er for our cables are :
% Er = 2.21 for 53MHz, and 2.25 for 200MHz
% Er then is chose to be 2.23 in average
%
% Reference 200MHz, regular 50Ohm MN with 50Ohm load
% 1V source, 2.17V induced on the 50Ohm load.
% Reference 53MHz, regular 50Ohm MN with 50Ohm load
% 1V source, 7.07V induced on the 50Ohm load.
%
% Raw impedance of coil@ 200MHz is 9.21545+178.7i
% which means R of 9.21545 Ohm, L of 0.1422uH
% Raw OPA impedance @200MHz is
% Raw impedance of coil@ 53MHz is 0.249712+32.242i

%% Regular 50 MN for 200MHz two caps
Element_1 = [ 4.99e-12 1 0 0]; %series C
Element_2 = [ 33.62e-12 1 1 0]; %shunt C
Components_Matrix = [
                    Element_1;
                    Element_2;
                    ];

%% Regular 50 MN for 200MHz #2 with three caps
% Element_1 = [ 5.37e-12 1 0 0]; %series C
% Element_2 = [ 15.98e-12 1 1 0]; %shunt C
% Element_3 = [ 14.4e-12 1 0 0]; %series C
% Components_Matrix = [
%
%             Element_1;
%             Element_2;
%             Element_3;
%             ];

%% Regular 50 MN for 53MHz
% Element_1 = [ 104.5e-12 1 0 0]; %series C
% Element_2 = [ 845e-12 1 1 0]; %shunt C
% Components_Matrix = [
%
%             Element_1;
%             Element_2;
%             ];

% % TL1 = [ 50 3 3 0.50]; % 1H 13C and 23Na
%
% TL1 = [ 50 3 3 0.5]; % TL
% % 1.2 for 30MHz
% Element_1 = [ 1 1 0 0]; % dummy series cap
% Tsfr = [6 2 2 0];
% Series_C = [ 9e-12 1 0 0]; %series C 6.8pF
% TL2 = [ 50 3 3 0.48]; % TL 0.44m
% Shunt_R = [100 4 1 0];
% Components_Matrix = [
% %
%             Element_1;

```

```

% %
% %           TL1;
% %           Tsfr;
% %           Shunt_R;
% %           Series_C;
% %           TL2;
% %           ];
%

% %% Trying Resistor, may not be a good idea.
% Element_1 = [ 93e-12 1 0 0]; %series C
%
% % TL1 = [ 50 3 3 0.50]; % 1H 13C and 23Na
%
% TL1 = [ 50 3 3 0.5]; % TL
% % 1.2 for 30MHz
% % Element_1 = [ 1 1 0 0]; % dummy series cap
% Tsfr = [1500 2 2 0];
% Series_C = [ 9e-12 1 0 0]; %series C 6.8pF
% TL2 = [ 50 3 3 0.48]; % TL 0.44m
% Shunt_R = [100 4 1 0];
% Components_Matrix = [
%           Element_1;
% %           TL1;
% %           Tsfr;
% %           Shunt_R;
% %           Series_C;
% %           TL2;
%           ];

% % LCC Trap for 1H/23Na
% LCC = [ 2.6e-12 6 1 20e-12 346e-9]; %LCC type 2
% Series_C = [6e-12 1 0 0 0];
% Components_Matrix = [
% %           LCC;
% %           Series_C;
%           [10e-6 1 0 0 0];
%           ];

% LCC = [ 6e-12 6 1 44.9e-12 90e-9]; %LCC type 2
% Series_C = [6e-12 1 0 0 0];
% Components_Matrix = [
%           LCC;
%           Series_C;
%           ];

[Z_right,Z_left,VI2] = AfterMatching( Freq, (Z(:,5) ), Z(:,3)
,Components_Matrix);

```

```

figure %smith plot need gamma to be horizontally matrix
SmithPlot2(Z_right,Data,256,0,0,"None",3,"NF_Area_On", "Nuclei_On",0);
% title({ 'Z right, impedance OPA that see', ' '})

% figure %smith plot need gamma to be horizontally matrix
% SmithPlot2(Z_left,Data,256,0,0,"None",3,"NF_Area_Off",
"Nuclei_On",0);
% title({ 'Z left, impedance Coil that see', ' '})

V2(:,1) = abs( reshape( VI2(1,1,:) , [401,1,1] ) );
% figure %smith plot need gamma to be horizontally matrix
% SmithPlot2(Z_right,Data,256,0,0,"None",3,"NF_Area_On",
"Nuclei_On_Voltage",V2);
% title({ 'Voltage induced on OPA', ' '})

%% Output NF and Decoupling Numbers

Z_final_OPA_See_1H = Z_right(Freq_200MHZ_Index);
Z_final_OPA_See_23Na = Z_right(Freq_53MHZ_Index);

Z_final_Coil_See_1H = Z_left(Freq_200MHZ_Index);
Z_final_Coil_See_23Na = Z_left(Freq_53MHZ_Index);

Rf = 200; % resistor values
Rg = 10;
Z_original = (Z_final_OPA_See_1H); % ideal source Z for OPA
Z_Cap = 1/(1i*2*pi*Freq(Freq_200MHZ_Index)*4.8e-12); %input parasitic
cap
R_withCap = 1 ./ ( (1./Z_original) + (1./Z_Cap) );
Rs = real( R_withCap ); %
[NFs] = NF_Calculation_LMH6629_NonInverting(Rf,Rg,Rs);
NF_1H_OPA = NFs

Z_original = (Z_final_OPA_See_23Na); % ideal source Z for OPA
Z_Cap = 1/(1i*2*pi*Freq(Freq_200MHZ_Index)*4.8e-12); %input parasitic
cap
R_withCap = 1 ./ ( (1./Z_original) + (1./Z_Cap) );
Rs = real( R_withCap ); %
[NFs] = NF_Calculation_LMH6629_NonInverting(Rf,Rg,Rs);
NF_23_OPA = NFs

%% Calculate Decoupling for 1H
Decoupling_1H = Decoupling_Calculation( Z(Freq_200MHZ_Index,5),z2gamma(
Z_final_Coil_See_1H ) )

%% Calculate Decoupling for 23Na
Decoupling_23Na = Decoupling_Calculation(
Z(Freq_53MHZ_Index,5),z2gamma( Z_final_Coil_See_23Na))

```

```

%% Outputting Voltage inducuede on the OPA

Voltage_1H = V2(Freq_200MHZ_Index)
Voltage_23Na = V2(Freq_53MHZ_Index)

%% timer
toc

% Rf = 200; % resistor values
% Rg = 10;
% Z_original = (1825-1i*691); % ideal source Z for OPA
% Z_Cap = 1/(1i*2*pi*21.25e6*0.01e-12); %input parasitic cap
% R_withCap = 1 ./ ( (1./Z_original) + (1./Z_Cap) );
% Rs = real( R_withCap ); %
% [NFs] = NF_Calculation_LMH6629_NonInverting(Rf,Rg,Rs);
% NF_1H_OPA = NFs
%
%
% % Z_original = (143+1i*336); % ideal source Z for OPA
% % Z_Cap = 1/(1i*2*pi*Freq(Freq_200MHZ_Index)*6.5e-12); %input
parasitic cap
% % R_withCap = 1 ./ ( (1./Z_original) + (1./Z_Cap) );
% % Rs = real( R_withCap ); %
% % [NFs] = NF_Calculation_LMH6629_NonInverting(Rf,Rg,Rs);
% % NF_1H_OPA = NFs
% %
% % Z_original = (7.3+1i*124); % ideal source Z for OPA
% % Z_Cap = 1/(1i*2*pi*Freq(Freq_53MHZ_Index)*6.5e-12); %input parasitic
cap
% % R_withCap = 1 ./ ( (1./Z_original) + (1./Z_Cap) );
% % Rs = real( R_withCap ); %
% % [NFs] = NF_Calculation_LMH6629_NonInverting(Rf,Rg,Rs);
% % NF_23_OPA = NFs

```

C.2 Sub-Functions

```

function [Z_right,Z_left,VI2] = AfterMatching( Freq,
Z_right_initial,Z_left_initial,Components_Matrix)

[row,column] = size(Components_Matrix);
[x,y] = size(Freq);

Z_right = Z_right_initial; % Original Value of Coil's raw impedance
a_inital = ones(2,2,x);

```

```

%% Compute Z_right, impedance that Opamp sees
for i = 1:row
    if Components_Matrix(i,2) == 0 %L
        % 0 for L
        Z_component = 1i*2*pi*Freq * Components_Matrix(i,1);
    elseif Components_Matrix(i,2) == 1 %C
        % 1 for C
        Z_component = 1./ (1i*2*pi*Freq * Components_Matrix(i,1) ) ;
    elseif Components_Matrix(i,2) == 2 %transformer
        Z_component = Components_Matrix(i,1); %impedance ratio
    elseif Components_Matrix(i,2) == 3 %TL
        Z0 = Components_Matrix(i,1); %Z0 of TL
    elseif Components_Matrix(i,2) == 4 % Resistor
        Z_component = zeros(x,1);
        Z_component(:,1) = Components_Matrix(i,1); % R
    elseif Components_Matrix(i,2) == 5 % LC-C Trap( L2C2 parallel,
series C1)
        Z_C1 = 1./ (1i*2*pi*Freq * Components_Matrix(i,1) ) ; % C1
        Z_C2 = 1./ (1i*2*pi*Freq * Components_Matrix(i,4) ) ; % C2
        Z_L2 = 1i*2*pi*Freq * Components_Matrix(i,5); % L2
        Z_component = Z_C1 + 1./ ( (1./Z_C2) + (1./Z_L2) );
    elseif Components_Matrix(i,2) == 6 % LC-C Trap( L2C3 series para
with C1)
        Z_C1 = 1./ (1i*2*pi*Freq * Components_Matrix(i,1) ) ; % C1
        Z_C2 = 1./ (1i*2*pi*Freq * Components_Matrix(i,4) ) ; % C2
        Z_L2 = 1i*2*pi*Freq * Components_Matrix(i,5); % L2
        Z_component = 1./ ( (1./Z_C1) + (1./ (Z_C2+Z_L2)) );
    else
        error('2nd column wrong, L, C, Tfs or TL')
    end

    if Components_Matrix(i,3) == 0 %Series
        % 0 for series
        Z_right = Z_right + Z_component;
        for j = 1:x
            a(:, :, j, i) = [ 1 Z_component(j) ; 0 1 ] ;
        end
    elseif Components_Matrix(i,3) == 1 %shunt
        % 1 for Parallel
        Z_right = 1 ./ ( (1./Z_right) + (1./Z_component) );
        for j = 1:x
            a(:, :, j, i) = [ 1 0 ; 1/Z_component(j) 1 ] ;
        end
    elseif Components_Matrix(i,3) == 2 %transformer
        Z_right = Z_right * Z_component;
        for j = 1:x
            a(:, :, j, i) = [ 1/sqrt(Z_component) 0 ; 0 sqrt(Z_component)
] ;
        end
    elseif Components_Matrix(i,3) == 3% TL
        L_Phy = Components_Matrix(i,4);
        Z_right = TransmissionLine_Z( Z0, L_Phy, Freq, Z_right);

```

```

        for j = 1:x
            Er = 2.23;
            Lambda = 3e8 ./ (Freq(j)*sqrt(Er)); %lambda
            yl = 1i * 2*pi * (L_Phy/Lambda ) ;
            a(:, :, j, i) = [ cosh(yl) Z0*sinh(yl) ; sinh(yl)/Z0 cosh(yl) ]
        ;
        end
    else
        error('3rd column wrong, series, shunt, Tfs or TL')
    end
end

%% compute Z_left, the impedance that Coil sees
Z_left = Z_left_initial; % Original Value
Components_Matrix = flipud(Components_Matrix);
for i = 1:row
    if Components_Matrix(i,2) == 0
        % 0 for L
        Z_component = 1i*2*pi*Freq * Components_Matrix(i,1);
    elseif Components_Matrix(i,2) == 1
        % 1 for C
        Z_component = 1./ ( 1i*2*pi*Freq * Components_Matrix(i,1) ) ;
    elseif Components_Matrix(i,2) == 2
        %transformer
        Z_component = 1 / Components_Matrix(i,1); % inversed here
    elseif Components_Matrix(i,2) == 3
        %TL
        Z0 = Components_Matrix(i,1); %Z0 of TL
    elseif Components_Matrix(i,2) == 4 % Resistor
        Z_component = Components_Matrix(i,1); % R
    elseif Components_Matrix(i,2) == 5 % LC-C Trap( L2C2 parallel,
series C1)
        Z_C1 = 1./ (1i*2*pi*Freq * Components_Matrix(i,1) ) ; % C1
        Z_C2 = 1./ (1i*2*pi*Freq * Components_Matrix(i,4) ) ; % C2
        Z_L2 = 1i*2*pi*Freq * Components_Matrix(i,5); % L2
        Z_component = Z_C1 + 1./ ( (1./Z_C2) + (1./Z_L2) );
    elseif Components_Matrix(i,2) == 6 % LC-C Trap( L2C3 series para
with C1)
        Z_C1 = 1./ (1i*2*pi*Freq * Components_Matrix(i,1) ) ; % C1
        Z_C2 = 1./ (1i*2*pi*Freq * Components_Matrix(i,4) ) ; % C2
        Z_L2 = 1i*2*pi*Freq * Components_Matrix(i,5); % L2
        Z_component = 1./ ( (1./Z_C1) + (1./ (Z_C2+Z_L2)) );
    else
        error('2nd column wrong, L, C, Tfs or TL')
    end

    if Components_Matrix(i,3) == 0
        % 0 for series
        Z_left = Z_left + Z_component;
    elseif Components_Matrix(i,3) == 1
        % 1 for Parallel
        Z_left = 1 ./ ( (1./Z_left) + (1./Z_component) );
    elseif Components_Matrix(i,3) == 2 %transformer

```

```

        Z_left = Z_left * Z_component;
    elseif Components_Matrix(i,3) == 3 % TL
        L_Phy = Components_Matrix(i,4);
        Z_left = TransmissionLine_Z( Z0, L_Phy, Freq, Z_left);
    else
        error('3rd column wrong, series, shunt, Tfs or TL')
    end
end

% find V1 and I1 for abcd matrix calculcation
Vsource= 1;
I1 = Vsource ./ ( Z_right_initial + Z_left );
V1 = I1 .* Z_left;
%Coil's inital impedance and the impedance coil see
% Freq_27MHZ_Index = 34; %17O 27.1284MHz
% Freq_30MHZ_Index = 40; %2H 30.7192 MHz
% Freq_50MHZ_Index = 78; %13C, 50.3294MHZ
% Freq_53MHZ_Index = 83; %23Na
% Freq_81MHZ_Index = 136; %31P, 81.0045MHZ
% Freq_188MHZ_Index = 341; %19F, 188.24MHZ
% Freq_200MHZ_Index = 363; %1H
% Index = [34,40,78,83,136,341,363];
for j = 1:x %freq count
    if row == 1
        a_cascaded(:, :, j) = a(:, :, j, 1);
    else
        a_cascaded(:, :, j) = a(:, :, j, 1);
        for i = 1:(row-1) % elements number count
            a_cascaded(:, :, j) = a_cascaded(:, :, j) * a(:, :, j, i+1);
        end
    end

    if j == 363
        abcd = 1;
    end

    VI1(:, :, j) = [ V1(j) ; I1(j)];
    VI2(:, :, j) = a_cascaded(:, :, j) \ VI1(:, :, j) ;
end

end

function [] = BenchSNR_1H_Measurement_Validation()
%this function add some bench measuremnt to validate the SNR
%Data were acquired late Apr 2021
%I manually match coil to the following impedance to test the SNR.
% SNR, decoupling, output Vpp were measured on bench

%impedance conversion with 40nH inductor at output

```

```

M = readtable(['Bench_Measurement_V3.csv'], 'HeaderLines',1);
M = M{:,:};
[y,x] = size(M);
Dis_R = 0.03;
Dis_I = 0.04;

map = flipud( parula(256) );
% Data = Data;
% Color_Index = ceil( rescale(Data, 1 , 256) );

%% 1H plot in the different color
% figure
% smithchart

SNR = M(:,10)-M(:,11);
SNR_max = max(max(SNR));
snrplot = SNR - SNR_max;
Data = snrplot;

Dmin = -3.5;
Below = Data < Dmin;
Data = (1-Below).* Data + Below.*(Dmin);
Color_Index = ceil( rescale(Data, 1 , 256) );

hold on
for i = 1:y

    Z(i,1) = M(i,7) + 1i*M(i,8);
    Gamma(i,1) = z2gamma(Z(i,1));
    p = Z(i,1);
    plot(real( z2gamma(p)
),imag(z2gamma(p)), 'ro', 'LineWidth',7, 'Color', map(Color_Index(i),:));
%     text(real( z2gamma(p)
)+Dis_R,imag(z2gamma(p))+Dis_I,[num2str(snrplot(i,1)), ' dB'],'Color',
map(Color_Index(i),:));
    text(real( z2gamma(p)
)+Dis_R,imag(z2gamma(p))+Dis_I,[num2str(snrplot(i,1)), ' dB'],'Color',
'k');
end
hold off
% title('1H Bench SNR in dBm vs Source Impedance')
title({ '1H Bench SNR in dBm vs Source Impedance ', ' ' })

figure
smithchart
hold on

for i = 1:y
    Z(i,1) = M(i,7) + 1i*M(i,8);
    Gamma(i,1) = z2gamma(Z(i,1));
    p = Z(i,1);

```



```

        plot(real( z2gamma(p)
),imag(z2gamma(p)), 'ro', 'LineWidth',3, 'Color', 'r');
        text(real( z2gamma(p) )+Dis_R,imag(z2gamma(p))+Dis_I, [num2str(-
43.12-M(i,12)), ' dB'], 'Color', 'r');

end
hold off
title('1H Decoupling in dB as Matched-to Impedance')

%% %% 1H plot all in the same color
%% %% figure
%% %% smithchart
%%
%% SNR = M(:,10)-M(:,11);
%% SNR_max = max(max(SNR));
%%
%% hold on
%% for i = 1:y
%%     Z(i,1) = M(i,7) + 1i*M(i,8);
%%     Gamma(i,1) = z2gamma(Z(i,1));
%%     p = Z(i,1);
%%     plot(real( z2gamma(p)
),imag(z2gamma(p)), 'ro', 'LineWidth',3, 'Color', 'r');
%%     text(real( z2gamma(p)
)+Dis_R,imag(z2gamma(p))+Dis_I, [num2str(M(i,10)-M(i,11)-SNR_max), '
dB'], 'Color', 'r');
%%
%% end
%% hold off
%% title('1H Bench SNR in dBm vs Source Impedance')
%% title({ '1H Bench SNR in dBm vs Source Impedance ', ' ' })
%%
%% figure
%% smithchart
%% hold on
%% for i = 1:y
%%     Z(i,1) = M(i,7) + 1i*M(i,8);
%%     Gamma(i,1) = z2gamma(Z(i,1));
%%     p = Z(i,1);
%%     plot(real( z2gamma(p)
),imag(z2gamma(p)), 'ro', 'LineWidth',3, 'Color', 'r');
%%     text(real( z2gamma(p) )+Dis_R,imag(z2gamma(p))+Dis_I, [num2str(-
43.12-M(i,12)), ' dB'], 'Color', 'r');
%%
%% end
%% hold off
%% title('1H Decoupling in dB as Matched-to Impedance')

```

```

%% Some old measurement

% Dis_R = 0.01;
% Dis_I = 0.01;
%
% hold on
% % #1
% p = 29.1+1i*156.9;
% plot(real( z2gamma(p) ),imag(z2gamma(p)),'ro','LineWidth',3,'Color',
'r');
% text(real( z2gamma(p) )+Dis_R,imag(z2gamma(p))+Dis_I,[" 50.14 dB
"],'Color', 'r');
% % #2
% p = 27.1+1i*193.4;
% plot(real( z2gamma(p) ),imag(z2gamma(p)),'ro','LineWidth',3,'Color',
'r');
% text(real( z2gamma(p) )+Dis_R,imag(z2gamma(p))+Dis_I,[" 52.5 dB
"],'Color', 'r');
% % #3
% p = 27.7+1i*231.4;
% plot(real( z2gamma(p) ),imag(z2gamma(p)),'ro','LineWidth',3,'Color',
'r');
% text(real( z2gamma(p) )+Dis_R,imag(z2gamma(p))+Dis_I,[" 51.31 dB
"],'Color', 'r');
% % #4
% p = 137+1i*489;
% plot(real( z2gamma(p) ),imag(z2gamma(p)),'ro','LineWidth',3,'Color',
'r');
% text(real( z2gamma(p) )+Dis_R,imag(z2gamma(p))+Dis_I,[" 51.05 dB
"],'Color', 'r');
% % #5
% p = 97.7+1i*315.2;
% plot(real( z2gamma(p) ),imag(z2gamma(p)),'ro','LineWidth',3,'Color',
'r');
% text(real( z2gamma(p) )+Dis_R,imag(z2gamma(p))+Dis_I,[" 54.21 dB
"],'Color', 'r');
% % #6
% p = 90.77+1i*255.4;
% plot(real( z2gamma(p) ),imag(z2gamma(p)),'ro','LineWidth',3,'Color',
'r');
% text(real( z2gamma(p) )+Dis_R,imag(z2gamma(p))+Dis_I,[" 55.18 dB
"],'Color', 'r');
% % #7
% p = 90.7+1i*163;
% plot(real( z2gamma(p) ),imag(z2gamma(p)),'ro','LineWidth',3,'Color',
'r');
% text(real( z2gamma(p) )+Dis_R,imag(z2gamma(p))+Dis_I,[" 54 dB
"],'Color', 'r');
% % #8
% p = 87+1i*82.6;
% plot(real( z2gamma(p) ),imag(z2gamma(p)),'ro','LineWidth',3,'Color',
'r');

```

```

% text(real( z2gamma(p) )+Dis_R,imag(z2gamma(p))+Dis_I,[" 54.8 dB
"],'Color', 'r');
% % #9
% p = 84.7+1i*20.8;
% plot(real( z2gamma(p) ),imag(z2gamma(p)),'ro','LineWidth',3,'Color',
'r');
% text(real( z2gamma(p) )+Dis_R,imag(z2gamma(p))+Dis_I,[" 55.71 dB
"],'Color', 'r');
% % #10
% p = 82.3-1i*37.3;
% plot(real( z2gamma(p) ),imag(z2gamma(p)),'ro','LineWidth',3,'Color',
'r');
% text(real( z2gamma(p) )+Dis_R,imag(z2gamma(p))+Dis_I,[" 52.9 dB
"],'Color', 'r');
% % #11
% p = 32.+1i*126.7;
% plot(real( z2gamma(p) ),imag(z2gamma(p)),'ro','LineWidth',3,'Color',
'r');
% text(real( z2gamma(p) )+Dis_R,imag(z2gamma(p))+Dis_I,[" 57.15 dB
"],'Color', 'r');
% % #12
% p = 32.2+1i*64;
% plot(real( z2gamma(p) ),imag(z2gamma(p)),'ro','LineWidth',3,'Color',
'r');
% text(real( z2gamma(p) )+Dis_R,imag(z2gamma(p))+Dis_I,[" 57.26 dB
"],'Color', 'r');
% % #13
% p = 31.3+1i*28.4;
% plot(real( z2gamma(p) ),imag(z2gamma(p)),'ro','LineWidth',3,'Color',
'r');
% text(real( z2gamma(p) )+Dis_R,imag(z2gamma(p))+Dis_I,[" 53.8 dB
"],'Color', 'r');
% % #14
% p = 31.6-1i*3.3;
% plot(real( z2gamma(p) ),imag(z2gamma(p)),'ro','LineWidth',3,'Color',
'r');
% text(real( z2gamma(p) )+Dis_R,imag(z2gamma(p))+Dis_I,[" 55.8 dB
"],'Color', 'r');
% % #15
% p = 32.6-1i*35.1;
% plot(real( z2gamma(p) ),imag(z2gamma(p)),'ro','LineWidth',3,'Color',
'r');
% text(real( z2gamma(p) )+Dis_R,imag(z2gamma(p))+Dis_I,[" 55.2 dB
"],'Color', 'r');
% % #16
% p = 33.1-1i*103;
% plot(real( z2gamma(p) ),imag(z2gamma(p)),'ro','LineWidth',3,'Color',
'r');
% text(real( z2gamma(p) )+Dis_R,imag(z2gamma(p))+Dis_I,[" 54.44 dB
"],'Color', 'r');
% % #17
% p = 35-1i*181;

```

```

% plot(real( z2gamma(p) ),imag(z2gamma(p)),'ro','LineWidth',3,'Color',
'r');
% text(real( z2gamma(p) )+Dis_R,imag(z2gamma(p))+Dis_I,[" 53.6 dB
"],'Color', 'r');
%
```

```

hold off
end
```

```

function [] = BenchSNR_23Na_Measurement_Validation()
%this function add some bench measurement to validate the SNR
%Data were acquired late Apr 2021
%I manually match coil to the following impedance to test the SNR.
% SNR, decoupling, output Vpp were measured on bench
```

```

%%impedance conversion with 40nH inductor at output
```

```

M = readtable(['Bench_Measurement_V3.csv'], 'HeaderLines',1);
M = M{:,:};
[y,x] = size(M);
Dis_R = 0.02;
Dis_I = 0.03;
%%
```

```

figure
smithchart
hold on
```

```

map = flipud( parula(256) );
```

```

SNR = M(:,4)-M(:,5);
SNR_max = max(max(SNR));
snrplot = SNR - SNR_max;
Data = snrplot;
```

```

Dmin = -3.5;
Below = Data < Dmin;
Data = (1-Below).* Data + Below.*(Dmin);
Color_Index = ceil( rescale(Data, 1 , 256) );
```

```

for i = 1:y
    Z(i,1) = M(i,1) + 1i*M(i,2);
    if Z(i,1) == 0
        continue
    end
end
```

```

        end
        Gamma(i,1) = z2gamma(Z(i,1));
        p = Z(i,1);
        plot(real( z2gamma(p)
),imag(z2gamma(p)), 'ro', 'LineWidth',3, 'Color', map(Color_Index(i),:));
        text(real( z2gamma(p)
)+Dis_R,imag(z2gamma(p))+Dis_I,[num2str(snrplot(i,1)), ' dB'],'Color',
'K');

end
hold off
title('23Na SNR Level in dBm as Matched-to Impedance')

figure
smithchart
hold on
for i = 1:y
    Z(i,1) = M(i,1) + 1i*M(i,2);
    if Z(i,1) == 0
        continue
    end
    Gamma(i,1) = z2gamma(Z(i,1));
    p = Z(i,1);
    plot(real( z2gamma(p)
),imag(z2gamma(p)), 'ro', 'LineWidth',3, 'Color', 'r');
    text(real( z2gamma(p) )+Dis_R,imag(z2gamma(p))+Dis_I,[num2str(-
39.3-M(i,6)), ' dB'],'Color', 'r');

end
hold off
title('23Na Decoupling in dB as Matched-to Impedance')
%% Some old measurement data
% Dis_R = 0.01;
% Dis_I = 0.01;
%
% hold on
% % #1
% p = 108.1+1i*67.6;
% plot(real( z2gamma(p) ),imag(z2gamma(p)), 'ro', 'LineWidth',3, 'Color',
'r');
% text(real( z2gamma(p) )+Dis_R,imag(z2gamma(p))+Dis_I,[" 53.71 dB
"], 'Color', 'r');
% % #2
% p = 114.3+1i*200.1;
% plot(real( z2gamma(p) ),imag(z2gamma(p)), 'ro', 'LineWidth',3, 'Color',
'r');
% text(real( z2gamma(p) )+Dis_R,imag(z2gamma(p))+Dis_I,[" 52.52 dB
"], 'Color', 'r');
% % #3
% p = 116.7+1i*311;
% plot(real( z2gamma(p) ),imag(z2gamma(p)), 'ro', 'LineWidth',3, 'Color',
'r');

```

```

% text(real( z2gamma(p) )+Dis_R,imag(z2gamma(p))+Dis_I,[" 51.17 dB
"],'Color', 'r');
% % #4
% p = 271 +1i*502;
% plot(real( z2gamma(p) ),imag(z2gamma(p)),'ro','LineWidth',3,'Color',
'r');
% text(real( z2gamma(p) )+Dis_R,imag(z2gamma(p))+Dis_I,[" 50.7 dB
"],'Color', 'r');
% % #5
% p = 218+1i*156;
% plot(real( z2gamma(p) ),imag(z2gamma(p)),'ro','LineWidth',3,'Color',
'r');
% text(real( z2gamma(p) )+Dis_R,imag(z2gamma(p))+Dis_I,[" 52.39 dB
"],'Color', 'r');
% % #6
% p = 210+1i*8.6;
% plot(real( z2gamma(p) ),imag(z2gamma(p)),'ro','LineWidth',3,'Color',
'r');
% text(real( z2gamma(p) )+Dis_R,imag(z2gamma(p))+Dis_I,[" 52.24 dB
"],'Color', 'r');
% % #7
% p = 211-1i*262;
% plot(real( z2gamma(p) ),imag(z2gamma(p)),'ro','LineWidth',3,'Color',
'r');
% text(real( z2gamma(p) )+Dis_R,imag(z2gamma(p))+Dis_I,[" 52.72 dB
"],'Color', 'r');
% % #8
% p = 196-1i*490;
% plot(real( z2gamma(p) ),imag(z2gamma(p)),'ro','LineWidth',3,'Color',
'r');
% text(real( z2gamma(p) )+Dis_R,imag(z2gamma(p))+Dis_I,[" 54.3 dB
"],'Color', 'r');
% % #9
% p = 185-1i*670;
% plot(real( z2gamma(p) ),imag(z2gamma(p)),'ro','LineWidth',3,'Color',
'r');
% text(real( z2gamma(p) )+Dis_R,imag(z2gamma(p))+Dis_I,[" 53.72 dB
"],'Color', 'r');
% % #10
% p = 241-1i*770;
% plot(real( z2gamma(p) ),imag(z2gamma(p)),'ro','LineWidth',3,'Color',
'r');
% text(real( z2gamma(p) )+Dis_R,imag(z2gamma(p))+Dis_I,[" 54.56 dB
"],'Color', 'r');
% % #11
% p = 80.1-1i*87;
% plot(real( z2gamma(p) ),imag(z2gamma(p)),'ro','LineWidth',3,'Color',
'r');
% text(real( z2gamma(p) )+Dis_R,imag(z2gamma(p))+Dis_I,[" 52.94 dB
"],'Color', 'r');
% % #12
% p = 80-1i*284;

```

```

% plot(real( z2gamma(p) ),imag(z2gamma(p)),'ro','LineWidth',3,'Color',
'r');
% text(real( z2gamma(p) )+Dis_R,imag(z2gamma(p))+Dis_I,[" 53.05 dB
"],'Color', 'r');
% text(real( z2gamma(p) )+Dis_R,imag(z2gamma(p))+Dis_I,[" 52.94 dB
"],'Color', 'r');
% % #13
% p = 79.4-1i*400;
% plot(real( z2gamma(p) ),imag(z2gamma(p)),'ro','LineWidth',3,'Color',
'r');
% text(real( z2gamma(p) )+Dis_R,imag(z2gamma(p))+Dis_I,[" 53.5 dB
"],'Color', 'r');
% % #14
% p = 70.3-1i*505;
% plot(real( z2gamma(p) ),imag(z2gamma(p)),'ro','LineWidth',3,'Color',
'r');
% text(real( z2gamma(p) )+Dis_R,imag(z2gamma(p))+Dis_I,[" 55.0 dB
"],'Color', 'r');
% % #15
% p = 78-1i*606;
% plot(real( z2gamma(p) ),imag(z2gamma(p)),'ro','LineWidth',3,'Color',
'r');
% text(real( z2gamma(p) )+Dis_R,imag(z2gamma(p))+Dis_I,[" 55.2 dB
"],'Color', 'r');
% % #16
% p = 61-1i*840;
% plot(real( z2gamma(p) ),imag(z2gamma(p)),'ro','LineWidth',3,'Color',
'r');
% text(real( z2gamma(p) )+Dis_R,imag(z2gamma(p))+Dis_I,[" 55.4 dB
"],'Color', 'r');
% % #17
% p = 52-1i*1055;
% plot(real( z2gamma(p) ),imag(z2gamma(p)),'ro','LineWidth',3,'Color',
'r');
% text(real( z2gamma(p) )+Dis_R,imag(z2gamma(p))+Dis_I,[" 55.0 dB
"],'Color', 'r');
%
%
% hold off

```

end

```
function [Ds] = Decoupling_Calculation(Zcoil,Gammas)
```

```

Zconv = conj(Zcoil);
Iconv = 1/(Zcoil + Zconv);

```

```

% Calculate decoupling
Zc = gamma2z(Gammas);

% Zs = 50^2./Zs;

Is = 1./(Zcoil + Zc);
Ds = 20*log10(abs(Is)/Iconv);

end

function [Gammas] = Gamma_Setup(Nrings,dfactor)

mags = linspace(1/Nrings,0.9999,Nrings);

Gammas = (0);

for ring = 1:Nrings
    Nangles = ceil(mags(ring)*dfactor);
    angles = linspace(0,2*pi-2*pi/Nangles,Nangles);
    for angle = 1:Nangles
        Gammas(end+1) = mags(ring)*exp(1i*angles(angle));
    end
end

end

function [Component_Matrix] = Gamma2MN(Z_Source, Gammas,Frequency)

%%%%%%%%%%%%%%%%%%%%%%%%%%%%%%%%%%%%%%%%%%%%%%%%%%%%%%%%%%%%%%%%%%%%%%%%
% 1st | 2nd | 3rd | 4th |
% H | L-0 | Series-0 | 0 |
% F | C-1 | Shunt-1 | 0 |
% Z Ratio | Tsfr-2 | Tsfr-2 | 0 |
% Z0 | TL-3 | TL-3 | Length(m) |
% Ohm | R-4 | | |
%%%%%%%%%%%%%%%%%%%%%%%%%%%%%%%%%%%%%%%%%%%%%%%%%%%%%%%%%%%%%%%%%%%%%%%%

Gammas_conj = conj(Gammas);
Z_Conj = gamma2z(Gammas_conj);
[row,column] = size(Gammas_conj);

% parfor i = 1: column
for i = 1: column

    mnobj =
    matchingnetwork('SourceImpedance',Z_Source,'LoadImpedance',...

```



```

        Z_Conj(i), 'CenterFrequency', Frequency, 'Components', 2);
[circuit_list, performance] = circuitDescriptions(mnobj);
MN = table2array(circuit_list);
%   MN(:,1) = [];

% here convert 1st element to format to mine
if MN(1,1) == "Series C"
    Temp1(1,:,i) = [
                                str2num(MN(1,2)) 1 0 0;
                                ];
elseif MN(1,1) == "Shunt C"
    Temp1(1,:,i) = [
                                str2num(MN(1,2)) 1 1 0;
                                ];
elseif MN(1,1) == "Series L"
    Temp1(1,:,i) = [
                                str2num(MN(1,2)) 0 0 0;
                                ];
elseif MN(1,1) == "Shunt L"
    Temp1(1,:,i) = [
                                str2num(MN(1,2)) 0 1 0;
                                ];
else
    error('Gamma2MN, something wrong, 1st element')
end

% here convert 2st element to format to mine
if MN(1,3) == "Series C"
    Temp2(1,:,i) = [
                                str2num(MN(1,4)) 1 0 0;
                                ];
elseif MN(1,3) == "Shunt C"
    Temp2(1,:,i) = [
                                str2num(MN(1,4)) 1 1 0;
                                ];
elseif MN(1,3) == "Series L"
    Temp2(1,:,i) = [
                                str2num(MN(1,4)) 0 0 0;
                                ];
elseif MN(1,3) == "Shunt L"
    Temp2(1,:,i) = [
                                str2num(MN(1,4)) 0 1 0;
                                ];
else
    error('Gamma2MN, something wrong, 2nd element')
end

end
Component_Matrix(1,::) = Temp1;
Component_Matrix(2,::) = Temp2;
end

```

```

function [Component_Matrix] = Gamma2MN_pCsC(Z_Source, Gammas, Frequency)

%%%%%%%%%%%%%%%%%%%%%%%%%%%%%%%%%%%%%%%%%%%%%%%%%%%%%%%%%%%%%%%%%%%%%%%%
% 1st | 2nd | 3rd | 4th |
% H | L-0 | Series-0 | 0 |
% F | C-1 | Shunt-1 | 0 |
% Z Ratio | Tsfr-2 | Tsfr-2 | 0 |
% Z0 | TL-3 | TL-3 | Length(m) |
% Ohm | R-4 | | |
%%%%%%%%%%%%%%%%%%%%%%%%%%%%%%%%%%%%%%%%%%%%%%%%%%%%%%%%%%%%%%%%%%%%%%%%

Gammas_conj = conj(Gammas);
Z_Conj = gamma2z(Gammas_conj);
[row,column] = size(Gammas_conj);

% parfor i = 1: column
for i = 1: column

    mobj =
    matchingnetwork('SourceImpedance', Z_Source, 'LoadImpedance', ...
        Z_Conj(i), 'CenterFrequency', Frequency, 'Components', 2);
    [circuit_list, performance] = circuitDescriptions(mobj);
    MN = table2array(circuit_list);
    % MN(:,1) = [];

    % here convert 1st element to format to mine
    % if MN(2,1) == "Series C"
    % Temp1(1,:,i) = [
    %
    % str2num(MN(1,2)) 1 0 0;
    % ];
    % if MN(2,1) == "Shunt C"
    % Temp1(1,:,i) = [
    %
    % str2num(MN(1,2)) 1 1 0;
    % ];
    % elseif MN(2,1) == "Series L"
    % Temp1(1,:,i) = [
    %
    % str2num(MN(1,2)) 0 0 0;
    % ];
    % elseif MN(2,1) == "Shunt L"
    % Temp1(1,:,i) = [
    %
    % str2num(MN(1,2)) 0 1 0;
    % ];
    % else
    % error('Gamma2MN, something wrong, 1st element')
    % Temp1(1,:,i) = [
    %
    % 0.001e-12 1 1 0;
    % ];
end

```

```

% here convert 2st element to format to mine
if MN(2,3) == "Series C"
    Temp2(1,:,i) = [
                                str2num(MN(1,4)) 1 0 0;
                                ];
% elseif MN(2,3) == "Shunt C"
%     Temp2(1,:,i) = [
%                                     str2num(MN(1,4)) 1 1 0;
%                                     ];
% elseif MN(2,3) == "Series L"
%     Temp2(1,:,i) = [
%                                     str2num(MN(1,4)) 0 0 0;
%                                     ];
% elseif MN(2,3) == "Shunt L"
%     Temp2(1,:,i) = [
%                                     str2num(MN(1,4)) 0 1 0;
%                                     ];
else
%     error('Gamma2MN, something wrong, 2nd element')
    Temp2(1,:,i) = [
                                10e-6 1 0 0;
                                ];
end

end

Component_Matrix(1,::) = Temp1;
Component_Matrix(2,::) = Temp2;
end

close all
clear all
clc

F_1H = 200e6;
F_23Na = 53e6;
Zcoil_1H = 4 + 1i*126;
Zcoil_23Na = 0.1 + 1i*37;

% calculated individual NF and Decoupling
Rf = 100; % resistor values
Rg = 10;
Z_original = 126.3+1i*139.4; % ideal source Z for OPA
Z_Cap = 1/(1i*2*pi*F_1H*4.8e-12); %input parasitic cap
R_withCap = 1 ./ ( (1./Z_original) + (1./Z_Cap) );
Rs = real( R_withCap ); %
[NFs] = NF_Calculation_LMH6629_NonInverting(Rf,Rg,Rs);
NF_1H_OPA = NFs

```

```

Z_original = 169.69+1i*61.5; % ideal source Z for OPA
Z_Cap = 1/(1i*2*pi*F_23Na*4.8e-12); %input parasitic cap
R_withCap = 1 ./ ( (1./Z_original) + (1./Z_Cap) );
Rs = real( R_withCap ); %
[NFs] = NF_Calculation_LMH6629_NonInverting(Rf,Rg,Rs);
NF_23_OPA = NFs

%% Calculate Decoupling for 1H
Decoupling_1H = Decoupling_Calculation(Zcoil_1H,14.8-1i*118.2)

%% Calculate Decoupling for 23Na
Decoupling_23Na = Decoupling_Calculation(Zcoil_23Na,1.04-1i*31.07)

function [Z_out] = Matching( Freq, Z_in,Components_Matrix)

[row,column] = size(Components_Matrix);

Z_out = Z_in; % Original Value
for i = 1:row
    if Components_Matrix(i,2) == 0
        % 0 for L
        Z_component = 1i*2*pi*Freq * Components_Matrix(i,1);
    elseif Components_Matrix(i,2) == 1
        % 1 for C
        Z_component = 1./1i*2*pi*Freq * Components_Matrix(i,1);
    end

    if Components_Matrix(i,3) == 0
        % 0 for series
        Z_out = Z_out + Z_component;
    elseif Components_Matrix(i,3) == 1
        % 1 for Parallel
        Z_out = 1 ./ ( (1./Z_out) + (1./Z_component) );
    end
end

end

function [NFs_1H] = NF_Cal_withC(Rf,Rg,Z_original,Frequency,Cap)

% Rf = 100; % resistor values

```

```

% Rg = 10;
% Z_original = gamma2z(Gammas); % ideal source Z for OPA
Z_Cap = 1/(1i*2*pi*Frequency*Cap); %input parasitic cap
R_withCap = 1 ./ ( (1./Z_original) + (1./Z_Cap) );
Rs = real( R_withCap ); %
[NFs_1H] = NF_Calculation_LMH6629_NonInverting(Rf,Rg,Rs);

```

```
end
```

```

function [NF] = NF_Calculation_LMH6629_NonInverting(Rf,Rg,R_s)
% NF of a non-inverting OPA is calculated based on 3 resistors value:
% Source Resistance(Rs), Feedback Resistance(Rf) and Shunt
Resistance(Rg)
% Equation are all come from TI's document :
%
https://www.ti.com/lit/an/slyt094/slyt094.pdf?ts=1618261747981&ref\_url=
https%253A%252F%252Fwww.google.com%252F
% R_s = 10:1:10e3;
% [A,B] = size(R_s);

k=1.38e-23;
T=300;
G = (Rf./Rg) + 1;
% Rf = 100;
% Rg = Rf/(G-1);
Req = 1./ ( (1./Rf) + (1./Rg) );
BW_3dB= 300e6;

en = 0.69e-9;
in = 2.6e-12 ;

%% Broadband Noise Component RMS:
BWn = 1.57 * BW_3dB ;
Enbb = en*sqrt(BWn) ;

%% 1/f Noise Component RMS:
Enormal = 1.3e-9 * sqrt(0.1);
Eflicker = Enormal*sqrt(log(BWn/0.1));

%% Total op-amp Voltage noise referred to the input RMS:
En_v = sqrt(Enbb^2+Eflicker^2);

%% Translating Current to Voltage Spectral Density:
en_i = in * (Req+R_s);

%% Convert Spec density to RMS
En_i = en_i * sqrt(BWn);

```

```

%% Resistor Thermol Noise RMS
En_r = sqrt(4*k*T*Req*BWn);

%% Total Noise RTI RMS:
Ent_in = sqrt(En_v.^2+En_i.^2+En_r.^2);

%% Total Noise RTO RMS:
Ent_out = Ent_in.*G;

%% Convert RMS to PP:
Ent_out_pp = Ent_out*6;

%% Source impedance Noise RMS:
% R_s = 10:10:5e3;
En_r_s = sqrt(4*k*T*R_s*BWn);

%% NF vs Source resistance

NF = 10*log10(1+ (Ent_in./En_r_s).^2 );

%% Ploting

% En_v_matrix(1,1:B) = En_v;
% En_r_matrix(1,1:B) = En_r;
%
% En_in_total = sqrt(Ent_in.^2+En_r_s.^2);
%
%
% figure
% hold on
% semilogx(R_s,En_v_matrix*1e6)
% semilogx(R_s,En_i*1e6)
% semilogx(R_s,En_r_matrix*1e6)
% semilogx(R_s,Ent_in*1e6)
% semilogx(R_s,En_r_s*1e6)
% semilogx(R_s,En_in_total*1e6)
% legend('Opa voltage noise','Opa current noise','Opa resistor
noise','Opa Total Noise','Source Noise','total noise')
% title('Input referred Noise voltage level for different source')
% xlabel('Source Resistor in Ohm')
% ylabel('Noise Voltage in uV, BW-471MHz')
% hold off
%
% figure
%
% semilogx(R_s,NF,'LineWidth',2)
% title('Calculated Noise Figure of OPA vs Different Source
Resistance')
% xlabel('Source Resistance in Ohm')
% ylabel('NF in dB')
% grid on

```

```
end
```

```
function [Z] = Parallel(Z1,Z2)
```

```
Z = 1./ ( (1./Z1) + (1./Z2) );
```

```
end
```

```
function Z = pointsToSurf(x,y,z)
```

```
% This function is made to create smooth surfaces from individual  
scattered
```

```
% points
```

```
% x, y, z, are the inputs in their respective axes
```

```
%% Todo
```

```
%
```

```
%% Robustness check
```

```
% Send error messages for non-vector quantities
```

```
% Send error messages for non equal sizes
```

```
nx = size(x); ny = size(y); nz = size(z);
```

```
cond_vectors = (min(nx)==1 && min(ny)==1 && min(nz)==1);
```

```
cond_sizes = (max(nx)==max(ny) && max(ny)==max(nz) &&
```

```
max(nz)==max(nx));
```

```
if ~cond_vectors
```

```
    disp('All the inputs should be vectors');
```

```
end
```

```
if ~cond_sizes
```

```
    disp('All the inputs should have same maximum size');
```

```
end
```

```
%% Actual code
```

```
% Converting all inputs to uniform column vector
```

```
x = x(:); y = y(:); z = z(:);
```

```
if cond_vectors && cond_sizes
```

```

n = 200;
%n = Number of points desired, I have put 100 to optimize between
speed and accuracy

x_edge=linspace(floor(min(x)),ceil(max(x)),n);
y_edge=linspace(floor(min(y)),ceil(max(y)),n);

[X,Y]=meshgrid(x_edge,y_edge);
Z=griddata(x,y,z,X,Y);
% surf(X,Y,Z)

```

end

```

function [RawS21,S11,S22,S21,S12] = Read_Sparameter(suffix)
% S-para have be measured in linear |Gamma|/Phase mode#2
% saved as CSV file directly from VNA.

```

```

T_11 = readtable(['S11_', suffix, '.csv'], 'HeaderLines',1);
T_11 = T_11{:,:};
Gammas_Sp(:,1) = T_11(:,2) .* exp(1i*T_11(:,3)*pi/180) ;

```

```

T_22 = readtable(['S22_', suffix, '.csv'], 'HeaderLines',1);
T_22 = T_22{:,:};
Gammas_Sp(:,2) = T_22(:,2) .* exp(1i*T_22(:,3)*pi/180) ;

```

```

T_21 = readtable(['S21_', suffix, '.csv'], 'HeaderLines',1);
T_21 = T_21{:,:};
Gammas_Sp(:,3) = T_21(:,2) .* exp(1i*T_21(:,3)*pi/180) ;

```

```

T_12 = readtable(['S12_', suffix, '.csv'], 'HeaderLines',1);
T_12 = T_12{:,:};
Gammas_Sp(:,4) = T_12(:,2) .* exp(1i*T_12(:,3)*pi/180) ;

```

```

S11 = Gammas_Sp(:,1);
S22 = Gammas_Sp(:,2);
S21 = Gammas_Sp(:,3);
S12 = Gammas_Sp(:,4);

```

```

RawS21 = T_21(:,2);
end

```

```

function [] = SmithPlot(Gammas,Data,Cres,Dmax,Dmin,ThreFlag,markersize)

```

```

% Set up color scale
% Cres = 256;
% map = flipud( parula(Cres) );
map = ( parula(Cres) );
% Dmax = 5;

```



```

% Dmin = 0;
% Thresholding data to maximum value
if ThreFlag == "Higher"
    Above = Data >Dmax;% don't see value above threshold
    Data = (1-Above).* Data + Above.*(Dmax);
    Color_Index = ceil( rescale(Data, 1 , 256) );
elseif ThreFlag == "Lower"
    Below = Data <Dmin;
    Data = (1-Below).* Data + Below.*(Dmin);
    Color_Index = ceil( rescale(Data, 1 , 256) );
elseif ThreFlag == "None"
    Data = Data;
    Color_Index = ceil( rescale(Data, 1 , 256) );
elseif ThreFlag == "2color"
    Above = Data >Dmax;
    Below = Data <= Dmax;
    Color_Index = Above*Cres + Below*1;
elseif ThreFlag == "2color_Flag"
    Above = Data;
    Below = ~Data;
    Color_Index = Above*Cres + Below*1;
end

[lines, hsm] = smithchart();
hold on
for i = 1:size(Gammas,2)% fliplr(1:size(Gammas,2))
    if i==950
        stophere=1;
    end
    [lines, hsm] = smithchart(Gammas(i));
    set(lines,'Marker', 'o','MarkerSize',markersize)
    set(lines,'Color', map(Color_Index(i,:), 'MarkerSize',markersize);
    set(lines, 'MarkerFaceColor', get(lines, 'Color'));
%     set(lines, 'Color', ThreshNF(NFs(i)));
end
hold off

end

function [] =
SmithPlot_ProgressReport(Z_right,Data,Cres,Dmax,Dmin,ThreFlag,markersiz
e,NF_Area,Nuclei,VI2)

Gammas = conj(z2gamma( Z_right )');
% 2H at 3.2680 MHz  43
% 31P at 8.6175 MHz, 115
% 1H at 21.2850 MHz, index at 284

```

```

% Freq_27MHZ_Index = 34; %17O 27.1284MHz
% Freq_30MHZ_Index = 43; %2H 30.7192 MHz
% Freq_50MHZ_Index = 78; %13C, 50.3294MHZ
% Freq_53MHZ_Index = 115; %23Na
% Freq_53MHZ_Index = 201; %23Na
% Freq_81MHZ_Index = 136; %31P, 81.0045MHZ
% Freq_188MHZ_Index = 341; %19F, 188.24MHZ
% Freq_200MHZ_Index = 284; %1H

% Freq_50MHZ_Index = 204; % 13C
% Freq_53MHZ_Index = 225; %23Na

% Freq_27MHZ_Index = 34; %17O 27.1284MHz
Freq_30MHZ_Index = 48; %2H 30.7192 MHz
Freq_50MHZ_Index = 114; %13C, 50.3294MHZ
Freq_53MHZ_Index = 181; %23Na
% Freq_53MHZ_Index = 201; %23Na
Freq_81MHZ_Index = 248; %31P, 81.0045MHZ
Freq_188MHZ_Index = 314; %19F, 188.24MHZ
Freq_200MHZ_Index = 381; %1H

% Set up color scale
% Cres = 256;
% map = flipud( parula(Cres) );
map = ( parula(Cres) );
% Dmax = 5;
% Dmin = 0;
% Thresholding data to maximum value
if ThreFlag == "Higher"
    Above = Data > Dmax;
    Data = (1-Above).* Data + Above.*(Dmax);
    Color_Index = ceil( rescale(Data, 1 , 256) );
elseif ThreFlag == "Lower"
    Below = Data < Dmin;
    Data = (1-Below).* Data + Below.*(Dmin);
    Color_Index = ceil( rescale(Data, 1 , 256) );
elseif ThreFlag == "None"
    Data = Data;
    Color_Index = ceil( rescale(Data, 1 , 256) );
elseif ThreFlag == "2color"
    Above = Data > Dmax;
    Below = Data <= Dmax;
    Color_Index = Above*Cres + Below*1;
end

[lines, hsm] = smithchart();
hold on
for i = 1:size(Gammas,2)
    [lines, hsm] = smithchart(Gammas(i));

```

```

set(lines,'Marker','o','MarkerSize',markersize)
set(lines,'Color',map(Color_Index(i,:),),'MarkerSize',markersize);
% set(lines,'Color',ThreshNF(NFs(i)));
if i <= 400
    x1 = real(Gammas(i));
    x2 = real(Gammas(i+1));
    y1 = imag(Gammas(i));
    y2 = imag(Gammas(i+1));
    plot([x1 x2],[y1 y2], 'Color','b')
end
end
hold off

if NF_Area == "NF_Area_On"
    % Area for good NF
    hold on

    r = 0.3;
    xc = 0.57;
    yc = 0.38;
    theta = linspace(0,2*pi);
    x = r*cos(theta) + xc;
    y = r*sin(theta) + yc;
    plot(x,y, 'b')

    r = 0.32;
    xc = 0.66;
    yc = 0.09;
    theta = linspace(0,2*pi);
    x = r*cos(theta) + xc;
    y = r*sin(theta) + yc;
    plot(x,y, 'r')
    %
    % r = 0.6;
    % xc = 0;
    % yc = 0;
    % theta = linspace(0,2*pi);
    % x = r*cos(theta) + xc;
    % y = r*sin(theta) + yc;
    % plot(x,y, 'r')
    % r = 0.9;
    % x = r*cos(theta) + xc;
    % y = r*sin(theta) + yc;
    % plot(x,y, 'r')
    % line([0,0.5504],[0,0.7987])
    % line([0,0.9011],[0,0.3799])
    % line([0,0.8879],[0,-0.4594])
    hold off
end

if Nuclei == "Nuclei_On"

```

```

hold on
%
% plot(real( z2gamma(Z_right(Freq_27MHZ_Index))
),imag(z2gamma(Z_right(Freq_27MHZ_Index))),'ro','LineWidth',3,'Color',
'k');
% text(real( z2gamma(Z_right(Freq_27MHZ_Index))
)+0.1,imag(z2gamma(Z_right(Freq_27MHZ_Index)))+0.1,["30MHZ ",
num2str(Z_right(Freq_27MHZ_Index)) ],'Color', 'k');

plot(real( z2gamma(Z_right(Freq_30MHZ_Index))
),imag(z2gamma(Z_right(Freq_30MHZ_Index))),'ro','LineWidth',3,'Color',
'm');
text(real( z2gamma(Z_right(Freq_30MHZ_Index))
)+0.1,imag(z2gamma(Z_right(Freq_30MHZ_Index)))+0.1,["30MHz ",
num2str(Z_right(Freq_30MHZ_Index)) ],'Color', 'm');

plot(real( z2gamma(Z_right(Freq_50MHZ_Index))
),imag(z2gamma(Z_right(Freq_50MHZ_Index))),'ro','LineWidth',3,'Color',
'b');
text(real( z2gamma(Z_right(Freq_50MHZ_Index))
)+0.1,imag(z2gamma(Z_right(Freq_50MHZ_Index)))+0.1,["40MHz ",
num2str(Z_right(Freq_50MHZ_Index)) ],'Color', 'b');

plot(real( z2gamma(Z_right(Freq_53MHZ_Index))
),imag(z2gamma(Z_right(Freq_53MHZ_Index))),'ro','LineWidth',3,'Color',
'r');
text(real( z2gamma(Z_right(Freq_53MHZ_Index))
)+0.1,imag(z2gamma(Z_right(Freq_53MHZ_Index)))+0.1,["50MHz ",
num2str(Z_right(Freq_53MHZ_Index)) ],'Color', 'r');

plot(real( z2gamma(Z_right(Freq_81MHZ_Index))
),imag(z2gamma(Z_right(Freq_81MHZ_Index))),'ro','LineWidth',3,'Color',
'g');
text(real( z2gamma(Z_right(Freq_81MHZ_Index))
)+0.1,imag(z2gamma(Z_right(Freq_81MHZ_Index)))+0.1,["60MHz ",
num2str(Z_right(Freq_81MHZ_Index)) ],'Color', 'g');

plot(real( z2gamma(Z_right(Freq_188MHZ_Index))
),imag(z2gamma(Z_right(Freq_188MHZ_Index))),'ro','LineWidth',3,'Color',
'm');
text(real( z2gamma(Z_right(Freq_188MHZ_Index))
)+0.1,imag(z2gamma(Z_right(Freq_188MHZ_Index)))+0.1,["70MHz ",
num2str(Z_right(Freq_188MHZ_Index)) ],'Color', 'm');

plot(real( z2gamma(Z_right(Freq_200MHZ_Index))
),imag(z2gamma(Z_right(Freq_200MHZ_Index))),'ro','LineWidth',3
,'Color', 'b');
text(real( z2gamma(Z_right(Freq_200MHZ_Index))
)+0.1,imag(z2gamma(Z_right(Freq_200MHZ_Index)))+0.1,["80MHZ ",
num2str(Z_right(Freq_200MHZ_Index)) ],'Color', 'b');

hold off

```

```

end

if Nuclei == "Nuclei_On_Voltage"
hold on

% plot(real( z2gamma(Z_right(Freq_27MHZ_Index))
),imag(z2gamma(Z_right(Freq_27MHZ_Index))),'ro','LineWidth',3,'Color',
'k');
% text(real( z2gamma(Z_right(Freq_27MHZ_Index))
)+0.1,imag(z2gamma(Z_right(Freq_27MHZ_Index)))+0.1,["27MHZ ",
num2str(VI2(Freq_27MHZ_Index)) "Voltz" ],'Color', 'k');
%
% plot(real( z2gamma(Z_right(Freq_30MHZ_Index))
),imag(z2gamma(Z_right(Freq_30MHZ_Index))),'ro','LineWidth',3,'Color',
'm');
% text(real( z2gamma(Z_right(Freq_30MHZ_Index))
)+0.1,imag(z2gamma(Z_right(Freq_30MHZ_Index)))+0.1,["3.2MHZ ",
num2str(VI2(Freq_30MHZ_Index)) "Voltz" ],'Color', 'm');

plot(real( z2gamma(Z_right(Freq_50MHZ_Index))
),imag(z2gamma(Z_right(Freq_50MHZ_Index))),'ro','LineWidth',3,'Color',
'b');
text(real( z2gamma(Z_right(Freq_50MHZ_Index))
)+0.1,imag(z2gamma(Z_right(Freq_50MHZ_Index)))+0.1,["13C ",
num2str(VI2(Freq_50MHZ_Index)) "dB" ],'Color', 'b');

plot(real( z2gamma(Z_right(Freq_53MHZ_Index))
),imag(z2gamma(Z_right(Freq_53MHZ_Index))),'ro','LineWidth',3,'Color',
'r');
text(real( z2gamma(Z_right(Freq_53MHZ_Index))
)+0.1,imag(z2gamma(Z_right(Freq_53MHZ_Index)))+0.1,["23Na ",
num2str(VI2(Freq_53MHZ_Index)) "dB"],'Color', 'r');

% plot(real( z2gamma(Z_right(Freq_81MHZ_Index))
),imag(z2gamma(Z_right(Freq_81MHZ_Index))),'ro','LineWidth',3,'Color',
'g');
% text(real( z2gamma(Z_right(Freq_81MHZ_Index))
)+0.1,imag(z2gamma(Z_right(Freq_81MHZ_Index)))+0.1,["81MHZ ",
num2str(VI2(Freq_81MHZ_Index)) "Voltz" ],'Color', 'g');
%
% plot(real( z2gamma(Z_right(Freq_188MHZ_Index))
),imag(z2gamma(Z_right(Freq_188MHZ_Index))),'ro','LineWidth',3,'Color',
'm');
% text(real( z2gamma(Z_right(Freq_188MHZ_Index))
)+0.1,imag(z2gamma(Z_right(Freq_188MHZ_Index)))+0.1,["188MHZ ",
num2str(VI2(Freq_188MHZ_Index)) "Voltz" ],'Color', 'm');

% plot(real( z2gamma(Z_right(Freq_200MHZ_Index))
),imag(z2gamma(Z_right(Freq_200MHZ_Index))),'ro','LineWidth',3
,'Color', 'b');

```

```

% text(real( z2gamma(Z_right(Freq_200MHZ_Index)
)+0.1,imag(z2gamma(Z_right(Freq_200MHZ_Index)))+0.1,[ "21.2MHZ",
num2str(VI2(Freq_200MHZ_Index)) "Voltz" ],'Color', 'b');
hold off

end

end

function [] = SmithPlot_NF_Contour(Z_right,Data,markersize)

[X,Y] = size(Z_right);

[lines, hsm] = smithchart();

P_ring = 500;

for i = 1:Y

    Contour_1(i,:) = (Z_right(i)) + 1i*linspace(0,10000,P_ring);
    Contour_2(i,:) = Z_right(i) - 1i*linspace(10000,0,P_ring);
    Contour_Z(i,:) = cat(2,Contour_1(i,:),Contour_2(i,:));
    Contour_Gamma(i,:) = z2gamma( Contour_Z(i,:));

Gammas = Contour_Gamma(i,:);
hold on
for i = 1:size(Gammas,2)
    [lines, hsm] = smithchart(Gammas(i));
    set(lines,'Marker', 'o','MarkerSize',0.1)
%     set(lines,'Color',
map(Color_Index(i,:),),'MarkerSize',markersize);
%     set(lines,'Color', ThreshNF(NFs(i)));
    if i <= ( P_ring*2 - 1 )
        x1 = real(Gammas(i));
        x2 = real(Gammas(i+1));
        y1 = imag(Gammas(i));
        y2 = imag(Gammas(i+1));
        plot( [x1 x2],[y1 y2] , 'Color','b')
    end
end
hold off

```

```
end
```

```
end
```

```
function [] =  
SmithPlot2(Z_right,Data,Cres,Dmax,Dmin,ThreFlag,markersize,NF_Area,Nucl  
ei,VI2)
```

```
Gamma = conj(z2gamma( Z_right )');
```

```
Freq_27MHZ_Index = 34; %17O 27.1284MHZ  
Freq_30MHZ_Index = 40; %2H 30.7192 MHZ  
Freq_50MHZ_Index = 78; %13C, 50.3294MHZ  
Freq_53MHZ_Index = 83; %23Na  
Freq_81MHZ_Index = 136; %31P, 81.0045MHZ  
Freq_188MHZ_Index = 341; %19F, 188.24MHZ  
Freq_200MHZ_Index = 363; %1H
```

```
% Set up color scale
```

```
% Cres = 256;
```

```
% map = flipud( parula(Cres) );
```

```
map = ( parula(Cres) );
```

```
% Dmax = 5;
```

```
% Dmin = 0;
```

```
% Thresholding data to maximum value
```

```
if ThreFlag == "Higher"
```

```
    Above = Data > Dmax;
```

```
    Data = (1-Above).* Data + Above.*(Dmax);
```

```
    Color_Index = ceil( rescale(Data, 1 , 256) );
```

```
elseif ThreFlag == "Lower"
```

```
    Below = Data < Dmin;
```

```
    Data = (1-Below).* Data + Below.*(Dmin);
```

```
    Color_Index = ceil( rescale(Data, 1 , 256) );
```

```
elseif ThreFlag == "None"
```

```
    Data = Data;
```

```
    Color_Index = ceil( rescale(Data, 1 , 256) );
```

```
elseif ThreFlag == "2color"
```

```
    Above = Data > Dmax;
```

```
    Below = Data <= Dmax;
```

```
    Color_Index = Above*Cres + Below*1;
```

```
end
```

```
[lines, hsm] = smithchart();
```

```
hold on
```

```
for i = 1:size(Gamma,2)
```

```
    [lines, hsm] = smithchart(Gamma(i));
```

```
    set(lines,'Marker','o','MarkerSize',markersize)
```

```

        set(lines,'Color', map(Color_Index(i),:),'MarkerSize',markersize);
    %     set(lines,'Color', ThreshNF(NFs(i)));
end
hold off

if NF_Area == "NF_Area_On"
    % Area for good NF
    hold on

    r = 0.3;
    xc = 0.57;
    yc = 0.38;
    theta = linspace(0,2*pi);
    x = r*cos(theta) + xc;
    y = r*sin(theta) + yc;
    plot(x,y, 'b')

    r = 0.32;
    xc = 0.66;
    yc = 0.09;
    theta = linspace(0,2*pi);
    x = r*cos(theta) + xc;
    y = r*sin(theta) + yc;
    plot(x,y, 'r')
    %
    % r = 0.6;
    % xc = 0;
    % yc = 0;
    % theta = linspace(0,2*pi);
    % x = r*cos(theta) + xc;
    % y = r*sin(theta) + yc;
    % plot(x,y, 'r')
    % r = 0.9;
    % x = r*cos(theta) + xc;
    % y = r*sin(theta) + yc;
    % plot(x,y, 'r')
    % line( [0,0.5504] , [0,0.7987] )
    % line( [0,0.9011] , [0,0.3799] )
    % line( [0,0.8879] , [0,-0.4594] )
    hold off
end

if Nuclei == "Nuclei_On"

    hold on
    %
    % plot(real( z2gamma(Z_right(Freq_27MHZ_Index))
    % ),imag(z2gamma(Z_right(Freq_27MHZ_Index))),'ro','LineWidth',3,'Color',
    % 'k');

```



```

% text(real( z2gamma(Z_right(Freq_27MHZ_Index))
)+0.1,imag(z2gamma(Z_right(Freq_27MHZ_Index)))+0.1,["27MHZ ",
num2str(Z_right(Freq_27MHZ_Index)) ],'Color', 'k');
%
plot(real( z2gamma(Z_right(Freq_30MHZ_Index))
),imag(z2gamma(Z_right(Freq_30MHZ_Index))),'ro','LineWidth',3,'Color',
'm');
text(real( z2gamma(Z_right(Freq_30MHZ_Index))
)+0.1,imag(z2gamma(Z_right(Freq_30MHZ_Index)))+0.1,["30MHZ ",
num2str(Z_right(Freq_30MHZ_Index)) ],'Color', 'm');

plot(real( z2gamma(Z_right(Freq_50MHZ_Index))
),imag(z2gamma(Z_right(Freq_50MHZ_Index))),'ro','LineWidth',3,'Color',
'c');
text(real( z2gamma(Z_right(Freq_50MHZ_Index))
)+0.1,imag(z2gamma(Z_right(Freq_50MHZ_Index)))+0.1,["50MHZ ",
num2str(Z_right(Freq_50MHZ_Index)) ],'Color', 'c');

plot(real( z2gamma(Z_right(Freq_53MHZ_Index))
),imag(z2gamma(Z_right(Freq_53MHZ_Index))),'ro','LineWidth',3,'Color',
'r');
text(real( z2gamma(Z_right(Freq_53MHZ_Index))
)+0.1,imag(z2gamma(Z_right(Freq_53MHZ_Index)))+0.1,["53MHZ ",
num2str(Z_right(Freq_53MHZ_Index)) ],'Color', 'r');

plot(real( z2gamma(Z_right(Freq_81MHZ_Index))
),imag(z2gamma(Z_right(Freq_81MHZ_Index))),'ro','LineWidth',3,'Color',
'g');
text(real( z2gamma(Z_right(Freq_81MHZ_Index))
)+0.1,imag(z2gamma(Z_right(Freq_81MHZ_Index)))+0.1,["81MHZ ",
num2str(Z_right(Freq_81MHZ_Index)) ],'Color', 'g');

plot(real( z2gamma(Z_right(Freq_188MHZ_Index))
),imag(z2gamma(Z_right(Freq_188MHZ_Index))),'ro','LineWidth',3,'Color',
'm');
text(real( z2gamma(Z_right(Freq_188MHZ_Index))
)+0.1,imag(z2gamma(Z_right(Freq_188MHZ_Index)))+0.1,["188MHZ ",
num2str(Z_right(Freq_188MHZ_Index)) ],'Color', 'm');

plot(real( z2gamma(Z_right(Freq_200MHZ_Index))
),imag(z2gamma(Z_right(Freq_200MHZ_Index))),'ro','LineWidth',3
,'Color', 'b');
text(real( z2gamma(Z_right(Freq_200MHZ_Index))
)+0.1,imag(z2gamma(Z_right(Freq_200MHZ_Index)))+0.1,["200MHZ ",
num2str(Z_right(Freq_200MHZ_Index)) ],'Color', 'b');
hold off

end

if Nuclei == "Nuclei_On_Voltage"
hold on

```

```

% plot(real( z2gamma(Z_right(Freq_27MHZ_Index))
),imag(z2gamma(Z_right(Freq_27MHZ_Index))),'ro','LineWidth',3,'Color',
'k');
% text(real( z2gamma(Z_right(Freq_27MHZ_Index))
)+0.1,imag(z2gamma(Z_right(Freq_27MHZ_Index)))+0.1,["27MHZ ",
num2str(VI2(Freq_27MHZ_Index)) "Voltz" ],'Color', 'k');
%
plot(real( z2gamma(Z_right(Freq_30MHZ_Index))
),imag(z2gamma(Z_right(Freq_30MHZ_Index))),'ro','LineWidth',3,'Color',
'm');
text(real( z2gamma(Z_right(Freq_30MHZ_Index))
)+0.1,imag(z2gamma(Z_right(Freq_30MHZ_Index)))+0.1,["30MHZ ",
num2str(VI2(Freq_30MHZ_Index)) "Voltz" ],'Color', 'm');

plot(real( z2gamma(Z_right(Freq_50MHZ_Index))
),imag(z2gamma(Z_right(Freq_50MHZ_Index))),'ro','LineWidth',3,'Color',
'c');
text(real( z2gamma(Z_right(Freq_50MHZ_Index))
)+0.1,imag(z2gamma(Z_right(Freq_50MHZ_Index)))+0.1,["50MHZ ",
num2str(VI2(Freq_50MHZ_Index)) "Voltz" ],'Color', 'c');

plot(real( z2gamma(Z_right(Freq_53MHZ_Index))
),imag(z2gamma(Z_right(Freq_53MHZ_Index))),'ro','LineWidth',3,'Color',
'r');
text(real( z2gamma(Z_right(Freq_53MHZ_Index))
)+0.1,imag(z2gamma(Z_right(Freq_53MHZ_Index)))+0.1,["53MHZ ",
num2str(VI2(Freq_53MHZ_Index)) "Voltz"],'Color', 'r');

% plot(real( z2gamma(Z_right(Freq_81MHZ_Index))
),imag(z2gamma(Z_right(Freq_81MHZ_Index))),'ro','LineWidth',3,'Color',
'g');
% text(real( z2gamma(Z_right(Freq_81MHZ_Index))
)+0.1,imag(z2gamma(Z_right(Freq_81MHZ_Index)))+0.1,["81MHZ ",
num2str(VI2(Freq_81MHZ_Index)) "Voltz" ],'Color', 'g');
%
% plot(real( z2gamma(Z_right(Freq_188MHZ_Index))
),imag(z2gamma(Z_right(Freq_188MHZ_Index))),'ro','LineWidth',3,'Color',
'm');
% text(real( z2gamma(Z_right(Freq_188MHZ_Index))
)+0.1,imag(z2gamma(Z_right(Freq_188MHZ_Index)))+0.1,["188MHZ ",
num2str(VI2(Freq_188MHZ_Index)) "Voltz" ],'Color', 'm');

plot(real( z2gamma(Z_right(Freq_200MHZ_Index))
),imag(z2gamma(Z_right(Freq_200MHZ_Index))),'ro','LineWidth',3
,'Color', 'b');
text(real( z2gamma(Z_right(Freq_200MHZ_Index))
)+0.1,imag(z2gamma(Z_right(Freq_200MHZ_Index)))+0.1,["200MHZ",
num2str(VI2(Freq_200MHZ_Index)) "Voltz" ],'Color', 'b');
hold off

end

end

```

```

function [CL,RL,CS,RS] = Stability_Circle(Freq, markersize, Cres,
Gamma_s, S11, S22, S21, S12, Freq_Index)

Gamma_in = S11(Freq_Index) + ( (
S12(Freq_Index)*S21(Freq_Index)*Gamma_s) ./ (1 - S22(Freq_Index)*Gamma_s)
) ;
Gamma_in = abs(Gamma_in);
Gamma_out = S22(Freq_Index) + ( (
S12(Freq_Index)*S21(Freq_Index)*Gamma_s) ./ (1-S11(Freq_Index)*Gamma_s
) );
Gamma_out = abs(Gamma_out);

Delta = S11(Freq_Index)*S22(Freq_Index)-
S12(Freq_Index)*S21(Freq_Index);
CL = conj( S22(Freq_Index) - Delta * conj(S11(Freq_Index)) ) / (
abs(S22(Freq_Index))^2 - abs(Delta)^2 );
RL = abs( ( S12(Freq_Index)*S21(Freq_Index) ) / (
abs(S22(Freq_Index))^2 - abs(Delta)^2 ) );

CS = conj( S11(Freq_Index) - Delta * conj(S22(Freq_Index)) ) / (
abs(S11(Freq_Index))^2 - abs(Delta)^2 );
RS = abs( ( S12(Freq_Index)*S21(Freq_Index) ) / (
abs(S11(Freq_Index))^2 - abs(Delta)^2 ) );

F = num2str( Freq(Freq_Index)*1e-6 );

figure
SmithPlot( Gamma_s ,Gamma_in,Cres,1,0,"2color",markersize)
title([F, ' MHz'], 'Stability vs Load Z, yellow-unstable, blue-stable
', ' ' })
figure
SmithPlot( Gamma_s ,Gamma_out,Cres,1,0,"2color",markersize)
title([F, ' MHz'], 'Stability vs Source Z, yellow-unstable, blue-
stable ', ' ' })

end

function [Zt] = TransmissionLine_Z(Z0, L_Phy, Freq, Zl)

Er = 2.23;
Lambda = 3e8 ./ (Freq*sqrt(Er)); %lambda
L = L_Phy ./ Lambda;
Zt = Z0* (Zl+Z0*1i*tan(L*2*pi))./(Z0+Zl.*1i.*tan(L*2*pi));

end

```

```
function [Z] = Z(LorC, Freq, CompValue)
if LorC == 'L'
    Z = 1i*2*pi*Freq*CompValue;
elseif LorC == 'C'
    Z = 1./ (1i*2*pi*Freq*CompValue);
end

end
```